esa

SP-391

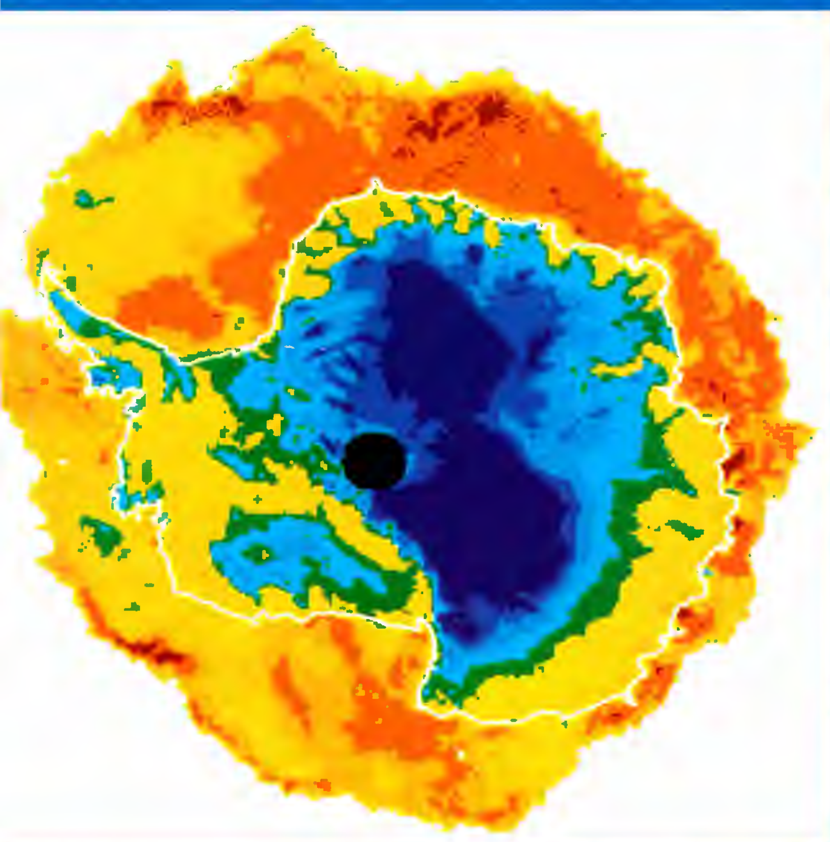

Fourth Circumpolar Symposium on

Remote Sensing of the Polar Environments

TUD Lyngby, Denmark

29 April – 1 May 1996

European Space Agency
Agence spatiale européenne

esa SP-391
July 1996

Fourth Circumpolar Symposium on

Remote Sensing of the Polar Environments

Lyngby, Denmark
29 April – 1 May 1996

Organised by: Danish Polar Center, Copenhagen

Sponsored by: Commission for Scientific Research in Greenland
Technical University of Denmark
European Space Agency
and European Association of Remote Sensing Laboratories

european space agency / agence spatiale européenne

ESA SP-391

Proceedings of the Fourth Circumpolar Symposium on Remote Sensing of the Polar Environments

TUD, Lyngby, Denmark, 29 April – 1 May 1996

Published by:	ESA Publications Division ESTEC, Noordwijk, The Netherlands
Compiled by:	T.-D. Guyenne
Price Code:	80 Dfl.
Copyright	© 1996 European Space Agency
ISBN 92-9092-247-8	Printed in The Netherlands

CONTENTS

PREFACE
P. Gudmandsen, *Symposium Chairman* 7

GENERAL

SAR DATA AND RESEARCH TOOLS TO SUPPORT HIGH-LATITUDE RESEARCH
T. H. George, *University of Alaska Fairbanks* 11

SNOW
K. Nadji, *MRAIC, OAQ* 13

CLIMATE, ATMOSPHERE, RADIATION

SATELLITE DETECTION OF ENHANCED GREENHOUSE WARMING IN THE POLAR REGIONS: SEASONAL ASPECTS AND IMPLICATIONS OF RECENT SEA ICE TRENDS
M. Miles, O. M Johannessen & E. Bjorgo, *Nansen ERSC & Univ. of Bergen* 21

INTERANNUAL VARIABILITY OF SEA ICE IN THE GRENNLAND SEA
L. Toudal, *TUD Lyngby* 22

TOVS PATH-P: A PATHFINDER DATASET OF ATMOSPHERIC AND SURFACE VARIABLES FOR PROCESS AND CLIMATE STUDIES OF THE ARCTIC BASIN
A. Schweiger, D. Rothrock & J. Francis, *Univ. of Washington, Seattle & Rutgers Univ.* 23

RADNET: A NEURAL NETWORK-BASED APPROACH TO THE RETRIEVAL OF THE SURFACE RADIATION FLUXES OF THE ARCTIC FROM TOVS BRIGHTNESS TEMPERATURES
A. Schweiger & J. Key, *Univ. of Washington & Boston Univ.* 24

SHIP-BASED REMOTE MEASUREMENTS OF STRATOSPHERIC NITROGEN DIOXIDE IN THE WEDDELL SEA, ANTARCTICA
A. S. Elokhov & A. N. Gruzdev, *Inst. of Atmospheric Physics* 25

ANALYSIS OF ANNUAL TEMPERATURE VARIATION IN THE TROPOSPHERE, STRATOSPHERE AND MESOSPHERE USING SATELLITE MEASUREMENTS
A. N. Gruzdev, *Inst. of Atmospheric Physics* 26

DETERMINATION AND INTERCOMPARISON OF RADIATION FLUXES AND NET RADIATION USING LANDSAT-TM DATA OF LIEFDEFJORDEN/NW-SPITSBERGEN
E. Parlow, *Univ. of Basel* 27

ESTIMATION OF THE SOIL HEAT FLUX/NET RADIATION RATIO OVER HIGH-LATITUDE NATURAL VEGETATION USING SPECTRAL VEGETATION INDICES
A. Jacobsen & B. U. Hansen, *Univ. of Copenhagen* 33

THE USE OF COINCIDENT DMSP SSM/I AND OLS SATELLITE DATA TO DETECT SNOW COVER
A. P. Standley & E. C. Barrett, *Univ. of Bristol* 39

GLACIERS AND SNOW

GLACIER MAPPING AND INVENTORY OF THE ILLECILLEWAET RIVER BASIN, BC, CANADA, USING LANDSAT-TM AND DIGITAL ELEVATION DATA
R. W. Sidjak & R. D. Wheate, *Univ. of Northern BC* 47

LANDSAT-TM-BASED MODELLING OF THE SNOW-MELT IN NW-SPITSBERGEN
M. Brun & D. Scherer, *Univ. of Basel* 52

TRANSFORMATION OF SPOT-HRV SCENES AND DIGITAL AERIAL PHOTOGRAPHS FROM A CENTRAL PROJECTION TO ORTHO-IMAGES: EXAMPLES FROM KRONEBREEN, N-NORWAY
C. Rolstad, J. Amlien & J. Kohler, *Norwegian Polar Inst. & Norw. Water Res. & Energy Managt.* 53

GLACIOLOGICAL STUDIES OF MELT-SENSITIVE AREAS IN DRONNING MAUD LAND, ANTARCTICA, USING LANDSAT-TM AND ERS-1 SAR DATA
J-G. Winther & O. Dalen, *Norwegian Polar Inst. & Univ. of Trondheim* 55

SAR INTERFEROMETRY FOR ANTARCTIC ICE AND SEA ICE
H. Kimura & al., *Hokkaido University of Education* 56

GEOSTATISTICAL APPROACHES TO INTERPOLATION AND CLASSIFICATION OF REMOTE-SENSING DATA FROM ICE SURFACES
U. Ch. Herzfeld & al., *Universität Trier & Univ. of Colorado* 59

SIMULTANEOUS OBSERVATIONS OF GLACIER NEAR-SURFACE PROPERTIES BY SATELLITE AND GROUND RADAR INSTRUMENTS
R. Engeset, *Dept. of Physical Geography* 65

LANDSAT-TM DATA AND GROUND RADIOMETER MEASUREMENTS FOR SNOW AND ICE-TYPE CLASSIFICATION IN THE VESTFOLD HILLS, EAST ANTARCTICA
L. Boresjö Bronge & Ch. Bronge, *Stockholm Univ.* 71

NEW RESULTS FROM MAPPING ANTARCTICA AT HIGH RESOLUTION FROM RADAR ALTIMETER
M. Matassa & al., *Univ. of Colorado & Univ. Trier* 81

IMAGE ANALYSIS BY GEOSTATISTICAL AND NEURAL-NETWORK METHODS APPLICATIONS IN GLACIOLOGY
U. Ch. Herzfeld & al., *Univ. Trier & Univ. of Colorado* 87

SEA ICE

EARLY RESULTS OF THE USE OF RADARSAT SCANSAR DATA IN THE CANADIAN ICE SERVICE
B. R. Ramsay & al., *Canadian Ice Service* 95

RADARSAT STATUS AND EARLY EXPERIENCE IN SEA ICE APPLICATIONS
M. Manore & B. Ramsay, *CCRS & Ice Services Environment Canada* 100

SEA ICE DRIFT IN THE EAST GREENLAND CURRENT
Th. Martin, *Alfred-Wegener Inst. for Polar & Marine Research* 101

ICE EDGE DETERMINATION IN THE GREENLAND WATERS USING FIRST-ORDER TEXTURE PARAMETERS OF THE ERS-SAR IMAGES
R. S. Gill, *Danish Meteorological Institute* 107

SEA ICE CHARACTERISTICS AND BACKSCATTER VARIABILITY IN THE BELLINGSHAUSEN SEA
K. Morris, M. Jeffries & S. Li, *Geophysical Institute, Univ. Alaska* 113

MULTIFREQUENCY SCATTEROMETER MEASUREMENTS OF BALTIC SEA ICE DURING EMAC '95
M. Petterson, W. Dierking & J. Askne, *Chalmers Univ. of Technology* 118

AIRBORNE LINE SCANNER MEASUREMENTS FOR ERS-1 SAR INTERPRETATION OF SEA ICE
A. Bochert, *Alfred-Wegener Institute for Polar & Marine Research* 119

ARCTIC OCEAN MELT SEASON CHARACTERISTICS AND SEA ICE MELT POND FRACTIONS USING ERS-1 SAR
M.O. Jeffries, K. Schwartz & S. Li, *Univ. of Alaska Fairbanks* 127

AIR MONITORING OF ICE CONDITIONS IN THE ARCTIC SEAS
V. I. Chernook & V. B. Zabavnikov, *Knipovich Polar Research Institute (PINRO)* 133

GEOLOGY, VULCANOLOGY

LITHOLOGIC MAPPING BY FIELD AND SATELLITE MULTISPECTRAL DATA, TARN FLAT
R. Casacchia & al., *CNR & Univ. degli Studi Roma* 141

QUANTITATIVE MAPPING OF ACTIVE AEOLIAN SURFACES IN NORTHERN FENNOSCANDIA – LANDSAT-TM HYBRID CLASSIFICATION
J. Käyhkö, K. Pye & P. Worsley, *Research Inst. for Sedimentology, Reading Univ.* 147

USE OF SAR DATA TO STUDY ACTIVE VOLCANOES IN ALASKA
K. G. Dean & al., *Univ. of Alaska Fairbanks* 153

ENVIRONMENT, VEGETATION, BIOLOGY

MAPPING PLANT COMMUNITIES IN A LOCAL ARCTIC LANDSCAPE APPLYING SCANNED INFRARED AERIAL PHOTOGRAPHS IN A GIS
L. Nilsen, Th. Brossard & D. Joly, *Univ. of Tromsö & Univ. de Franche-Comté* 159

SUMMER ENVIRONMENTAL MAPPING APPLICATIONS OF A LARGE-SCALE MOSAIC OF THE STATE OF ALASKA GENERATED FROM ERS-1 SAR IMAGES
S. Li & al., *Univ. of Alaska Fairbanks* 169

SER-1 SAR MONITORING OF ICE GROWTH ON SHALLOW LAKES TO DETERMINE WATER DEPTH AND AVAILABILITY IN N-W ALASKA
M. Jeffries & K. Morris, *Univ. of Alaska,* G. Liston, *Colorado State Univ.* 177

FOREST BIOMASS ESTIMATION IN NORTHERN EUROPE USING NOAA-AVHRR DATA
T. Häme & al., *CEC/JRC & VIT Automation* 183

IMPROVING THE CLASSIFICATION OF SATELLITE IMAGES FROM HIGH ARCTIC ENVIRONMENT BY MEANS OF MODELLING THE TOPOGRAPHIC INFLUENCE ON THE ILLUMINATION
J. Amlien & O. W. Brude, *Norwegian Polar Institute* 191

MODELLING EVAPOTRANSPIRATION BY MEANS OF SATELLITE AND SYNOP DATA – AN EXAMPLE FROM THE JAMESON LAND, EAST GREENLAND
A. Eiby, *COWI - Consulting Engineers & Planners* 193

MOVEMENTS AND SWIMMING SPEED OF NARWHALS INSTRUMENTED WITH SATELLITE TRANSMITTERS IN MELVILLE BAY, N-W GREENLAND
R. Dietz & M. Heide-Jorgensen, *Nat. Envir. Res. Inst. & Greenland Inst. of Natural Resources* 195

SOME CHARACTERISTICS OF NARWHAL DIVING BEHAVIOUR IN BAFFIN BAY
M. P. Heide-Jorgensen & R. Dietz, *Greenland Inst. of Natural Resources & NERI* 196

REMOTE SENSING DATA USED DURING AERIAL SURVEYS OF SPRING CONCENTRATIONS OF SEABIRDS IN THE SEA ICE EASTERN BAFFIN BAY
A. Mosbech & al., *National Environmental Research Institute & TUD* 197

LIST OF PARTICIPANTS 199

PREFACE

Preben Gudmandsen
Symposium Chairman

Six to seven years ago, a small group of people came to the conclusion that among the many meetings, workshops and symposia that were organised concerning remote sensing of the environment, we were missing one that was directed specifically towards the problems in the Arctic. Due to the specific conditions prevailing in the Arctic environment, with tundra and permafrost, boreal forest and vegetation, sea ice and frozen lakes, the techniques applied should be adjusted to satisfy the applications of the researchers and administrators involved in these areas. Also, due to the inaccessibility and the harsh environment in the areas in question, remote sensing is often the only way of obtaining valuable information about the situation and the environmental changes that might occur due to climate change and the intervention of man.

A First Circumpolar Symposium was therefore called in Yellowknife, Northwest Territory, Canada in May 1990, concerning Remote Sensing of the Arctic Environments, chaired by Helmut Epp. It covered many aspects of Arctic research including satellite and airborne remote sensing and complementary ground measurements of snow and ice, lake and river ice, permafrost, boreal forest and muskox and bison habitats, etc. This successful symposium was followed two years later by another one held in Tromso, Norway and headed by Sigmund Spjelkavik, with contributions largely within the same subjects, including characteristic aspects of 'Eastern Arctic' and Svalbard in particular. In 1994, still another symposium was organised at University of Alaska, Fairbanks, with the same research subjects giving a broad picture of the often multidisciplinary research carried out – and of course with emphasis on problems in Alaska. At this meeting, that was headed by Ken Dean, it was agreed to broaden the range of the following symposia to also include the Antarctic environment, so that the title rightly became *Symposia on Remote Sensing of the Polar Environments.*

At the latest symposium held at the Technical University of Denmark in Lyngby, in April-May 1996, the presentations were of the same nature as previously but now also including papers on Antarctic problems. They fall under the following headings: Climate, Atmosphere & Radiation; Glaciers & Snow; Sea Ice; Geology & Volcanology; and Environment, Vegetation & Biology.

As will be seen from the subsequent pages, the majority of the papers are devoted to 'real' applications of remote sensing for monitoring the Arctic and the Antarctic but they also give examples of new techniques that may be useful for remote sensing in general. The multidisciplinary nature of the symposium was maintained which made it a fascinating, thus following the experiences from previous symposia. About 45 papers were presented during three full days with well-disciplined authors so that management became an easy task.

Unfortunately not all authors have been able to find time to write a contribution to these Proceedings. In those cases only the abstract is included but several of these are so detailed that the reader easily may get the flavour of the work carried out.

The symposium was opened by Dr. Knut Conradsen, Vice-President of the Technical University of Denmark. The opening address was given by Dr. Jens Peter Har Hansen, Chairman of the Commission for Scientific Research in Greenland. Then, Dr. Johnny Johannessen spoke on behalf of the European Space Agency (ESA).

The symposium was sponsored by the Technical University of Denmark, the Commission for Scientific Research in Greenland, the European Space Agency (ESA) and the European Association of Remote Sensing Laboratories (EARSeL). This support is gratefully acknowledged. It was organised with the good assistance of the Danish Polar Center (DCP). The secretary of the symposium, Mrs. Iris Madsen of DCP, did an excellent job in keeping contact with all participants and organising the many details of the meeting.

The present Proceedings are edited and published by the Publications Division of the European Space Agency, ESTEC, Noordwijk, The Netherlands, as was also the Abstract Book that was forwarded to the symposium participants prior to the meeting. This valuable contribution is highly appreciated and the skilful editor, Mr. Tan-Duc Guyenne, is to be warmly thanked.

GENERAL

SYNTHETIC APERTURE RADAR (SAR) DATA AND RESEARCH TOOLS TO SUPPORT HIGH LATITUDE RESEARCH

Thomas H. George
Alaska SAR Facility
Geophysical Institute
University of Alaska Fairbanks
Fairbanks, AK 99775-7320

907-474-7621 phone
907-474-5567 fax
tgeorge@gi.alaska.edu

SHORT PAPER

A new tool for studies of the polar environment is now available to the research community. Synthetic Aperture Radar (SAR) instruments on polar orbiting satellites improve our ability to predictably observe high latitude areas independent of season or weather conditions. As active devices, this class of sensors allows observations to be obtained through cloud cover and during the winter season, when solar illumination is inadequate for passive optical sensors.

SAR data is typically processed into images which may be interpreted visually, combined with other data sets, or evaluated radiometrically to quantify the characteristics of features on the earth's surface. While the ability to obtain reliable observations is a strength of SAR data, the oblique viewing geometry of the sensors induces distortion in moderate to high relief terrain, as can be seen in Fig. 1. Additional processing with digital terrain models may be performed to compensate for this limitation [Logan, et al., 1996]. In addition, current investigations into interferometric processing of SAR data are exploring the use of SAR to generate terrain models from data pairs [Zebker, et al., 1994].

The Alaska SAR Facility (ASF) has been acquiring Synthetic Aperture Radar (SAR) data from a ground station in Fairbanks, Alaska since 1991. Supported by NASA, the facility presently acquires SAR data from ERS-1 and 2, JERS-1, and RADARSAT. The availability of tape recorders on some satellites, and a receiving station in the Antarctic, have expanded our ability to acquire, process, archive and distribute data for the research science community. By the end of 1995, the archives of SAR data at ASF held some 73,000 minutes of SAR signal data, yielding a volume of well in excess of 55 terabytes of data.

Because so much of the information about this project is dynamic, printed documents undergo frequent revisions. ASF has established a World Wide Web site to provide information to current and prospective users of our data (**http://www.asf.alaska.edu/**).

The following are two of the services available on the web site which may be of specific interest to the research community. (1) As routine access to ongoing SAR data has only been available since 1991, the scientific uses of the data are still being actively explored and reported. To help researchers locate recent literature on SAR data, a research bibliography has been developed and is available on the ASF web site. (2) In addition to processing and distributing SAR data to science users, ASF has been involved in developing software tools to facilitate the reading and manipulation of these data sets. A user contributed software library is maintained on the web site to provide convenient access to these tools.

In summary, SAR satellites provide a significant new source of satellite remote sensing data, from ASF and other data providers, which should benefit the high latitude research community. While SAR has qualities which overcome some of the limitations of optical sensors, it is a very different type of data, which must be carefully evaluated to learn its strengths and shortcomings as a tool for polar research.

REFERENCES

Logan T., R. Guritz, S. Li, J. MacMahon, M. Shindle & J. Groves 1996, Generation of a Large-Scale Mosaic of the State of Alaska from ERS-1 SAR Images, proceedings of the 4th Circumpolar Symposium of Remote Sensing of Polar Environment

Zebker H.A., C.L. Werner, P. Rosen, & S. Hensley 1994, Accuracy of Topographic Maps Derived from ERS-1 Interferometric Radar, *Journal of Geophysical Research*, 32 (4), 823-836

Proceedings of the Fourth Symposium on Remote Sensing of the Polar Environments, Lyngby, Denmark, 29 April – 1 May 1996
(ESA SP-391, July 1996)

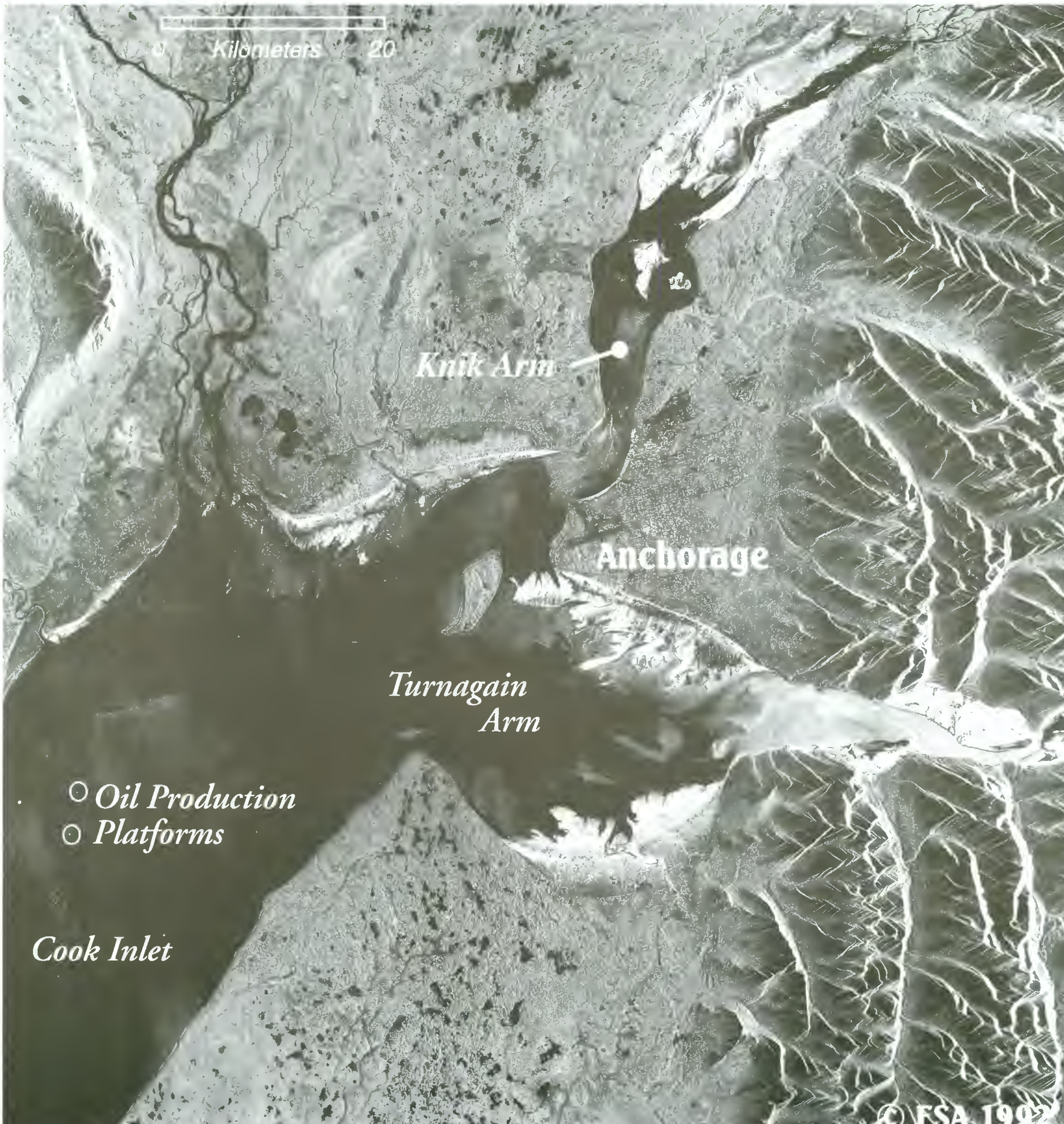

Figure 1. An ERS-1 SAR image of south central Alaska, recorded on 8 August 1992. This image displays a wealth of features including current and/or wave patterns on Cook Inlet, and adjacent water bodies, glacial landforms on the valley bottoms, and major roads and airports in the city of Anchorage. The mountains on the eastern side of the scene depict the geometric distortions characteristic of SAR, in areas of high relief landscapes. Image copyright by the European Space Agency, processed by the Alaska SAR Facility.

SNOW

Kayhan Nadji
Architect, MRAIC, OAQ
41 Gold City Court, Yellowknife NT Canada X1A 3P7
Phone/Fax: (403) 873-3455 (h) Phone: (403) 920-6331 (w)

ABSTRACT

This paper will provide information regarding how life in geographical areas of snow can be enhanced by utilizing the beneficial properties of snow. It should be of interest to researchers and of use in the area of Snow Management. An extended definition of Snow, Snowdrifting, Avalanches, Ice and glaciers as important elements of the arctic and subarctic environment will be provided.

This research will also illustrate the problems that snow presents, as well as how snow affects the environment, human and animal life. It will describe a variety of measures to prevent or minimize the structural, functional and maintenance problems caused by snow deposits and drifting. The phenomenon of snow drifting and compaction which provides strength and natural insulative properties for snow will be presented.

Observations on how snow is used by indigenous peoples to provide shelter in the severe arctic climate will be offered. The construction of one kind of indigenous architecture, the igloo, will be explored. The final section of the study will briefly examine how the design and fabrication of skis responds to the properties and conditions of ice and snow in a recreational context.

This research information is based on the geographical area of the Canadian Arctic, north of the 60th parallel.

1. INTRODUCTION

Inuit lives are so intricately related to snow that they phrase the question "How old are you?" by asking "How many winters have you seen?".

Inuit distinguish a minimum of two dozen forms of snow. Examples include:

- windblown snow
- newfallen snow
- soft snow
- fluffy deep snow that fell without accompanying wind
- wind-packed snow firm enough to walk on
- wet snow belonging to springtime
- dry and sugary snow
- snow for igloos

One characteristic of cold regions is snow. About 53% of the land area and 10% of the ocean surface have snow cover at some time during the year. In the area of the Northern Hemisphere called the "taiga", the snow cover is different from that of the "tundra" regions. Taiga snow usually occurs as six-armed stars having diameters of 1-5 mm and a thickness of about 0.1 mm. Tundra snow more frequently occurs as needles or tiny prisms, having diameters of 0.01 to 0.2 mm and ranging in length from 0.1 to 3 mm. Tundra snow is characterized by having been moved by the wind. Tundra snow can be further characterized into three areas defined by the Inuit:

- API: snow consisting of those particles which are not picked up by wind
- UPSI: snow which has been reworked by wind, deposited and consolidated into a firm mass
- SIQOQ: moving snow in the air, above or on the surface of the snow cover.

2. RELATED PHENOMENA

Drifting snow has a considerable economic impact in Northern Canada, where significant amounts of snow falls during the winter. Large sums of money are spent annually to remove drifted snow from roads, airports and building areas. Snow loads on roof tops can be increased substantially by drifting and this affects the safety and cost of buildings and their maintenance. Snowdrifting also affects animal migration and agricultural production.

The following solutions could be applied to the drifting problems in the north, as observed in Rankin Inlet (one of the northern communities of Canada):

- Snow Fence - Usually a 3 to 5 m high 50% porous fence. Must be set no closer than 100 to 200 m upwind of critical area.
- Snow Berm - Snow is piled in a long berm 2 to 12 m high and placed no closer than 20 to 100 m upwind of critical areas.
- Regard road/surroundings - Surface of the road should be raised and/or the height of the surroundings reduced such that the road surface is approximately 1 m above the surface of the surroundings.
- Small obstructions should be relocated.

In the Arctic regions that are characterized by low to moderate slopes, slush avalanches (rapid mass movements

Proceedings of the Fourth Symposium on Remote Sensing of the Polar Environments, Lyngby, Denmark, 29 April – 1 May 1996
(ESA SP-391, July 1996)

of water-saturated snow) are more common than dry-snow avalanches. These slush avalanches usually occur during the early part of the melting season both on the land surface and on the melt zone of glaciers and ice caps. Slush avalanching is a major form of "run-off" in northern Canada, occurring on any slope of more than a few degrees on both land and ice surfaces.

The most spectacular form of ground ice is the pingo. This terms refers to conical ice-cored hills found in the Mackenzie River delta. Pingo is a word of Inuit origin. Pingos range from a few meters to several tens of meters in height. Some of the largest pingos in the world occur in the Tuktoyaktuk area of the NWT. Pingos are formed as a result of a "closed system" of unfrozen soil developing within an area of permafrost. The formation procedure is as follows:

- A large lake fills with sediment or partially drains away.
- Permafrost forms on the bottom and sides trapping a huge core of unfrozen, water-saturated soil above it.
- Year by year, the freezing continues. Hydrostatic pressure forces the water upward toward the surface of the land. A huge ice PINGO forms.

Ice and glaciers are important elements of the Arctic and Subarctic environment. They influence meteorological and climatic conditions and some have local economic significance. Glaciers are useful monitors of climate change, responding to change in both temperature and precipitation in a more obvious way than other forms of ice.

3. EFFECTS ON HUMAN, ANIMAL AND PLANT LIFE

Snow is a porous medium with a high content of air and possessing a high insulation capacity. It plays an important role in preserving soil and protecting micro-organisms, plants and animals of the tundra and taiga from wind and freezing. Its low thermal conductivity is very important in animal ecology.

Snow holds in the warmth of the earth and wards off the frost of winter air, functioning as a thermal blanket for soil. One Russian comparative study showed that with a six-inch blanket of snow, frost penetrated less than an inch into the soil, whereas adjoining snow-free fields were frozen more than a foot. Snow not only insulates against low minimum temperature, but also against temperature fluctuations.

Snow is a reservoir for water, chemicals and organic debris, providing habitat and food sources for various life stages of microbes and small mammals. Snow moves as a particulate flux as it is relocated by the wind in an open environment, or intercepted by vegetation in forests.

In Canada, provincial and territorial governments have winter road programs to facilitate transport of supplies to northern communities. In most northern communities, dog sleds are still being used as a means of transportation. However, the most significant contribution to winter travel in the 20th century has been the development of a wide range of oversnow vehicles. In Canada, the development of oversnow vehicles (popularly referred to as "snowmobiles") can be attributed to the work of Joseph Armand Bombardier of Quebec, and W. Bruce Nodwell of Alberta. The use of snowmobiles affects the environment in several ways. Research conducted in central Alberta indicates that the use of snowmobiles in a given area leads to serious reductions in the number of mammals, such as mice, voles and shrews, and damages tree seedlings. The effects of noise and the packing of trails which affect snow drift patterns is a major concern, particularly for wildlife.

Snow stores and releases energy, reflects most shortwave radiation and absorbs and re-emits most thermal infrared radiation. This reflection is a critical characteristic of the global climate system.

4. IGLOO

Contrary to popular belief, the Inuit word "igloo" refers to any dwelling, not specifically a snow house. Thus, igloo includes any roofed place to live made of solid materials.

The size of the structure could be between 2 and 5 m in diameter and 3 to 4 m high, depending on several factors, such as:

- whether the dwelling was to be a travelling or permanent structure.
- the number of people living in it.
- the amount of fuel available to heat it.

Snow houses are constructed of blocks of about 1 to 1.5 m in length, 0.6 m in height and from 0.15 to 0.3 m in thickness. Each block could weigh from 9 to 14 kg.

The key aspect of building an igloo is to produce a spiral building. The Inuit builder undercuts the bottom edge of the blocks so that each one tilts slightly inward when set into position. The blocks spiral up to the top like a screw. When nearing the roof, the circle is less than half the diameter of the original ground circle. The last block, which sometimes contains a hole for ventilation, serves as a keystone to the structure.

The igloo is not a hemisphere, a true hemisphere would collapse. An igloo is a catenary. As the igloo settles and the snow becomes compressed, the structure becomes reduced in height. Snow houses built on sea ice tend to be warmer, since the water is not as cold as permafrost.

Constructing an igloo usually takes no more than two people. A small snowhouse for emergency overnight shelter can be built in an hour. In it, a person can wait out a storm for days without food by not moving, using little energy (as when animals hibernate). Like the hollow hair of caribou, the air trapped in the tundra snow acts as insulation to keep out cold. The temperature inside a well built igloo never falls much below 0° C and then can be raised quickly up to 20° C or even more.

It would be difficult to design a more efficient shelter against the Arctic winter than the igloo. The shape of the igloo is well suited to the harsh climate, and is the secret of its success as a northern dwelling. It has neither a roof that has to be held up with posts nor beams or walls for the wind to push against. The snow house exposes the least possible surface area to wind and cold, and encloses a large volume within a small structure.

5. EFFECTS ON BUILDING DESIGN, STRUCTURE AND ROOFS

In the Arctic regions, drifting snow presents many problems. Arctic snow is very fine and powdery, and is therefore easily acted upon by the wind. Therefore, control of snowdrifting is one of the primary design considerations for buildings in the Arctic. The lack of natural vegetation barriers in most regions of the Arctic will increase the problem of drifting snow. Rain water load combined with snow load is one important roof design consideration in the north.

Based on research conducted in Iqaluit, Rankin Inlet and some other northern Canadian communities, in design of buildings, the following should be taken into account:

- Shape of the roof
- Elevating the building a minimum of 0.6 m above the surface
- Entrance design location
- Wind deflectors
- Air exhaust and intakes
- Orientation of walkways and roadways.

6. USES OF SNOW IN RECREATION

Skiing: Today, skiing is generally viewed as a form of recreation, but for people living in snow-filled areas, it was a means of survival. Skiing is at least 4000 to 5000 years old, and is one of mankind's oldest modes of transportation.

Snowshoes: One of the most important northern inventions was snowshoes. They were traditionally used in Sweden, Norway and by pastoralists in northern Spain. Snowshoe frames are made of willow or spruce, or whalebone, depending on materials available in any one particular geographical location.

In Canada, even within one particular tribe, natives constructed different styles of snowshoes for different snow situations. The "bent toe" and "square toe" snowshoes were restricted to the regions characterized by dense snow (the freeze-thaw and Prairie regions). Snowshoes with no toe-hole were found only in some regions of hard, dense or infrequent snow. The "hexagonal" type of netting weave was found over most of the Northern Forest region (characterized by light, fluffy snow cover). The "rectangular" weave was restricted to those taiga regions with the fluffiest, lightest snow cover. The Northern Forest region is also characterized by snowshoes with three supporting crosspieces.

Northern Athapascan snowshoes worn for hunting and trapping were 1.35 to 1.65 m long and 0.20 to 0.25 m wide. Trail shoes were only about 0.9 m long. In Fort McPherson, Canada, the men made snowshoe frames of split birch, women laced them with raw caribou hid specially cut into long strips called babich.

Sled Dogs: Dog teams in northern Canada have three uses - recreation, racing and working. The recreational teams are variegated in colour and often mismatched but fun-loving. Different types of sleds are used for various conditions. Sleds travel well over hummocks and rough areas, and are mostly used in the tundra. Toboggans handle soft snow better and are used within treeline areas.

7. CONCLUSION

Snow has played a very important role in human life. Although it is believed that virgin snow is usually contaminated in some way, the usefulness, cleanliness, pureness and even the colour of snow has been praised in many cultures and literatures. The terms of "Snow-White Spot" and "Snow-White Brow", and Shakespeare's idea of perfection in Hamlet: "as pure as snow" refers to this.

In this paper, the effect of snow as a natural medium was briefly studied. Focus was given to one kind of Inuit architecture, the "snow house".

By studying this aboriginal architecture, one will realize that modern complex structures are not always superior. Simple architecture of an igloo can be quite advanced, with a high degree of sophistication, performance and relevance to the user's needs, and in respect for the environment and nature as a divine trust for which we are answerable.

8. REFERENCES

Alberta Building Envelope Council <u>Snow, Ice and the</u>

Building Envelope. Proceedings, Seminar No. 8, Calgary, Alberta, February 25, 1993

Armstrong, Terence, Roberts, Brian, Swithinbank, Charles Illustrated Glossary of Snow and Ice, Cambridge, 1966

Black, Bill Snowdrifting Studies, School of Architecture, Nova Scotia Technical College, Halifax, NS April 1978

Boas, Franz The Central Eskimo, University of Nebraska Press, 1964

Boyd, Donald W. Maximum Snow Depth and Snow Loads on Roofs in Canada, Ottawa, 1961

Canadian Heritage, February-March, 1987

Codd, Carol Chooki and the Ptarmigan, New York, Walker, 1976

Colbeck, Samuel C. Roof Loads Resulting from Rain-on-Snow, CRREL, Report 77-12

Collins, M. and J. Dog Driver, a Guide for Serious Mushers, Alpine Publications, 1991

Davenport, A.G. Canadian Journal of Civil Engineering, National Research Council of Canada, Vol. 1, 1974

Debenham, F. The Polar Record, Scott Polar Research Institute, Vol. 8, No. 28, Great Britain, 1942

Effendi, Shoghi God Passes By, Baha'i Publishing Trust, Wilmette, Illinois, 1970

Effendi, Shoghi The World Order of Baha'u'llah, Baha'i Publishing Trust, Wilmette, Illinois, 1974

Elsner, Robert W., Pruitt, William O. Jr. Some Structural and Thermal Characteristics of Snow Shelters Arctic, V. 12, No. 1, March 1959 p. 20-27

Eranti, E., Lee, G.C. Cold Region Structural Engineering McGraw-Hill Book Co. 1986

Formozov, A.N. Snow Cover as an Integral Factor of the Environment and its Importance in the Ecology of Mammals and Birds Moscow Society of Naturalists, Moscow USSR 1946

Fort McPherson, A Community Study, published by the Department of Education, Government of the Northwest Territories, 1987

Freres, Revillon Eskimo Life of Yesterday 1922

Gold, Lorne W. The Journal of Glaciology, British Glaciological Society, Vol. 2, No.11, March 1952

Gray, D.M., Male, D.H. Handbook of Snow Pergamon Press Canada Ltd. 1981

Green, Paul, aided by Abbe Abbott I am Eskimo Alaska Northwest Publishing Company 1959

Hogarth, Elizabeth Wigwams, Igloos and Bungalows

Hucheon, Neil B., Handegord, Gustave O.P. Building Science for a Cold Climate, National Research Council of Canada, 1983, 1989

Hughes, Jill Eskimos, Gloucester Press, New York, 1978

Illingworth, Frank Men Against the Arctic, Dawson & Goodall Ltd., Bath, Somerset, 1949

Jones, H.G., Pomeroy, J.W., Walker, D.A., Wharton, R. Snow Ecology: A Report on a New Initiative, Information North, Vol. 20, No. 2, June, 1994

Kirk, Ruth Snow, U.S.A., 1977

Kurelek, William The Last of the Arctic, Pagurian Press, Toronto, Ontario, 1976

Lane, J.W., Marshall, S.J., Munis, R.H. Roof Response to Icing Conditions, CRREL Report 79-17

Manning, Mrs. Tom Igloo for the Night, Hodder & Stoughton Limited, London, 1943

Morrison, Hershfield, Theakston & Rowan Ltd., Consulting Engineers Report on Snow Control Study of Proposed Housing Development Frobisher Bay, NWT September, 1975

Nabokov, Peter, Easton, Robert Native American Architecture, Oxford University Press, New York, Oxford, 1989

Nobels, H. Laurence International Symposium on Scientific Aspects of Snow and Ice Avalanches, Davos, Switzerland, April, 1965

Odar, Fuat Simulation of Drifting Snow, CRREL Research Report 174, October, 1965

O'Rourke, M., Kock, P., Redfield, R. Analysis of Roof Snow Load Case Studies Uniform Loads CREEL Report 83-1

Palmer, Rose A. The North American Indians, Cooper Square Publishers Inc., 1975

Powers, D.J., Colbeck, S.C., O'Neil, K. Thermal Convection in Snow CREEL Report 85-9

Pressman, Norman Northern Cityscape, Winter Cities Association, 1995

Pruitt, W.O. Jr. Ecology of the Subarctic Regions, Proceedings of the Helsinki Symposium, UNESCO, 1970

Rice, Eb Building in the North, Geophysical Institute of the University of Alaska, Fairbanks

Rowan Williams Davies & Irwin Inc. Keewatin Region Snowdrift Abatement Concept Study, Rankin Inlet, NWT January 1992

Sharp, P. Robert Glaciers in the Arctic, Arctic, Vol. 9, No. 1 & 2, 1956

Scullion, Anthony How the Experts Build an Igloo Canadian Geographic, Oct/Nov 1981

Shemie, Bonnie Houses of Snow, Skin and Bones Tundra Books, 1989

Stefansson, Vilhjalmur Eskimos from the Stone Age to the Present. American Educator Encyclopedia

Steltzer, Ulli Building an Igloo, Douglas & McIntyre, Vancouver, 1981

The Canadian Encyclopedia, Vol. III, 1985

Turner, Geoffrey Indians of North America, Sterling Publishing Co., New York, 1992

Weiss, Harvey Shelters From Tepee to Igloo, Thomas Y. Crowell, New York, 1988

Whittaker, C.E. Arctic Eskimo, Seeley, Service & Co. Ltd., London, 1937

Wilkinson, Douglas The Illustrated Natural History of Canada/ The Arctic Coast, Natural Science of Canada Limited, 1970

Williams, C.J. Arctic Snowdrifting, Morrison Hershfield Ltd. Consulting Engineers, September, 1984

Young, Joel, Boyce, Arlow Recreational Uses of Snow and Ice in Michigan and some of its effect on Wildlife and People, Snow and Ice in Relation to Wildlife and Recreation Symposium, Iowa State University Memorial Union, proceedings, February, 1971

Yue, Charlotte and David The Igloo, Houghton Mifflin Co., Boston, 1988

CLIMATE
ATMOSPHERE
RADIATION

SATELLITE DETECTION OF ENHANCED GREENHOUSE WARMING IN THE POLAR REGIONS: SEASONAL ASPECTS AND IMPLICATIONS OF RECENT SEA ICE TRENDS

Martin Miles[1], Ola M. Johannessen[1] and Einar Bjørgo

Nansen Environmental and Remote Sensing Center
Edvard Griegsvei 3a, N-5037 Solheimsviken/Bergen, Norway
Ph.: +47 55 29 72 88, fax: + 47 55 20 00 50, e-mail: martin.miles@nrsc.no

[1] Also with Department of Geography, University of Bergen

Remote sensing studies of the polar sea ice covers may be useful for the early detection of global climate change induced by increases in greenhouse gases. Recent studies using satellite microwave data have revealed statistically significant negative trends in Arctic sea ice extent and area, with no such trends in the Antarctic. Here, we extend these studies to include data from 1995, and expand them with a seasonal analysis. The data are SMMR (1978-87) and SSM/I (1987-95) microwave brightness temperatures. From these we produce continuous time series of ice extent, ice area, and overall ice concentration for the Arctic and Antarctic, 1978-95. Statistically significant decreases are evident in each ice parameter in the Arctic, with no reliable trends seen in the Antarctic.

The overall trends should not be expected to be monotonic spatially or temporally; here, we investigate the latter aspect. First, we perform a seasonal and monthly breakdown, and estimate the trends and their statistical significance. This reveals the relative contributions of the particular seasons and months to the overall variability and trends. It is evident that the summer ice extent and ice area in the Arctic have been decreasing fastest in recent years. Second, we investigate the "temporal dependencies" in the ice parameters, by estimating the autocorrelations in the monthly time series. Statistically significant leads and lags are identified, revealing the critical times within the seasonal cycle that most strongly influence subsequent ice conditions. The existence of: a) decreases in ice extent, ice area, and ice concentration, b) seasonal differences in the trends and c) particular temporal autocorrelations, has potentially important geophysical implications. It may imply decreases in the multi-year ice area and attendant changes in ice thickness distribution; however, this remains speculative.

INTERANNUAL VARIABILITY OF SEA ICE IN THE GREENLAND SEA

Leif Toudal

Institute of Electromagnetic Systems,
Building 348, Technical University of Denmark, DK-2800 Lyngby, Denmark,
Ph.: +45 45 25 37 91, fax: +45 45 93 16 34, e-mail: ltp@emi.dtu.dk

Passive microwave radiometer data from the last 25 years have been used to study the interannual variability of the large-scale sea ice cover in the Greenland Sea.

Data from the NIMBUS-5-ESMR (Electrically Scanning Microwave Radiometer) (1972-1976) the NIMBUS-7 SMMR (Scanning Multichannel Microwave Radiometer) (1978-1987), and the DMSP SSM/1's (Special Sensor Microwave/Imager) (1987-1996) have been intercalibrated using data from overlap periods. The resulting dataset is evaluated for it's long term accuracy and subsequently used in the analysis.

Results show that the 1990's have seen far less ice in this 500 000 square kilometer area than did the 1970's. Results are compared with ice information available from none remote sensing sources as well as with other remote sensing data from the NOAA AVHRR and the ERS-1 SAR instruments.

TOVS PATH-P: A PATHFINDER DATA SET OF ATMOSPHERIC AND SURFACE VARIABLES FOR PROCESS AND CLIMATE STUDIES OF THE ARCTIC BASIN

Axel Schweiger[1], Drew Rothrock[1] and Jennifer Francis[2]

[1] Applied Physics Laboratory/Polar Science Center, University of Washington, Seattle, WA, USA
Ph.: +1 206 543 6613, fax: +1 206 543 3521, e-mail: axel@apl.washington.edu

[2] Institute of Marine and Coastal Sciences, Rutgers University, New Brunswick, NJ, USA
e-mail: francis@ahab.rutgers.edu

Recent studies have demonstrated that valuable information about the mechanisms by which energy is transferred within the atmosphere and at the air/ice interface over the Arctic ocean can be obtained from the TOVS sensor package. However, data and retrievals from TOVS have been vastly under-utilized for providing information that may aid in understanding these processes because errors over snow and ice surfaces were unacceptably large, suitable validation data were unavailable and until the advent of the pathfinder program, the radiances were too expensive to obtain in any quantity. TheTOVS Polar Path (so-called Path-P) team has begun the task of generating a data set designed specifically to fill this void and cater to the needs of the polar research community. To date we have completed processing TOVS level-1b data for the TOVS Pathfinder benchmark period (April 1987 through November 1988), and the gridded fields are available through the National Snow and Ice Data Center (NSIDC) DAAC. An extension of this data set to the lifetime of the TOVS sensor package (1979-present) is currently under way with support from the NASA Pathfinder program. The Path-P product is generated with a version of the Improved Initialization Inversion ("31") algorith developed by the Laboratoire de Météorology Dynamique. Using recently available validation data sets, the Path-P team has made modifications to 31 to improve retrieval accuracy in snow- and ice-covered regions, and has developed several new parameters that are of particular interest to polar researchers. Both standard retrieval information (temperature profiles, humidity amounts, cloud parameters, and surface temperature) and these new products (boundary layer stratification parameter, geostrophic drag coefficient, and surface wind turning angle) constitute the Path-P data set. The product is generated daily and gridded on the EASE grid, which is fast gaining acceptance as the standard polar grid because of its ease of use for polar applications and its compatibility with other polar data sets. In this paper we will describe this data set, provide an error assessment, and provide examples of applications.

RADNET: A NEURAL NETWORK - BASED APPROACH TO THE RETRIEVAL OF THE SURFACE RADIATION FLUXES OF THE ARCTIC FROM TOVS BRIGHTNESS TEMPERATURES.

Axel Schweiger[1] and Jeff Key[2]

[1]Applied Physics Laboratory/Polar Science Center, University of Washington, Seattle, WA, USA, Ph.: +1 206 543 6613, fax: +1 206 543 3521, e-mail: axel@apl.washington.edu

[2] Dept. of Geography, Boston University, Boston, Massachussetts, USA
e-mail: jkey@bu.edu

A new method for calculating downwelling shortwave and longwave fluxes in the Arctic from TOVS HIRS and MSU brightness temperatures is presented. This method employs a neural network to bypass computationally intensive inverse and forward radiative transfer calculations required in traditional retrieval algorithms. Results and comparisons with surface observations from two field experiments during 1988 (Cearax) and 1992 (Leadex) and a land-based station are presented. Results show that downwelling fluxes can be estimated with RMS errors of 20 Wm^{-2} for longwave radiation and 35 Wm^{-2} for shortwave radiation. Mean errors are less than 4 Wm^{-2} and are well within the bounds required for climate process studies. The performance of this method is compared with the results from the retrieval method developed by Francis (1994). Advantages and disadvantages of each method are discussed.

SHIP-BASED REMOTE MEASUREMENTS OF STRATOSPHERIC NITROGEN DIOXIDE IN THE WEDDELL SEA, ANTARCTICA

Aleksandr S. Elokhov and Aleksandr N. Gruzdev

Institute of Atmospheric Physics, Russian Academy of Sciences
Pyzhevsky per. 3, 109017 Moscow, Russia
Ph.: +7 095 592 1219, fax: +7 095 233 1652, e-mail: antoly@zbase.iaph.msk.ru

During September-October 1989, stratospheric column NO_2 abundances were measured by a zenith-viewing visible spectrometer aboard the ship "Akademik Feodorov" in the Weddell Sea (West Antarctica) at latitudes from 62 S to 66 S. Very large variations of stratospheric NO_2 were observed which correlated with stratospheric temperature. From the second half of September to the end October three "waves" of low and high values of columnar NO_2 were noted which were accompanied by the similar "waves" of stratospheric temperature. The intervals between consecutive "waves" were about two weeks. These variations were superimposed by the positive trend, both in NO_2 and temperature. The lowest NO_2 value equal to 10^{15} mol/sq cm (by evening measurements) was observed on September 23. Such a value is typical for the period of the ozone "hole" over Antarctica. At the same time the lowest temperature was noted in the stratosphere. The largest NO_2 content was observed at the end of October and equaled 4.3 10^{15} mol/sq cm, more than four times as large as the lowest value. Synchronous variations of the NO_2 content and temperature are connected with the evolution (deformation) of the stratospheric circumpolar vortex. The vortex edge is known to be the domain of large gradients of total ozone, NO_2, and temperature. The reversal of the stratospheric circulation, which caused filling ozone "hole" over Antarctica, was noted later, in November.

ANALYSIS OF TEMPERATURE ANNUAL VARIATION IN THE TROPOSPHERE, STRATOSPHERE AND MESOSPHERE USING DATA OF SATELLITE MEASUREMENTS

Aleksandr N. Gruzdev

Institute of Atmospheric Physics, Russian Academy of Sciences
Pyzhevsky per. 3, 109017 Moscow, Russia
Ph.: +7 095 5921219, fax: +7 095 233 1652, e-mail: antoly@zbase.iaph.msk.ru

Data from the temperature reference model for the middle atmosphere (Barnett and Corney, 1985) based on satellite measurements are analysed by special method of amplitude and phase characteristics. The annual dynamics of the height-latitude temperature field is presented in terms of propagation of special amplitude and phase characteristics related to a few important regimes of the temperature annual variation (e.g. regimes of warming and cooling, regimes of forming temperature annual maximum and minimum). Space-time peculiarities of the thermal structure of different latitude belts have been revealed in the troposphere, stratosphere, and mesosphere. The analysis exhibits the role of different atmospheric parts and objects in climate dynamics: the role of the atmospheric boundary layer, the tropospheric and stratospheric layers, the equatorial, mid-latitude and high-latitude belts of the atmosphere, the subtropical jet streams, Earth and ocean surfaces, with their interrelations, for different seasons. The analysis exhibits, particularly, that dynamics of warming of the atmosphere-earth surface-ocean surface system and dynamics of cooling of the system can be quite different, especially in the nothern polar and middle latitudes. The different role of the Antarctic continent and the Arctic Ocean in the dynamics of the atmospheric temperature annual evolution is exhibited by the analysis. Two-dimensional, height-latitude, distributions of the computed amplitude and phase characteristics clearly visualise the findings.

DETERMINATION AND INTERCOMPARISON OF RADIATION FLUXES AND NET RADIATION USING LANDSAT-TM-DATA OF LIEFDEFJORDEN/NW-SPITSBERGEN

Eberhard Parlow

Meteorology, Climatology & Remote Sensing Lab (MCR Lab)
University of Basel, Spalenring 145, CH-4055 Basel
phone: +41-61-273 6480, fax: +41-61-272 6923, email: parlow@ubaclu.unibas.ch

ABSTRACT

Two Landsat-TM scenes from June 26 and August 19, 1990 are used to compute the spatially distributed radiation fluxes and all-wave net radiation for a high-arctic environment at Liefdefjorden/NW-Spitsbergen. The area was investigated during three geoscientific Svalbard expeditions during 1990-1992 with norwegian, german and swiss participation. In addition to micrometeorological ground measurements of turbulent heat fluxes at 10 m towers and eddy correlation systems, high resolution satellite data are integrated to work out the spatial variations of radiation fluxes due to terrain conditions and surface characteristics. As a testsite the catchment area of two small glaciers, Småbreen and Kvikkåabreen, was selected. The two satellite data sets used cover the onset of the melting period and the end of the arctic summer. To compute all-wave net radiation numerical radiation models were used in combination with Landsat-TM data and a digital terrain model to calculate input and output radiation fluxes. Finally statistical analysis was carried out to find interrelations between solar irradiance or terrestrial emission and net radiation.

1. INTRODUCTION

During the short and - as far as snow melting is concerned - highly dynamic transition from arctic winter to arctic summer the spatially distributed radiation balance plays an important role for the melting processes and intensities. During three Svalbard expeditions to Liefdefjord research of MCR Lab covered radiation and heat balance studies especially during intensive melting periods. The characteristic onset of the melting period in arctic landscapes is generally connected to slush flows, i.e. water saturated snow which looses its stability on gentle slopes with only a few degrees of slope angle. Under steeper terrain conditions drainage of the water table in the snow matrix is improved and therefore slush flows normally are stabilized (Scherer 1994, Gude and Scherer 1995). Consequently there is a striking difference between slush flows and avalanches. The latter only occurs in steep slopes due to gravitational forces whereas slush flows are initialized by the hydraulic pressure gradient within the water table of the snow matrix. Under maximum energetic input during melting slush flows can develop into highly dynamic processes which then are called slush torrents according to Barsch et al. (1993). To study these extreme fluvial and melting processes and to model water discharge of the catchment area net radiation, i.e. the balance of all solar and terrestrial input and output radiation fluxes, is an important meteorological variable which can be derived from high resolution remotely sensed data of Landsat-TM in combination with numerical radiation models (Parlow 1990, Parlow 1992, Parlow and Scherer 1991, Schneider et al. 1996). Fig. 1 and 2 gives an impression of the snow conditions at the beginning of the melting season and at the end of the arctic summer.

Fig. 1 : Småbreen and Kvikkåabreen, May 26, 1992 2:00 CET. (Courtesy of F. Siegrist)

Fig. 2 : Småbreen and Kvikkåabreen, August 12, 1991 2:00 CET. (Courtesy of F. Siegrist)

Proceedings of the Fourth Symposium on Remote Sensing of the Polar Environments, Lyngby, Denmark, 29 April – 1 May 1996
(ESA SP-391, July 1996)

2. METHODOLOGICAL CONCEPTION

Net radiation R_n is the key factor for the energy fluxes at the soil-vegetation-atmosphere interface. It balances all terms of solar and terrestrial radiation and controls turbulent heat fluxes and can be written :

$$R_n = E_S\downarrow(1-\alpha) + E_l\downarrow - \varepsilon\sigma T^4 \qquad (1)$$

with :

$E_S\downarrow$	:	Solar irradiance
α	:	Albedo
$E_l\downarrow$	:	Atmospheric counter radiation
ε	:	Emissivity
σ	:	Stefan-Boltzmann-constant
T	:	Surface temperature

To compute R_n in a high spatial resolution and with respect to topography and landuse a fusion of data from Landsat-TM and a digital terrain model (DTM) in combination with numerical radiation models is proposed. Fig. 3 illustrates the model conception: rounded boxes indicate input data, ellipses indicate numerical models and rectangular boxes results. For cloudless conditions solar irradiance ($Es\downarrow$) can be computed quite accurately by using a numerical radiation model like the Shortwave Irradiance Model SWIM (Parlow 1996, Parlow and Scherer 1991, Scherer and Parlow 1994, Scherer 1994).

Albedo was calculated directly from Landsat-TM data by Brun (1996). Atmospheric counter radiation ($El\downarrow$) is a longwave input term of net radiation resulting from the emission of molecules and clouds. It varies only slightly in time and space, depending mostly on air temperature and humidity. For cloudless conditions it can be parametrized by using the following formula (Brutsaert, 1982):

$$E_l\downarrow = 0.552 \cdot \sqrt[7]{e} \cdot \sigma \cdot T^4 \qquad (2)$$

where e = vapor pressure at 2 m, T = air temperature at 2 m in Kelvin, σ = Stefan-Boltzmann-constant.

Since there is normally a vertical gradient of temperature and humidity there is a vertical decrease of atmospheric counter radiation which can not be detected from satellite data. According to the conceptional model (Fig. 3) this radiative term can be calculated by using vertical temperature ($\partial T/\partial z$) and humidity ($\partial e/\partial z$) profiles from observation data and a digital elevation model.

After correction of the atmospheric influence brightness temperature of land surface can be calculated from channel 6 of LANDSAT-TM using a formula from Schott and Volchok (1985). Nevertheless, in mountain areas the thickness of the atmosphere differs considerably. A digital elevation model helps to improve the correction by considering the thickness of the individual atmospheric column over each pixel. Then longwave emission ($E_l\uparrow$) can be derived from the formula of Stefan-Boltzmann:

$$E_l\uparrow = \sigma T^4 \qquad (3)$$

All radiative terms can be summarized and it is possible to calculate net radiation in the spatial context according to equation 1. The result considers all influences from landuse, altitude, slope and aspect.

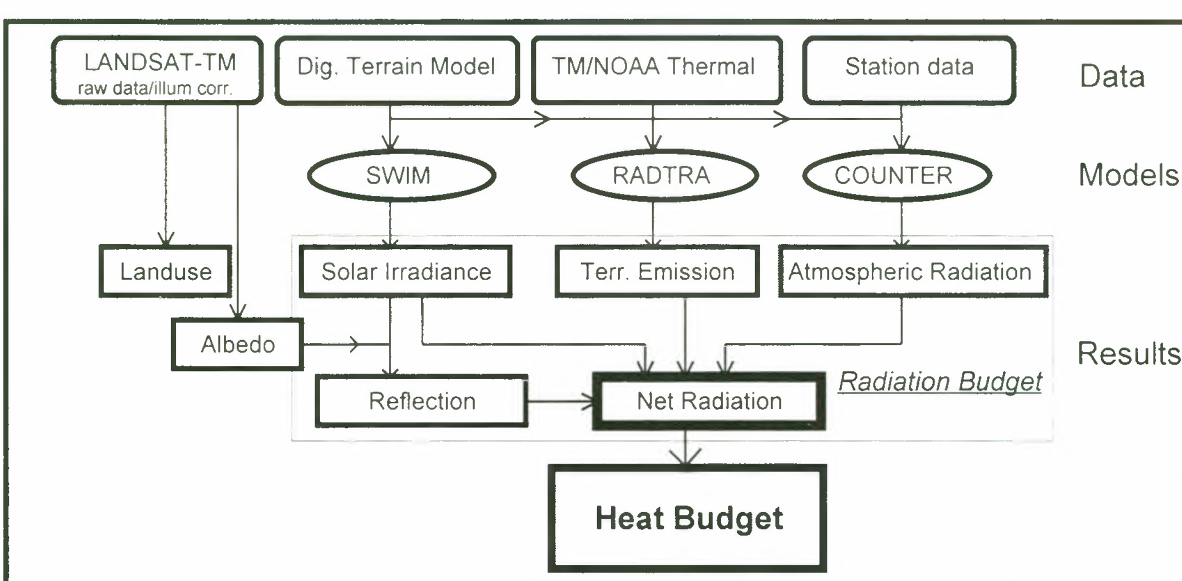

Fig. 3 : Model conception to compute net radiation

Fig. 4 shows some of the data layers of the digital terrain model (DTM), which was produced from stereo aerial photography (Brunner and Hell 1994). The spatial resolution of the DTM is 20 m.

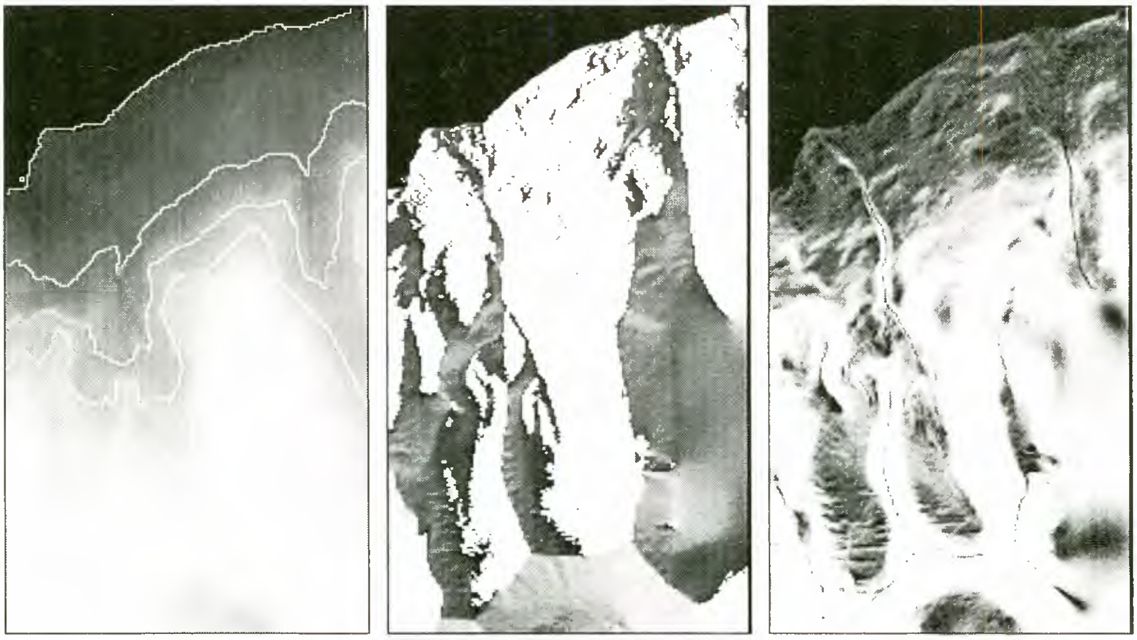

(a) (b) (c)

Fig. 4 : Digital Terrain Model Liefdefjord ((a) altitude (equidistance : 100 m), (b) aspect, (c) slope)

3. RESULTS

In a first step solar irradiance was computed by using the DTM of fig. 4 and the numerical radiation model SWIM (Short Wave Irradiance Model, Parlow 1996). Fig. 5 shows the solar irradiance on inclined surfaces during satellite overpass on June 26, 1990 and August 19, 1990. Both horizon reduction through steep slopes and atmospheric effects like altitudinal variations of direct and diffuse radiation are considered. A subpolar-arctic summer atmosphere is used to parametrize optical thickness. Since satellite overpass was at 13:09 local time on June 26 and 12:30 local time on August 19 fig. 5 shows the situation shortly after sun culmination in the early afternoon. South and southwest facing slopes receive highest solar input with up to 800 Wm^{-2} (June 26) and 600 Wm^{-2} (August 19). Solar irradiance on horizontal surfaces is in the range of 450 – 500 Wm^{-2} for June and 200 – 300 Wm^{-2} for August. It can clearly be pointed out to what extend solar radiation input is modified by terrain conditions.

Albedo was directly calculated from Landsat-TM data (Brun 1996). Then shortwave reflectance ($E_S\uparrow$) is easily to obtain by multiplication of albedo and solar irradiance according to :

$$E_S\uparrow = \alpha\, E_S\downarrow \qquad (4)$$

and shortwave net radiation can be computed. A further step deals with longwave input and output fluxes. For clear sky conditions atmospheric counter radiation can be calculated with good results according to formula (2). Longwave terrestrial radiation fluxes were calculated from Landsat-TM channel 6 data. The result is presented in fig. 6.Values range between 250 – 450 Wm^{-2} depending on exposition to the sun and surface characteristics. Although solar irradiance differs substantially between the two dates the longwave emissions are quite similar. Highest values can be found on August 19 in the southfacing slopes. The reason for the similar longwave emission in spite of the different shortwave input is the influence of snow cover. The high albedo of snow during June 26 is compensating high solar input with equivalent results compared to August 19.

The water surface of Liefdefjord in the top left corner has also similar values although in the data of June the fjord had a high albedo due to melting sea ice. But melting sea ice has about the same temperatures as open arctic water and therefore longwave emission differs only slightly.

Having all radiation fluxes computed from Landsat-TM satellite data or by using numerical models in combination with DTM data the spatially distributed net radiation can be calculated according to formula (1). Net radiation is the key factor for the heat balance and is a decisive variable for melting processes. Fig. 7 shows the spatial variations of net radiation for both satellite overpasses. It integrated the influences of terrain (altitude, slope and aspect) and surface properties.

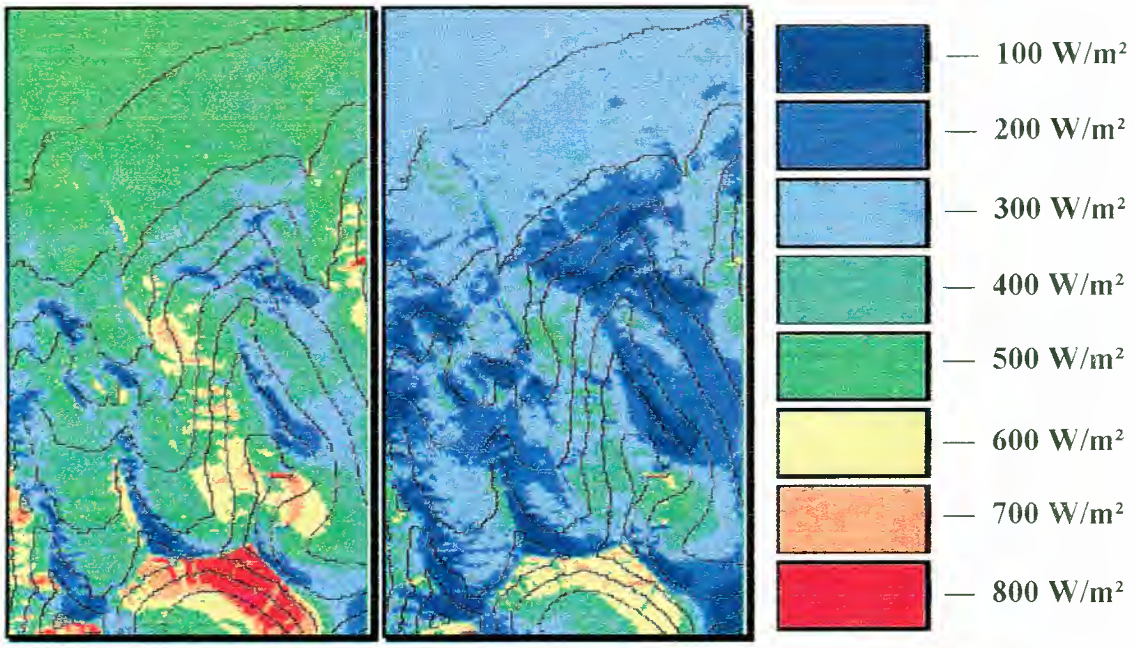

(a) June 26, 1990 (b) August 19, 1990

Fig. 5 : Solar irradiance at satellite overpass

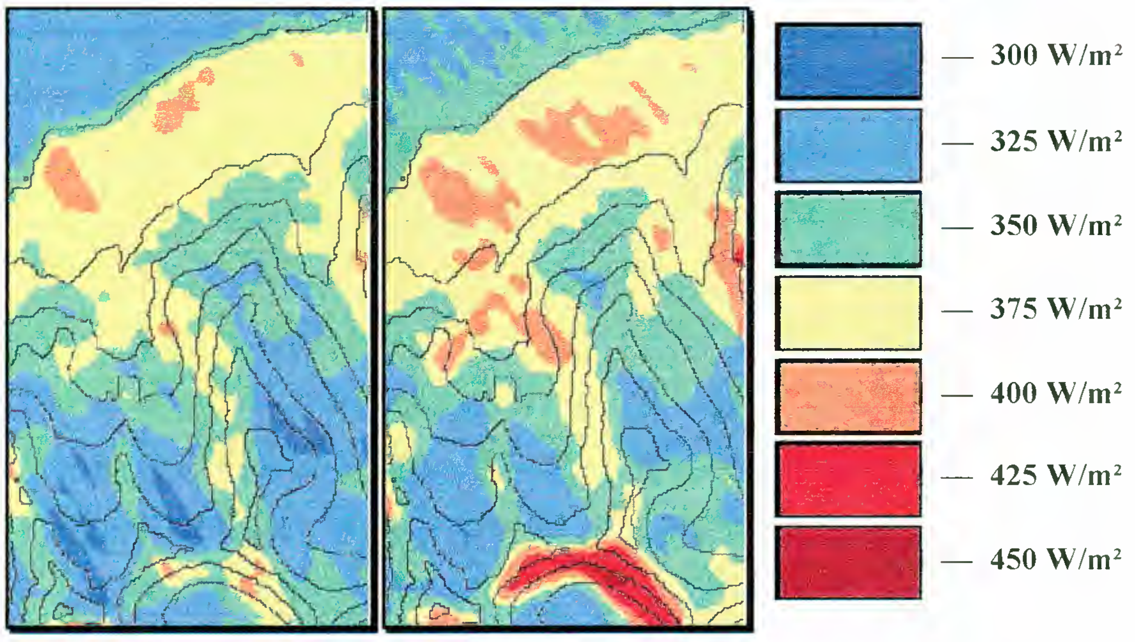

(a) June 26, 1990 (b) August 19, 1990

Fig. 6 : Terrestrial emission during satellite overpass, calculated from Landsat-TM channel 6 data

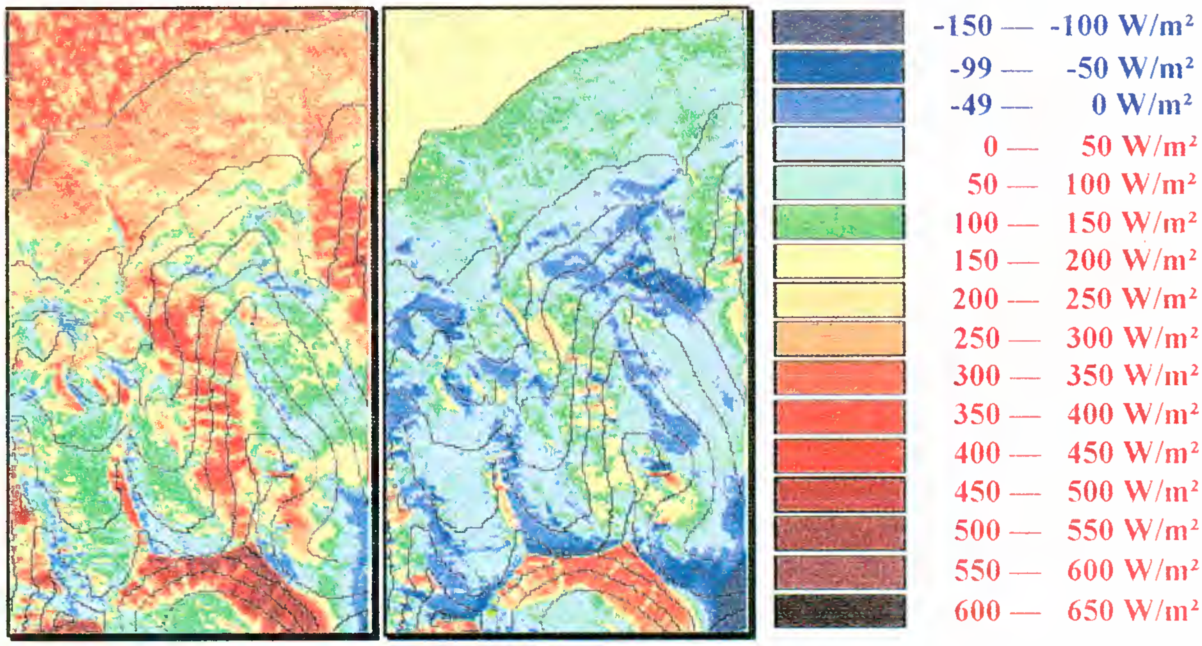

(a) June 26, 1990 (b) August 19, 1990

Fig. 7 : Net radiation during satellite overpass

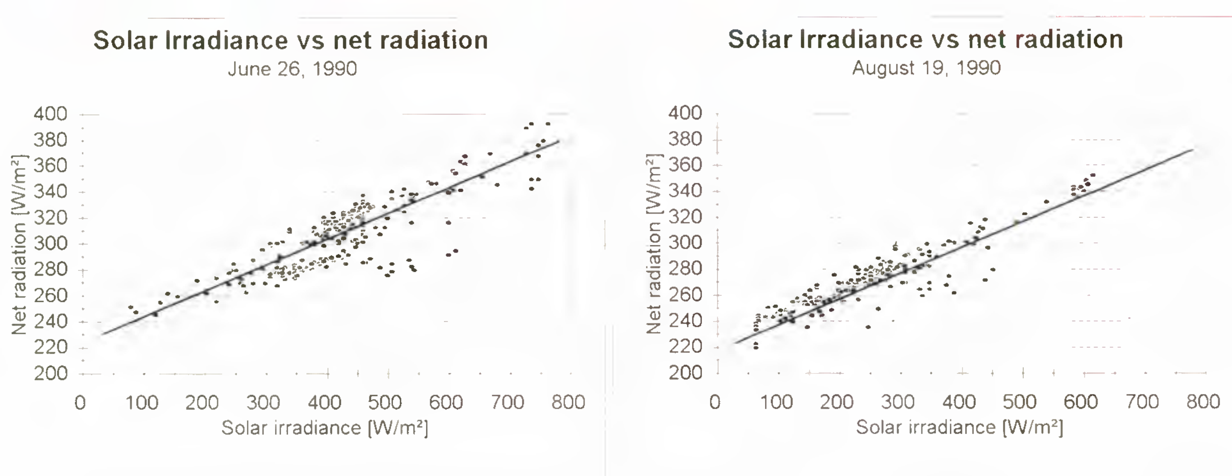

Fig. 8 : Correlation between solar irradianced and net radiation during satellite overpass

Along a north-south transsect a correlation between solar irradiance and net radiation was carried out. Fig. 8 shows that in both cases (June 26 and August 19) there is a rather good agreement between both variables and even a comparison between the June and August data illustrates that the linear regression is nearly the same. From this result it seems possible to approximate the net radiation with its spatial modifications from the computed solar irradiances. The latter can be calculated without satellite data and for each time desired. So the diurnal dynamic of net radiation can be obtained with fairly good results and the disadvantage of a pure satellite based analysis with only one scene can be reduced .

CONCLUSIONS

A combination of satellite data analysis of Landsat-TM data with a digital terrain model and numerical models enables to study the radiation and energy budget in the spatial context including all influences related to terrain effects and surface properties. It gives insights to the importance of snow in arctic regions and the available energy for melting processes. Since the amount of data is very large statistical analysis can be carried out. This enables to work out a regression model to simulate net radiation in the time scale with sufficient accuracy for many applications like snow melt runoff modelling etc..

REFERENCES

Barsch, D., M. Gude, R. Mäusbacher, G. Schukraft, A. Schulte & D. Strauch 1993. Slush stream phenomena – process and geomorphic impact. *Ann. of Geomorphology*, N.F., Suppl.-Vol. 92, p. 39–53.

Brun, M. 1996. LANDSAT-TM gestützte Modellierung der Schneeschmelze in NW-Spitzbergen. Diploma thesis MCR Lab University Basel (unpublished).

Brunner, K. & G. Hell 1994. Topographische und thematische Karten zur Ergebnisdarstellung der Spitzbergen-Expedition (SPE) 1990–1992. Ann. of Geomorphology, N.F. Suppl.-Vol. 97, 1–13.

Brutsaert, E. (1982): Evaporation into the Atmosphere - Theory, History and Application. - Dortrecht.

Gude, M. & D. Scherer 1995, Snowmelt and slush torrents - preliminary report from a field campaign in Kärkevagge, Swedisch Lappland. *Geografiska Annaler*, 77A, 4, 199–206.

Parlow, E. & D. Scherer 1991. Studies of the radiation budget in polar areas using satellite data and GIS-techniques. Proceedings IGARSS-Helsinki 1991, IEEE-Catalog Number 91CH2971-0, Vol. 1, 29-32.

Parlow, E. 1990. Spatial patterns of radiation fluxes using LANDSAT-TM-data and GIS-Techniques. Proceedings of the 9th EARSeL-Symposium, Espoo/Finland 1989, Comm. of European Communities (ed.) Brussels-Luxemburg 1990, 441-447

Parlow, E. 1992. Klimaökologie und Fernerkundung: Integration von Meßergebnissen und Fernerkundungsdaten zur Erstellung klimarelevanter Flächendatensätze. *Stuttgarter Geographische Studien* Bd. 117 (Zwischenbericht Geowissenschaftliche Spitzbergen-Expedition 1990 und 1991, 73-88.

Parlow, E. 1994. Faktoren und Modelle für das Klima am Oberrhein - Ansätze und Ergebnisse des Regio-Klima-Projektes REKLIP. *Geographische Rundschau* 3/1994, 160-167.

Parlow, E. 1996. Correction of Terrain Controlled Illumination Effects in Satellite Data. In : Parlow, E.: Progress in Environmental Remote Sensing Research and Applications, Balkema Rotterdam, 139-145.

Scherer, D. & E. Parlow 1994. Terrain as an important controlling factor for climatological, meteorological and hydrological processes in NW-Spitsbergen. *Ann. of Geomorphology*, N.F., Suppl.-Bd. 97, p. 175-193

Scherer, D. 1992. Klimaökologie und Fernerkundung: Erste Ergebnisse der Meßkampagnen 1990/1991. *Stuttgarter Geographische Studien* Bd. 117 (Zwischenbericht Geowissenschaftliche Spitzbergen-Expedition 1990 und 1991), 89-104.

Scherer, D. 1994. Slush Stream Initiation in a High Arctic Drainage Basin in NW-Spitsbergen- An Energy Balance Based Approach Combining Field Methods, Remote Sensing and Numerical Modells. *Stratus* 1.

Scherer, D. 1995. Distributed surface properties and energy flux over complex terrain in the High Arctic of NW-Spitsbergen. *Annales Geophysicae*, 13 (Suppl. II), 1995: C317.

Scherer, D. 1996. Significance of satellite data for studying atmospheric and hydrological processes in the High Arctic. In : Parlow, E.: Progress in Environmental Remote Sensing Research and Applications, Balkema Rotterdam, p. 361-367.

Scherer, D., E. Parlow, N. Ritter & F. Siegrist 1993. Datenübersicht der Liefdefjord-Expeditionen SPE'90 und SPE'91 : Klimaökologie und Fernerkundung. In: Leser, H.:- Methoden- und Datenübersicht der geowissenschaftlichen Spitzbergenexpeditionen 1990 und 1991 zum Liefdefjorden (Datenband), *Materialien zur Physiogeographie* H 15, p. 51-58 and p. 121-151, Basel.

Scherer, D., M. Gude & G. Lange 1996. Sulzströme - eine verkannte Gefahr. *Spektrum der Wissenschaft*, 3, 14-16.

Schneider, C., E. Parlow & D. Scherer 1996. GIS-based modelling of the energy balance of a subpolar ecosystem in Scandinavia using Landsat-TM data. In : Parlow, E.: Progress in Environmental Remote Sensing Research and Applications, Balkema Rotterdam, 401-408.

Schott, J.R. & W.J. Volchok 1985. Thematic Mapper Thermal Infrared Calibration. - *Photogrammetric Engineering and Remote Sensing* 51, 9: 1351-1357.

ESTIMATION OF THE SOIL HEAT FLUX/NET RADIATION RATIO OVER HIGH LATITUDE NATURAL VEGETATION USING SPECTRAL VEGETATION INDICES

Anne Jacobsen
Institute of Geography, University of Copenhagen
Øster Voldgade 10, DK-1350 Copenhagen K, Denmark
Presently: National Environmental Research Institute, Dept. of Landscape Ecology
Grenåvej 14, Kalø, DK-8410 Rønde, Denmark
Phone: +45 8920 1700, fax: +45 8920 1515, e-mail: aja@dmu.dk

Birger U. Hansen
Institute of Geography, University of Copenhagen
Øster Voldgade 10, DK-1350 Copenhagen K, Denmark
Phone: +45 3532 2519, fax: +45 3532 2501, e-mail: buh@geogr.ku.dk

ABSTRACT

The vegetation communities in the Arctic environment are very sensitive to even minor climatic variations and estimation of surface energy fluxes in high latitude vegetated areas is an important issue to be pursued. This study used micro meteorological data, spectral reflectance signatures and plant physiological parameters to establish the relationship between the soil heat flux/net radiation (G/Rn) ratio and vegetation indices (VIs). Comparison of VIs and measured plant physiological parameters showed that the ratio vegetation index (RVI) had the best linear expressions and the normalized difference vegetation index (NDVI) had the best exponential expressions. An exception was the VIs and dry/wet biomass ratio correlation, where a power function was found. Comparison of VIs and the surface energy flux ratio G/Rn showed that NDVI had the best linear expression. The results indicate that the G/Rn-NDVI relationship is valid also in vegetated high latitude Arctic areas. Accordingly, spectral satellite data can be used to extrapolate field measured surface energy fluxes and regional and temporal changes can be mapped over difficultly accessible areas.

1. INTRODUCTION

Cold regions are often difficultly accessible and estimates of the G/Rn ratio from vegetation indices may prove to be a good tool to monitor surface energy fluxes in a high Arctic area through remote sensing. Investigations of the relationship between G/Rn and vegetation indices have presently primarily been carried out over agricultural crops (Clothier et al., 1986; Daughtry et al., 1990; Kustas and Daughtry, 1990; Kustas et al., 1993) and it is the aim of this study to investigate the suitability of the method in cold regions with sparse natural vegetation cover.

G/Rn over bare soil ranges from 20-50% dependent on soil moisture (Idso et al., 1975) and from 5-30% for alfalfa and cotton dependent on vegetation cover (Clothier et al., 1986; Kustas and Daughtry, 1990). Even sparse vegetation are found to dominate soil moisture dependency (Clothier et al., 1986) and the magnitude of midday G/Rn is thus essentially a function of the amount of vegetated cover (Kustas et al., 1993). Vegetation indices express plant physiological parameters such as biomass, leaf area and vegetation cover and VIs versus G/Rn may thus be regarded as a physically based relationship. Simplified relationships between LAI and G/Rn and LAI and VIs reveal an acceptable analytically based formula of a non-linear expression but empirical studies do often emphasize that the relation of G/Rn to vegetation parameters better fit a linear expression (Kustas et al., 1993).

2. STUDY AREA

The study area is located at Zackenberg (74°30"N, 20°30"W) in Northeastern Greenland. It is a gently undulated lowland in a delta environment surrounded by mountains up to 1200 m.a.sl.. The mean annual air temperature is -10.3 °C and mean temperatures of the warmest and coldest months (July and February) are 4.0 °C and -23.6 °C indicating high Arctic conditions. The mean annual amount of precipitation is 214 mm water equivalent and as much as 87 % falls as snow. The prevailing wind direction is from N and NNE and during the winter and spring heavy snowdrifting appears. The redistribution of the snow has a strong effect on the vegetation. Snowbed and grassland vegetation are found on southfacing slopes with sufficient water supply throughout the summer period from melting upslope snowdrifts. Dry fell field is found on the windswept northfacing slopes, where the snow cover is either missing or very thin. Dry dwarf shrub heath dominates the plains,

Proceedings of the Fourth Symposium on Remote Sensing of the Polar Environments, Lyngby, Denmark, 29 April – 1 May 1996
(ESA SP-391, July 1996)

while wet graminoid fens occur in depressions with wet soil.

3. DATA

The data used in the investigation were collected between 25th July (DOY 207) and 13th August (DOY 226) 1992 as a series of continuous measurements and plot measurements. Continuous data were registered as part of a micro meteorological flux gradient mast situated on a gently sloping dry Cassiope heath. The data used include data of soil temperature in 2 different levels, soil heat flux, surface temperature and net radiation. Additionally, 27 plots were established in the area. Every plot consisted of 6 measurements of spectral reflectance, 6 biomass measurements including colour photo registration for later estimation of vegetation cover percentage and 6 measurements of surface temperature and net radiation. The vegetation plots cover dry and moist tundra communities representing the vegetation types fell field (FF), dry dwarf shrub (DDS), snowbed/grassland (SG) and fens (F).

4.1. VIs AND PLANT PHYSIOLOGICAL PARAMETERS

A primary goal of many remote sensing projects is to characterize the type, amount and condition of the vegetation within a scene, and the technique involves linear or ratio combinations of spectral bands measuring reflectance in the red (600-700 nm) and near-infrared (750-1100 nm) regions. Radiances in the red region are inversely related to the in situ chlorophyll density while radiances in the near-infrared are directly related to the projected leaf area index. Today the ratio of reflected infrared light to reflected red light is referred to as the ratio vegetation index (RVI, eq. 1).

$$RVI = R_{NIR}/R_{RED} \qquad \text{eq. 1}$$

where R_{NIR} and R_{RED} are the near-infrared and red reflectance respectively. RVI values range from 1.1 for bare soil to 12.5 for dense green luxuriant fen vegetation. For dense green vegetation the amount of red light reflected from the canopy is very small, and as red band reflectance approaches zero, the RVI increases without bound. Thus, the amount of reflected red light must be measured with considerable accuracy if reasonable values of RVI are to be expected. If the red band is measured with sufficient precision, the RVI is quite sensitive to vegetation changes during the time of peak growth, but it is not very sensitive when the vegetation cover is sparse.

Tucker (1979) found that the low dynamic range of the RVI over sparse vegetation could be enhanced by rationing the difference between the NIR and the RED bands to the sum of the two bands. This VI was subsequently named the normalized difference vegetation index (NDVI, eq. 2), that is

$$NDVI=(R_{NIR}-R_{RED})/(R_{NIR}+R_{RED}) \qquad \text{eq. 2}$$

NDVI values range from 0.05 for bare soil to 0.87 for dense green luxuriant fen vegetation. Many other variations of the vegetation index have been developed over the years, but they contain in general the same amount of information, and are therefore considered to be functionally equivalent.

4.1.1. Percentage vegetation cover

The definition of RVI and NDVI indicates an increase in RVI and NDVI with increasing percentage of green vegetation cover (VC%). Fig. 1 shows a significant linear relationship (r^2=0.897) between VC% and RVI, while a significant exponential relationship (r^2=0.818) between VC% and NDVI was found (fig. 2). The VC% of dry fell field ranges from 0 % to 15 % with a single tussock covering 50 %, while VC% ranges from 10% to 100 % for moist fens. Stow et al. (1993) also found a similar but linear significant relationship (r^2=0.67) between Arctic tundra shrub cover and NDVI, but NDVI values only ranges from 0.40 to 0.60 and a percentage shrub cover from 10 % to 50 %.

4.1.2. Biomass

Simple linear regression analysis shows a significant relationship (r^2=0.872) between RVI and total green wet biomass (fig. 3) while the linear relationship between NDVI and total green wet biomass (fig. 4) was smaller but still significant (r^2=0.586). Daughtry et al.(1990) found a very significant (r^2 = 0.95) linear relationship between NDVI and total biomass, but they were studying very homogenous agricultural crops. Linear regression has also been used by both Hope et al. (1993) and Shippert et al. (1995) to evaluate the relationship between NDVI and photosynthetic biomass of various heterogenous Arctic vegetation cover types. They found that up to 51% and 97% of the variance in the amount of photosynthetic biomass in the moist tussock and dry heath communities was explained by NDVI.

Fig. 4 shows that the maximum value for NDVI asymptotic approaches 1.0 as the biomass increases implying that the chlorophyll in the vegetation had absorbed all incident red light. Tucker (1976) was the first to find this relationship and he used an exponential equation to describe the relationship between reflectance data and biomass for grass canopies. A strong exponential relation

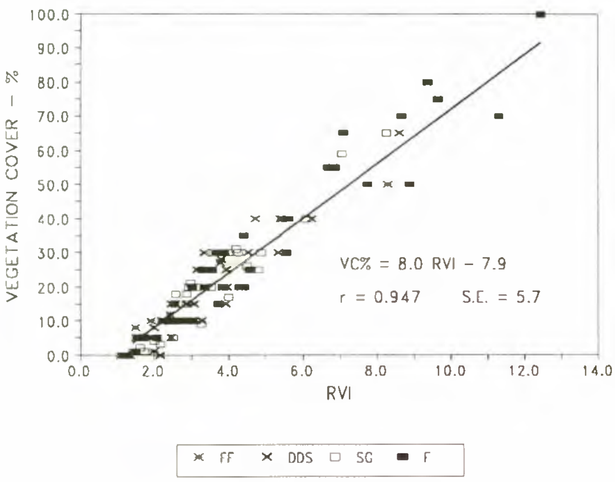

Figure 1: Regression of RVI on vegetation cover procent.

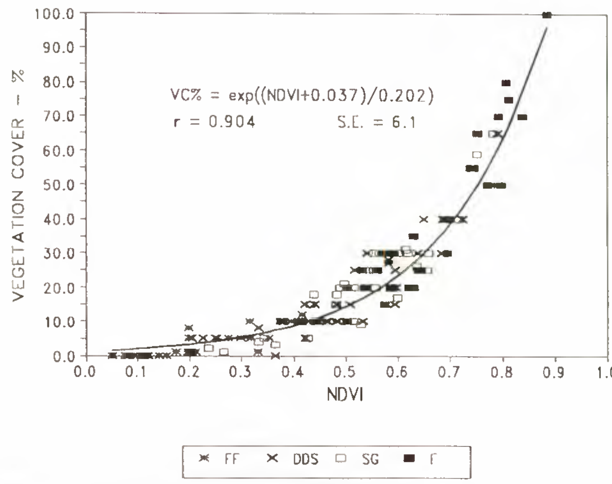

Figure 2: Regression of NDVI on vegetation cover procent.

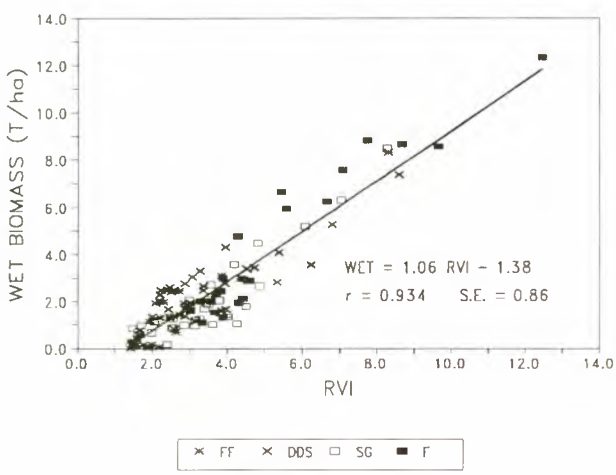

Figure 3: Regression of RVI on wet biomass.

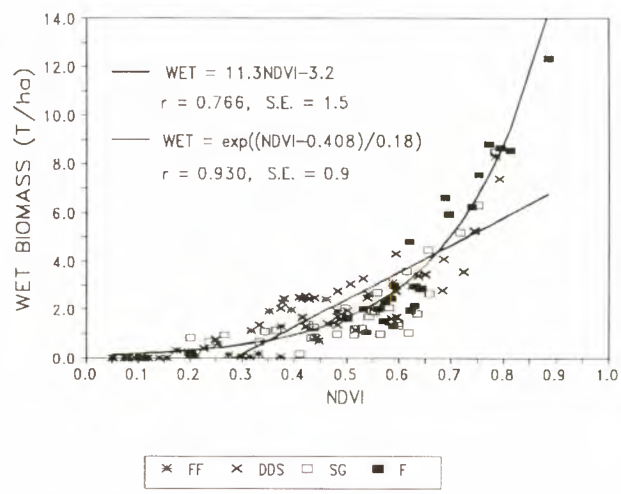

Figure 4: Regression of NDVI on wet biomass.

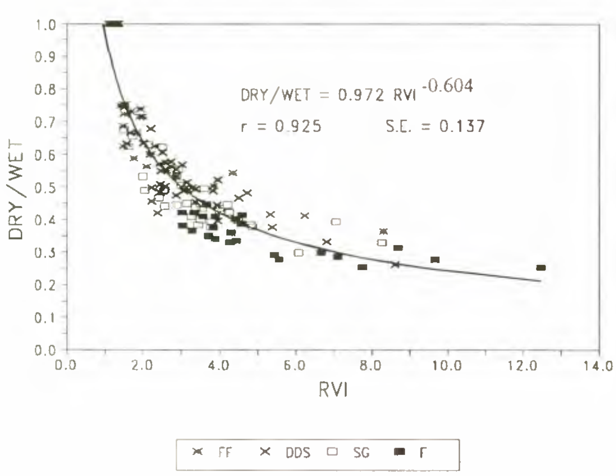

Figure 5: Regression of RVI of the ratio between dry and wet biomass.

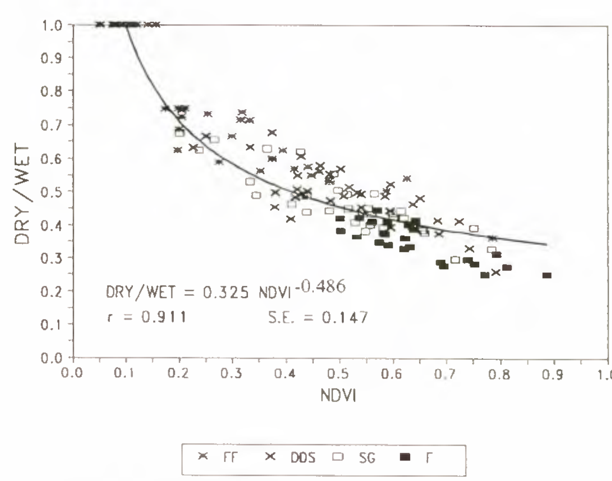

Figure 6: Regression of NDVI on the ratio between dry and wet biomass.

ship between NDVI and biomass in Arctic areas was previously found by Hansen (1991) and Hope et al. (1993), and the same was found for the Zackenberg data (r^2=0.865, fig. 4).

4.1.3. Dry/wet biomass ratio

The ratio between dry and wet biomass is an indication of the water content in the vegetation. Figs. 5 and 6 show a strong relationship between the dry/wet-ratio and RVI (r^2=0.855) and NDVI (r^2 = 0.830), when a simple power curve is used. The dry/wet-ratio is decreasing with increasing vegetation index which indicates an increasing water content in the vegetation with increasing vegetation index. The dry/wet-ratio ranges from 0.5 to 0.75 for the dry fell field vegetation, while for the snowbed and moist fen vegetation the dry/wet-ratio ranges between 0.25 and 0.50. Both classes has an increasing amount of mosses. In contrast to vascular plants succulent species such as mosses tolerate extremely low water content, yet typically has a very high water content, which can explain the decreasing dry/wet-ratio with increasing NDVI.

NDVI values between 0.0 and 0.5 dominate the Zackenberg area, while NDVI values between 0.5 and 0.8 is restricted to small scattered areas with dense luxuriant vegetation. As NDVI was more sensitive to sparse vegetation, NDVI should show the highest significant relationship to the tested plant physiological parameters, but RVI was slightly stronger for both percentage vegetation cover, wet biomass and dry/wet-ratio. Where satellite data have been used, it has been proven that NDVI reduces variations in scene brightness due to terrain, view and solar angles as well as some atmospheric effects and NDVI is focused upon in the following.

4.2. G/Rn

Estimates of the thermal conductivity k (W/m K) and the thermal diffusivity κ (m^2/s) were used to calculate the daily variation of the volumetric heat capacity C (MJ/m^3 K) (eq. 3):

$$C = k/\kappa \qquad \text{eq. 3}$$

Soil heat flux G (W/m^2) at the surface was calculated using the combination method that is by adding the soil heat flux measured at 0.04m $G_{0.04}$ (W/m^2) to the storage heat flux between 0-0.04m estimated from the heat capacity and the change in temperature with time dT/dt (K/s) (eq. 4):

$$G = G_{0.04} + C(dT/dt)dz \qquad \text{eq. 4}$$

Continuous measurements of soil heat flux and surface temperature representing 15 days of approximately cloudless conditions were investigated and a high correlation (r^2 = 0.901) were found using a (5*20) min sliding mean of surface temperature, Ts (°C) (eq. 5). The Ts to G correlation is used to estimate soil heat flux from plot measurements of surface temperature.

$$G = 4.73\,(Ts) - 20.87 \qquad \text{eq. 5}$$

4.2.1. Daily G/Rn ratio

The daily G/Rn ratio at Zackenberg in the measurement period including all days was 0.18. Several investigations have found a G/Rn ratio around 0.10 which is generally the case in temperate regions but a higher ratio could be expected in permafrost regions (Halliwell and Rouse, 1987). Halliwell and Rouse (1987) found a G/Rn ratio between 16-18% which they consider to be relatively high but reasonable as the latent heat sink in the thawing front limits soil warming. This maintains a larger temperature gradient between the surface and intermediate depths (0.5-1.0 m) and a large soil heat flux can be expected during the thaw period.

4.2.2. Diurnal variation of G/Rn

Diurnal variation of G/Rn for 15 days in the measurement period with approximately cloudless conditions (fig. 7) show that G/Rn was positive from 04 LAT and increased until maximum 0.28 at 12 LAT. The ratio decreased subsequently until 18 LAT, time of turnover between positive and negative values being dependent on G. The pattern is equivalent to other investigations (e.g. Kustas and Daughtry, 1990) on more temperate latitudes and underlines the importance of obtaining midday values in remote sensing studies. The average maximum at 12 LAT at 0.28 is 55% higher than the daily G/Rn ratio.

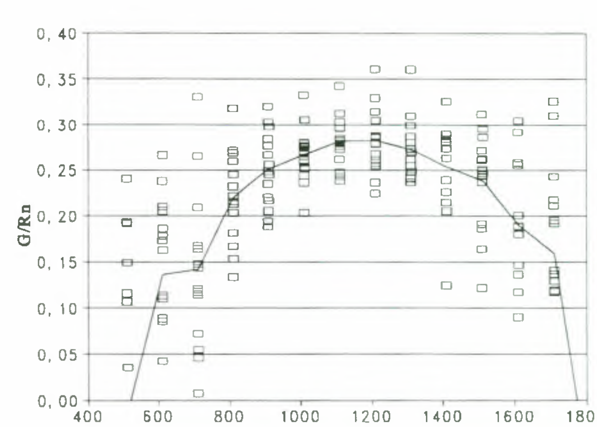

Figure 7: Diurnal variation of G/Rn for 15 days in the measurement period with appr. cloudless conditions. Full drawn line indicates the mean.

4.3. G/RN AND VIs

Mean values of NDVI and G/Rn based on the 6 measurements in the 27 plots are shown in fig. 8. A grouping of data points with respect to vegetation type appears from the data.

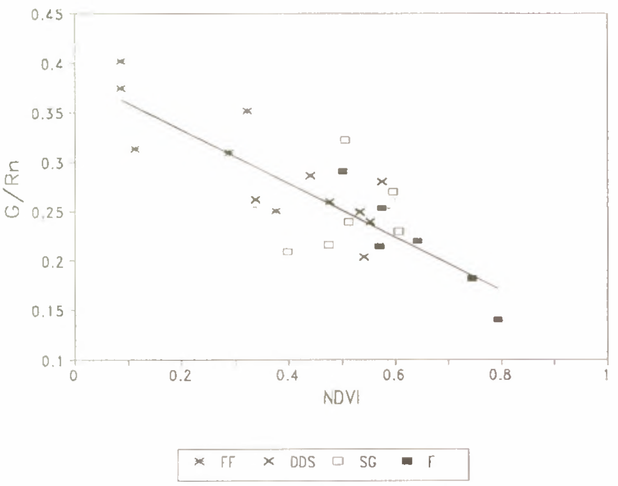

Figure 8: Linear regression of NDVI on G/Rn

Fell fields have high G/Rn and low NDVI. Vegetation is only very sparse and the moraine ridges and wind exposed fluvial planes where fell fields are found, were dominated by bare soil and crust. Dry dwarf shrub heath and snowbed/grassland plots are centred around G/Rn 0.25 and NDVI 0.5. The dry dwarf shrub plots represent relatively dry surfaces but a high vegetation coverage percent limits the soil heat flux. Fens have a large variation in NDVI values due to the presence of different plants in the different plots. Plots with blooming Euriophorum scheuzeri will have a large reflectance in the visible spectrum causing a low NDVI while plots with many very green mosses will have a high reflectance in near infrared causing a high NDVI. Generally, the soil heat flux to net radiation ratio is low due to a high soil moisture content.

The regression of NDVI on G/Rn estimated from the 27 observations in fig. 8 (eq. 6) has a regression coefficient r^2=0.66 and a standard error of estimate of 0.04. Estimation of the G/Rn ratio on RVI (eq. 7) has a regression coefficient r^2=0.56 and a standard error of estimate of 0.04.

$$G/Rn = -0.27\ NDVI + 0.39 \quad \text{eq. 6}$$

$$G/Rn = -0.025\ RVI + 0.35 \quad \text{eq. 7}$$

The results of eq. 6 and 7 are compared with other investigations in table 1.

Study	n	VI	alfa	beta	r^2	S.E.
Clothier et al., 1986	4	RVI	-0.013	0.35	0.87	0.01
Kustas and Daughtry, 1990	11	RVI	-0.017	0.32	0.74	0.04
Kustas et al., 1993	42	RVI	-0.0094	0.30	0.70	0.06
Present paper	27	RVI	-0.025	0.35	0.56	0.04
Kustas and Daughtry, 1990	11	NDVI	-0.21	0.32	0.86	0.02
Kustas et al., 1993	42	NDVI	-0.33	0.40	0.80	0.05
Present paper	27	NDVI	-0.27	0.39	0.66	0.04

Table 1: Intercept (alfa), gain (beta), regression coefficient (r^2) and standard error of estimate (S.E.) from the regression of vegetation indices (VI) on G/Rn.

Generally, the NDVI regressions have the highest regression coefficients but a close agreement on both slope and intercept are found between all the investigations cited. Clothier et al. (1986) work on sparse alfalfa stubble and full vegetative canopy, Kustas and Daughtry (1990) work in an arid climate on alfalfa and cotton cover, and Kustas et al. (1993) is working in a humid climate over bare soil and soybeans. Together with the present investigation from a high arctic tundra locality with natural vegetation, the slope and intercept of the regression of VIs on G/Rn show little sensitivity to a wide range of environmental conditions.

5. CONCLUSION

The empirical derived correlations between the G/Rn ratio and VIs showed that the NDVI described the relationship better than the RVI, which were consistent with other investigations and the slope and intercept of the expression were comparable with estimates over middle latitude agricultural crops. The coefficients of the NDVI and G/Rn regression were determined with a regression coefficient r^2=0.66. The overall correspondence between the present paper covering an Arctic study area with natural vegetation with permafrost in the ground and quoted investigations supports the suggestion of universality of the expression as proposed by Kustas et al. (1993) and we conclude that the methodology is a valid tool for estimation of energy surface fluxes in an high Arctic area.

6. ACKNOWLEDGEMENTS

The present paper is a part of the long term multidisciplinary ecological research program ZERO (Zackenberg Ecological Research Operation) under Danish Polar Centre. It is the purpose of the program to elucidate status quo in a high Arctic ecosystem still undisturbed and thus extremely valuable as a "zero-line" to be compared with future climate induced changes. The project 1992 was financially supported the Man and Biosphere Project and SNF (Danish Research Council).

7. REFERENCES

Clothier, B.E., Clawson, K.L., Pinter, P.J., Jr., Moran, M.S., Reginato, R.J., and Jackson, R.D. (1986): Estimation of Soil Heat Flux from Net Radiation During the Growth of Alfalfa. Agricultural and Forest Meteor., 37, pp. 319-329.

Daughtry, C.S.T., Kustas, W.P., Moran, M.S., Pinter, Jr.,P.J., Jackson, R.D., Brown, P.W., Nichols, W.D., and Gay, L.W. (1990): Spectral Estimates of Net Radiation and Soil Heat Flux. Remote Sens. Environ., 32:111-124.

Halliwell, D. and Rouse, W.R. (1987): Soil Heat Flux in Permafrost; Characteristics and Accuracy of Measurement. J. Climatology, vol. 7, pp. 571-584.

Hansen, B.U. (1991): Monitoring Natural Vegetation in Southern Greenland Using NOAA AVHRR and Field Measurements. Arctic 44(1):94-101.

Hope, A.S., Kimball, J.S. and Stow, D.A. (1993): The Relationship Between Tussock Tundra Spectral Reflectance Properties and Biomass and Vegetation Composition. Int. J. Rem. Sens. 14(10):1861-1874.

Idso, S.B., Aase, J.K., and Jackson, R.D. (1975): Net Radiation - Soil Heat Flux Relations as Influenced by Soil Water Content Variations. Boundary-Layer Meteor., 7:113-122 (1975.

Kustas, W.P. and Daughtry, C.S.T. (1990): Estimation of the Soil Heat Flux/Net Radiation from Spectral Data. Agricultural and Forest Meteor., 49, 205-223.

Kustas, W.P., Daughtry, C.S.T., and Van Oevelen, Peter J. (1993): Analytical Treatment of the Relationships between Soil Heat Flux/Net Radiation Ratio and Vegetation Indices. Rem. Sens. Environ., vol. 46, no. 3, pp. 319-330.

Shippert, M.M., Walker D.A., Auerbach, N.A. and Lewis, B.E. (1995): Biomass and Leaf Area Index Maps Derived from SPOT Images for the Toolik Lake and Imnavait Creek Area, Alaska. Polar Record 31(177):147-154.

Stow, D.A., Hope, A.S., George, H (1993): Reflectance Characteristics of Arctic Tundra Vegetation from Airborne Radiometry. Int. J. Rem. Sens. 14(6):1239-1244.

Tucker, C.J. (1976): Asymptotic Nature of Grass Canopy Spectral reflectance. Appl. Optics 16(5):1151-1156.

Tucker, C.J. (1979): Red and photographic infrared linear combinations for monitoring vegetation. Remote sensing of Environment 8(2):127-150.

The Use of Coincident DMSP SSM/I and OLS Satellite Data to Detect Snow Cover

A. P. Standley[1] and E. C. Barrett

Centre for Remote Sensing, University of Bristol, Bristol BS8 1SS, United Kingdom

1. ABSTRACT

The use of SSM/I data for both surface snow cover detection and precipitation monitoring have been well documented since the launch of the DMSP in 1987. One of the major problems yet to be resolved is the successful discrimination of precipitation from snow cover in high latitudes. Both precipitation and snow cover can exhibit similar responses at SSM/I microwave frequencies. The majority of snow cover/precipitation discrimination algorithms rely on a single temperature threshold at either 19 or 22 GHz and perform adequately under most conditions. It has been observed that this threshold can vary under given surface and atmospheric conditions by as much as 5-10 K. By using additional thermal infrared (IR) data from the DMSP OLS instrument a further check can be applied which is independent of the microwave instrument. In theory a precipitating cloud will have a very much lower IR temperature than a surface snow cover. The OLS also has the advantage that it has an improved spatial resolution over the SSM/I and a synergistic approach will at least maintain the spatial resolution of the SSM/I estimate.

2. Introduction

The SSM/I is a valuable tool for both snow cover monitoring and snowpack investigation because it has the ability to sense the Earth's surface through the atmosphere in most conditions and, by interacting with the volume of the snowpack, it can reveal information about the snowpack including the depth and water equivalent. A snowpack has in general a very different microwave response compared to other land surface types due to the scattering of microwave radiation by ice crystals within the snow. However, the same microwave response is seen within the distribution of ice crystals in precipitating clouds. The SSM/I is limited in that it cannot provide further information to discriminate these two conditions. The potential use of OLS IR data is investigated as a tool to increase the confidence of this discrimination.

Most precipitation/snow cover discrimination algorithms rely on the estimation of the surface temperature using the low frequency channels (V19 or V22) on the SSM/I (*Ferraro et al.* [1994],*McFarland et al.* [1990] etc) . This threshold has been shown to vary in both time and space (*Ferraro et al.* [1994]) due to surface warming or atmospheric cooling, and by as much as 5-10 K. This can result in large errors in both precipitation or snow cover monitoring (*Negri et al.* [1995], *Bauer and Grody* [1995]). Further refinement of the technique has been attempted using the DMSP SSM/T2 (*Bauer and Grody* [1995]) and has proved useful in case studies but does not comprise a complete solution. This technique has the advantage of using higher frequency channels that detect radiation that is not expected to have emanated from the surface but only from the atmosphere, and hence if scattering is detected it must be an atmospheric phenomenon. A disadvantage is the poor resolution of the SSM/T2 (≈100 km) compared to the SSM/I (≈25 km).

A second instrument that is flown alongside the SSM/I is the DMSP Operational Line Scanner (OLS). In theory, a scattering and precipitating cloud should have a low thermal IR temperature compared with its surroundings (and, in particular, snow cover) and the OLS should be able to discriminate the two with some success. It has the further advantages of being independent of the microwave processes of the SSM/I and having a vastly superior resolution (≈3 km). This last feature should permit increased detection near coasts where the low frequency SSM/I channels must be masked due to mixed pixel effects.

3. Data Description

3.1. SSM/I

The SSM/I is a seven-channel passive microwave radiometer flown on board the DMSP. All channels apart from the 22 GHz channel are dual-polarised. From here on the vertical frequencies will be ascribed a V (ie V85) and the horizontal frequencies an H.

[1] email : andy.standley@bris.ac.uk

Proceedings of the Fourth Symposium on Remote Sensing of the Polar Environments, Lyngby, Denmark, 29 April – 1 May 1996
(ESA SP-391, July 1996)

Further details about the instrument characteristics can be found in *Hollinger et al.* [1987].

Based on the algorithm of Ferraro, Grody and Marks (*Ferraro et al.* [1994]) the discrimination of precipitation from snow cover is a threefold process, but where the majority of this discrimination is performed by one threshold using the V22. (A similar approach where the V19 channel is used has also been tested (*McFarland et al.* [1990])). The assumption behind the choice of the V22 threshold is that firstly snow crystals are larger in general than ice crystals within clouds and will scatter more at this frequency, and secondly that precipitation usually will emanate from a warmer surface and atmosphere than snow cover. On global scales this approach has been shown to be successful. Problem areas do occur and have been noted in regional case studies where some areas and some seasons are more problematic than others. It would appear that the optimal threshold at 22 GHz to discriminate snow cover from precipitation is variable in both space and time, but attempts to define the threshold accurately can not be obtained purely using SSM/I data.

3.2. OLS

The OLS is a two-channel radiometer that has an IR sensor in the 10.2 to 12.8μm range and a Visible sensor in the 0.4 to 1.1μm range. Fine resolution data has a spatial resolution of approximately 0.56 km but the more usual output is a degraded "smoothed" resolution of 2.7 km. In this paper the "smoothed" resolution data has been used. OLS IR data are calibrated internally and converted to a linear range of 190 K to 310 K. Saturation can occur below 200 K.

3.3. Surface Data

Daily surface data have been obtained for the case study periods for meteorological stations over Scandinavia and the United Kingdom. Data were obtained from the global summary of the day www/ftp site (*http://www.ncdc.noaa.gov/pub/data/globalsod* or *ftp://ftp.ncdc.noaa.gov/pub/data/globalsod*).

4. Scandinavia Case Study

4.1. Surface Data Interpretation

SSM/I and OLS IR data for 13-16 April, 1995 have been obtained and mapped to a UTM zone 32 projection at 2 km resolution. Figure 1 shows the IR image for 14 April with an overlay of the corresponding SSM/I V22 265 K contour. Due to the different swath widths of the SSM/I and OLS the area of coverage is less in the SSM/I imagery. During the case study period a frontal system passed over Norway preventing thermal and IR sensing of the Earth's surface on 14 and 15 April but some detection of snow would be possible on 16 April using the OLS alone.

Table 1 show surface reports (Snow Depth (D (cm)), maximum and minimum temperature (Max, Min (K)) and precipitation type (P (Rain - rain, S - snow, N - none))) , SSM/I channel Tb values (V85 and V22 (K)) and IR temperatures (IR (K)) for the case study period. Stations have been chosen that represent the variation in conditions seen. FOKSTUA is a high altitude station in Norway. Minimum temperatures remain below 273 K but some melting of the large snow depth will have taken place as maximum temperatures reached above 273 K. The SSM/I identifies this pixel as a scatterer with the V22 (and V19) value being above 265 K on all but the last day. Snow is reported on 15 April but the OLS IR temperatures suggest only very low temperatures on 14 April. SARINA is a station in southern Sweden. Surface reports show rain on 14 and 15 April and a declining snow depth. Minimum temperatures would suggest there is snow melt but some re-freezing at night. The SSM/I detects rain on 14 and 15 April then snow on 16 April. The OLS IR has very low temperatures on 14 April but they recover on 15 and 16 April. LAINIO is a station in northern Sweden. Snow depths are declining slowly but the minimum temperature is well below freezing so melt conditions will take place for only a short time of each day. The surface reports indicate rain only on 16 April but the SSM/I would suggest rain on two of the three days with data. The OLS IR has low values on 14 and 15 April. TVEITSUND is a lower altitude station in southern Sweden. Rain is reported on the same days as FOKSTUA but for this pixel the SSM/I detects no scattering due to the very shallow snow depths and melting conditions due to the high temperatures. SSM/I channel values decrease on 16 April to leave a snow scattering signature. The OLS IR temperatures suggest low temperatures on 14 April but not when surface reports show rain.

These pixel comparisons give some insight into the nature of the OLS and SSM/I data and the response to the given surface and atmospheric conditions. Over the case study area temperatures exceeded 273 K over large areas of snow cover and snow free surfaces inducing snow melt. Many stations also reported some precipitation (both rainfall and snowfall), the nature of the precipitation vary-

Table 1. Surface (and Satellite) Data for Four Selected Stations

Date April	D (cm)	Max (K)	Min (K)	P	V85 (K)	V22 (K)	IR (K)
FOKSTUA II at 62.07N 009.17E 974m							
13 am	24	278	272	N	233	268	273
14 am	24	275	271	N	248	268	233
14 pm	24	275	271	N	-	-	233
15 am	24	273	270	RS	216	265	258
15 pm	23	273	270	RS	-	-	262
16 am	22	274	265	N	228	260	258
SARNA at 61.42N 013.10E 438m							
13 am	25	283	268	R	-	-	274
14 am	24	281	270	N	266	266	262
14 pm	24	281	270	N	-	-	232
15 am	22	275	274	S	262	264	248
15 pm	22	275	274	S	-	-	253
16 am	22	275	270	S	256	264	262
LAINIO at 67.46N 022.21E 317m							
13 am	27	280	268	N	-	-	259
14 am	26	277	271	N	-	-	254
14 pm	26	277	271	N	210	257	237
15 am	26	276	267	N	242	266	261
15 pm	26	276	267	N	-	-	242
16 am	25	276	262	R	241	265	260
TVEITSUND at 59.02N 008.31E 255m							
13 am	02	286	272	N	268	266	271
14 am	00	286	275	N	269	266	260
14 pm	00	286	275	N	-	-	225
15 am	00	284	275	R	264	266	267
15 pm	00	284	275	R	-	-	262
16 am	00	279	271	N	244	263	256

ing due to the large range of altitudes and latitudes. Periods of very low (< 240 K) OLS IR temperatures suggest an increased chance of precipitation but this may also be confused with an increase in the cloud height. The SSM/I data show great fluctuations at 85 GHz which would also suggest changes in atmospheric moisture and transparency. These tables also emphasise the difficulty in comparing surface point data with satellite areal data that are not coincident in time.

The surface data for 13 April show the warmest surface temperatures of the 4 days and this has a direct influence on the V22 value. In this situation the snow condition may be subject to melt. The V22 value has a much poorer resolution than the V85 value and represents an average temperature for a large region, some of which is obviously warmer than 265 K. The data from station FOKSTUA (Table 1) show a low V85 value. This is due to the better resolution of the V85 identifying the higher altitude areas and the low microwave temperatures due to the snow. The SSM/I identification of rain in this area is not supported by the surface or IR data.

By 14 April the frontal system has become more dominant over the case study area. It would appear that in the afternoon image (Figure 1) there are large areas of high IR temperatures that are within the 265 K contour. The selected surface reports also show no rain for this date. This is not the case for the whole of the case study area where some stations report rain, but a small total accumulation. (This is most likely drizzle, and most of the stations are in western coastal locations of Norway). Once again the SSM/I identification of rain in this area is not supported by the surface or IR data.

The frontal system has started to move away from Norway by 15 April. Despite this, surface reports of rain are more extensive and three of the four selected stations report rain. On the final day the main extent of the frontal system was to the east of the case study area. Despite this the area of V22 $>$ 265 K is large and covers an area of warm OLS IR temperatures. Surface reports for the whole area suggest that the rain was confined to the eastern coast of Sweden.

The general outcome of this case study is therefore that the SSM/I is over estimating the extent of rainfall with the threshold used. It is expected that the use of OLS IR data would aid in the discrimination process due to the help OLS IR provides in identifying cold clouds and hence rainfall potential.

4.2. SSM/I Interpretation

The case studies presented above show that high V22 values can be observed in Spring snow melt situations and some snow covered areas are misclassified as rain areas. In order to allow for the variability of the V22 threshold a relaxation of the SSM/I algorithm is performed to ascribe certainties to the classifications of snow cover and precipitation. If the 265 K threshold is increased it is expected that fewer snow cover pixels will be misclassified as precipitation. A similar assumption is made about reducing the threshold to prevent precipitation being misclassified as snow cover.

4.3. OLS Interpretation

Given the IR temperature and visible albedo of AVHRR data, Garand (*Garand* [1989]) suggests an

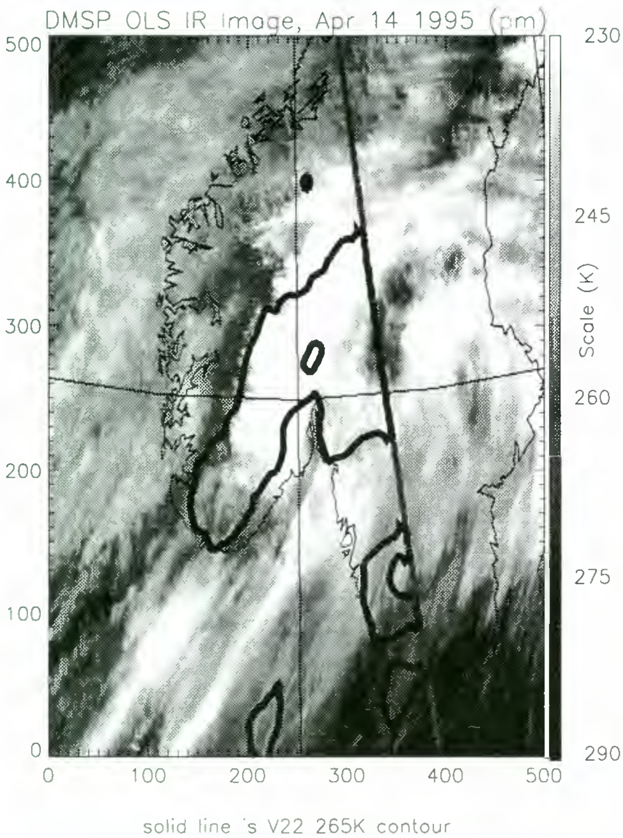

Figure 1. DMSP OLS IR (and coincident SSM/I V22 265 K contour) Image for April 14 (pm) 1995. Norway is covered only by small areas of cold cloud.

IR temperature threshold of 235 K for a minimum of 28 % probability of precipitation given an albedo of 55-70 %, rising to 65 % for an albedo of 85-100 %. With no information of albedos obtainable from the DMSP for the cloud areas the IR temperature information has to be used on its own, but an IR temperature threshold of 235-245 K would suggest a reasonable probability of precipitation.

Given the inclusion of IR temperature information the following scenario is proposed for the detection of snow cover. Once pixels are described as unknown within the SSM/I data the OLS IR data are used to obtain more information. The precipitation is inferred from the measurement of cloud top temperature. For a precipitating cloud it is expected that the cloud top temperature would be much lower than the temperature of a snowpack. The comparison is thus made between the IR value and a fixed threshold to detect cold precipitating areas and (relatively) warm snow cover areas.

A synergistic algorithm can thus be developed:

1. Given a V22 value of between 260 and 270 K, a scattering pixel is flagged as UNKNOWN-CLASS. The OLS IR value is then used.
2. Given a value below 240 K the pixel is flagged as OLS-PRECIP and given a value above 260 K OLS-SNOW.
3. Between 240 and 260 K the pixel is flagged as OLS-CLOUD-SNOW (cloud covered snow).
4. Above 273 K the pixel is flagged as OLS-SNOW-MELT.

5. Synergistic Discrimination

5.1. Scandinavia Case Study

The above synergistic algorithm has been applied to the Scandinavian case study images (Section 4). Figure 2 shows the synergistic approach applied to Figure 1. The area of modification is substantial, with large areas of SSM/I precipitation being reclassified as OLS-SNOW, OLS-PRECIP and OLS-CLOUD-SNOW. The result is more in agreement with the surface data which suggests less precipitation as the weather front has yet to pass over most of the case study area. As the suggested OLS thresholds are based on work on other sensors it important to assess the sensitivity of them. Due to the inclusion of the new class OLS-CLOUD-SNOW the sensitivity to the snow cover/precipitation discrimination problem can not be addressed directly. A histogram of the OLS IR temperatures for all scattering pixels identifies peaks at 258 K and 241 K. The lower peak may not contain all precipitating pixels' for cold cloud below 240 K and may also be thin non-precipitating cloud. The histogram suggests that a higher IR threshold might better separate the two peaks, but this may introduce too much OLS-PRECIP into the classification. Over the whole case study period the synergistic algorithm identifies areas of scattering that have warm V22 and IR temperatures and re-classifies them as either OLS-CLOUD-SNOW or OLS-SNOW, consistent with the surface reports. Areas of possbile snow melt are also identified as OLS-SNOW where the IR temperature is close to or below 273 K.

5.2. United Kingdom Case Study

A second case study has been used to test the approach described above in a lower slightly latitude and under different meteorological conditions. In this case study a depression is centred over the UK on

2 March, 1995 and has deposited snow (and rainfall in some areas) over large areas of southern England (this is confirmed by surface reports and by personal observation). Figure 3 shows the OLS IR image for this day and the outline of the frontal system is evident in it. Within the frontal system, variation in IR temperature can be seen and some precipitation would be expected. The SSM/I alone would classify all of the scattering regions as snow cover because the V22 value is below 265 K.

Using the OLS information, the synergistic algorithm re-classifies the majority of the scattering areas (Figure 4) to OLS-PRECIP. In the southern half of England and into Wales the area is dominated by precipitation but at the southern extremes of the two scattering regions there are areas classified as OLS-SNOW and OLS-CLOUD-SNOW. This is consistent with the system pushing north-eastwards, with precipitation near its leading edge, and snow cover being left after the front has moved on. In this case the OLS-identified precipitation could also be active snowfall. There is little extra evidence within the satellite data that could be used to separate precipitation as rain from precipitation as snow, as both sensors would only sense radiation from the active layer of ice crystals at the cloud top, but the radiation temperatures observed by the SSM/I low frequency channels would be reduced by the surface scattering of the snow cover.

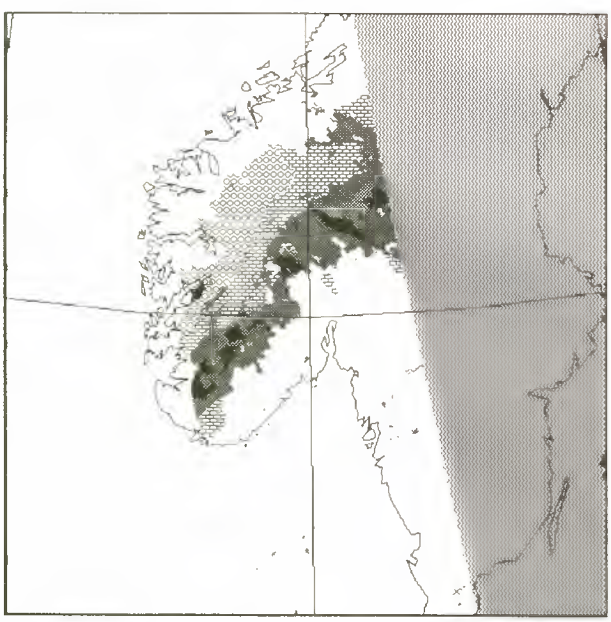

Figure 2. DMSP SSM/I and OLS classified product Image for 14 April (pm) 1995. Circles - SNOW, Grey - OLS-CLOUD-SNOW, Brick - OLS-SNOW, Black OLS-PRECIP

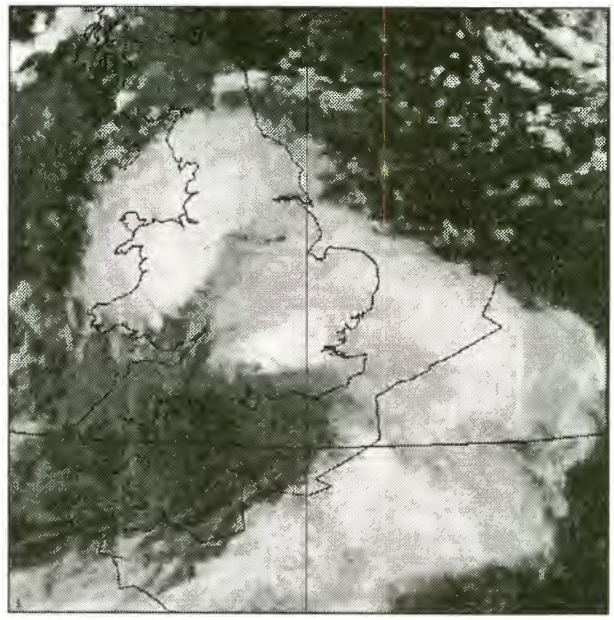

Figure 3. DMSP OLS IR Image for 2 March (pm) 1995.

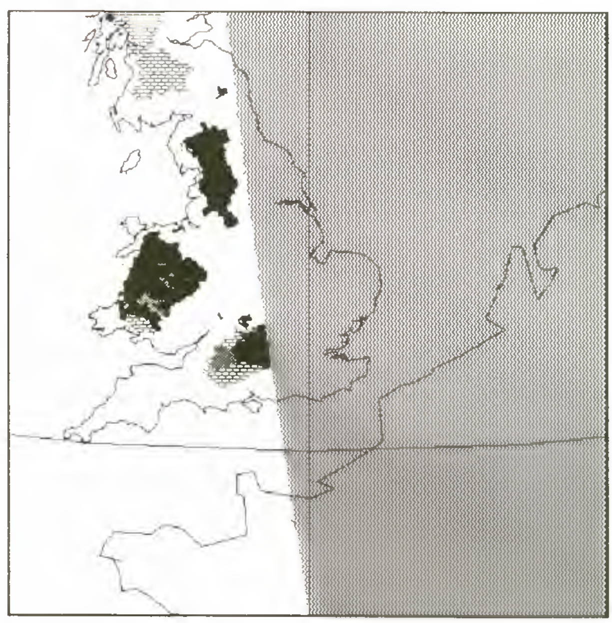

Figure 4. DMSP SSM/I and OLS classed Image for 2 March (pm) 1995. Circles - SNOW, Grey - OLS-CLOUD-SNOW, Brick - OLS-SNOW, Black - OLS-PRECIP

6. Discussion

It is evident from the above two case studies that a synergistic approach to snow cover and precipitation discrimination using the DMSP SSM/I and OLS instruments can provide additional information that improves classification over techniques involving a single instrument. The choice of SSM/I and OLS IR temperature thresholds are intuitive at present due to the limitations of the information the two instruments provide. The SSM/I V22 threshold used alone produces misclassifications when there is a snow cover, the air temperature is high and there is increased atmospheric opacity as seen in the first case study (Section 5.1). In the case of active precipitation over snow cover, the OLS IR data can provide this extra information in order that snow depth determination could be modified (Section 5.2).

The synergistic algorithm relies on three additional thresholds. Note also that:

1. The choice of these thresholds was based on analyses of many SSM/I snow cover and precipitation case studies.
2. The sensitivity of the re-classification to these thresholds can be quite large due to the small microwave temperature range between the two states of snow cover and precipitation.
3. The synergistic algorithm allows for the re-classification to be the same class as the original SSM/I classification so the sensitivity to OLS induced misclassification is reduced (for instance SNOW can become OLS-SNOW).

7. Conclusion

In using the SSM/I for snow cover and precipitation monitoring it is clear there is some misclassification of precipitation and snow cover identified by the SSM/I and that it is difficult to resolve this problem using the SSM/I data alone. In case studies conventional surface data can be used to infer the precipitation and snow depth regimes for an area but do not have the temporal resolution (generally being a daily report) to clearly assert the true nature of scattering identified by the SSM/I. In some countries (e.g UK), hourly data are available but in most regions of regular snow cover the data are sparse in space and time.

In this paper two case studies have shown the potential use of a combined SSM/I and OLS IR classification scheme to differentiate precipitation from snow cover. The SSM/I is always used to provide a first guess field due to its ability to detect the precipitation and/or snow cover. In regions of doubt, however, the OLS IR data can provide extra information by being able to estimate the surface temperature (where surface is the cloud top, or the snow cover on the ground). Although the spectral resolution of the OLS does not allow accurate determination of temperatures it can be used to identify cases where the SSM/I is identifying incorrectly either precipitation or snow cover. Since interest in snow cover is greatest when phase changes are likely (e.g. with new snow falls, or with the initiation of snow melt), it is particularly important to be able to better discriminate between falling precipitation and snow on the ground than is possible using either SSM/I or OLS data alone, or to be able to identify areas of doubt.

Acknowledgments We would like to thank all those in the CRS, Norman Grody and Ralph Ferraro at NOAA, Tom Anderson of Statkraft and Mike Kennett and Gunnar Atteras of NVE for their guidance and help with this work.

References

Bauer, P., and N. Grody, The potential of combining SSM/I and SSM/T2 measurements to improve the identification of snowcover and precipitation, *IEEE Trans. Geoscience and Remote Sensing, 33, No. 2*, 252–261, 1995.

Ferraro, R. R., N. C. Grody, and G. F. Marks, Effects of surface conditions on rain identification using the DMSP SSM/I, *Remote Sensing Reviews, 11*, 195–209, 1994.

Garand, L., Two automated methods to derive probability of precipitation fields over oceanic areas from satellite imagery, *Journal of Applied Meteorology, 28*, 913–924, 1989.

Hollinger, J., R. Lo, G. Poe, R. Savage, and J. Pierce, *Special Sensor Microwave/ Imager User's Guide*. Washington, DC: Naval Res. Lab., 1987.

McFarland, M. J., R. L. Miller, and C. M. U. Neale, Land surface temperature derived from the SSM/I passive microwave brightness temperatures, *IEEE Transactions on Geoscience and Remote Sensing, 28, no. 5*, 839–845, 1990.

Negri, A. J., E. J. Nelkin, R. F. Adler, G. J. Huffman, and C. Kummerow, Evaluation of passive microwave precipitation algorithms in wintertime midlatitude situations, *Journal of Atmospheric and Oceanic Technology, 12, no. 1*, 20 – 32, 1995.

GLACIERS & SNOW

GLACIER MAPPING AND INVENTORY OF THE ILLECILLEWAET RIVER BASIN, BRITISH COLUMBIA, CANADA, USING LANDSAT TM AND DIGITAL ELEVATION DATA.

Robert W. Sidjak and Roger D. Wheate

Geography Programme, Faculty of Natural Resources and Environmental Studies,
University of Northern British Columbia, 3333 University Way, Prince George, B.C., V2N 4Z9, Canada.
Fax: 604-960-5538 (Wheate); email: wheate@unbc.edu, sidjakr@ugrad.unbc.edu

ABSTRACT

Glacier inventory is important both to provide an estimate of freshwater storage and as an indicator of climate change. Glacier records in Canada are not as extensive as in most other countries owing to the large landmass and recent human history. Landsat Thematic Mapper (TM) data was combined with Provincial 1:20,000 digital elevation data to classify and map the Illecillewaet Glacier in Glacier National Park, B.C. and update earlier records from the 1950's. The best results were obtained by using the second principal component of the sub-scene as a mask in order to isolate the glacier extent from the surrounding terrain, and then to generate principal component images for just the glacier plus a TM4/5 ratio and NDSI (normalised difference snow index). This procedure can be applied to more northerly and less accessible glaciers, with the possible addition of other data sources such as radar.

1. INTRODUCTION

The glaciers of the Columbia Mountains in British Columbia represent a significant reservoir of water in the Columbia River Basin. Various water supply interests depend to a significant degree on runoff from these glaciers, while long term glacier change is considered an effective index of overall climate change. Periodic inventory of glacier attributes is an important component of assessing glacier volume. Attributes such as equilibrium line altitude and accumulation area ratio of these glaciers can indicate mass balance trends.

Previous mapping and inventory efforts in the 1950's and 1970's have utilised aerial photograph interpretation techniques. This method is expensive and laborious. A single Landsat scene captures an area covered by many hundreds of airphotos, minimizes relief displacement, and affords sufficient resolution to discriminate the features of interest. When combined with provincial level 1:20,000 scale digital mapping data, Landsat scenes available for almost three decades (since 1972 for MSS, 1982 for TM), can be geocoded and orthorectified to provide an accurate integrated data base from which important glacier inventory attributes can be derived using image processing methods.

The project endeavours to demonstrate the applicability of combined Landsat TM multispectral and digital elevation data for mapping glacier extent and distribution in a format compatible with existing glacier inventory. Compared to alternative sensing platforms such as radar, Landsat provides a large area captured per scene, multispectral resolution, repetitive and near global coverage and a retrospective archive of data.

2. STUDY AREA

The Illecillewaet Glacier in Glacier National Park, Province of British Columbia, was selected as a glacier that has a relatively good historic record (by Canadian standards) from ground observations since the beginning of the century, being accessible from the railway and later the Trans-Canada Highway, from aerial photographs in the 1950's and updated in 1978, after a major effort undertaken in the Canadian Glacier Inventory following the International Hydrologic Decade (1965-74). Located about 51°15' N, 117°30' W, it is south of circumpolar latitudes, but can be considered representative of many alpine glaciers in the province and further north. The steps used in this study will involve data integration, image processing, image classification and creation of map and tabular results. A limited time span for the project prevented a field season for ground surveys.

3. DATA SOURCES

A Landsat TM quad scene covering the area of interest recorded September 21, 1994 was acquired from the National Hydrology Research Institute. Requisite features of the scene were minimal cloud cover and a date as late in the ablation season as possible so as to best represent the end of the mass balance year. Topographic and cloud shadows in the scene are relatively minimal, but still a significant hindrance. Digital elevation data in vector format from the Province of British Columbia TRIM (Terrain Resources Inventory Mapping) program is available at 1:20,000 scale in tiles of 0.2° longitude x 0.1° latitude extent. Elevation data are represented as points, breaklines and feature outlines derived from analytic stereoplotting.

Proceedings of the Fourth Symposium on Remote Sensing of the Polar Environments, Lyngby, Denmark, 29 April – 1 May 1996
(ESA SP-391, July 1996)

Locations where the stereoplotter cannot adequately resolve the surface, such as snow areas, are manually digitized by the technician from contour line data. Four tiles were combined for the Illecillewaet sub-scene.

4. METHODOLOGY.

Data from vector and raster formats were integrated into a georeferenced database by creating a continuous raster image DEM from the planimetrically correct TRIM data to which the TM subscene was registered.

The DEM creation involved selection of compatible vector data from the TRIM file, importation into the PCI image processing package, rasterization of the vector points, and interpolation into a continuous image. Resolution of elevation values in meters was retained by creating the DEM as a 16-bit image file. Several trials were attempted using different combinations of the vector data types and interpolation algorithms. The best results were obtained by using all point elevation data, no line data, and the conic interpolation algorithm resident in PCI. The conic interpolator identifies an unknown pixel's morphological association with a slope, depression or peak and assigns its value accordingly (PCI User's Manual, 1996). DEM noise was filtered with a single pass of a 3x3 median filter. The DEM is illustrated as a perspective view in figure 1.

Geo-correction of the TM sub-scene was accomplished through identification of twenty-five ground control points on both the TM image and a shaded relief image created from the DEM overlaid with TRIM planimetric vectors depicting hydrography and roads. GCP's were identified as topographic features and stable hydrographic and cultural features. The TM image was resampled to 25m pixel spacing using a second order cubic convolution; TM band 4 is shown as figure 2. The PCI package includes a satellite orthorectification program capable of correction of relief displacement when satellite orbital data is read to the database in a specific format. However, difficulty obtaining the orbital data segment in the proper format prevented such orthorectification of this scene.

5. IMAGE PROCESSING

Image processing efforts were directed toward producing input data for an efficient, effective and reproducible supervised classification of glacier extent and facies discrimination. Principal components analysis (PCA) was employed to reduce correlation between TM bands and enhance contrast in the features of interest (Orheim and Luccitta, 1987). In an effort to minimize the scene specific nature of principal components, the analysis was applied under a mask of the glaciated area of the scene. The mask was created from a threshold of the second principal component of an unmasked PCA in which the glacier area strongly contrasts with other terrain in the scene (figure 3a).

Pixel saturation is a typical problem over glaciers and snow covered scene areas (Hall and Chang, 1988). PCA was found to reduce this by identifying most of the scene brightness variance, and thus the saturation, with the first principal component. Subsequent principal components, especially the second, third and fourth, were found to depict strong, unsaturated contrast over the glacier areas, enhancing surface features and facies (figure 3. b, c and d).

Further image processing involved ratioing and a normalized difference snow index (NDSI). The TM4/TM5 ratio is cited by Hall and Ormsby (1987) as effective for discriminating ice and snow facies in glaciological studies. NDSI (Dozier, 1989) is calculated as:

$$NDSI = (TM2-TM5)/(TM2+TM5)$$

This has shown to be an effective index for mapping snow cover in rugged terrain (Hall and Foster, 1995).

A cosine correction for radiometric normalization was found to yield no significant improvement over the glacierised portions of the scene. This may be attributable to insufficient DEM and data registration accuracy for illumination modeling, the anisotropic radiometry of old snow, and an overly simplistic illumination model. Results of the radiometric normalization were not employed in further image processing or classification.

6. IMAGE CLASSIFICATION

Challenges facing automated mapping of glacier areas include the discrimination of the ice and snow facies of the glacier, identification of debris covered ice, topographically and cloud shadowed areas and water bodies marginal to the glaciers. Glacier facies are fundamentally divided into the ice and snow facies, with the border between the two describing the transient snowline. Late in the mass balance year, the transient snowline can be regarded as approximating the glacier equilibrium line. The difference between water saturated snow and wet firn or ice at the transient snowline can be difficult to discriminate, particularly when physical and radiometric conditions vary through a scene. Debris covered ice includes supraglacial moraine, ice-cored marginal moraine and buried ice. A thin supraglacial debris cover significantly alters the spectral signature of ice, while thickly covered ice cannot be discriminated from surrounding moraine spectrally. Shadowed areas are less spectrally varied than illuminated areas, resulting in greater classification difficulty. Additionally, it is noted that cloud shadow on snow in the study scene shows a signature very similar to illuminated ice, leading to their confusion in many classification attempts. Water bodies also have a signature very similar to that of glacier ice, leading to potential misclassification of marginal lakes as ice.

Numerous trials using different band combinations as input to maximum likelihood classification were conducted, with visual assessment of their performance in the potential problem areas mentioned. Manual interpretation of enhanced imagery and field knowledge of the area were used as the benchmark for comparison.

The supervised classification was trained on eleven classes representing three glacier facies, snow, firn and ice, bedrock and moraine forefield facies and water each under both illuminated and shadowed conditions; vegetation and cloud classes were not trained.

Maximum likelihood classifications were performed on many band combinations. The following were selected as representative of preliminary results: TM 3,4,5; ratio 4/5 + NDSI; PC 1-4; PC 2-4; PC 1-4 + ratio 4/5 + NDSI, and PC 2-4 + ratio 4/5 + NDSI. Class thresholds were maintained at 3 σ with no class biases. Resulting theme maps were mode filtered and classes aggregated. The theme maps produced were compared against each other and visual interpretation of the TM image.

7. RESULTS AND DISCUSSION

Supervised classification for glacier mapping of unprocessed TM scenes, as represented by the TM 3,4,5 trial, were found to be badly hindered by cloud and topographic shadows. Areas of the scene with very low brightness values were typically identified in the "shadowed glacier" class. This results in large areas of topographically and cloud-cast shadow and water bodies to be erroneously committed to glacier classes. In some cases, areas of snow oriented on slopes facing the sun were even omitted from the snow class. These results are interpreted to be attributable to brightness variance dominating the classification procedure.

Classification using the NDSI + ratio TM4/TM5 produced a map with poor discrimination of glacier facies and misclassified shadow areas. This is likely due to the compression of the range of pixel values associated with ratios and differences.

Classification using the first four principal components produced markedly better results than with unprocessed TM bands. However, mis-identification of shadowed areas persisted and there was strong over-representation of the "debris covered ice" class. The presence of PC1 in the classification might allow overall brightness to dominate this classification, thus losing classification resolution in poorly illuminated portions of the scene.

Classification using the second, third and fourth principal components yielded results which avoided significant misclassification of shadowed areas and water bodies. However, overall glacier area was slightly under-represented, recognized by overlaying the classification result on a TM5,4,3 composite. The addition of the NDSI and ratio TM4/TM5 promoted the inclusion of the whole glacier area. Nunataks are correctly identified under all illumination conditions, as are medial and dispersed supraglacial moraines. Ice marginal water bodies are correctly discriminated.

Some classification difficulties are still apparent. Most significant is the mis-classification of snow areas under cloud and topographic shadow as firn, which affects accumulation area ratio calculation by identifying some areas of accumulation erroneously as ablation area. This is particularly significant in steep cirque and valley glaciers, where in some cases no snow area was identified. Overall accumulation and ablation areas were calculated and presented in Table 1 below.

TABLE 1.

Illecillewaet Icefield	
Accumulation Area:	13.04 km^2
Ablation Area:	8.35 km^2
Total Area:	21.39 km^2
Accumulation Area Ratio =	0.612
Illecillewaet Glacier	
Accumulation Area:	4.92 km^2
Ablation Area:	3.91 km^2
Total Area:	8.83 km^2
Accumulation Area Ratio =	0.557

8. DIRECTIONS FOR FUTURE WORK

Refinement of the classification method and rigorous accuracy assessment promise to facilitate the production of accurate maps of glacier extent and facies. Identification of the transient snowline under varying radiometric conditions is difficult, but refinement of the discrimination between firn and wet snow classes should improve this. Integration of the digital elevation model with the dataset will facilitate the derivation of important glacier inventory attributes. Location and extent of each glacier are implicite to the dataset, as are accumulation and ablation areas, from which the accumulation area ratio (AAR) is derived. Maximum, minimum and median elevations, hypsography, orientation of accumulation and ablation areas, and elevation of the transient snowline are all important factors of mass balance which can be easily extracted from the dataset (Ommanney, 1980, Østrem and Haakensen, 1980). Maintenance of the inventory within a GIS environment will allow queries to be made and reports generated for any scale of enquiry, from individual glaciers, to icefield and glacier regions. This reduces the need to compile the extensive tabular reports which characterize past glacier inventories.

9. CONCLUSIONS

The areal extent and surface classification of glaciers can be adequately measured and updated by utilising the multispectral capabilities of Landsat Thematic Mapper and augmented by digital elevation data. Principal components analysis, image ratioing and image differencing provided superior classification input over original TM bands. This procedure with further refinement may be applied to other glaciers in polar and arctic regions. Continued studies will attempt to standardize tabular data extraction and examine the integration of ground survey data and other image data sources, such as radar.

10. ACKNOWLEDGEMENTS

The study was in collaboration with Drs. Brugman and Pietroniro of the National Hydrology Research Institute and the Environment Canada cryospheric systems research initiative (CRYSYS), a Canadian contribution to the NASA Earth Observing System (EOS) program. The authors wish to acknowledge CRYSYS for providing the operating funds for this study.

11. REFERENCES

Dozier, J., 1989. Spectral signature of Alpine snow cover from the Landsat Thematic Mapper. *Remote Sensing of Environment* 28:9-22.

Hall, D.K., and Ormsby J.P., 1987. Characterization of snow and ice reflectance zones on glaciers using Landsat TM data. *Annals of Glaciology* 9:104-108.

Hall, D.K., and Chang, A.T.C., 1988. Reflectances of glaciers as calculated using Landsat-5 Thematic Mapper Data. *Remote Sensing of Environment* 25:311-321.

Hall, D.K., and Foster J.L., 1995. Determination of actual snow covered area using Landsat TM and digital elevation model data in Glacier National Park, Montana. *Polar Record* 31 (177): 191-198.

Ommanney, C.S.L., 1980. The inventory of Canadian glaciers: procedures, techniques, progress and applications. World Glacier Inventory (Proceedings of the Riederalp Workshop, September 1978): IAHS-Aish Publ. no. 126. pp. 35-44.

Orheim, O. 1987. Numerical analysis of Landsat Thematic Mapper images of Antarctica: surface temperatures and physical properties. *Annals of Glaciology* 9: pp.109-120.

Østrem, G., and Haakensen N., 1980. The Scandinavian glacier inventory - two glacier atlases. World Glacier Inventory (Proceedings of the Riederalp Workshop, September 1978): IAHS-Aish Publ. no. 126. pp. 161-171.

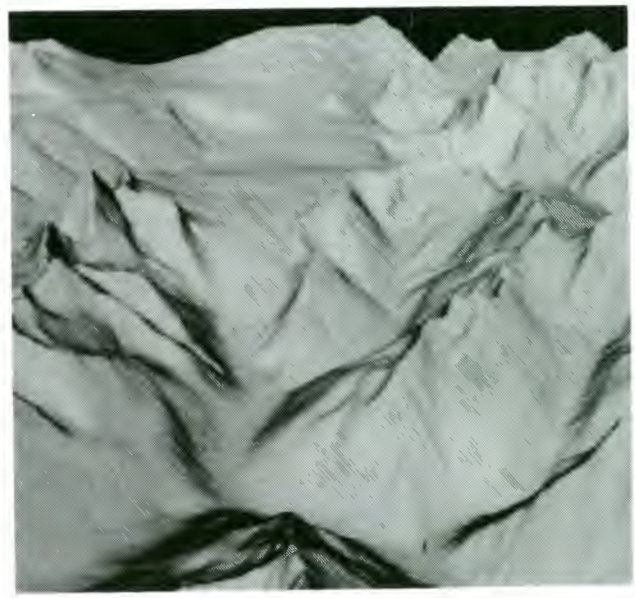

Figure 1: DEM of Illecillewaet Glacier area

Figure 2: Landsat TM band 4

Figure 3 a-d (clockwise from top left):
a. PC2 from whole sub-scene; b. PC2 from masked area for glacier; PC3 from masked area; PC4 from masked area.

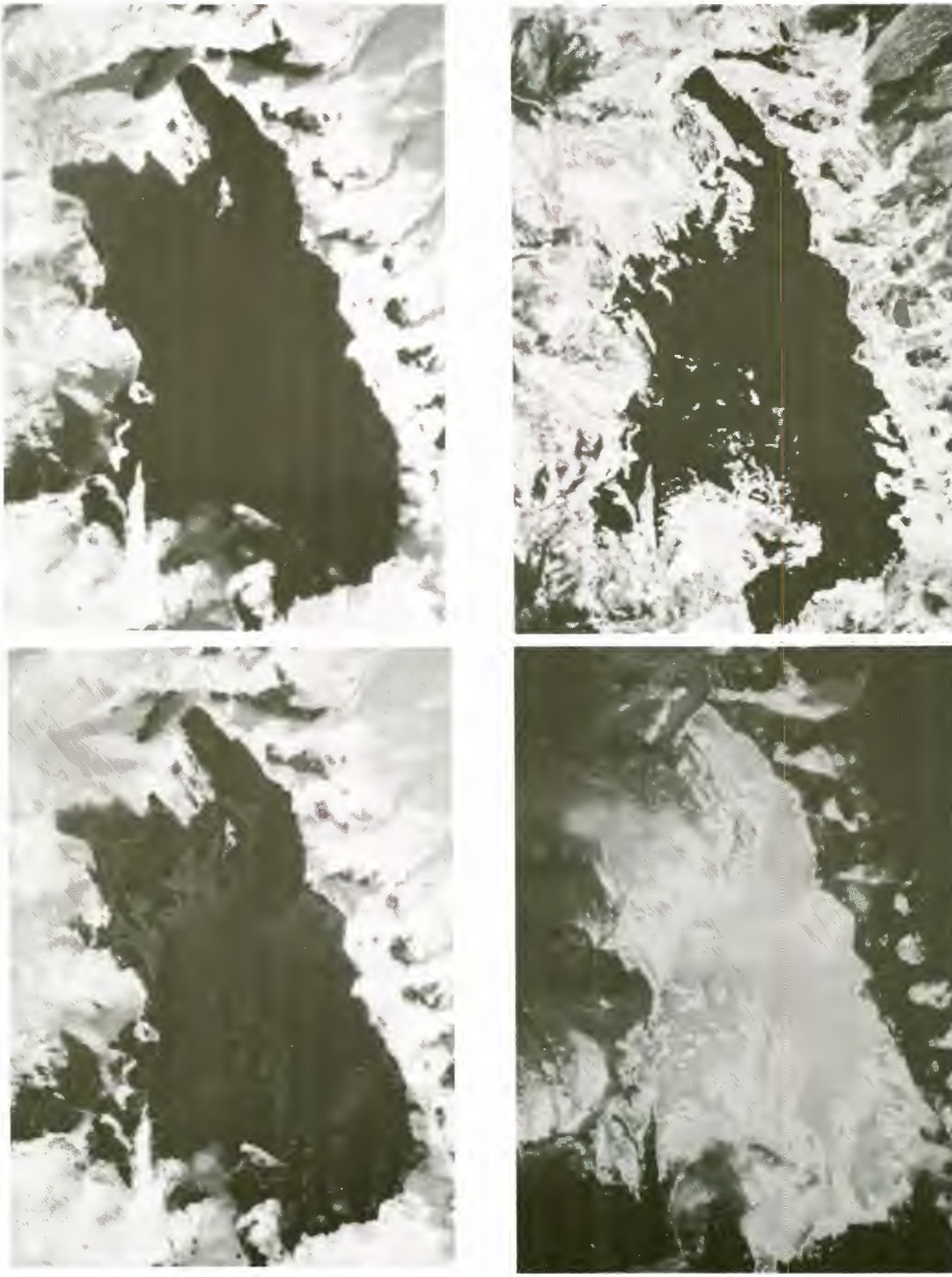

LANDSAT-TM-BASED MODELLING OF THE SNOW-MELT IN NW-SPITSBERGEN

Matthias Brun and D. Scherer

MCR Lab, Department of Geography, University of Basel, Spalenring 145, CH-4055 Basel
Ph.: +41 61 272 64 80, e-mail: brunm@ubaclu.unibas.ch

Snow-melt runoff was modelled in the high-arctic Kvikkåa drainage basin for the summers of 1990 and 1991 using the snow-melt-runoff model HB-V3-ETH. Model input data were measured during field campaigns to the Liefdefjord-region in NW-Spitsbergen (SPE ´90-92), situated at almost 80° N. An image of snow-cover-distribution in the drainage basin was derived from satellite data analysis. With the help of a 20 x 20m^2 digital elevation model (DEM) a relationship between inclination, aspect and snow-cover distribution was found. It was used to validate and improve the model results of the snow-water equivalent development. The runoff model (using a temperature index-approach) produces insufficient results in this specific high-arctic environment. To get better runoff model results the influence of radiation and the decisive influence of the terrain in this smaller drainage basin must be considered appropriately.

The above mentioned snow-cover-distribution in the drainage basin was derived with the help of an albedo calculation. The snow-albedo has great importance for the local (and global) energy-budget and for the processes of snow-melt. It can be derived through a calculation of the shortwave irradiance (by using the DEM) on one hand and the calculation of the outgoing flux from the satellite bands on the other hand. The influence of the atmosphere, the influence of surrounding terrain and shadowing effects were considered in the calculation. With the help of the albedo image a degree of snow-cover can be specified for every pixel by using a model-relationship between the snow-albedo and the snow coverage. Especially for a dissolving snow-cover with many smaller snow patches this approach is more accurate than an ordinary (threshold-) classification, which only spcifies if a pixel is snow covered or not.

TRANSFORMATION OF SPOT HRV-SCENES AND DIGITAL AERIAL PHOTOGRAPHS FROM A CENTRAL PROJECTION TO ORTHO IMAGES, FOR DETERMINATION OF GLACIER VELOCITY USING FEATURE TRACKING: EXAMPLES FROM KRONEBREEN, SVALBARD AND ENGABREEN, NORTHERN NORWAY

Cecilie Rolstad[1] & Jostein Amlien[1], and Jack Kohler[2]

[1] The Norwegian Polar Institute, Postboks 5072, Majorstua N-0301 Oslo, Norway.
[2] The Norwegian Water Resources and Energy Administration
Postboks 5091, N-0301 Oslo, Norway;
e-mail: cecilie@npolar.no

Glacier velocity is dependent on such factors as local topography, temperature and ice accumulation. Glacier velocity can be determined by measuring the movement of the glacier during the period between two recordings of a pair of satellite images or aerial photographs. This movement can be measured by means of digital image processing. Computer-based tracking of crevasses and other identifiable details in the ablation area of the glacier will yild of belocity vectors, which represents the average velocity during the period.

However, in order to get correct results, the images must be corrected for geometrical distotions caused by variations in the altitude of the terrain. An ortho-image is an image in which these distortions have been removed, and it has thus the same planimetric correctness as a map. This paper presents a computer program written to make ortho images from an original remotely sensed image and a digital elevation model.Aerial photographs map the terrain in a central projection. The distortion of a point at the ground surface varies according to the altitude of the point and its distance to the projection center. It is also dependent on the position and orientation of the camera. For a SPOT scene each scanline has its own projection center, and therefore a SPOT scene can be handled in a similar way as an aerial photograph. The inputs to the programs are a digital elevation model, and necessary photogrammetrical parameters. The tracking of corresponding details is then carried out by means of digital matching of the ortho images.

In connection with development of the hydroelectric plant near Svartisen, Northern Norway, aerial photographs of Engabreen have been recorded several times during the summer. The Norwegian Water Resources and Energy Administration wishes to monitor the glacier in order to discover changes in the glacier dynamics caused by the local changes of the environment. The velocity field for July 1991 has been determined from digital photographs with a pixel size of 1 m.

The fast moving tidewater glacier Kronebreen near Ny-Ålesund, Svalbard, has been studied for some years, with mass-balance and velocity measurements. Changes in the mass-balance are due to climate and will influence the glacier velocity. SPOT HRV images (August and September 1986) has been applied to measure the glacier movement. The pixel size for SPOT P is 10 m, and SPOT XS is 20 m.

Aerial photographs from Engabreen yild very accurate velocity measurement compared to both in-situ and photogrammetric measurement with use of autograph. The digital method is much less time-consuming compared to the manual tracking of crevasses, and therefore more vectors can be located. The glacier velocity can be determined on the basis of a large number of vectors, and the velocity field is determined almost continually spatially over the glacier surface. In addition, this method gives a digital terrain model which give information about the mass balance by describing changes of the glacier volume. For the SPOT images the accuracy is poorer, due to the large pixel size, but the results agree with measurements reported from Kronebreen glacier. Glacier velocity data extracted from digital images are qualitatively equivalent to ground surveyed velocity measurements, but are far less costly.

The method is in these days used for determination of glacier velocity on Jutulstarumen, Antarctica.

GLACIOLOGICAL STUDIES OF MELT-SENSITIVE AREAS IN DRONNING MAUD LAND, ANTARCTICA, USING LANDSAT TM AND ERS-1 SAR DATA

Jan-Gunnar Winther and Øyvind Dalen

Norwegian polar Institute, Middelthunsgate 29, P.O. Box 5072 , Majorstua N-0301 Oslo, Norway.
Ph.: +47 22 95 95 00, fax: +47 22 95 95 01, e-mail: winther@npolar.no

The University of Trondheim
The Norwegian Institute of Technology, Department of Surveying and Mapping,
N-7034 Trondheim, Norway

Large scale melting phenomena like melt water drainage channels and melt water accumulation basins of frozen lakes have been surveyed on the land ice mass in Jutulgryta in Dronning Maud Land, Antarctica, during the Norwegian Antarctic Research Expedition in 1993/94. The Jutulgryta area is located tens of kilometres away from the closest nunatak and about 130 kilometres from the ice shelf barrier in a north-sloping area that is favourably exposed to incoming solar radiation. In addition, katabatic winds provide very low winter snow accumulation. The melt features are probably quite sensitive to variations in local and regional air temperatures and energy balance and can be used as indicators of a changing climate (Bøggild et al. 1995; Bøggild and Winther 1995). Here, these melting features have been further investigated using three Landsat TM images from 1985, 1986 and 1990, respectively, and one ERS-1 SAR scene from winter 1992 and one from summer 1993. Image analysis of the optical Landsat TM data clearly show that the melting phenomena can be enhanced. Further, supervised classification of the Landsat TM data indicates that the melt areas increased from about 4 km^2 in 1985 to about 10 km^2 in 1986 while the change from 1986 to 1990 was modest. The ERS-1 SAR data did not reproduce the melting phenomena very well and was only useful when combined with the optical data. However, the SAR data distinguished blue ice fields from surrounding snow covered areas quite well due to diffferences in surface roughness. Finally, the SAR data was found to be better than the Landsat data for detecting crevassed areas. This is probably because the radar signal penetrates some of the snow bridges that covers many of the crevasses in this area.

SAR INTERFEROMETRY FOR ANTARCTIC ICE SHEET AND SEA ICE

Hiroshi Kimura, Masao Furukawa and Takashi Mitomi

Fumihlko Nishio
Hokkaido University of Education
1-15-55, Shiroyama, Kushiro-City, Japan 085.
Ph: +81 154 41 6161, fax: +81 154 43 0855, e-mail: fnishio@atson.kus.hokkyodal.ac.jp

In order to interpret changes in the Antarctic ice sheet as indication of global climate change it is necessary to observe the local changes in a regional context. This requires a comprehensive monitoring effort which addresses both the inland ice and changes in the ice margin. We describe our program for regional investigation of the Antarctic ice sheet using synthetic aperture radar (SAR), and discuss the utility of SAR data including the interferometry SAR technique for detection of changes in the ice sheet margin. ERS-1 & JERS-1 SAR allow us to map the boundaries of snow facies on the ice sheet and investigate recent changes in the ice margin. We demonstrate the utility of SAR for detecting recent changes in the ice margin. SAR images clearly show the ice edge, moraines, and ice marginal lakes. These features can be compared with published maps and earlier images in order to document changes in the margin of the ice sheet. We show evidence of recession of floating ice of the Shirase glacier in the East Antarctic ice sheet. The recession, which occurred between 1960 and 1993, is approximately 80 km. ERS-1 & JERS-1 SAR provide the opportunity to pursue a comprehensive investigation of the state of outlet glacier of the Antarctic ice sheet. The ability to address conditions on the ice sheet and to look at the margin changes in a systematic way will allow us to develop a stronger framework for interpreting changes in the ice sheet in terms of climate variation.

Glacier movements by SAR

The movements of the Shirase and Kaya glaciers in the Lutow-Holm Bay in East Antarctica were analyzed using ERS-1 & JERS-1 SAR imagery as well as Landsat and MOS-1 MESSR imagery. First, the velocities of both glaciers were derived from multi-temporal satellite data analysis. As for the Shirese glacier, the velocity was obtained by Landsat images of two different period and calculated to 2.9 km/yr for 1988-89 and 2.6 km/yr for while most velocities of the Kaya glacier were found to be 0.6 km/yr in the period 1973-1991. This velocity difference of the two glaciers was related to the sea ice extent associated with the bathymetry in the Lutow-Holm Bay. Second, MOS-1 MESSR imagery from 1990 was compared with ERS-1 SAR imagery from 1991 for the Kaya glaicer. Edges and crevasses of the floating ice tongue were distinguished much more clearly in the SAR image than in the MESSR image. However, the difference of open water and thin sea ice appeared much more clearly in the MESSR imagery than in the SAR imagery. These results show the advantages of using SAR imagery and the importance of combining with visible/near-IR imagery for the study of glacier flow and snow surface signature on the glacier and ice sheet as well as sea ice.

SAR interferometry

Satellite-borne imaging SAR presents the opportunity for measuring surface displacement fields interferometrically by use of the coherence of the radar beam. Application to the glacial and sea ice, the fringe pattern contains the combined effects of ice flow and tidal action in the period ietween repeate satellite observations made at the Syowa Station. We discuss some results of Interferometry for sea ice and the Kaya Glacier movement flowing down from the ice sheet. The interferogram reflects one or more components in surface deformation. The example of the Kaya Glacier in December. 1991 displays a dense, colorful fringe pattern indicating deformation. Discontinuities in the pattern may reflect cracks that separate the fast sea ice into discrete segments, which were applied by either compression or tilting between two passes. These interferogram for sea ice and glaciers are potentially useful for many studies in polar regions. Additional work is important to verify the nature of discontinuities and reduce the uncertainties in the interpretation.

GEOSTATISTICAL APPROACHES TO INTERPOLATION AND CLASSIFICATION OF REMOTE-SENSING DATA FROM ICE SURFACES

Ute Christina Herzfeld[1,2], Helmut Mayer[2], Chris A. Higginson[2], Michael Matassa[2]

[1] Geomathematik, Fachbereich Geowissenschaften, Universität Trier
D-54286 Trier, Germany
Ph: +49 651 201 4611, fax: +49 651 201 3815, e-mail: uch@denali.uni-trier.de

[2] Institute of Arctic and Alpine Research, University of Colorado Boulder
Boulder, Colorado 80309-0450, U.S.A.
Ph: +1 303 492 6198, fax: +1 303 492 6388, e-mail: herzfeld@tryfan.colorado.edu

ABSTRACT

Geostatistical methods for interpolation and extrapolation are fairly well known, and their usefulness for glaciological data analysis has been demonstrated a number of times. Application of ordinary kriging to satellite radar altimeter data from Antarctic ice streams yields maps of 3-km resolution that are useful for glaciodynamic investigations.

While interpolation utilizes the primary information in the data, a newly developed geostatistical surface classification method is geared at deriving secondary information from elevation data or beckscatter data. Based on statistical properties, elements of surface structures are used for automated mapping.

A combination of high-resolution and low-resolution techniques is attempted in a study of the 1993-1995 surge of Bering Glacier, Chugach Mountains, Alaska. GPS-located video data collected from small aircraft are used in combination with ERS-1 Synthetic Aperture Radar (SAR) images to (a) help understand the relationships between ice velocity, surface stress patterns, crevassing, and iceberg calving during the surge, and (b) provide a technique for surface classification based on SAR data in general. A critical issue in satellite data analysis is the availability of ground truthing, for instance, to distinguish between high-resolution geophysical variability and noise, and to determine small-scale sources of variation in backscattering. From the perspective of SAR data analysis, the Bering Glacier surge has presented a unique opportunity to sample and characterize the surface of fast-flowing ice and rapid changes in surface roughness. Geostatistical surface classification could be used in situations where interferometry was not applicable because the ice movement led to lack of correlation.

GEOSTATISTICAL INTERPOLATION FOR ELEVATION MAPPING

Geostatistical methods for interpolation and extrapolation of irregularly spaced data are kriging methods. 'Kriging' comprises a family of such methods based on the least-squares optimization principle and usually introduced in a probabilistic framework (Matheron 1963; Journel and Huijbregts 1989). However, it can be viewed as a numerical interpolation technique only (Herzfeld 1992a). Kriging consists of two steps: 1. analysis of spatial structures (variography), and 2. estimation, interpolation and extrapolation (kriging).

In mapping Antarctica from satellite radar altimeter data, a need for interpolation of the widely spaced data onto a regular grid arises. Data from exact repeat cycles feature ground tracks with rhombic gaps of 40 km diameter (for GEOSAT ERM and SEASAT data). It is impossible to get a two-dimensional impression of the ice surface from the uninterpolated data.

In the first step, a variogram is calculated according to

$$\gamma(h) = \frac{1}{2n}\sum_{i=1}^{n}\left[z(x_i) - z(x_i + h)\right]^2 \qquad (1)$$

where $z(x_i)$, $z(x_i + h)$ are measurements at locations x_i, $x_i + h$, respectively, inside a region D, and n is the number of pairs separated by the vector h. The residual variogram is

$$res(h) = \gamma(h) - \frac{1}{2}m(h)^2 \qquad (2)$$

where

Proceedings of the Fourth Symposium on Remote Sensing of the Polar Environments, Lyngby, Denmark, 29 April – 1 May 1996
(ESA SP-391, July 1996)

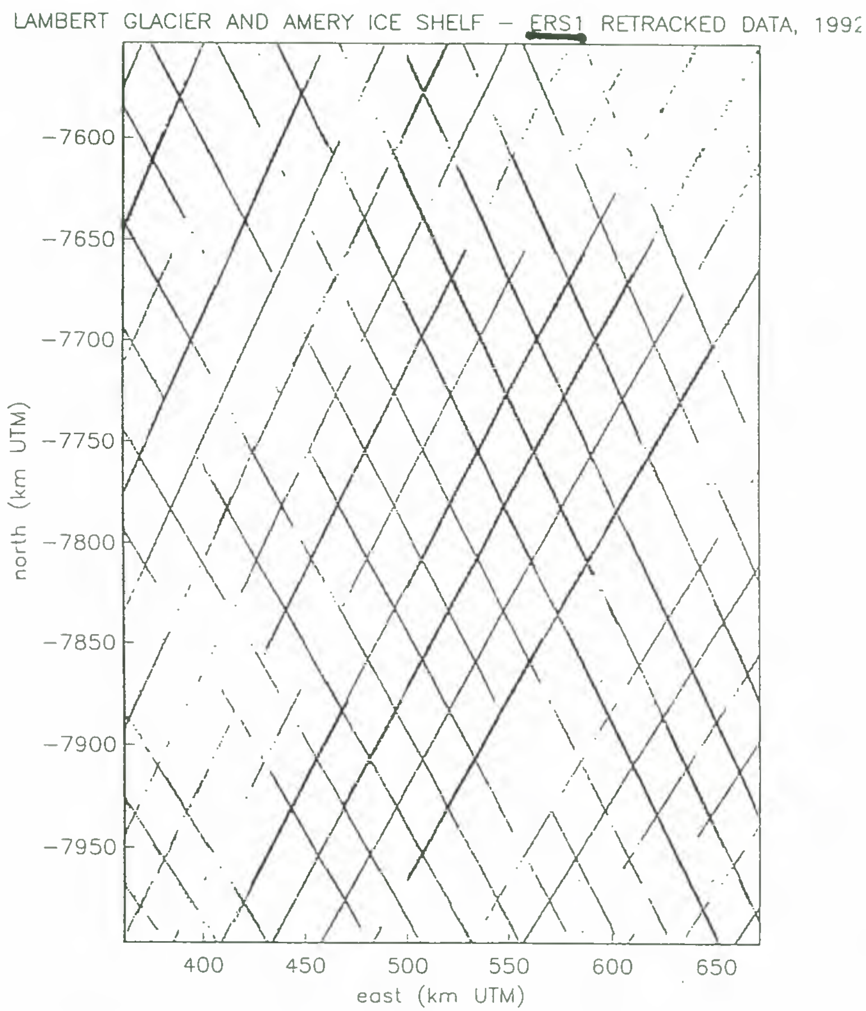

Figure 1 Ground Tracks 920710–921009, 940713

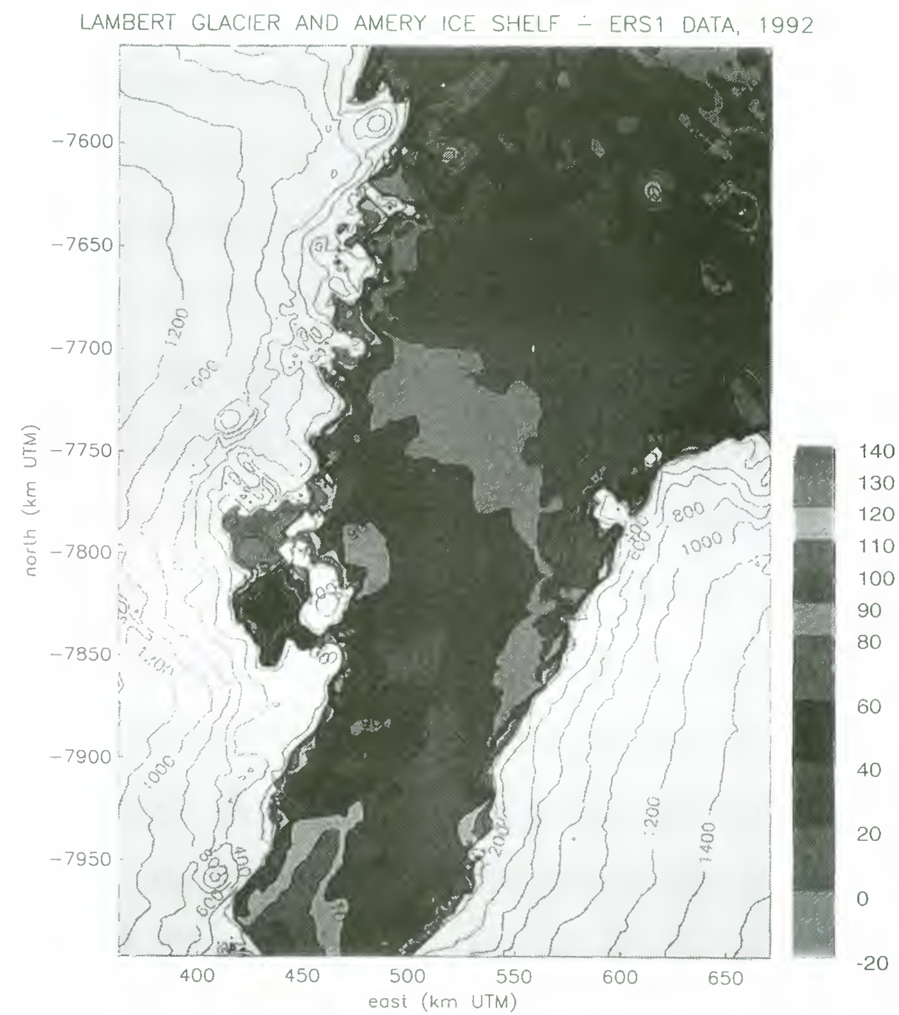

Figure 2 Contour map of lower Lambert Glacier and Amery Ice Shelf made from a digital terrain model with 3km grid node spacing

$$m(h)=\frac{1}{n}\sum_{i=1}^{n}\left[z(x_i)-z(x_i+h)\right] \qquad (3)$$

is the drift component. The experimental variograms are calculated in bins from the measurements, in our case from the radar altimeter (RA) data, then are fitted by analytical variogram models. A variogram model describes the type of transition from the strong covariation between closely neighboring samples to the weaker covariation typical of samples further apart. The variogram model is characterized by its function type (which has to meet certain mathematical requirements, so the inversion in kriging is unique).

ERS-1 altimeter data of Lambert Glacier/Amery Ice Shelf are best fitted using a Gaussian variogram model defined by

$$\gamma(h)=C_0+C_1\left(1-exp\left(-\frac{h^2}{\alpha^2}\right)\right) \qquad (4)$$

with C_0 = 250 m^2
C_1 = 343 m^2
α' = 18000 m.

This has a practical quasi-range of $\alpha'=\sqrt{3\alpha}$. The Gaussian variogram function is smooth in its origin (for $h \rightarrow 0$); this indicates that the ice surface is very smooth. The large nugget effect corresponds to the noisiness of the RA data.

The kriging method called "ordinary kriging" (universal kriging of order 0) is better suited for interpolation of RA data than universal kriging of a higher order, because the drift parts modelled by a polynomial component in the higher order universal kriging methods is likely to create artefacts in the gaps.

In ordinary kriging, the value $z_0 = z(x_0)$ at a node x_0 is estimated by

$$Z_0^*=\sum_{i=1}^{n}\alpha_i Z_i \qquad with \qquad \alpha_i \in IR \qquad (6)$$

with data $z_i = z(x_i)$ at locations x_i (i = 1,...,n) in a neighborhood of the grid node x_0; the coefficients are determined such that the estimation error has minimum variance and the estimation is unbiased, which requires a condition

$$\sum_{i=1}^{n}\alpha_i=1 \qquad (7).$$

A solution of the kriging system is obtained using the variogram model specified earlier. (For a derivation of the kriging system, see Herzfeld 1992a,b.) This is carried out for every grid node in the map area. The 3-km grid size is chosen so that the resultant maps (grids) can be used in glaciodynamic investigations. The horizontal resolution of a DTM should be sufficiently high for numerical models that take into account longitudinal stress gradients and be coarse enough so the so-called "T" term in the longitudinal stress equilibrium equation (Kamb and Echelmeyer 1986) can be omitted (3 km is about 3 times the ice thickness at grounding line). The resultant map of Lambert Glacier / Amery Ice Shelf from 1992 ERS-1 data is given in Figure 2. The glacier surface is well mapped, but notice that the ice front appears irregular. The latter is due to the data collection, however, not to kriging.

GEOSTATISTICAL SURFACE CLASSIFICATION FOR THEMATIC MAPPING

A surface classification methodology is developed which finds application in the analysis of crevasse patterns and stress regimes during the 1993-1995 surge of Bering Glacier, Alaska (Lingle et al. 1993).

Kriging utilizes the primary information in the data, in the case of Lambert Glacier elevation mapping the altimeter-derived elevation data. Our geostatistical classification method employs secondary information contained in the elevation data (for RA) or backscatter data (for SAR).
The spatial variability captured in the structure function (the residual variogram) is parameterized. Parameters are combined to feature vectors, and feature vectors are joined in classes characteristic of given surface features. Examples of ice surface classes are (1) areas without crevasses, (2) areas with crevasses reminiscent of one strain state or (3) of two interfering strain states, (4) chaotic areas (the maze - too many overprinting strain states to be discernible from crevasse patterns), (5) extensional features, (6) compressional features.

Discrimination of crevasse patterns as mentioned in the examples requires high-resolution data. The combination of high- and low-resolution techniques is an objective of the Bering Glacier study. Since June 1993 the Bering Glacier / Bagley Ice Field system, the largest glacier in North America (Molnia and Post 1995) and located in the Chugach Mountains, Alaska, has been surging. (Our most recent observations are from August 1995.)
In field studies in 1993-1995, we undertook the following experiment: Flying in a small aircraft approximately at constant elevation above the ice surface along a flowline of the glacier, video data were

Figure 3: Bering Glacier surface 1994. Video Frame
Two-directional blocky crevasses.

Figure 4: Geostatistical ice surface classification with parameter 2
(significance of crevasse steps/relative size.

collected port and starboard at a constant looking angle and coregistered with GPS data. A sequence of transformation steps (hardware and software) is necessary to extract video scenes from the tapes and facilitates their analysis in the classification system. Results from the surface classification are related to ice velocity, surface stress patterns, crevassing and iceberg calving during the surge. The relationships investigated bear on a number of open glaciological questions.

A second field of application is the analysis of SAR data. The geostatistical surface classification provides a new approach to the utilization of SAR data.
From the perspective of SAR data analysis, the Bering Glacier surge has provided a unique opportunity to observe and collect field data of fast flowing ice and of surface structures and crevasse patterns changing rapidly under changing strain states. A few velocity measurements on the ice were also obtained (Herzfeld et al. 1994). The advantage of geostatistical classification over interferometry is that it is more generally applicable. Interferograms can only be obtained if the images are sufficiently correlated, and it was found that surge activity yields decorrelation already over a short time.

ACKNOWLEDGEMENTS

Funded in part through NASA Office of Polar Programs (NAGW-3790 to UCH) and Deutsche Forschungsgemeinschaft (Heisenberg Fellowship to UCH).

REFERENCES

Herzfeld, U.C. 1992a, Least squares collocation, geophysical inverse theory, and geostatistics: a bird's eye view, *Geophys. J. Internat.*, 111 (2), 237-249

Herzfeld, U.C. 1992b, Quantitative spatial models of Atlantic primary productivity: an application of geomathematics, *J. Geophys. Res.*, 97 (C1), 717-732

Herzfeld, U.C., J.J. Roush, K. Lohuis & B.F. Molnia 1994, Surge crevasse patterns, ice surface roughness and ice velocity - an attempt at quantitative analysis of 1993 and 1994 observations on Bering Glacier, Alaska. *Eos Trans. Amer. Geophys. Union,* 75 (44 suppl.), 63

Journel, A. G., & C. Huijbregts 1989, Mining geostatistics, 2nd Ed., Academic Press, London, 600 p.

Lingle, C.S., A. Post, U.C. Herzfeld, B.F. Molnia, R.M. Krimmel & J.J. Roush 1993, Bering Glacier Surge and Iceberg-Calving Mechanism at Vitus Lake, Alaska, U.S.A., *J. Glaciol.*, 39 (133), 722-727

Matheron, G. 1963, Principles of Geostatistics, *Econ. Geol.*, 58 (8), 1246-1266

Molnia, B.F. & A. Post 1995, Holocene history of Bering Glacier, Alaska: A prelude to the 1993-1994 surge, *Phys. Geography*, 16 (2), 87-117

SIMULTANEOUS OBSERVATIONS OF GLACIER NEAR-SURFACE PROPERTIES BY SATELLITE AND GROUND RADAR INTRUMENTS

Rune Engeset

Department of Physical Geography, P.O. Box 1042 Blindern, N-0316 Oslo, Norway.
E-mail: rune.engeset@geografi.uio.no, Fax: +47 22 85 72 30

ABSTRACT

Information on the near-surface structure of glaciers is obtained by satellite SAR and GPR instruments. Previous work has shown that SAR has the potential of mapping glacier zones, such as the accumulation and ablation areas. In this study, winter SAR images acquired after years with very negative and very positive mass balance were investigated. The aim was to see if the redistribution of the glacier zones from one year to another was possible to detect using SAR. The near-surface structure was mapped by GPR measurements in parallel with the last SAR acquisition. In the SAR image from the year with a very negative mass balance, zones corresponding to the firn area, slush and superimposed ice, and the glacier ice surface could be identified. Identical zones were found at the same positions in the SAR image from the year with a very positive mass balance. Hence, the change in mass balance from one year to another could not be detected on this glacier using SAR backscatter data only.

1. INTRODUCTION

The Arctic glaciers are sensitive to climate changes, hence temporal variation in glacier properties can be used as indicators of climate change. However, measurements on the state of these ice masses are sparse as they are situated in very remote areas with extreme weather and light conditions. Promising results have been demonstrated by satellite remote sensing techniques. As the Arctic receives no sunlight during mid-winter and clouds frequently corrupts data collection by optical sensors, active microwave instruments represent promising tools for data collection.

Information on glacier properties can be derived from satellite radar data (e.g. Jezek et al. 1993, Rees et al. 1995). Previous work on ERS-1 synthetic aperture radar (SAR) data by Engeset and Weydahl (1995) indicates that the equilibrium line can be identified in winter SAR images. Unambiguous derivation of this information enables monitoring of the regional distribution of glacier mass balance in the Svalbard archipelago. This would provide new, important information on the response of the Arctic ice masses to climate change. This paper investigates the possibility of locating the equilibrium line using data from two subsequent years of very negative and very positive mass balance. This is to find out if the observed zonation in winter SAR images represents the inter-annual changes in glacier mass balance. Ground penetrating radar (GPR) profiles were acquired two days ahead of the last SAR acquisition and was used for the analysis on the glacier Slakbreen on Spitsbergen, Svalbard.

2. STUDY AREA

The study was conducted on the glacier Slakbreen (Fig. 1) located 78°N and 16°30"E in the Svalbard archipelago. Fig. 1 shows the location of the study area and the glacier geometry.

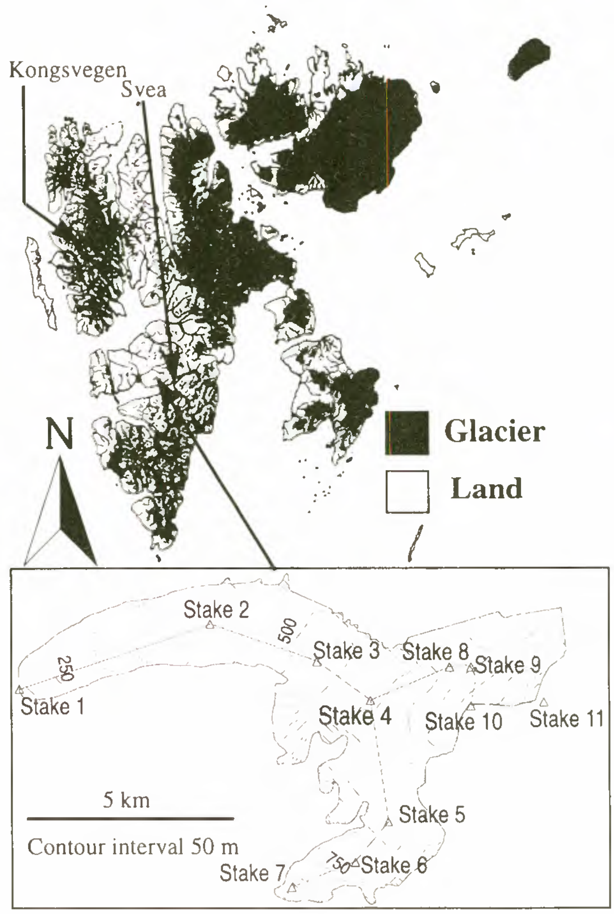

Figure 1. Key map of the Svalbard archipelago and Slakbreen with location of stakes and GPR profiles.

3. MATERIALS

3.1 GPR data

Field GPR data was collected by a Geophysical Survey Systems Inc. (GSSI) SIR-2 georadar on April 10, 1995. A pair of closely spaced antennae, operating at a centre-frequency of 500 MHz were used. The radar control unit was mounted on a snow-mobile, which pulled a sledge with the antennae at a velocity of approx. 6.9 ms^{-1}. Vertical scans were triggered at a rate of 32 Hz, which amounts to one scan every 0.22 m. The time-range of a vertical scan was 80 ns and each scan was made up by 512 byte samples. A total profile-length of 15 km was sampled.

Proceedings of the Fourth Symposium on Remote Sensing of the Polar Environments, Lyngby, Denmark, 29 April – 1 May 1996
(ESA SP-391, July 1996)

The GPR profiles were geopositioned by measuring the position of stakes, which identified breakpoints along the profiles. Intra-profile positioning was achieved by the use of an electronic marker and a wheel, registering a tick every 100 m.

3.2 Satellite data

The SAR on board the ERS-1 satellite operates at a frequency of 5.3 GHz and emits and receives vertically polarized radiation. The incident angle in the centre of the swath is 23 degrees. ERS-1 SAR data were delivered by Tromsø Satellite Station as 3-look square-root-intensity FRI imagery. The SAR data were acquired on November 28, 1993, and on April 12, 1995, both in descending satellite paths.

An ERS-1 SAR PRI image from January 19, 1994, was also available. This image has been investigated in an earlier study by Engeset and Weydahl (1995) and provided cross-reference to the glacier Kongsvegen (Fig. 1). An optical image acquired by Landsat Thematic Mapper (TM) on August 15, 1993, was also used in the study.

3.3 Glaciological data

No high-quality mass balance data were available for Slakbreen, so mass balance data from the glacier Kongsvegen was used. Data available for estimating the mass balance of Slakbreen was from Hagen et al. (1993), aerial photographs from 1990, TM imagery from autumn 1993, and SAR image from January 1994.

In the field, snow depth and structure observations at stakes were carried out (for position of stakes, see Fig. 1). The purpose of these observations was to support interpretation of GPR data.

4. GLACIER ZONES AND MASS BALANCE

Glacier near-surface structure is mainly governed by the accumulation of snow, summer air temperature and precipitation. Most Svalbard glaciers are polythermal with a cold surface layer of below 0 °C temperature in the ablation area, and temperatures at the pressure melting point in the accumulation zone. Typical near-surface stratigraphy is illustrated in Fig. 2.

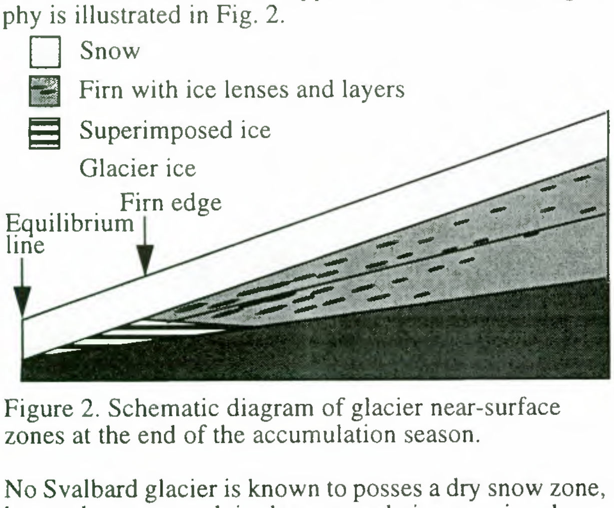

Figure 2. Schematic diagram of glacier near-surface zones at the end of the accumulation season.

No Svalbard glacier is known to posses a dry snow zone, hence the snow pack in the accumulation area is subjected to melting and refreezing of percolating melt water. This process causes ice lenses and layers within the snow pack, as well as a layer of refrozen ice superimposed on the cold glacier ice surface. At the end of the ablation season the equilibrium line will usually not correspond to the surface snow-ice border, but rather the border between superimposed ice and snow. In the event of a very negative mass balance year preceding a very positive year the near-surface stratigraphy will provide a record of the situation from both years. Hence, the near-surface zonation not only depends on the previous year, but a series of preceding years.

Mass balance data acquired by the Norwegian Polar Institute show a drop of 160 m (from 570 m a.s.l. to 410 m a.s.l.) in the equilibrium line altitude (ELA) for Kongsvegen from the 1992/93 to the 1993/94 balance year. Hagen et al. (1993) estimates an ELA of 470 m a.s.l. for Kongsvegen and 530 m a.s.l. for Slakbreen, hence the annual ELA of the two glaciers is believed to be not very different, and the changes in annual ELA of the glaciers are believed to correlate well. The correspondence in ELA of the two glaciers is supported by aerial photographs from 1990. If a constant difference of 60 m is assumed in ELA between Slakbreen and Kongsvegen, the ELA of the two glaciers would have varied according to Fig. 3, i.e. the ELA of Slakbreen would have decreased from 630 m a.s.l. in 1992/93 to 470 m a.s.l. in 1993/94.

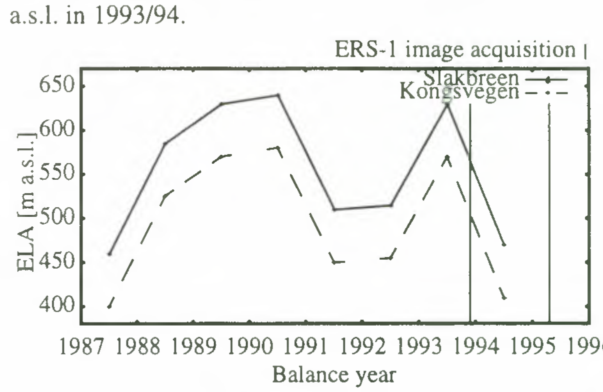

Figure 3. Estimated equilibrium line altitude (ELA) of Kongsvegen and Slakbreen.

The Landsat TM image was investigated visually, using different band colour combinations and contrast stretch functions. Three distinct surface classes could be identified, and were interpreted as a firn zone (above 690 m a.s.l.), a water-saturated slush and superimposed ice zone (570 to 690 m a.s.l.), and a zone with exposed glacier ice (below 570 m a.s.l.). The image was acquired on August 15, and meteorological data from Svea (located at sea-level 5 km South-East of Slakbreen, see Fig. 1) indicate that melting continued until second week of September, i.e. a period of tree weeks. Hence, the observed zones probably moved up-glacier during this period.

5. RADAR OBSERVATION OF SNOW AND ICE

Scattering of radio waves is caused by inhomogeneity in the host medium, which in this case is a mixture of air and ice. In this work inclusion of liquid water is ignored, as meteorological data from Svea indicates dry conditions in the relevant near-surface layer of the glacier. The radar return is determined by the geometrical and electrical properties of the scattering medium. The electromagnetic (EM) properties of snow and ice can be described by its complex dielectric constant $\varepsilon = \varepsilon' + i\,\varepsilon''$. Surface scattering takes place at large changes in the real part of the complex dielectric constant, which for pure ice is constant $\varepsilon' = 3.17$ throughout the microwave spectrum. In the near-surface layer, changes in ε' are related to changes in density. Variation in ε' causes reflection of the radiation from both GPR (60 cm wavelength) and SAR (5.6 cm wavelength). The reflections may be affected by destructive or constructive interference, depending on the thickness of the ice layer relative to the radar wavelength in the ice layer. Hence, some horizontal ice layers may not be detected by GPR.

In snow and ice, very little energy is absorbed, as the imaginary part of complex dielectric constant is small, in the order of 10^{-3}. Hence, considerable penetration depths are possible, and a substantial depth contributes to volume scattering. The SAR wavelength of 5.6 cm is not very different from typical firn grain sizes and structure irregularities. Hence, volume scattering is dominant in the accumulation area. Volume scattering depends mainly on the depth of the contributing layer and size of the scattering elements, i.e. the grain sizes. Rott el al. (1993) estimates the extinction coefficient at 5.2 GHz $K_e = 0.046\ m^{-1}$. This was an average value for the top 3 m of antarctic firn, and implies a penetration depth $d_p = 1 / K_e = 21$ m. The penetration depth in firn at Svalbard glaciers is believed to be much less, due to the availability of liquid water and a much faster metamorphism produce larger grains and more ice layers.

As dry snow absorbs very little energy, the winter snow layer does not significantly modify the SAR signal. In the parts of the glacier where glacier ice is exposed at the end of the ablation season, the backscatter is mainly caused by scattering at the snow-ice interface. If this interface is smooth relative to the SAR wavelength, specular scattering takes place at the interface and little energy is returned in the SAR direction. A rough interface acts as a diffuse scatterer and causes higher backscatter towards the SAR. A surface is considered rough on the scale of the ERS-1 SAR wavelength if the surface height variation is greater than one cm.

In the parts of the glacier where net annual mass gain takes place, the surface layer is dominated by large firn grains, and ice layers and lenses. In this type of heterogeneous medium, volume scattering is dominant. Density changes associated with thin ice layers and lenses also cause reflections and scattering in this part. The stratification and depth of this firn layers depend on the surface topography. Even on glaciers with a relatively even surface, such as Slakbreen, this variation is observed. The variation in surface topography induces complicated mass accumulation (snow and superimposed ice) and ablation patterns. This is in particular pronounced in the zone, in which the equilibrium line fluctuates from one year to another.

6. DATA CALIBRATION AND CO-REGISTRATION

6.1 GPR data

The GPR transmits EM pulses, and records received pulse amplitude as a function of time. The recording time for each pulse (scan) was set to $t_r = 8.0 \times 10^{-8}$ s. The glacier is covered by a layer of snow and firn, and the dielectric properties of this layer varies. A first order approximation to the EM propagation velocity in this kind of medium is given by the complex refractive index model (CRIM) given in Eq. 1 (Birchak et al. 1974), which includes the velocity of light in vacuum $c_0 = 2.988 \times 10^8\ ms^{-1}$, the relative permittivity of snow and ice ε_i, and the volume fraction of ice $f_i = \rho / \rho_i$, where ρ is the density and $\rho_i = 0.917$ is the density of ice.

$$c_i = \frac{c_0}{\left(1 - f_i\right) + f_i\sqrt{\varepsilon_i'}} \qquad \text{(Eq. 1)}$$

ρ typically varies between 0.050 - 0.400 Mg m^{-3} for snow, and between 0.400 - 0.830 Mg m^{-3} for firn (Paterson 1995). Given the scanning time t_r and a sampling number s = 512 samples per scan, the vertical difference d between adjacent samples is given in Eq. 2.

$$d = \frac{c_i \cdot t_r}{2 \cdot s} \qquad \text{(Eq. 2)}$$

In snow the GPR profile depth would typically be in the order of 10 m.

Graphs showing amplitude as a function of time were extracted at stake positions in the profiles. This enables calibration of GPR data by the use of the snow observations. Average snow density at stakes may be calculated from snow depth measurements and measured two-way travel time from GPR data.

The depth of the snow layer was extracted from the GPR data along the entire profile (Fig. 4), using Eq. 2 and assuming an average snow density of 0.3 Mg m^{-3}.

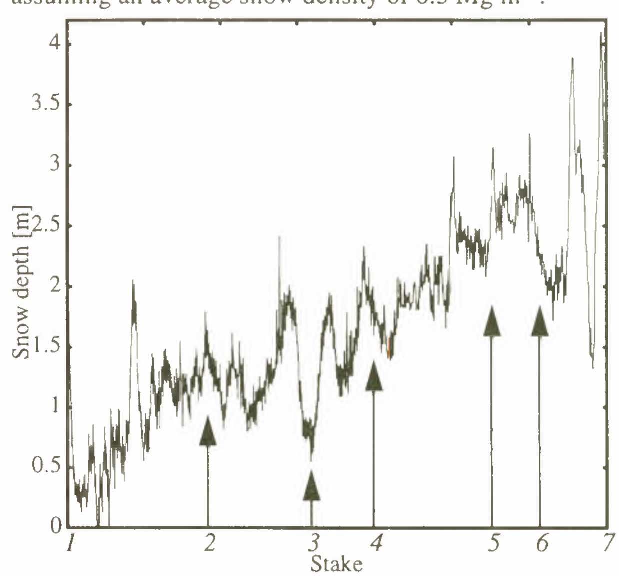

Figure 4. Depth of the snow layer along GPR profile from stake 1 to 7.

Information on the snow and firn stratigraphy was present in the GPR profiles. The GPR profiles were investigated visually, to identify the different zones on the glacier.

6.2 SAR data

S-1 SAR images were calibrated according to s to give the backscatter coefficient (Laur et al. [n Eq. 3, the pixel value squared P^2 was used of local average intensity <I>, as square-root-y values are represented in these images.

$$\sigma^0 = \frac{10 \cdot \log P^2}{K} = \frac{20}{K} \cdot \log P \qquad \text{(Eq. 3)}$$

The calibration constant K is 54.2 dB for FRI images processed at TSS after summer 93 (Weydahl 1994). Corrections for variation in incident angle, range-spread-loss, and antenna pattern over the swath was not taken into account, as this work focused on the relative changes in the backscatter coefficient over the glacier. The two SAR images are shown in Fig. 5 and Fig. 6.

Figure 5. ERS-1 SAR image from November 30, 1993. SAR raw data is courtesy ESA/TSS. Stake positions are superimposed.

A dry snow layer hardly affects the SAR signal, and the meteorological observations at Svea indicate that the liquid water in the near-surface snow and firn is frozen. Hence, the SAR image from 1993 is believed to be influenced by the near-surface structure at the end of the ablation season 1993, and the 1995 image is affected by the structure at the end of the ablation season 1994.

Figure 6. ERS-1 SAR image from April 12, 1995. SAR raw data is courtesy ESA/TSS.

Profiles were identified in the SAR images, in order to analyse the variation in the backscatter coefficient on the glacier, and compare satellite SAR and GPR data. The selected profiles were from stake 1 to 7, that is a profile from the front to the top of the glacier (see Fig. 1). The backscatter profile from the SAR acquisition on November 28, 1993 is shown in Fig. 7, and from April 12, 1995 in Fig. 8.

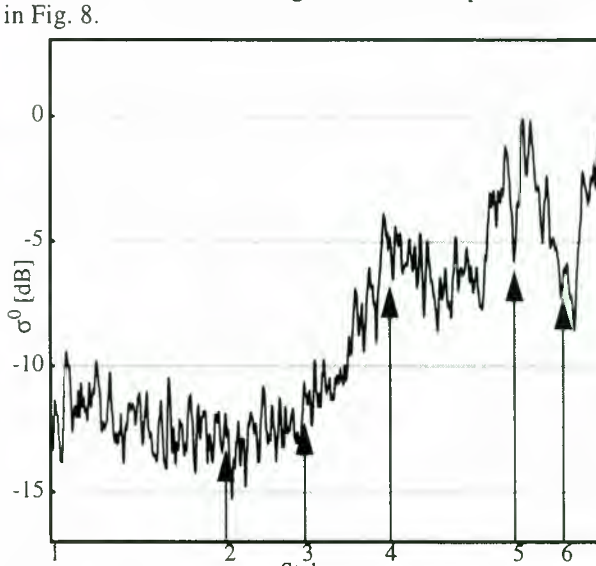

Figure 7. Calibrated ERS-1 SAR backscatter coefficient from the acquisition on November 28, 1993. The image was first convoluted with a 3 x 3 mean filter.

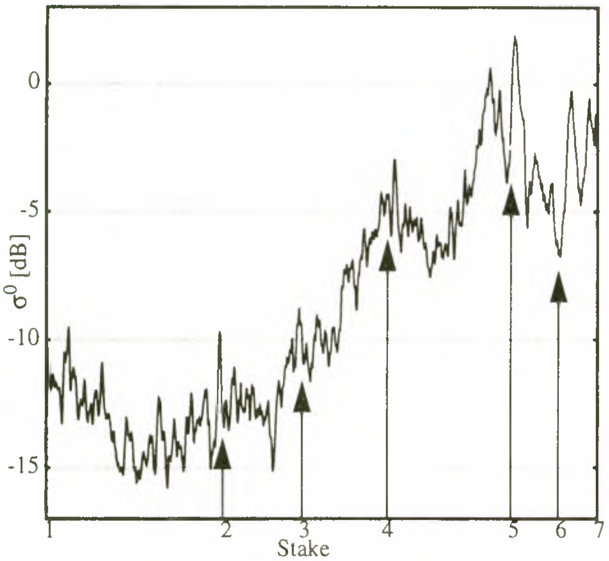

Figure 8. Calibrated ERS-1 SAR backscatter coefficient from the acquisition on April 12, 1995. The image was first convoluted with a 3 x 3 mean filter.

6.3 Data co-registration

The field, cartographic, GPR, and SAR data were found in different reference systems. The principal use of the data sets in this work was to combine satellite SAR and GPR data. The GPR data was geopositioned by GPS measurements. However, no algorithm for SAR geocorrection was available in this project. Hence, relevant data sets were co-registered with the SAR images visually. Aerial infrared photographs were used for support. This approach implied that no pixel by pixel analysis was possible. It was possible to achieve relatively good positioning of the extracted data from the multitemporal SAR images. Less accurate co-registration of GPR profiles with SAR images was achieved, especially in the very upper parts of the glacier, where the SAR images were geometrically distorted.

7. GLACIAL INFORMATION IN THE RADAR DATA

In the analysis of the GPR data, the following near-surface structure was identified. From stake 1 and up to approx. 450 m before stake 4, only one strong reflector was present. This reflector is interpreted as the glacier ice surface, having a relative homogeneous snow layer on top. This single reflector then becomes weak or degrades into a set of weak close-spaced reflectors. This could be the lower limit of superimposed ice at the end of the ablation season 1994. 650 m after stake 4, two and three reflectors substitute the fuzzy reflectors. This could be the lower extension of the firn layer at the end of the ablation season 1994. Starting 400 m before stake 5 and continuing for 600 m, a series of very strong reflectors are found. These are probably caused by summer surfaces in the deep layer of multi-year firn, and the start of these is interpreted as the lower limit of the firn area at the end of the 1993 ablation season.

This GPR-derived information, mass balance estimates from Kongsvegen, and the TM image interpretation constituted the basis for the analysis of the 1993 SAR image. The TM image and the GPR data both indicate that the firn edge was located somewhere around 700 m a.s.l. in 1993. This corresponds to some hundred meters before stake 5.

In the 1993 SAR image, an up-glacier increase in σ^0 is found before stake 5. Hence, the firn area causes a distinct region in the image, characterised by very high backscatter values between -5 and 0 dB. However, the backscatter strength varies within the firn area. The thickness of the annual firn layers vary according to the surface topography and elevation. Less snow accumulates in convex areas, and the GRP data show that the depth of firn layers is much less in these areas. The SAR backscatter strength is also much lower in these areas, relative to the firn area in general. This is the case after stake 6, which shows values as low as -8 dB. A drop of 5 dB is observed at stake 5 in the 1993 image. Both TM, SAR and GPR data indicate that the firn edge is located in this area, and that the GPR and SAR profiles do not transect this firn edge line perpendicularly. Hence, the SAR profile probably crosses parts of the firn area before the position of stake 5 in the SAR image. Around stake 5 in the SAR image, only a thin firn layer or no firn layer is present. After stake 5 in the SAR image, the backscatter strength increases and approaches 0 dB. The small discrepancy between the SAR backscatter and the GPR information is believed to be due to errors in the data co-registration.

Based on data from Kongsvegen, the 1992/93 ELA of Slakbreen was estimated to 630 m a.s.l., which corresponds to somewhere a few hundred meters after stake 4. In the TM image, an intermediate zone (characterised by slush and superimposed ice) extends down to a few hundred meters before stake 4. However, during the three weeks of prolonged ablation which probably took place after August 15, this border could have moved up-glacier up to approx. 630 m a.s.l. An intermediate zone was identified in the 1993 SAR image, characterised by backscatter values between -10 and -4 dB. This zone starts before stake 4, and terminates before stake 5. This zone corresponds to the intermediate zone on the TM image. Delineation of this zone in the SAR image is difficult. This could be because no exact limit existed in this area of the glacier. The physical properties, which are characteristic of the different surface zones may have changed gradually and or in irregular patterns. A highly irregular pattern is observed in this area in the TM image.

The 1995 SAR image shows a zonation, which is remarkably similar to the 1993 image. The position of the SAR zones do not change from 1993 to 1995, despite that a considerable lowering and repositioning of the near-surface zones took place. However, the backscatter strength along the profile did change. In the lower parts of the glacier between stake 1 and 3, sections of the profile show a decrease in backscatter from 1993 to 1995. Within the intermediate zone observed in the 1993 image, not much change in backscatter strength is observed from one year to another. The upper parts of the glacier gave higher backscatter values in 1995 than in 1993. An explanation for the decrease in backscatter in the lower parts could be a change in the roughness and structure of the glacier ice surface. The increased backscatter from the firn area could be that the positive mass balance in 1993/94 lead to a thicker firn layer and a greater scattering volume. The change may also be due to an increase in grain size or presence of liquid water at some level in the firn pack at the time of image acquisition in 1993. The intermediate zone found in the 1993 image is not found further down-glacier in the 1995 image. Two explanations are proposed. Very positive mass balance was recorded in the two years preceding 1992/93. Hence, the intermediate zone in the 1993 image could be the result of a freezing of water supersaturated firn from these two years. This firn would probably drain easily, during the on-set of the winter, and the result could have been a zone, which possesses different backscatter properties than the slush zone from the autumn 1994. The slush zone of the latter year, if it existed, was probably made up by water saturated snow. Another explanation may be that in years of negative mass balance, zones of slush and superimposed ice cover large areas, as they will be located in near horizontal parts of the glacier with pour drainage. In years of very positive mass balance, these zones occur at lower elevations, where the glacier surface is steeper. A steeper surface drains the water and reduces effectively the extension of slush and superimposed ice.

8. CONCLUSIONS

This study has confirmed that the near-surface structure affects SAR and GPR measurements of glaciers. The analysis of SAR images acquired during typical winter conditions, indicates that the firn edge and possibly the equilibrium line can be located in years of very negative mass balance, as was the case in 1992/93. The redistribution of these zones in the proceeding year, which had a very positive mass balance, could not be identified in the SAR image from the end of the winter 1994/95.

This shows that the glaciological information content in winter ERS SAR imagery depends on a multi-year history of processes related to accumulation, ablation, and snow metamorphism in the near-surface layer. Hence, this history should form the basis for interpretation of SAR backscatter imagery.

9. ACKNOWLEDGMENTS

This work could not have been carried out without the participation and support of a series of people and organisations. GRADAR SNC made the GPR SIR-2 available free of charge, the University Courses on Svalbard (UNIS) covered the expenses associated with the field work and Rune Ødegård (UNIS) took part in the field work. The Department of Physical Geography, University of Oslo, made data processing tools and work room available, GEOMAP AS provided the GPR antenna free of charge, and ESA/Tromsø Satellite Station provided the ERS-1 data.

10. REFERENCES

Birchak JR, Gardner CG, Hipp JE, and Victor JM 1974, High dielectric constant microwave probes for sensing soil moisture, *Proc. IEEE*, 62, 93-98.

Engeset R and Weydahl DJ 1995, Analysis of glaciers and geomorphology on Svalbard using multitemporal ERS-1 SAR images, *Proc. Retrieval of bio- and geophysical parameters from SAR data for land applications*, 10-13 Oct. 1995, CNES, Toulouse, France.

Hagen JO, Liestøl O, Roland E, and Jørgensen T 1993, Glacier atlas of Svalbard and Jan Mayen, *Norsk Polarinstitutt Meddelelser*, 129.

Jezek KC, Drinkwater MR, Crawford JP, Bindschadler R, and Kwok R 1993, Analysis of synthetic aperture radar data collected over the southwestern Greenland ice sheet", *J. Glaciol.*, 39, 119-132.

Laur H, Meadows P, Sanchez JL, and Dwyer E 1993, ERS-1 SAR radiometric calibration, *SAR Calibration Workshop*, 20-24 Sept. 1993, ESTEC, Noordwijk, The Netherlands.

Paterson WSB 1995, The physics of glaciers, 3rd ed., *Pergamon Press.*

Rees WG, Dowdeswell JA, and Diament AD 1995, Analysis of ERS-1 synthetic aperture radar data from Nordaustlandet, Svalbard, *Int. J. Remote Sens.*, 16(5), 905-924.

Rott H, Sturm K, and Miller H 1993, Active and passive microwave signatures of Antarctic firn by mean of field measurements and satellite data, *Ann. Glaciol.* 17, 337-343.

Weydahl DJ 1994, Absolute calibration of the fast delivery SAR product processed at Tromsø Satellite Station, *Proc. European Symp. Satellite Remote Sens.*, 26-30 Sept. 1994, Rome, Italy.

LANDSAT TM-DATA AND GROUND RADIOMETER MEASUREMENTS FOR SNOW AND ICE TYPE CLASSIFICATION IN THE VESTFOLD HILLS, EAST ANTARCTICA.

Laine Boresjö Bronge and Christian Bronge

Department of Physical Geography
Stockholm University, S-106 91 Stockholm, Sweden
phone: +46 8 164785, 164814 fax: +46 8 164818
e-mail: laine@natgeo.su.se, bronge@natgeo.su.se

ABSTRACT

The aim with the present project was to find simple satellite-based methods to be used in glaciological-climatological research in Antarctica. A Landsat TM recording from 16 February 1991 was used together with field data to study the spectral charcateristics of different types of snow and ice in the Vestfold Hills, East Antarctica (68°35'S, 78°10'E). Radiometer measurements were made simultaneously with the satellite passage and at several other occasions using a handheld Photodyne 44XLA. 72 test sites selected in the Landsat TM image formed the basis for the analysis of the spectral characteristics. Principal component analysis, ratioing, and maximum-likelihood classification were also performed. The analysis revealed a large and interesting information content in the TM image. Blue-ice of different character as well as snow of various degree of metamorphosis are discernible and possible to spatially map using maximum-likelihood classification. The TM3/TM4-ratio was found to be a simple tool for distinguishing between blue-ice and snow of various character. It also showed to be insensitive to influence from thin clouds and cloud shadows. The TM3/TM5-ratio was found to enhance snow grain-size variations.

1. INTRODUCTION

The conditions in Antarctica are of great interest since the stability of the Antarctic environment seems to be of crucial importance for the development of the global climate. However, field work in Antarctica is expensive and connected with large practical problems. In such an area remote sensing has a great potential for providing data of ground features and make possible analysis of large areas to a relatively low cost, provided that the parameters of interest may be extracted from the data. With the objective to find simple satellite-based methods to be used in glaciological-climatological research in Antarctica, a Landsat TM scene was analysed together with ground radiometer measurements in the Vestfold Hills area at the East Antarctic ice sheet margin (Fig. 1). The aims were 1) to map physical features and areal distribution of various types of blue-ice and snow using their spectral characteristics, 2) to find appropriate TM bands or combinations of TM bands for discriminating various physical features and properties of the blue-ice and the snow, 3) to pave the ground for future change studies in an Antarctic marginal area which is probably a sensitive indicator of climate. More tentatively, the prospect of making quantitative estimates of ablation (ice-melt) appears.

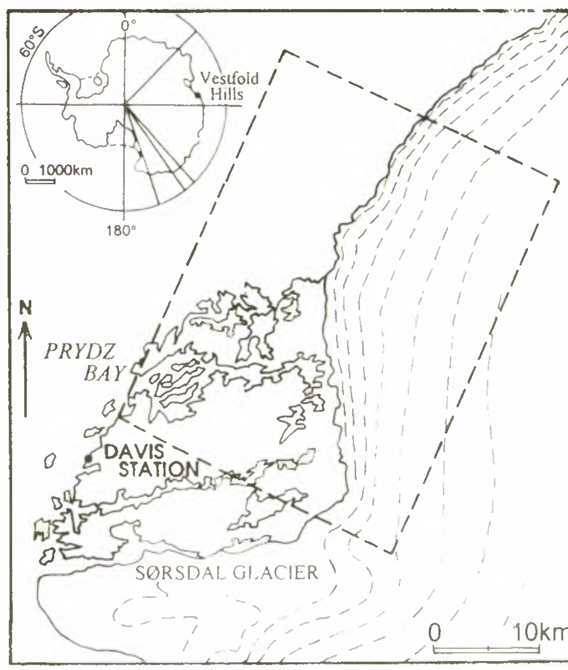

Fig 1. The Vestfold Hills. The small rectangle (hatched line) shows the area selected for detailed analysis.

The Vestfold Hills

The Vestfold Hills are a 410 km^2 large, ice-free coastal region of subdued relief on the northeastern shore of Prydz Bay, East Antarctica (Fig. 1). It is bordered to the east by the continental ice-sheet and to the south by an outlet glacier, the Sørsdal Glacier. The test area covers an Antarctic marginal area, where snow of various degree of transformation is present, as well as blue-ice of varying character. Along the margin of the

Proceedings of the Fourth Symposium on Remote Sensing of the Polar Environments, Lyngby, Denmark, 29 April – 1 May 1996 (ESA SP-391, July 1996)

ice-sheet there is a zone of perennial snowdrift, formed by the prevailing east-north-easterly winds on the lee-side of the sloping ice-front. Above this zone there is blue-ice up to about 6 km inland from the ice-margin. Close to the ice-margin ice-melt takes place, which has created several deeply incised meltwater gullies. Above a certain level on the ice-sheet sublimation is the only ablation process, and hence no meltwater is generated.

2. METHODS

A Landsat-5 TM recording from 16 February 1991 (floating quadrant path/row 124/108) was analysed together with ground radiometer measurements of various types of ice and snow. Radiometer measurements were made simultaneously with the Landsat TM passage and at several other occasions during the 1990/91 Austral summer. A handheld Photodyne 44XLA with filters for measurements in red, near IR, and mid-IR, was used (Table 1).

For calibration of the measurements, a white-painted wooden board, sized 52 x 60 cm^2, was used, to which were attached three layers of baryte-paper. The measurements were carried out in nadir from a height of approximately 1.35 m. Each object was normally measured three times interspersed by measurements on the white reference. Photographic and written documentation were made at the measured spots.

The white-reference used in the field was calibrated against a well documented baryte-painted reference normally used for laboratory measurements. The correction factor was calculated:

$$k = \frac{\overline{x}_{wf}}{\overline{x}_{wl}} \qquad (1)$$

where $\overline{x}_{wf}$ and $\overline{x}_{wl}$ are the mean values of the three measured values from the field white-reference and from the laboratory white-reference respectively. The factor, calculated from 12 readings at times from 10.30 to 16.30, displayed no systematic deviation with the changing sun elevation, and had the values of 1.01, 1.01 and 0.86 for the red, near IR and mid-IR bands respectively. It was used to adjust the reflectance factors obtained from the field measurements according to the equation:

$$r_{adj} = \overline{r} \cdot k = \overline{\left(\frac{x_{ob}}{x_{wf}}\right)} \cdot k \qquad (2)$$

where $\overline{r}$ is the mean value of the "raw" reflectance factors and x_{ob} is the measured value of the object (snow, ice etc.) and hence r_{adj} is the final, adjusted reflectance factor.

The Landsat TM image was processed and analysed using the Erdas Image software programme (ver. 8.2).

Table 1. Filter specifications for ground measurements.

Filter	Band edges at 50 % band pass (nm)	Wavelength region	Corresponding to
659	631 - 699	red	TM3
841	786 - 901	near IR	TM4
1676	1571 - 1771	mid-IR	TM5

To enhance the available information in the TM data set, a principal component analysis (PC analysis) was carried out. To obtain maximal contrast between the most interesting objects, the PC analysis was performed only for areas covered by ice and snow. Grey level slicing in TM3 was used to create a mask for separating ice and snow from the ice-free area and water. As reported by several authors (Dozier 1984, Orheim and Lucchitta 1988, Hall *et al.* 1990, Winther 1993), TM1 was disturbed by a relatively severe sensor saturation. Nevertheless, the PC transform including TM1 gave a better result concerning discernible features than the transform without TM1. Therefore, TM1 was included in the PC enhancement, but otherwise excluded from the analysis. Colour images consisting of different combinations of the calculated PCs were analysed and used for delineation of homogeneous areas in the images representing different features on the ice. Since the physical interpretation of the principal components is difficult, the selected areas were used for extraction of statistics from the original TM bands. This data set formed the basis for the analysis of the spectral characteristics of the various ice and snow features that were discernible in the PC images. In total 72 areas were delineated (Table 2).

The analysis also included maximum-likelihood classification and ratioing between the bands. Ratios between TM4/TM5, TM3/TM4 and TM3/TM5 were calculated on the basis of the mean values from the selected test sites, as well as from the ground measurements.

Table 2. Total number of test sites of snow and ice selected for the spectral analysis.

Object	# of test sites	Σ of pixels
Blue-ice	27	15 403
Blue-ice below cloud	3	6 471
Blue-ice in cloud shadow	4	6 475
Snow	26	30 850
Snow below cloud	5	5 924
Snow in cloud shadow	7	5 275
Total number:	72	70 398

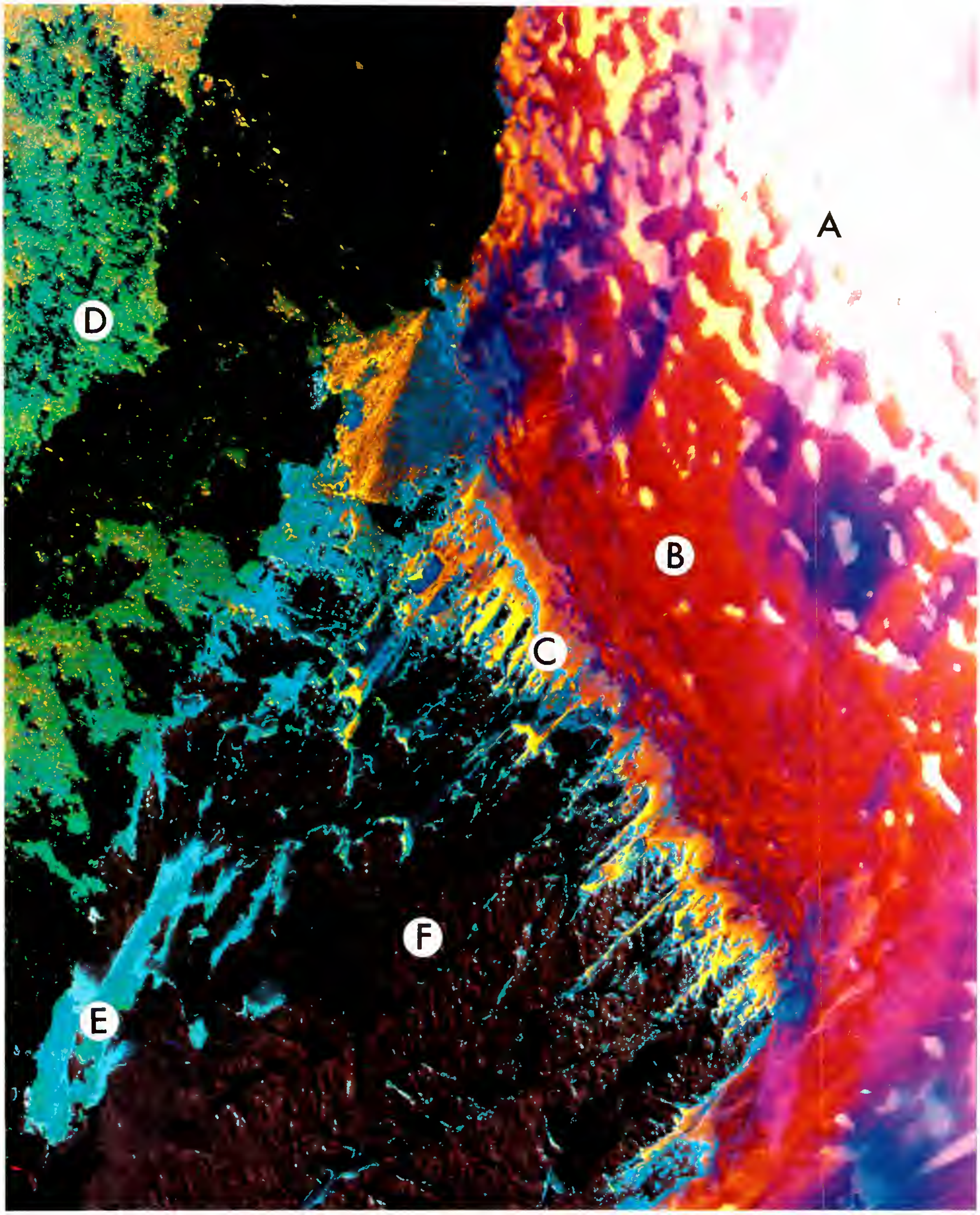

Fig. 2. Colour composite image of PC1, PC2 and PC3 (RGB) of snow and ice areas. The principal component image is merged with an IR-colour composite of the ice-free area.
A. Snow on the ice plateau. B. Blue-ice. C. Perennial snowdrift. D. Pack-ice. E. Fjord-ice, older than 1 year. F. Ice-free area. The discoloured areas in the upper and lower right quadrants are caused by cirrus clouds with shadows.

3. RESULTS AND DISCUSSION

The PC image reveals a variety of well discernible features on the ice (Fig. 2). Along the margin of the ice-sheet, the zone of perennial snowdrift is clearly distinguishable, revealing snow patches of different character, and strips of superimposed ice. Above this zone the blue-ice area extends some 5 km upwards the ice-sheet, after which snow patches become more numerous and finally merge to form a continuous cover. Within the blue-ice area there is a pattern of elongated features parallel to the contour lines, interpreted as minor topographic undulations of the ice surface, visible in the image because of the low sun elevation and the variable illumination conditions on the ice caused by these factors. There is also a zone with darker colour close to the zone of perennial snowdrift. This zone probably represents the part of the blue-ice area where ice-melt takes place. Clouds with shadows can be seen in the upper right quadrant of the image, and in the lower right corner.

The TM spectral signature curves (Fig. 3) and the signature curves from the ground measurements (Fig. 4) show that the near IR band (TM4) gives the best separation between blue-ice and the various types of snow. In the red wavelengths (TM3) there is good separation between blue-ice and snow with low degree of metamorphosis, but not between blue-ice and highly transformed snow. Clouds are easily detectable in the mid-infrared bands (TM5 and TM7), since they increase the reflectance for both snow and blue-ice in these wavelengths. This is physically explained by the fact that the small ice crystals in cirrus clouds are much more reflective than snow in these wavelengths (Warren 1982, Dozier 1987).

The TM3/TM4-ratio (red/near IR) was found to be a very good tool for discriminating between blue-ice and snow of various types, and in contrast to the TM3/TM5 and the TM4/TM5-ratios insensitive to influence from thin clouds and cloud shadows (Table 3). This finding is supported by the ground measurements (Table 4). The red/near-IR-ratios of the reflectance factors give a complete separation between the blue-ice and the snow sites. Fig. 5 shows an image based on the TM3/TM4-ratio. Blue-ice is easily distinguished from snow-covered areas as well as a zone within the blue-ice area interpreted as blue-ice with a large content of air-bubbles and/or snow patches. Fig. 5 covers the same area as Fig. 2. As can be noted, the effects of the thinner parts of the cloud and its pertaining shadows are completely removed. Fig. 6 shows a classification of blue-ice and snow based on a simple grey level slicing of the TM3/TM4-ratio image.

Table 3. Landsat TM-ratios based on the mean values of the test sites.

Object	Ratio TM3/TM4	TM3/TM5	TM4/TM5
Blue-ice	2.0 - 2.3	21.6 - 30.5	9.7 - 14.6
Blue-ice below cloud	2.0	7.4 - 8.0	3.7 - 4.1
Blue-ice in cloud shadow	2.1 - 2.2	21.5 - 25.4	10.4 - 12.0
Snow	1.6 - 1.7	14.8 - 27.0	9.5 - 16.9
Snow below cloud	1.5 - 1.6	9.0 - 10.7	5.9 - 7.0
Snow in cloud shadow	1.6 - 1.7	11.3 - 22.8	7.0 - 13.8

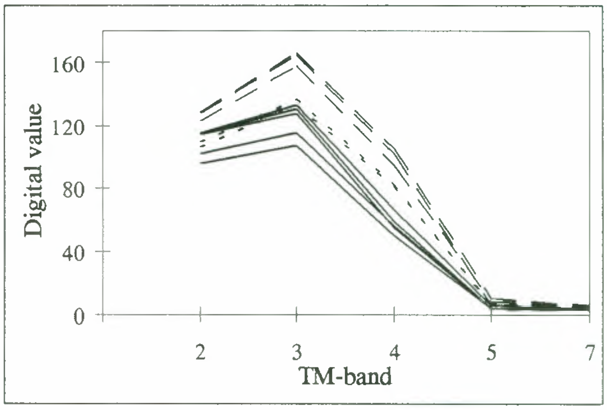

Fig. 3. Landsat TM spectral signature curves of blue-ice compared to snow.
——— Blue-ice.
- - - - - - - Old metamorphosed snow.
— — — — Snow at a low degree of metamorphosis.

Blue-ice

In the satellite image it seems to be possible to discern the zone of blue-ice within which ice-melt takes place (Fig. 2). This zone is visible in the PC-image as a darker zone on the blue-ice bordering the perennial snowdrift. The TM signature curves from test sites within this zone differ from other blue-ice sites mainly by having lower reflectance in the visible and near IR bands (Fig. 7). This is interpreted as an effect of shadowing caused by a micro-relief in the ice, probably together with small amounts of englacial debris, emerging on the ice surface in the meltzone. Dust from the ice-free area is less likely because of the prevailing east-north-easterly winds. Impurities in snow have a strong lowering effect on the albedo for wavelengths up to 1 µm, even though it is most pronounced in the visible region (Warren 1982). The effect is amplified by increased snow grain-size. Effects of shadowing from the ice dome itself could be excluded as an explanation since the slope angle of the ice, despite a relatively low sun elevation at the recording time, was never steep enough to cause any shadowing. On the contrary, it is probable that a micro-relief could have caused "micro-shadows" at the recording time. Large

Table 4. Reflectance factors obtained from the ground measurements and ratios based on the factors.

Description	Object Date	Time	Red	Refl. factor Near IR	Mid-IR	Red/ Near IR	Ratio Red/ Mid-IR	Near IR/ Mid-IR
Blue-ice, smooth, relatively pure	26/2-91	10.40	0.65	0.29	0.02	2.2	32.5	14.5
Blue-ice, with air-bubbles/snow [x]	16/2-91	10.25	0.77	0.36	0.02	2.1	38.5	18.0
Blue-ice, with air-bubbles	28/2-91	17.00	0.77	0.37	0.03	2.1	25.7	12.3
Snow, "freshly fallen" [1]	3/3-91	13.25	0.90	0.85	0.07	1.0	12.9	12.1
Snow, hardblown, smooth surface [2]	28/2-91	10.30	0.97	0.77	0.06	1.3	16.2	12.8
Snow, hardblown, wave structure [2) x]	16/2-91	10.05	0.89	0.67	0.03	1.3	29.7	22.3
Snow, highly metamorphosed [3]	15/2-91	12.10	0.81	0.64	0.02	1.3	40.5	32.0
Snow, highly metamorphosed [3]	15/2-91	14.20	0.88	0.67	0.02	1.3	44.0	33.5

1) Snow field about 3 km northeast of Davis Station consisting of a few days old snow with grainy structure
2) Snow field high up on the plateau
3) From the zone of old perennial snowdrift, icy snow with large crystals
x) Measured simultaneously with satellite passage

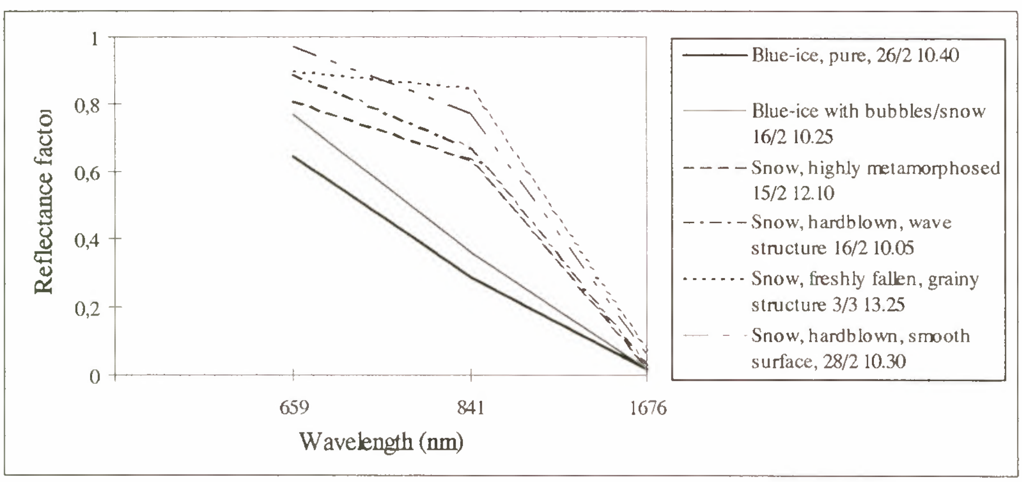

Fig. 4 Spectral signature curves from ground measurements.

parts of the marginal zone of the ice are scoured by gullies caused by meltwater. This zone faces the sun during mid-daytime to afternoon, resulting in direct exposure for the insolation, which causes a rough surface in the meltzone. Stake measurements from the actual season have also revealed that the upper limit of ice-melt was about 180 m a.s.l. (Bronge 1996), which coincides fairly well with the upper limit of the zone in the TM image. Maybe this zone should be interpreted in a wider sense, representing the melting area during several years, rather than the meltzone a specific year.

Above the meltzone, a similar dark colour can be seen as a less distinct pattern of elongated features parallel to the contour lines (Fig. 2). As already mentioned, these features have been interpreted as minor topographic undulations of the ice surface, visible in the image because of the low sun elevation. The TM signatures of these features are similar to the meltzone signatures, but show slightly higher values in the visible bands. In the TM signatures it is also possible to discern areas of pure blue-ice from blue-ice areas affected by snowpatches and/or air-bubbles since the latter cause an increase in reflectance in the red and near-IR (Fig. 7). This interpretation is supported by the ground measurements (Fig. 4, Table 4). In general, there is a trend of increasing values in TM4 towards the zone where the snowpatches begin to dominate.

Fig. 5. TM3/TM4-ratio image of snow and ice areas. Snow is dark grey. Pure blue-ice is light. Blue-ice with a large content of air bubbles and/or snow patches is light grey. The influence of the thinner parts of the cirrus cloud and its shadows is completely removed (compare with fig. 2). The ratio image of snow and ice is merged with an IR-colour composite of the ice-free area.

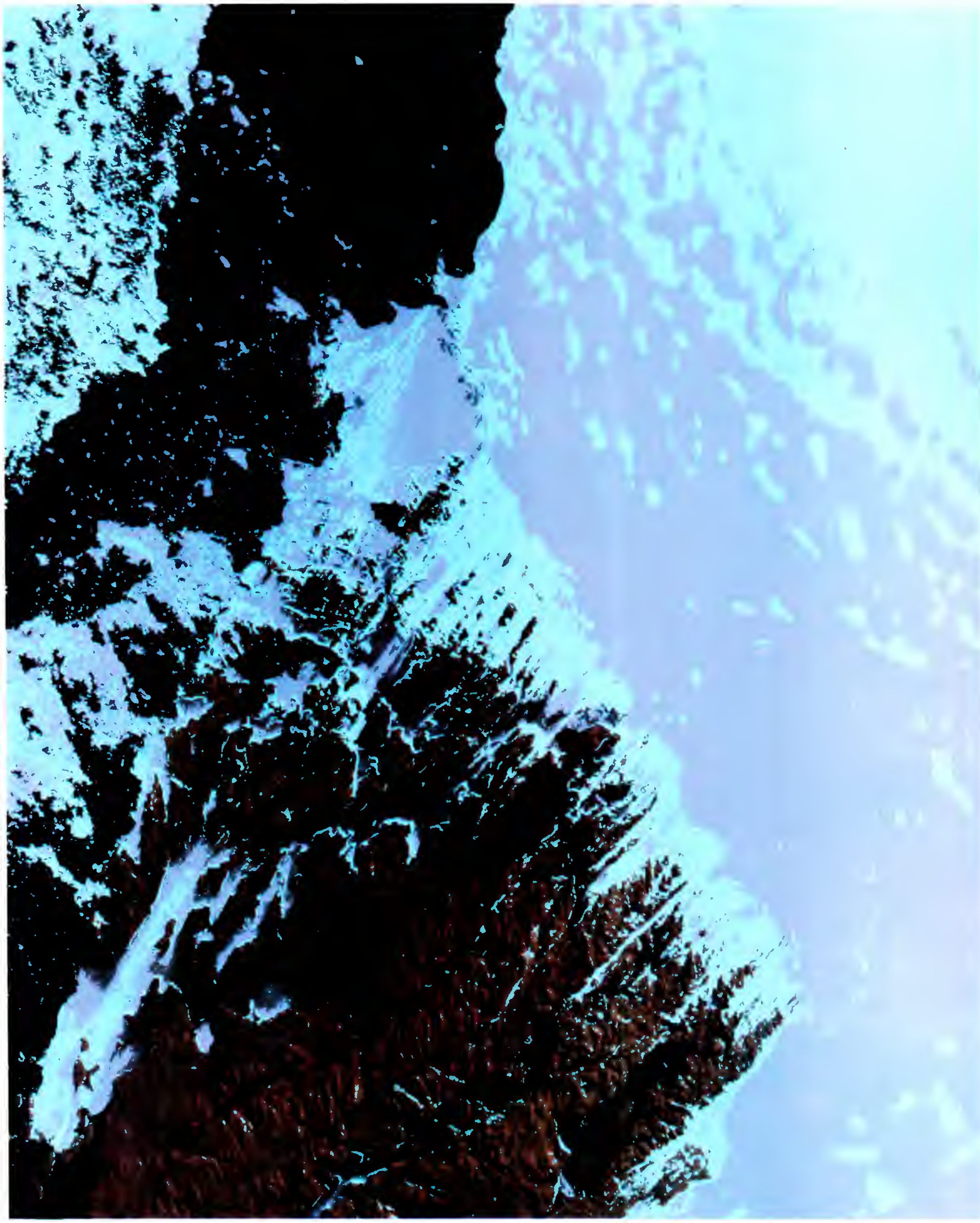

Fig. 6. Classification of blue-ice (dark blue) and snow (cyan) by grey level slicing in the TM3/TM4-ratio image.

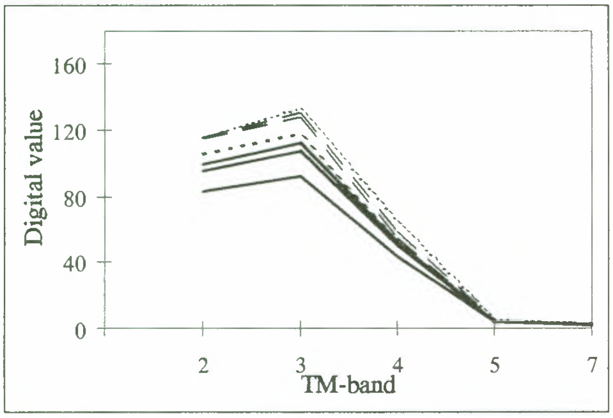

Fig. 7. Landsat TM spectral signature curves of blue-ice of various types.

————	Blue-ice sites in the zone where ice-melt probably occurs.
- - - - - - -	Pure blue-ice. The selected site is interpreted as being located downslope a minor undulation in the ice.
— — — -	Pure blue-ice.
··············	Blue-ice with a large content of air-bubbles and/or incorporated snow patches.

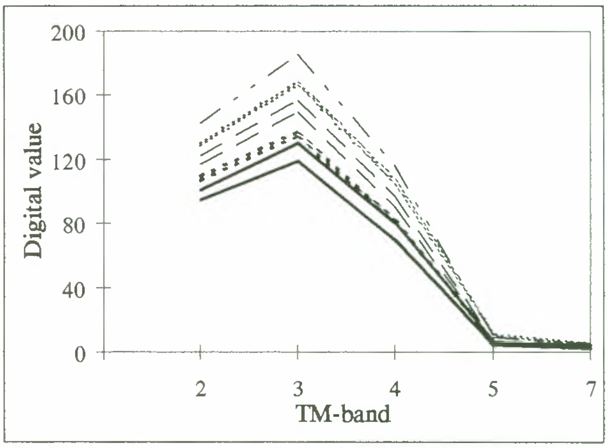

Fig. 8. Landsat TM spectral signature curves of snow of various types.

— ·· — --	Half-year old snow on the perennial snowdrift, very little metamorphosed.
············	Snow from the ice plateau at a low degree of metamorphosis.
— — — —	Moderately metamorphosed snow.
- - - - - - - -	Highly metamorphosed snow.
————	Highly metamorphosed snow with superimposed ice.

Most likely, this is due to increasing amounts of air-bubbles and incorporated snow further up on the plateau. This zone of blue-ice with incorporated snow and air-bubbles is difficult to distinguish in the PC-image (Fig. 2), but is easily seen in the TM3/TM4-ratio image (Fig. 5) where the small differences in spectral response are enhanced.

Snow

The spectral properties of various kinds of snow are generally linked to the degree of transformation of the snow (grain-size), which in turn is a function of time. Model calculations of semi-infinite diffuse albedo show that the albedo decreases at all wavelengths with increasing grain-size, although it is most pronounced in the infrared region (Warren 1982). This is notable also in the TM spectral signatures. The least transformed snow, which can be found higher up on the ice-plateau, and along the perennial snow-patches, displays the highest values in all reflective TM bands (Fig. 8). With increasing degree of transformation, an overall lowering of the reflectance is noted. The lowest values are displayed by the parts of the perennial snowdrifts which are soaked through by meltwater originating from the nearby blue-ice and from the snowdrifts themselves (Fig. 8). The decrease in the visible wavelengths is notable, since model calculations show that the visible region is relatively insensitive to grain-size compared to the sensitivity of longer wavelengths (Dozier *et al.* 1981, Warren 1982). Probably, this is also an effect of snow depth and impurities in the snow. According to Dozier *et al.* (1981), the penetration capacity is greater in the visible wavelengths than in the near infrared, especially for larger grain-sizes. This means that the underlying substrate, in this case the ice, will influence the reflectance, if there is only a thin layer of snow. The albedo in the visible region is also, compared to the infrared region, very sensitive for impurities. Even very small amounts of absorbing particles present in concentrations of only 1 part per million weight, can cause a reduction of the albedo by 5 - 15 %, compared to pure snow (Warren and Wiscombe 1980). Since the decrease in albedo with increasing grain-size is relatively larger in the infrared region according to theory, especially for wavelengths longer than 1 µm, a ratio between the visible and mid-IR bands would be positively correlated to the degree of transformation of the snow. A ranking of the test sites for snow based on the TM3/TM5-ratio confirms this assumption. It shows an increasing trend of the ratio from the ice plateau towards the ice-margin (Table 5), which would imply an increasing grain-size from the plateau towards the coast. This is in accordance with the findings of Bourdelles and Fily (1993), who found an increasing snow-grain size towards the coast in Terre Adélie when comparing calculated at-satellite TM reflectances with theoretically modelled reflectances computed for different grain radii.

On the perennial snowdrift the ratio varies, probably because these patches are built up from both old highly metamorphosed snow and younger snow deposited by the wind during the previous winter. The

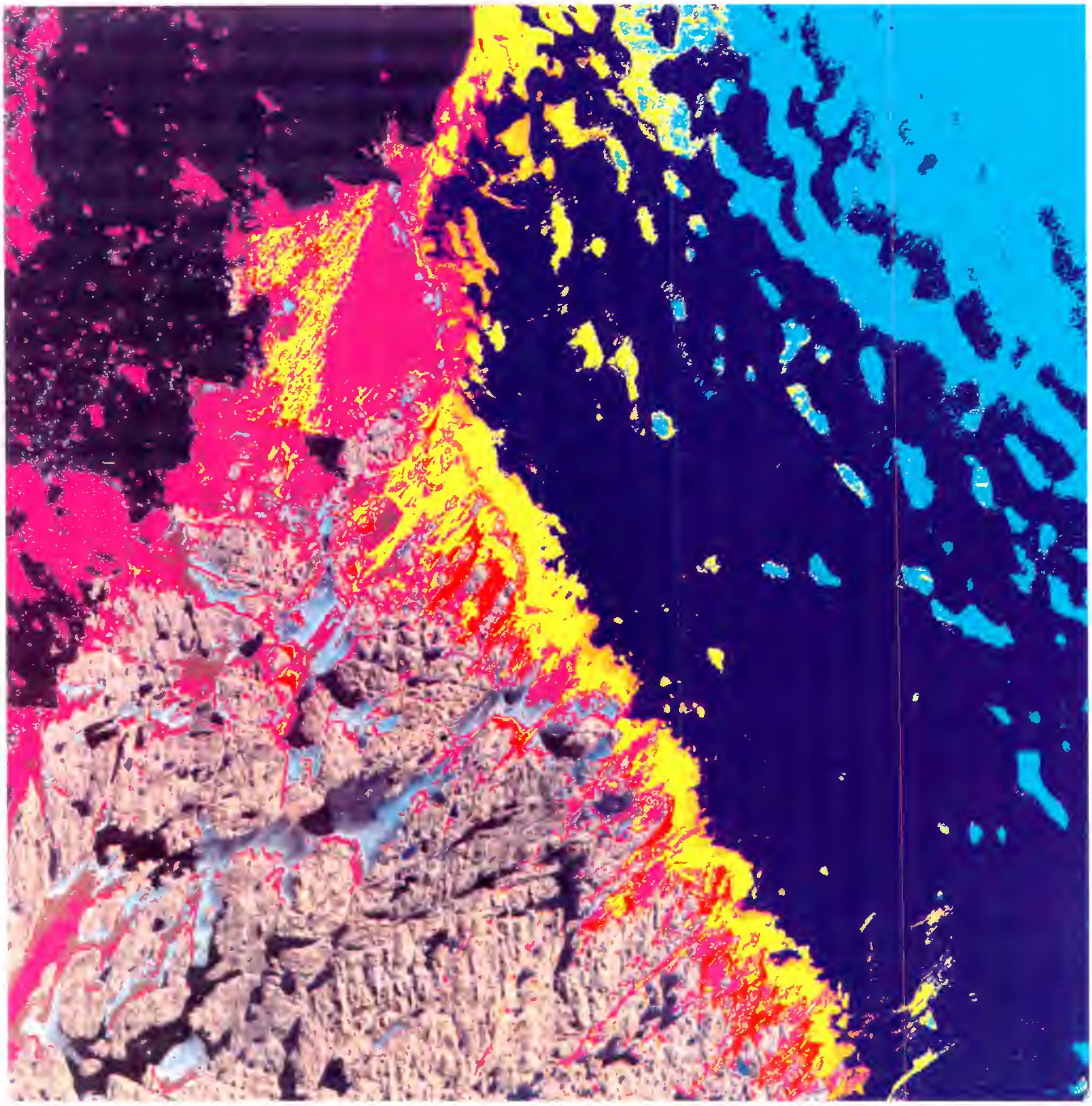

Fig. 9. Classified image of snow and ice areas. The classification result is merged with an IR-colour composite of the ice-free area (RGB=TM4,TM3,TM2). Maximum-likelihood classification was used on the principal components.

Dark blue: Blue-ice.
Cyan: Hardblown, fine-grained snow of low degree of metamorphosis (small grain radii).
Yellow: Snow, highly metamorphosed.
Orange: Snow, highly metamorphosed with superimposed ice.
Red: Snow, half-year old, partly metamorphosed.
Cerise: Pack-ice and old fjord-ice with snow.
Brown grey: Fjord-ice, older than 1 year.

Table 5. Ranking of the snow test sites according to the TM3/TM5-ratio.

Object	Test site		TM3/TM5-ratio
Snow on the ice	Site A		14.8
	Site B	⇓ decreasing	17.3
	Site C	distance	22.4
	Site D	to the ice	23.9
	Site E	margin	25.8
	Site F		25.8
	Site G		26.2
Snow on the perennial snowdrift	Site H		27.0
	Site I		25.7
	Site J (from previous winter)		19.6
Blue-ice	Several sites		25.2 - 32.2

ratio of the snowdrift may also be influenced by other factors such as dust blown from nearby nunataks or dust melted out from the ice. As a comparison, the TM3/TM5-ratios of blue-ice from sites above the meltzone vary from levels comparable with the highly metamorphosed snow to values a few levels higher (Table 5). The pure blue-ice sites display the highest ratios.

The decrease in reflectance with increasing degree of transformation of the snow is also confirmed by the ground measurements (Fig. 4, Table 4). The freshly fallen snow displays the highest reflectance factors in near IR and mid-IR, with the blue-ice on the other extreme. Looking at the red/mid-IR-ratio there is also in the ground measurements a positive trend of higher ratios with increasing degree of transformation of the snow.

Maximum-likelihood classification

To separate the major discernible features on the ice, a maximum-likelihood classification was carried out, based on the analysis of the spectral characteristics of ice and snow (Fig. 9). Blue-ice and snow of various degree of metamorphosis were separated. It was also possible to classify blue-ice of different character, but the occurrence of cloud shadows on the ice caused misclassification of these parts, and the blue-ice was therefore treated as one class in the result.

4. CONCLUSIONS

The analysis of the ground radiometer measurements and the Landsat TM image has revealed a large and interesting information content in the TM image. Blue-ice of different character as well as snow of various degree of transformation were discernible and possible to spatially map using maximum-likelihood classification. The TM3/TM4-ratio was found to be a simple tool for distinguishing between blue-ice and snow of various character. It also showed to be insensitive to influence from thin clouds and cloud shadows. The presence of clouds, even thin ones, was detectable in TM5, since they caused an increase in reflectance for both snow and blue-ice areas. The TM3/TM5-ratio was found to be a useful tool for enhancing snow gain-size variations. It was positively correlated with the degree of snow metamorphosis and showed an increasing trend from the plateau towards the coast.

REFERENCES

Bourdelles, B. and Fily, M., 1993: Snow grain-size determination from Landsat Imagery over Terre Adélie, Antarctica. *Annals of Glaciology*, 17:86-92.

Bronge, C., 1996: Hydrographic and climatic changes influencing the proglacial Druzhby drainage system, Vestfold Hills, Antarctica. (Submitted to Antarctic Science.)

Dozier, J., 1984: Snow reflectance from LANDSAT-4 Thematic Mapper. *IEEE Transactions on Geoscience and Remote Sensing*, GE-22(3):323-328.

Dozier, J., 1987: Remote sensing of snow characteristics in the southern Sierra Nevada. *In* "Large Scale Effects of Seasonal Snow Cover", Proceedings of the Vancouver Symposium, August 1987, pp. 305-314.

Dozier, J., Schneider, S.R. and McGinnis, D.F., 1981: Effect of grain-size and snowpack water equivalence on visible and near-infrared satellite observations of snow. *Water Resources Research*, 17(4):1213-1221.

Hall, D.K., Bindschadler, R.A., Foster, J.L., Chang, A.T.C. and Siddalingaiah, H., 1990: Comparison of *in situ* and satellite-derived reflectances of Forbindels Glacier, Greenland. *International Journal of Remote Sensing*, 11(3):493-504.

Orheim, O. and Lucchitta, B., 1988: Numerical analysis of Landsat Thematic Mapper images of Antarctica: Surface temperatures and physical properties. *Annals of Glaciology*, 11:109-119.

Warren, S.G., 1982: Optical properties of snow. *Reviews of Geophysics and Space Physics*, 20(1):67-89.

Warren, S.G. and Wiscombe, W.J., 1980: A model for the spectral albedo of snow. II: Snow containing atmospheric aerosols. *Journal of the Atmospheric Sciences*, 37(12):2734-2745.

Winther, J.-G., 1993: Studies of snow surface characteristics by Landsat TM in Dronning Maud Land, Antarctica. *Annals of Glaciology*, 17:27-34.

NEW RESULTS FROM MAPPING ANTARCTICA AT HIGH RESOLUTION FROM RADAR ALTIMETER DATA

Michael Matassa[1], Chris A. Higginson[1], Helmut Mayer[1], Ute Christina Herzfeld[1,2]

[1] Institute of Arctic and Alpine Research, University of Colorado Boulder
Boulder, Colorado 80309-0450, U.S.A.
Ph: +1 303 492 6198, fax: +1 303 492 6388
e-mail: herzfeld@tryfan.colorado.edu / matassam@tryfan.colorado.edu

[2] Geomathematik, Fachbereich Geowissenschaften, Universität Trier
D-54286 Trier, Germany
Ph: +49 651 201 4611, fax: +49 651 201 3815, e-mail: uch@denali.uni-trier.de

ABSTRACT

It is often argued that satellite radar altimeter data over ice cannot be used to map ice surfaces with a slope exceeding 0.5°. In the work presented in this paper, we are trying to push the limits of altimeter data evaluation using geostatistical methods.
Application of ordinary kriging to altimeter data from the GEOSAT Geodetic Mission (chosen for its denser coverage, as compared to the Exact Repeat Mission) yields maps of high resolution and accuracy. The maps presented here are part of an atlas (under construction) containing high-resolution maps of all of Antarctica north of 72.1° S (*spatial segment of the project*).
Construction of a time series of such grids from altimeter data of SEASAT (1978), GEOSAT GM (1985-1986), GEOSAT ERM (1987-1989), and ERS-1 (since 1992) facilitates analyses of changes in Antarctic ice-stream/ice-shelf systems, such as elevation changes and changes in the position of the grounding line. This is applied to study the Lambert Glacier/Amery Ice Shelf system (*temporal segment of the project*).

INTRODUCTION

The dynamics of the Antarctic Ice Sheet have long been of interest, and the relationship of glacial retreat/advance has been discussed in relation to climatic changes. The possibility of a retreat of the West Antarctic Ice Sheet was first mentioned in 1962 (Hollin 1962), and changes in the dynamics of the East Antarctic Ice Sheet have also been considered ranging from ice creep instabilities to surges (Colhoun 1991; Huybregts 1993; Clarke et al. 1977). The mechanisms that may lead to ice sheet collapse have been investigated and modeled in many studies, but are still a matter of debate.
A collapse of the West Antarctic Ice Sheet would cause as much as 6 m of sea-level rise (Bindschadler 1991). That rapid retreat does occur at present time is documented by the examples of catastrophic retreat of Columbia Glacier, Alaska (Meier and Post 1987) and of break-up of the Wordie Ice Shelf, Antarctic Peninsula (Vaughan 1993).

A prediction based on any model, however, can only be as good as the information the model is based on. Many studies suffer from the fact that they are simulations lacking adequate data support. Satellite observations provide an efficient source of information for remote areas and for large parts of Antarctica they are the best information presently available - once we understand how to use it right. One problem with investigations of the Antarctic ice mass is the lack of accurate topographic maps for large parts of the continent.

A map based on grids of 20 km resolution has been compiled by Bamber (1994) from ERS-1 radar altimeter data. That elevation grid is, however, not accurate in areas with slopes steeper than 0.65° (Bamber 1994). Although most of Antarctica is less than 0.65° steep, this leaves out large parts of the glaciologically interesting areas of the ice streams and glaciers and the margins of Antarctica. A topographic map of the Filchner-Ronne-Schelfeis based on satellite images and ground-based geodetic surveys was recently published by Sievers et al. (1993).

ATLAS

We are currently working on calculating 3 km x 3 km resolution maps of Antarctica. In this paper we present some of the first results of this mapping project. A major objective of the project is to cover smaller ice streams and glaciers and the margin of Antarctica. It is well known that evaluation of radar data in terrain with higher relief means pushing the limits of altimetry, but on the other hand altimetry provides (to date) the only elevation data available at this resolution and coverage. High resolution mapping requires fully retracked and corrected altimeter data. At the time the project was started, only Geosat data were available with all

Proceedings of the Fourth Symposium on Remote Sensing of the Polar Environments, Lyngby, Denmark, 29 April – 1 May 1996
(ESA SP-391, July 1996)

corrections for large areas and enough repititions to provide sufficient coverage.

Data from the GEOSAT Geodetic Mission were chosen because of the dense ground-track pattern that resulted when the satellite was allowed to drift freely (as opposed to repeat fixed orbits spaced at 17-day repeat cycles during the Exact Repeat Mission) (cf. Fig. 1). These data were collected in 1985/86.
Retracking and slope correction have been carried out by the Ice Sheet Altimetry Group at NASA Goddard Space Flight Center (H.J. Zwally, J. DiMarzio and coworkers). For data transfer the direct link to the Ice Sheet Altimetry Group is employed.
For each map, a track plot of the data is constructed to investigate coverage and assure that coverage by retracked data is sufficient. All retracked slope-corrected data are used in this interpolation. Data are transformed to UTM coordinates.
Grid values are calculated using ordinary kriging (a least-squares-based optimum interpolation technique from geostatistics, the theory of regionalized variables, cf. Journel and Huijbregts 1978; Herzfeld et al. 1993). In kriging, a Gaussian variogram is used for all maps. Computation is carried out on a multiprocessor SUN HYPERSPARC computer.

There are two approaches possible to map Antarctica: The first is to map the entire area as one (as, e.g., in Bamber 1994), the second is to produce an atlas.
Atlas mapping requires cartographic considerations, including projection algorithms, elimination of distortion, overlap of areas, optimal size and tiling. The tiles are as follows. Row 1: 68-72.1° S, row 2: 64-68° S, row 3: 60-64° S; columns: 9° longitude per map with 1° overlap on each margin.

A few examples of the resultant maps are given in Figures 2-5. Mapping of the Antarctic Ice Sheet works very well. An indication of the accuracy of the maps is that they match very well along edges and overlapping areas between two adjacent maps. Consistent isolines are resulting for areas (with ice streams) along the margins of the ice sheet (e.g., Cook Ice Shelf, Fig. 3; and Queen Mary Coast, Fig. 4). Fig. 5 shows a part of the Antarctic Peninsula.

It is possible to locate small outlet glaciers of the Antarctic Ice Sheet, for instance, Rennick Glacier is seen on map 68to72.1-e154to163 (Fig. 2). Of course, such small glaciers are not mapped exactly, because they lie in deep valleys in which the radar signal is often lost and retracking becomes difficult. The error level increases with topographic relief (Herzfeld et al. 1993). However, the maps are sufficiently accurate to determine the surroundings and the general shape of the small glaciers.

APPLICATION

The quality of the maps suggests their use in the study of changes of Antarctic Ice Stream/Ice Shelf systems, the key points in ice dynamics. This is the objective of the temporal segment of our project. Our approach to monitor changes is centered around the analysis of time series of grids, each constructed from radar altimeter data using geostatistics, as described in the previous section. In a comparison of Lambert Glacier maps from 1978 SEASAT data and 1987-89 GEOSAT (ERM) data, we discovered that Lambert Glacier/ Amery Ice Shelf, the largest ice stream/ ice shelf system in East Antarctica, advanced: (i) The maps are sufficiently accurate to identify the approximate location of the grounding line, and (ii) the grounding line of Lambert Glacier/ Amery Ice Shelf advanced about 10 km between 1978 and 1987/89 (Herzfeld et al. 1994). In recent work, the new members have been added to the time series of Lambert Glacier maps, which includes now maps from the following data and years:

SEASAT - 1978
GEOSAT GM - 1985-86
GEOSAT ERM - 1987, 1988, 1989
ERS-1 - since 1992

DISCUSSION

There is ongoing work on the construction of elevation maps from synthetic aperture radar (SAR) stereo images, but that has yet to be completed. SAR interferometry can be expected to permit decimeter-resolution topographic mapping (Zebker and Villasenor 1992), albeit SAR images can only be collected for 10 minutes per revolution, and topographic mapping from interferometry requires interferometric pairs of high quality with ground tracks very close together (4 m in Goldstein et al. 1993), which is a rare occasion. Therefore, SAR interferometry is certainly not a possible data source for mapping large areas of the Antarctic ice. This leaves ample necessity for altimetry-based mapping.

Altimetry fills a gap in availability and coverage and high-resolution quantitative mapping of Antarctic ice sheets. The data distribution is dense enough to construct grids of 3 km resolution and full coverage.
These high-resolution grids find application in remote-sensing technology for the correction of SAR images and in glaciology for the study of ice-sheet elevation and ice dynamics.

ACKNOWLEDGEMENTS

Funded in part through NASA Office of Polar Programs (grant no. NAGW-3790 to UCH) and Deutsche Forschungsgemeinschaft (Heisenberg Fellowship to UCH).

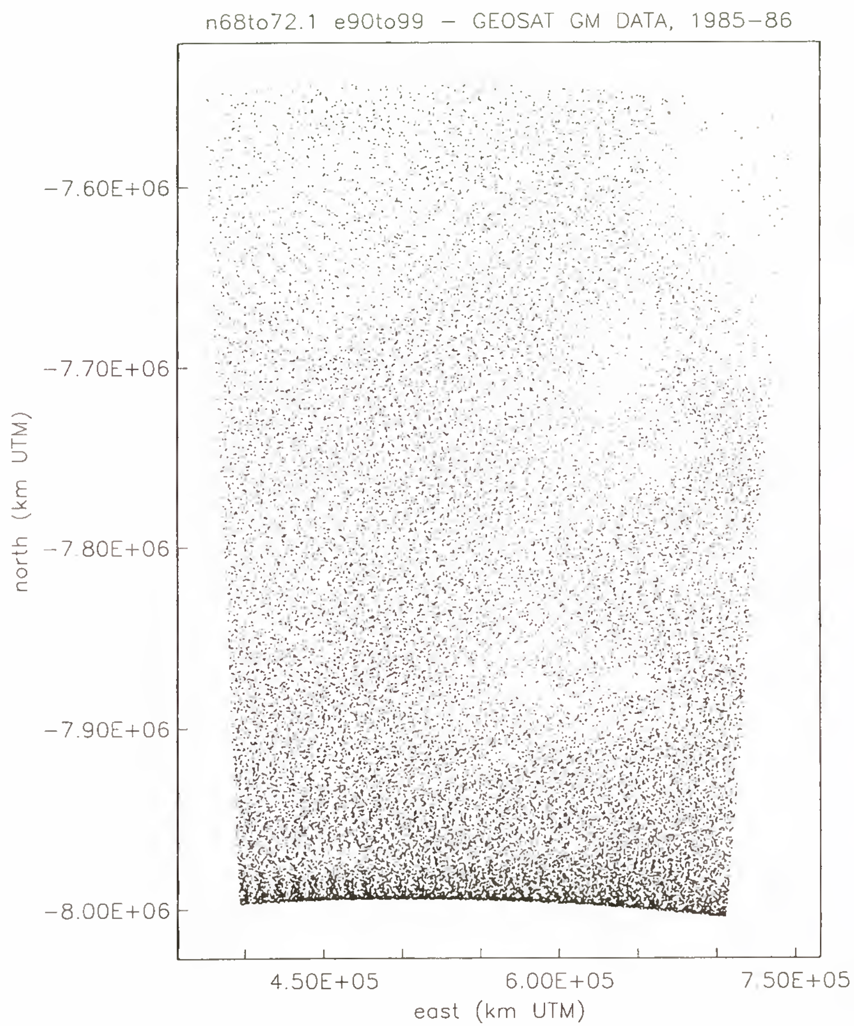

Figure 1

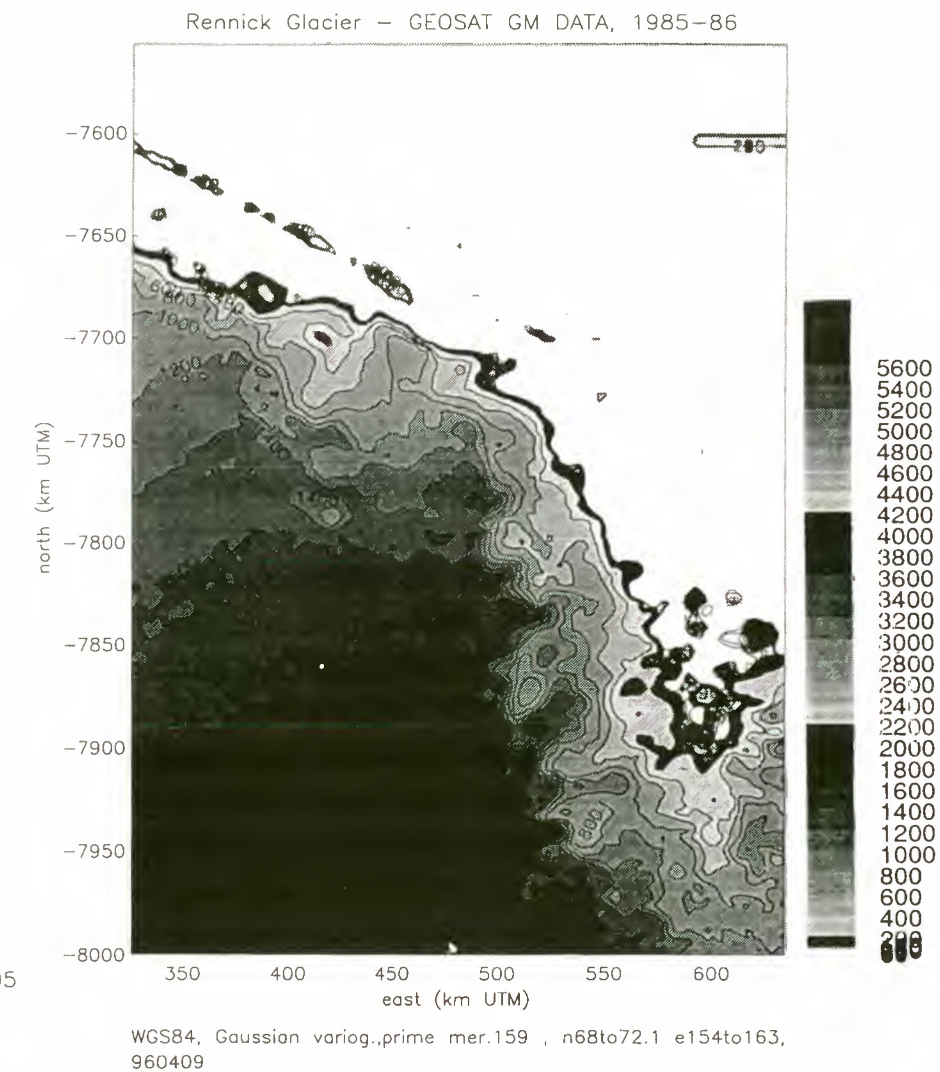

Figure 2

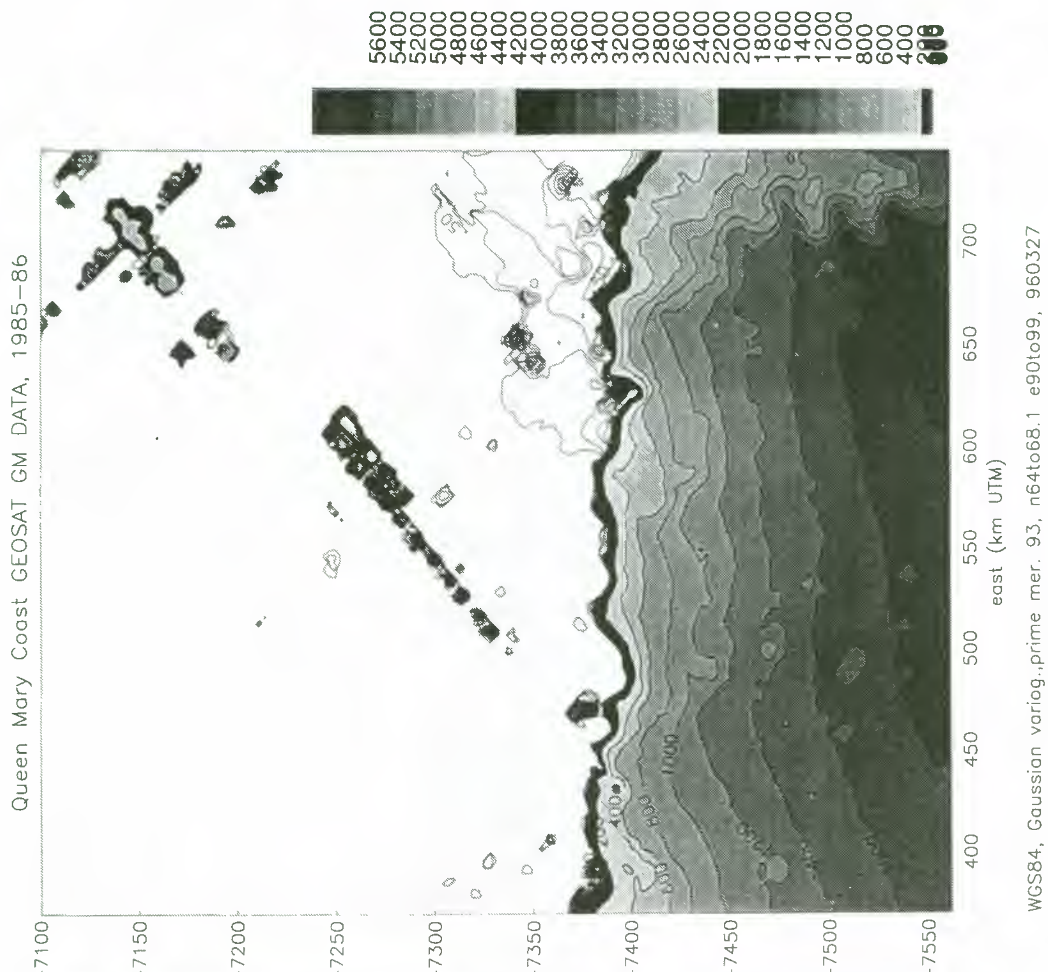

Figure 4

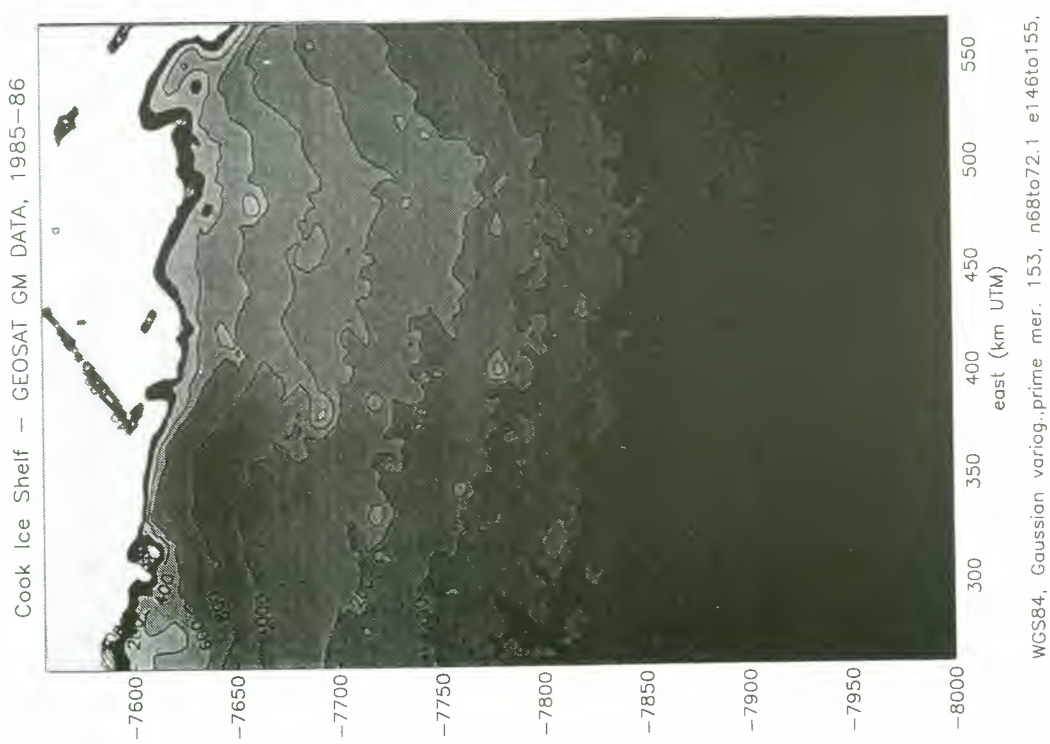

Figure 3

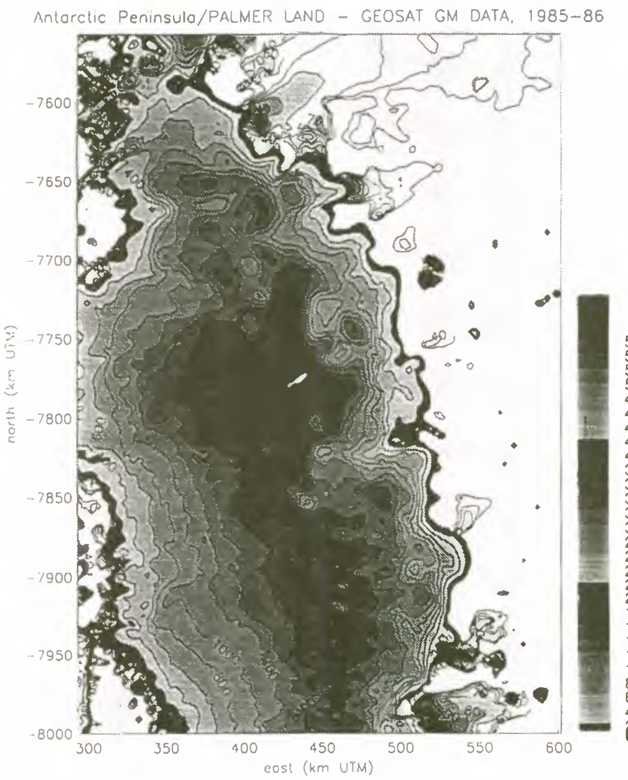

Figure 5 WGS84, Gaussian variog.prime mer 297 0. n68to72 1 e291to300. 950823

REFERENCES

Bamber, J.L., 1994, A digital elevation model of the Antarctic ice sheet, derived from ERS-1 altimeter data and comparison with terrestrial measurements, *Ann. Glaciol.*, v. 20, 48-53

Bindschadler, R.A., (ed.), 1991, West Antarctic Ice Sheet Initiative, Science and Implementation Plan, Proc. of a workshop held at Goddard Space Flight Center, Greenbelt, Maryland, Oct. 16-18, 1990, NASA Conference Publication Preprint, 53 p.

Clarke, G.K.C., Nitsan, U., and Patterson, W.S.B., 1977, Strain heating and creep instability in glaciers and ice sheets, *Rev. Geophys. Space Phys.*, 15, 235-247

Colhoun, E.A., 1991, Geological evidence for changes in the East Antarctic ice sheet (60° -120° E) during the last deglaciation, *Polar Record*, 27, 163, 345-355

Goldstein, R.M., Engelhardt, H., Kamb, B., Frolich, R.M., 1993, Satellite radar interferometry for monitoring ice sheet motion: Application to an Antarctic ice stream, *Science*, v. 262, p. 1525-1530

Herzfeld, U.C., Lingle, C.S. and Lee, L.-h., 1993b, Geostatistical evaluation of satellite radar altimetry for high resolution mapping of Lambert Glacier, Antarctica, *Annals Glaciol.*, 17, 77-85

Herzfeld, U.C., Lingle, C.S. and Lee, L.-h., 1994, Recent advance of the grounding line of Lambert Glacier, Antarctica, deduced from satellite radar altimetry, *Annals Glaciol.*, v. 20 (1994), p. 43-47

Hollin J.T., 1962, On the glacial history of Antarctica, *J. Glac.*, v. 4, no. 32, 173-195

Huybrechts P. 1993, Glaciological modelling of the late cenozoic East Antarctica Ice Sheet: Stability or dynamism?, *Geografiska Annaler*, 75 A, 221-238

Journel, A.G., & Huijbregts, C., 1989, Mining geostatistics, 2nd Ed., Academic Press, London, 600 p.

Meier, M.F. & Post, A., 1987, Fast tidewater glaciers, *J. Geophys. Res.*, 92, B9, p. 9051-9058

Sievers, J., Vaughan, D.G., Bombosch, A., Doake, C.S.M., Heidrich, B., Mantripp, D.R., Pozdeev, V.S., Ritter, B., Sandhäger, H., Schenke, H.W., Swithinbank, C., Thiel, M., & Thyssen, F., 1993, Topographische Karte (Satellitenbildkarte) 1 : 2 000 000 Filchner-Ronne-Schelfeis, Antarktis, Institut für Angewandte Geodäsie (IfAG), Frankfurt am Main

Vaughan, D.G., 1993, Implications of break-up of Wordie Ice Shelf, Antarctica for sea level, *Antarctic Science*, v.5, no.~4, p. 403-408

Zebker, H.A., & Villasenor, J., 1992, Decorrelation in interferometric radar echos, IEEE Trans. *Geoscience and Remote Sensing*, v. 30, no. 5, 950-959

IMAGE ANALYSIS BY GEOSTATISTICAL AND NEURAL-NETWORK METHODS APPLICATIONS IN GLACIOLOGY

Ute Christina Herzfeld[1,2], Oliver Zahner[1], Helmut Mayer[2], Chris A. Higginson[2] and Monika Stauber[1]

[1] Geomathematik, Fachbereich Geowissenschaften, Universität Trier
D-54286 Trier, Germany
Ph: +49 651 201 4611, fax: +49 651 201 3815, e-mail: uch@denali.uni-trier.de

[2] Institute of Arctic and Alpine Research, University of Colorado Boulder
Boulder, Colorado 80309-0450, U.S.A.
Ph: +1 303 492 6198, fax: +1 303 492 6388, e-mail: herzfeld@tryfan.colorado.edu

ABSTRACT

Data from Bering Glacier, Chugach Mountains, Alaska, are used to explore the applicability of neural network techniques in classification of ice surfaces and crevasse patterns. During the 1993-1995 surge, the surface patterns changed rapidly.

Video data repeatedly collected over the ice surface in a survey area in central Bering Glacier are combined with simultaneously collected GPS data. Individual scenes characteristic of certain strain states are extracted from the video and transformed into a format suitable for image analysis on a workstation. In a first pass, a geographical information system (ERDAS) is utilized to test the usefulness of standard approaches, including histograms, cut-off values, Fourier-type filters, image enhancement. It is apparent that the information in the image needs to be reduced prior to classification. The reduction is performed with a fast variogram algorithm sampling in three oblique directions. The resultant vectors provide the input for the neural network.

While the slow movement of a typical Alpine glacier resembles the situation of ductile deformation as it occurs during orogenesis (for instance), the patterns observed during a surge resemble the situation of brittle deformation, as it occurs during crust generation in a slow-spreading oceanic environment. As surge-type glaciers may be considered intermediate in their dynamics between 'normal' (non-surging) glaciers and fast-flowing ice streams, it may be hypothesized that fast ice streams may be analogous to brittle deformation in fast spreading ocean rigde environments.

INTRODUCTION

During spring 1993, Bering Glacier, North America's largest glacier (ca. 200 km from the Bagley Ice Field to the Gulf of Alaska) started a surge (Lingle et al. 1993) that continued through 1995 (last observations from August 1995).
Surging of glaciers is to date a geophysical phenomenon that is not well understood despite a large study of the surge of Variegated Glacier, Alaska (Kamb et al. 1985; Raymond 1987). Apparently, changes in the glacier's hydrological system play a key role. A surge glacier accumulates more mass than it can drain over a number of years, leading to a thickening. During a short phase of rapid movement (one to a few seasons), the glacier advances and loses a lot of its mass until the surge terminates, and the process repeats itself in a quasi-periodic manner. Other than for the much smaller Variegated Glacier, almost no glaciological field data were available, which constitutes both a challenge and a necessity for studies using remote-sensing data (cf. Herzfeld et al., this issue).

EXPERIMENT SETUP

In the summers of 1994 and 1995, video data of the ice surface were collected from small aircraft in a survey area on central Bering Glacier and combined with GPS data recorded aboard the aircraft during survey flights. A GPS base station was operated (in 1994) by the U.S. Geological Survey in the Bering Glacier field camp.
The video data were converted to a format readable by a SUN workstation in a number of hardware and software transformations, and form the basis of the image analysis described herein. This is part of a larger project to develop a new technology for SAR data analysis.

Proceedings of the Fourth Symposium on Remote Sensing of the Polar Environments, Lyngby, Denmark, 29 April – 1 May 1996 (ESA SP-391, July 1996)

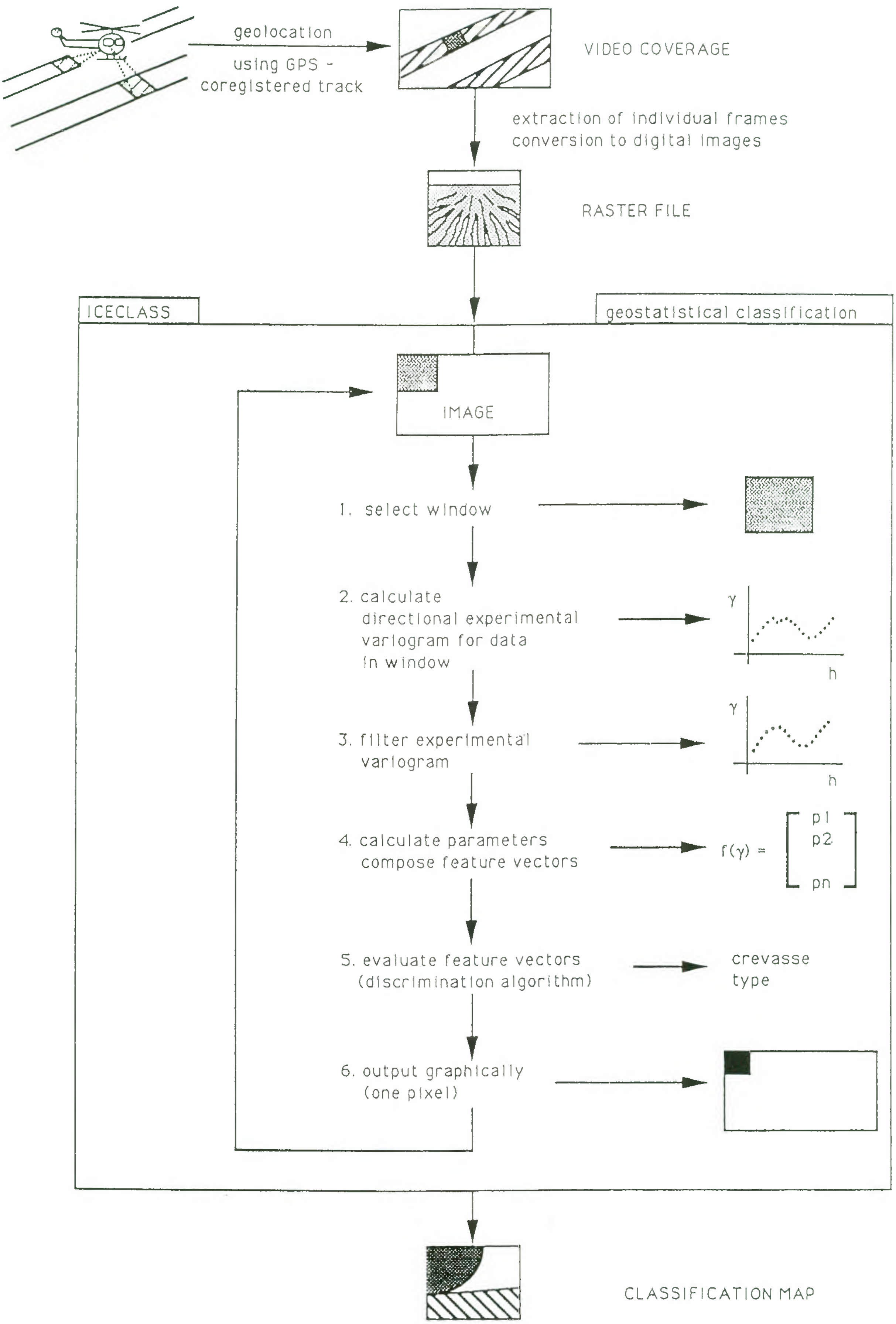

Figure 1: Flow diagram of geostatistical classification with ICECLASS system

STANDARD IMAGE ANALYSIS APPROACH

Before embarking on the development of a new method, we first tested whether standard methods implemented in image-analysis tools may yield satisfactory results. In the following example a Geographical Information System (ERDAS) was used.

Each video scene has three layers, red, green, and blue, of which the green layer data are used. (We employ the light-shadow effect caused by the crevasses, so the other two channels work about as well; however, analysis of one channel is sufficient.) The most promising filter for segmentation or edge-detection purposes was the signum of the Laplace operator based on a 5x5-pixel window, followed by a 7x7-pixel window smoothing. This method enhances the center of the crevasses, but otherwise blurs the picture. All other methods offered in the GIS - of which there are many - blurred the picture rather than simplified it, so are not deemed useful as a basis for classification.
Template matching and texture analysis using a simple co-occurrence matrix were also tested.

Recognition of crevasse patterns from video images requires a procedure that identifies patterns that belong to the same class modulo translation, scaling, and rotation. Consequently, commonly used methods for pattern recognition are not applicable.

A variogram-based approach similar to that of the geostatistical classification system is used. The variogram is particularly suited in this context, because it requires only that the intrinsic hypothesis is satisfied, and works on the increment process.

THE GEOSTATISTICAL SURFACE CLASSIFICATION SYSTEM

The objective of automated surface classification is to employ surface properties such as roughness and anisotropy, and to do so automatically. In the ice surface classification of Bering Glacier, the classes are determined by the strain states in various parts and stages of the surging glacier represented by specific crevasse patterns.

In the geostatistical surface classification system ICECLASS, the surface structures are analyzed by calculating variogram functions in several directions. The variogram is the structure function most commonly used in geostatistics, the theory of regionalized variables (Journel and Huijbregts 1989). Parameters are extracted from variograms, and feature vectors are composed, to which the classes are associated (cf. Fig. 1). The method is described for seafloor analysis in Herzfeld (1993) and Herzfeld and Higginson (1996).

THE NEURAL NETWORK SURFACE CLASSIFICATION SYSTEM

Decision rules in the geostatistical surface classification system are, at this stage, based on a deterministic decision tree. These rules were determined by geological knowledge and extended test phases leading to reformulations and specifications of the decision rules, according to the criteria stated in the previous section.

With an increasing number of feature vector components and with increasing complexity of the surface structures, the knowledge-and-criteria-based approach to decision rules becomes increasingly time-consuming. Therefore, we test the applicability of neural-network methods to replace decision rules.
There are three ways to do this:
(1) Neural nets are simply used to replace the deterministic decision rules that assign a class to the feature vector (neural nets are trained on feature vectors in the geostatistical surface classification system).
(2) Neural nets are trained on images to recognize surface classes.
(3) Neural nets are trained on functions calculated globally for an image.

In the sequel, first results from approach (3) are summarized. The important step in any neural network application is to train a net properly. The information contained in an entire video scene is too much to train a neural net effectively; therefore, it is necessary to come up with a suitable method for information reduction that preserves the surface properties characteristic of a given video scene. One way to reduce the information is to convert the grey-scale image into a binary image. However, the cut-off values had to be determined by investigating the histograms individually per image.

Experimental variograms calculated from the entire image in 3 oblique directions, called x, y, and w over lags of 0-200 pixels constitute the input vectors. Variogram calculation can, of course, be fully automated. Neural nets of different designs are trained on such input vectors derived from simulated crevasse images. A typical learning curve is given in Figure 2, an example of a network in Figure 3.

GLACIOLOGICAL RESULTS FROM STRUCTURAL CLASSIFICATION

A classification of ice surface types from the viewpoint of structural geology, carried out for photographs and

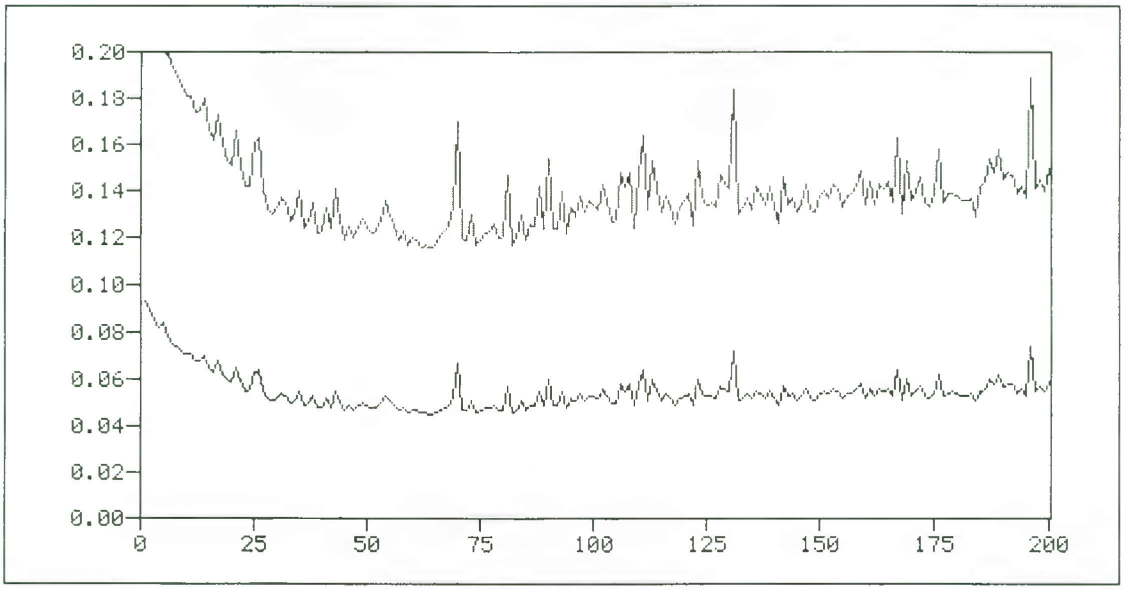

Figure 2: Learning curves for training a neural-network using simulated crevasse patterns

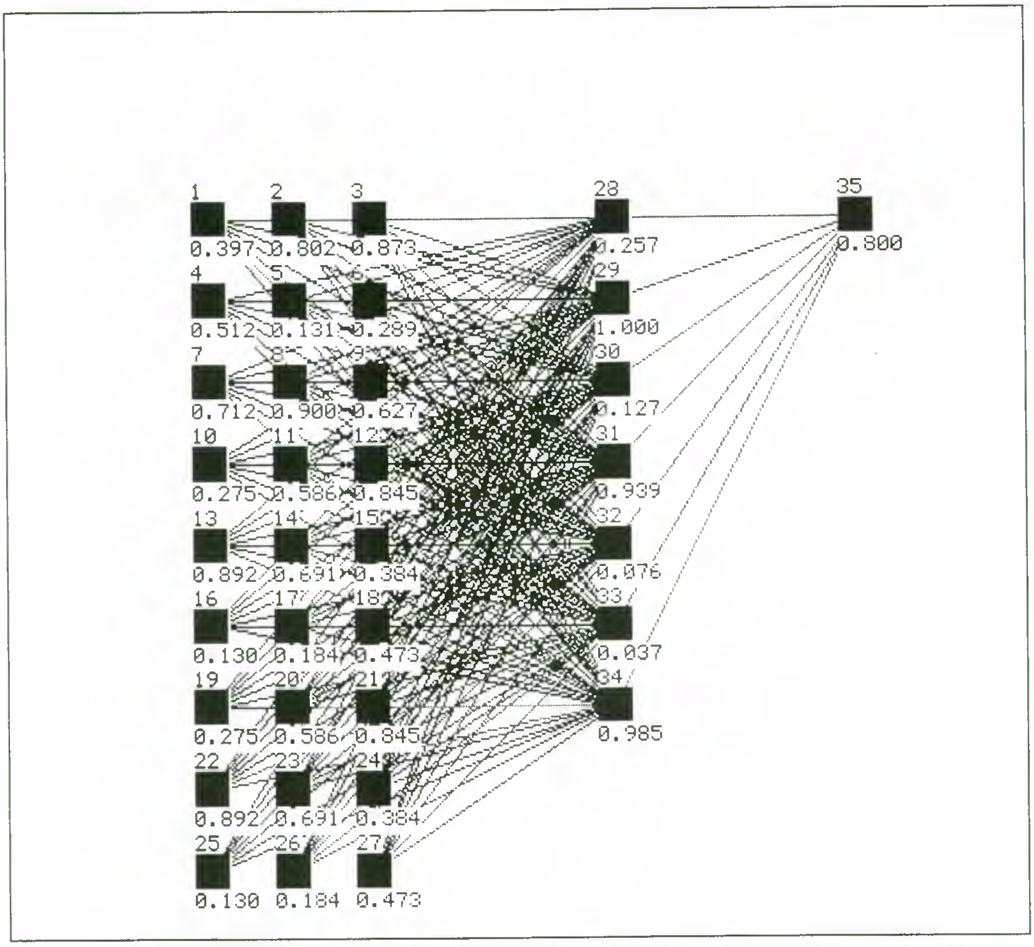

Figure 3: Feed-forward neural-network with one hidden layer, trained using back propagation - momentum term and flat-spot elimination to classify 100 pixel by 100 pixel image (one-directional patterns vs. two-directional patterns).
Above boxes: unit numbers. Below boxes: activations.

video footage of the 1993-1995 Bering Glacier surge, leads to interesting results.

Investigations akin to structural geology have been conducted for Alpine glaciers (e.g. Hambrey and Milnes 1977). The methods in their paper on Griesferner are those used to analyze metamorphic deformation common to orogenesis to study folds and foliations. While the deformation at lower levels of a slowly moving Alpine glacier resembles the geologic situation of ductile deformation under lower-crust conditions, the deformation patterns observed during a surge resemble upper-crustal brittle deformation as occurs, for instance, in slow-spreading oceanic crust at the Mid-Atlantic Ridge. As surge-type glaciers may be considered intermediate in their dynamics between non-surge-type glaciers and fast-flowing ice streams, the question arises whether fast-flowing ice streams may be analogous to fast-spreading ocean ridge environments in their deformation style.

ACKNOWLEDGEMENTS

Funded in part through NASA Office of Polar Programs (grant no. NAGW-3790 to UCH) and Deutsche Forschungsgemeinschaft (Heisenberg Fellowship to UCH).

REFERENCES

Hambrey, M.J. & A.G. Milnes 1977, Structural geology of an Alpine glacier (Griesgletscher, Valais, Switzerland), *Eclogae geol. Helv.*, 70 (3), 667-684

Herzfeld, U.C. 1993, A method for seafloor classification using directional variograms, demonstrated for data from the western flank of the Mid-Atlantic ridge, *Math. Geol.*, 25 (7), 901-924

Herzfeld, U.C. & C.A. Higginson 1996, Automated geostatistical seafloor classification - principles, parameters, feature vectors, and discrimination criteria, *Computers & Geosciences*, 22 (1), 35-52

Herzfeld, U.C., H. Mayer, C.A. Higginson & M. Matassa 1996, Geostatistical approaches to interpolation and classification of remote-sensing data from ice surfaces, *this issue*

Journel, A. G., & C. Huijbregts 1989, Mining geostatistics, 2nd Ed., Academic Press, London, 600 p.

Kamp, B. & 7 others, 1985, Glacier surge mechanism: 1982-1983 surge of Variegated Glacier, Alaska, *Science*, 227 (4686), 469-479

Lingle, C.S., A. Post, U.C. Herzfeld, B.F. Molnia, R.M. Krimmel & J.J. Roush 1993, Bering Glacier Surge and Iceberg-Calving Mechanism at Vitus Lake, Alaska, U.S.A., *J. Glaciol.*, 39 (133), 722-727

Raymond, C.F., 1987, How do glaciers surge? A review, *J. Geophys. Res.*, 92 (B9), 9121-9134

SEA ICE

EARLY RESULTS OF THE USE OF RADARSAT SCANSAR DATA IN THE CANADIAN ICE SERVICE

Bruce R. Ramsay[1] Laurie Weir [2] Katherine Wilson[3] and Matthew Arkett[4]
[1,3,4] Canadian Ice Service
373 Sussex Drive, Block "3E", Ottawa, Ontario, Canada K1A OH3
Ph: (613)-996-4671 Fax: (613)-996-4218
e-mail: ramsayb@aesott.am.doe.ca

[2]Canadian Ice Service
373 Sussex Drive, Block "3E", Ottawa, Ontario, Canada K1A OH3
Ph: (613)-996-1599 Fax: (613)-996-4218
e-mail: weirl@aesott.am.doe.ca

ABSTRACT

The Canadian Ice Service Environment Canada (CIS) is the Government agency responsible for providing ice information on Canada's offshore areas to marine operators. Daily service is provided year-round to a variety of clients. The Canadian Ice Service has been receiving approximately 3 RADARSAT passes daily since early February, 1996. ScanSAR data has been used routinely at the Canadian Ice Centre to monitor ice formation and motion in the Gulf of St. Lawrence, across the Great Lakes and along the Labrador and Newfoundland coasts. Information extracted has been incorporated into ice products; including daily ice charts, bulletins and warnings, and ice forecasts. Image products have been transmitted to Canadian Coast Guard icebreakers and Ice Operations Offices for display and analysis on shipboard workstations. Information extracted from these images has provided icebreaking operations a valuable new tool for ice navigation and ice avoidance. In addition to using RADARSAT fast-turnaround data for routine East Coast operations, data was collected from 12 orbits across the Canadian Arctic. This data is being mosaiced and analysed to form a snapshot of mid-winter ice conditions. These images, charts and derived information will be published in the Arctic Winter Ice Atlas by June. This data is used to establish the ice regime across the Arctic prior to the summer navigational season.

1. INTRODUCTION

Canada's RADARSAT was launched on November 4th, 1995 from Vandenberg Air Force Base, California. The Canadian Ice Service is the main user of fast-delivery data from the onboard C-band Synthetic Aperture Radar (SAR). This data will largely replace the X-band radar data previously collected by reconnaissance aircraft (Ref 1). The product of most interest to CIS is the ScanSAR Wide georeferenced (SCW) product. It has the best combination of swath width (500km) and resolution (100m with 50mx50m pixel spacing) for synoptic ice monitoring (Ref 2). Additionally, ScanSAR narrow georeferenced (SCN) data (300km swath width and 25mx25m pixel spacing) is acquired for tactical support purposes on behalf of the main marine client - the Canadian Coast Guard. Already, in excess of 1 gigabyte of RADARSAT per day is being processed and delivered to the Canadian Ice Service.

2. END-TO-END DATA ACQUISITION

Canada has two receiving stations for RADARSAT data - at Gatineau, Quebec and at Prince Albert, Saskatchewan. CIS orders data acquisitions from these stations through a on-site node of the Mission Control Order Desk System (ODSys). All data is processed into image products at the Canadian Data Processing Facility (CDPF) at Gatineau, Quebec. An Anik satellite link is used to move signal data from the Prince Albert site to Gatineau prior to processing. The processed data is received at the Ottawa Ice Centre by means of a dedicated T1 digital connection - the Image Transfer Network (ITN). Turn-around is guaranteed under contract with RADARSAT International (RSI) to be less than 4 hours from data acquisition (Ref 3).

The Ice Services Integrated System (ISIS) is used to process, display, and analyse RADARSAT SAR data received across the ITN. Each image is georeferenced to a Lambert Conformal projection and enhanced to improve visual interpretability. The images can then be individually displayed and analysed, or "tiled" together and integrated with other image, chart or alphanumeric data. The interpretation of imagery is performed visually by experienced ice analysts within this integrated display environment. The GIS capabilities of the system are then used to produce the final "ice chart" familiar to many marine operators, in addition to a variety of other image and map products. These products are then relayed to a variety of marine customers by means of satellite, cellular phone and land line links. The major customer of CIS is the Canadian Coast Guard (CCG). All major icebreaker vessels and the Ice Operations Offices are equipped with Ice-Vu systems for capture and display of RADARSAT and ancillary data. Out in the field, Ice-Vu is used to extract information from the imagery to assist the ship's

Proceedings of the Fourth Symposium on Remote Sensing of the Polar Environments, Lyngby, Denmark, 29 April – 1 May 1996 (ESA SP-391, July 1996)

Captain in making navigation decisions.

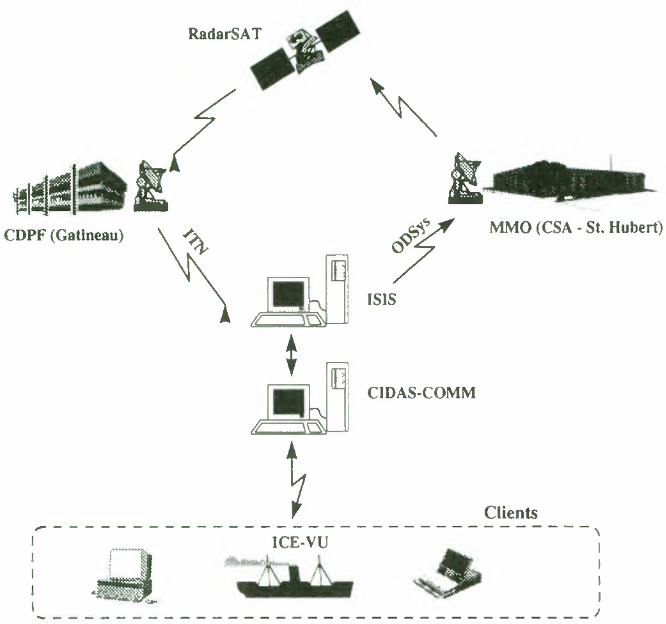

Figure1. Schematic of end-to-end Radarsat data acquisition, processing, product preparation and delivery.

3. PERFORMANCE

The following table delineates the processing performance for RADARSAT images to date. RSI had agreed contractually that it would deliver a RADARSAT pass to the Ice Centre within four hours. An efficient ITN transfer link has seen passes being delivered in just under half the contractual agreement.

The implementation of block-averaging saw ISIS processing times improve drastically and compliment the quick CDPF delivery time. As a result, the Ice Centre is provided with an excellent total turnaround time with aspirations of further improvement.

	Average Time
1. ISIS PROCESSING TIME	
- Before Block Averaging	1:36:19
- After Block Averaging	0:24:09
2. CDPF DELIVERY TIME	1:55:35

* Time shown for ISIS Processing is the total time taken to process one full frame

* Time shown for CDPF Delivery is the total time taken to send one pass via the ITN link

(Average pass = 3-4 frames)

4. IMAGE QUALITY

The RADARSAT ScanSAR wide and narrow products are comprised of 4 separate beams processed together to create the 300 to 500 kilometre products. The data received to date has been a challenge to analyse because of the dark to light banding seen from beam to beam. The integration of these beams to create a smooth image and to provide consistent signatures across the RADAR image is presently being studied and corrected.

It has also been seen that similar ice types will have very different spectral signatures within each beam due to the varying incidence angles of each beam and distance from the sensor. For visual analysis purposes the first 75 KM in the near range of the swath is saturated to such a degree that it is not normally used. Digital numbers in the near range beam, are extremely high and saturate the image. At the far range, the digital numbers and dynamic range are very low causing little contrast between ice and water requiring interpreters to be aware of these limitations.

5. CASE STUDIES

Our initial experiences working with RADARSAT imagery has shown the data to be an important and beneficial new tool for providing icebreaking operations with ice information for navigation and ice avoidance.

Case 1

RADARSAT imagettes (a 1 MByte jpeg compressed subset of the 500 by 500 km RADARSAT scene) are routinely sent to the Canadian Ice Services bulletin board using the ISIS system . They can be downloaded by our Canadian Coast Guard Clients using the Ice-Vu workstation. On March 6 1996 a Gulf of St. Lawrence ScanSAR Narrow 10z pass was captured, processed, analysed and an imagette was available for downloading on the bridge of the Canadian Coast Guard ship Terry Fox to aid her in her escort of the MV Medallion from the Cabot Strait to the Bay of Chaleur. (Figure 2) The main shipping route at that time would have taken the ships north of the Magdelan Islands and into Chaleur Bay. The RADARSAT ice information contained in the imagette and accompanying RADARSAT analysis indicated easier ice conditions on the route south of the Magdelan Islands. (Figure 3 and 4) With this timely ice information the captain of CCG ship Terry Fox decided to complete her escort of the MV Medallion using a route south of the Magdelan Islands thus expediting the escort of the MV Medallion to Chaleur Bay.

Although RADARSAT was still in its commissioning phase at this point in time, this case is indicative of RADARSAT 's utility to maritime navigation. It is expected that the use of RADARSAT ScanSAR imagery onboard the Canadian Coast Guard ships in the form of imagettes will become part of the standard suite of ice products issued by the Canadian Ice Service.

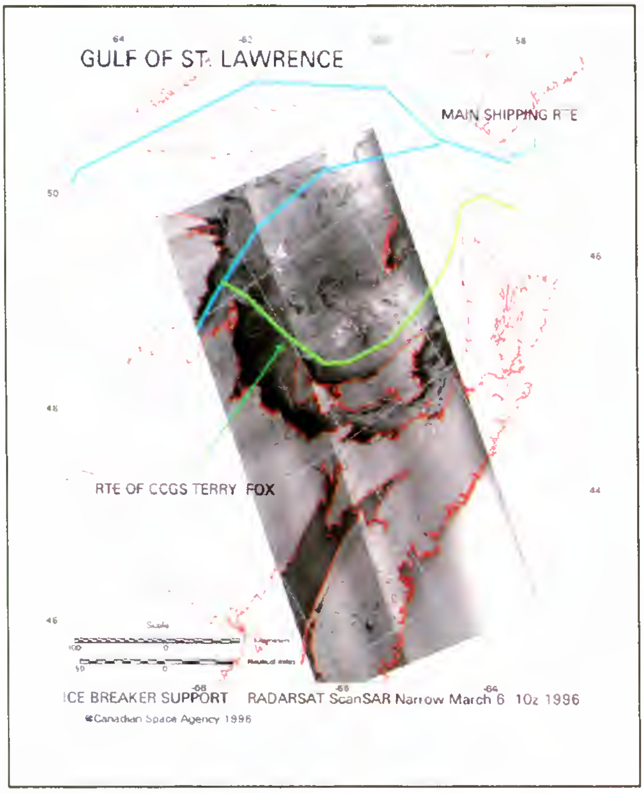

Figure 2 CCGS Terry Fox Transit of the Gulf of St. Lawrence Using ScanSAR Narrow RADARSAT March 6 10z 1996

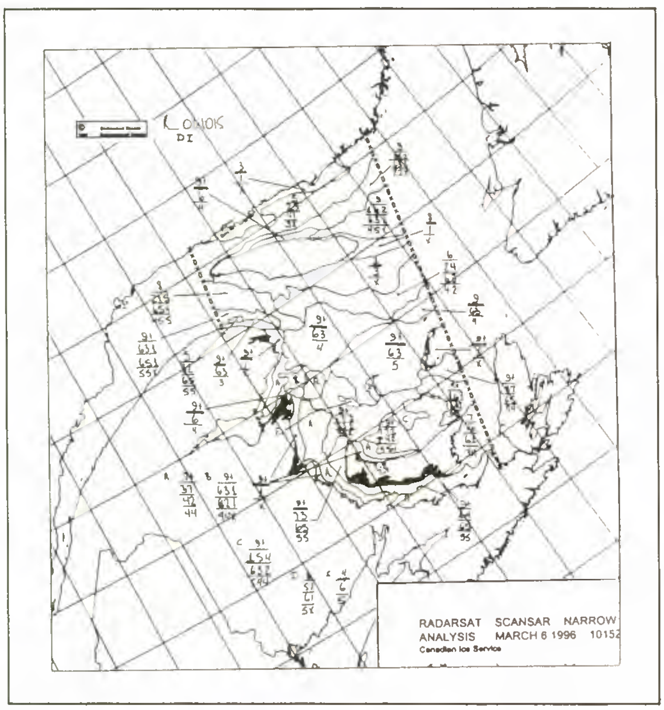

Figure 4 RADARSAT Imagery Analysis Chart sent CCG Terry Fox March 6 1996

Case 2

RADARSAT ScanSAR data is not used as a stand alone data set but is an important component of the suite of data sources used to monitor ice formation, motion and break-up. Included in the suite of data sources are ice observations from helicopters, aircraft reconnaissance, airborne SLAR observations, NOAA AVHRR, SSMI, and ERS1. During the winter months the operations division of the Canadian Ice Services is responsible for issuing daily ice charts, forecasts and warnings for the Gulf of St. Lawrence, the East Newfoundland, Labrador Coast, Davis Strait and the Great Lakes. All are ice covered waterways used by maritime transportation and fishing companies. Our early experiences with RADARSAT as part of this suite of data sources has been very positive. It was relied on extensively to monitor the break up of the Great Lakes this March and April. With the opening of the Eisenhower locks on March 28 1996, the Welland Canal on March 29 and the St. Lawrence Seaway on April 2 more than 55 ships were expected to be transiting the Great Lakes at the start of the shipping season. Many commercial shipping companies had requested ice charts and forecasts be provided to them on a daily basis. During the 2 weeks leading up to the opening of the St. Lawrence Seaway 16 orbits were ordered and analysed. The ice information extracted from these images was incorporated into the daily ice chart (Figure 5) and was provided to commercial shipping on a cost re-covery basis. RADARSAT imagettes were provided to the Canadian Icebreaker Pierre Radisson and the American Icebreaker Mackinaw working to open the shipping lanes of the Great Lakes. (Figure 6 & 7)

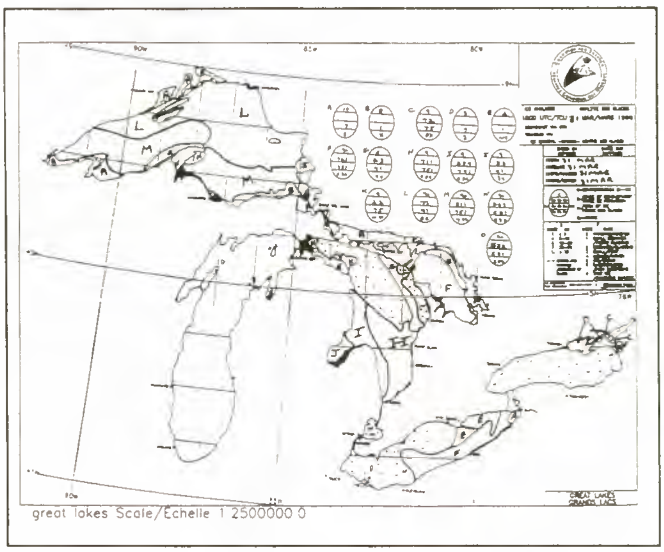

Figure 5 Daily Great Lakes Ice Chart , March 31, 1996

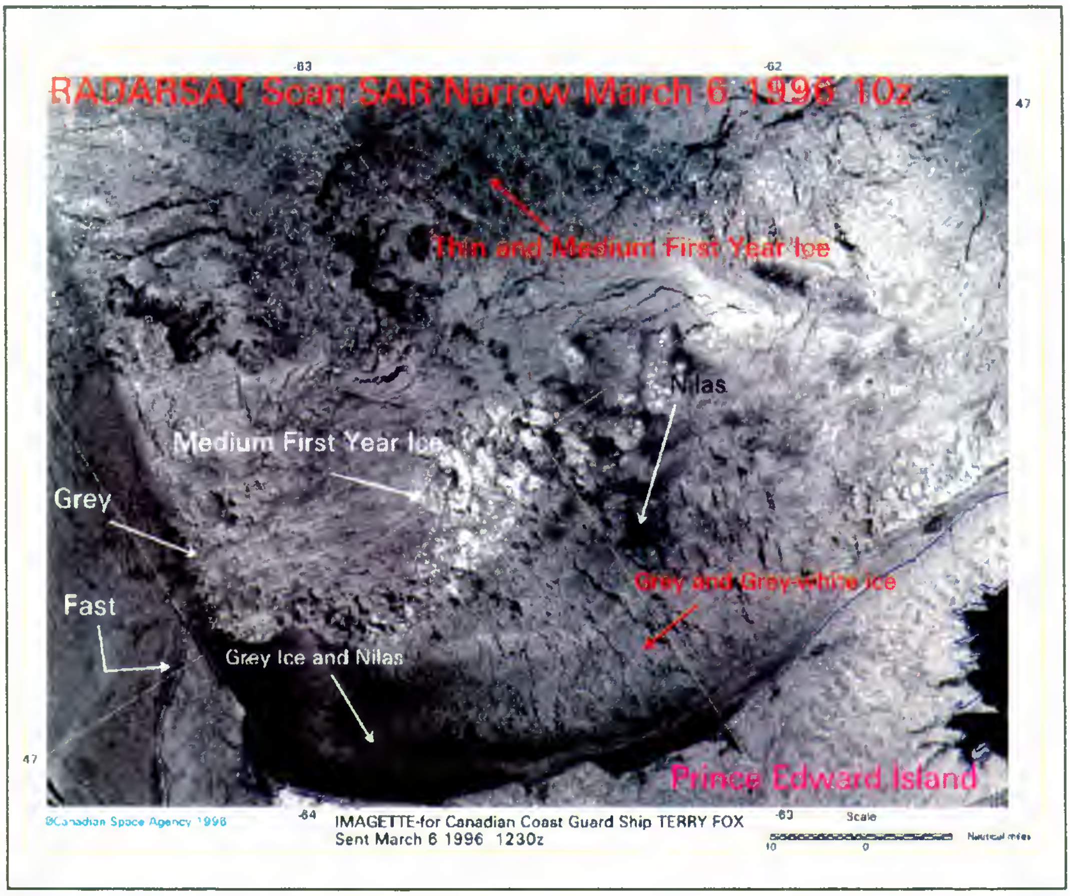

Figure 3 Shipboard imagette sent to CCG Ship Terry Fox March 31, 1996 1230z

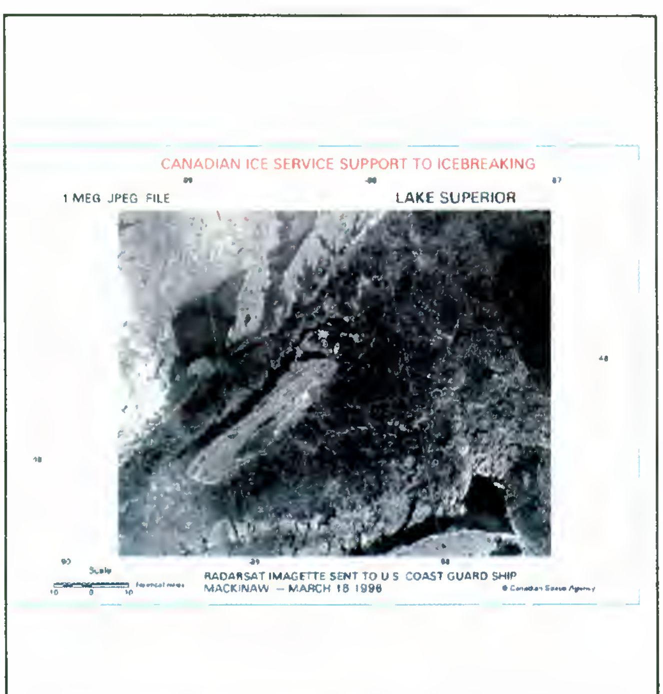

Figure 6 RADARSAT imagette sent to U.S. Coast Guard Ship Mackinaw, March 16, 1996

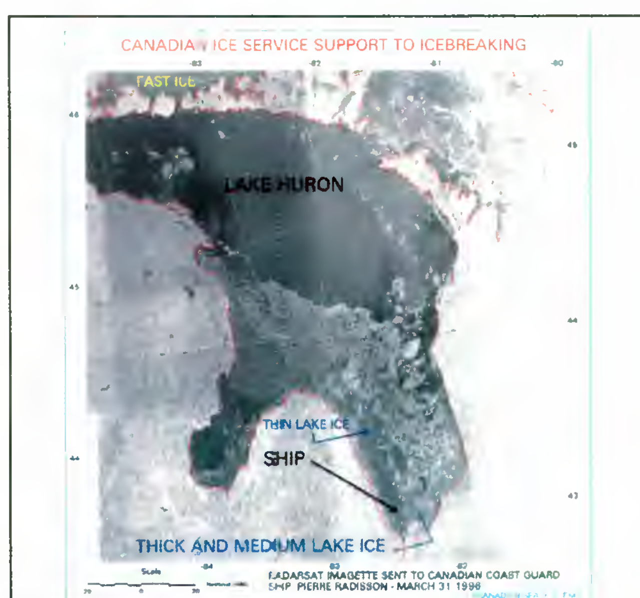

Figure 7 RADARSAT imagette sent to CCG Pierre Radisson, March 31, 1996

Case 3

RADARSAT ScanSAR imagery, in addition to its routine use in the operational areas of the East Coast and Great Lakes, was used as the principle data source for the 1996 **Arctic Winter Ice Atlas**. (Figure 8) The Atlas is a detailed analysis of winter ice conditions using SAR imagery that has been carried out since 1986. The series represents an important climatological ice archive and will provide ice information to marine operations in the forthcoming 1996 Arctic Shipping Season. In previous years up to 10 aerial missions have been flown over a 2 week period to image the ice. Last year ERS1 imagery was used for the first time to compliment the aircraft SAR imagery. However the very narrow swath width of the ERS1 made the mosaicing and analysis of the data difficult and time consuming. So it was with great anticipation that the CIS looked to using the 500 Km swath width of ScanSAR wide. This year instead of aerial SAR missions, 12 ScanSAR wide orbits were ordered, captured, mosaiced and analysed at a significant cost savings. The resulting album will form a mid-winter snap shot of the ice conditions in the Canadian Arctic for the period Feb 12-15 1996. It will be an important planning tool for government departments, federal agencies and commercial sector clients planning on working in the Arctic this summer.

6. FUTURE PLANS

The Canadian Ice Services will continue to build and improve upon the infrastructure necessary to deliver fast turn around RADARSAT ice products to its clients. A communications package called CIDAS-COMM will allow each icebreaker to input a "standing order" of RADARSAT imagery and ice products they wish to have downloaded daily to their shipboard mail boxes.

RADARSAT imagettes will be available to commercial clients through a partnership with the private sector and RSI, at an attractive price for the marine community.

Daily ice charts valid at 18z will become RADARSAT image analysis charts valid at the time of the RADARSAT image pass over each operational region.

The large volume of RADARSAT data available to the Canadian Ice Service has prompted the CIS to fund the development of systems employing algorithms to automatically extract ice information (ice motion, edge, concentration classification, etc.) (Ref 4). If these system prove themselves the goal is to have automatically-generated ice information products in a variety of formats and presentations.

7. REFERENCES

1. Ramsay, B., Hirose, H. *et al*: "Potential of RADARSAT for Sea Ice Applications", Canadian Journal of Remote Sensing, Volume 19, No. 4, pp. 352-362, November-December, 1993
2. Ramsay, B., Manore, M., Porter, K., Bretz, T. and Clark, K. (1994), "RADARSAT Simulations of Sea Ice Monitoring Image Products", proceedings of the Second Thematic Conference, Remote Sensing for Marine and Coastal Environments, New Orleans, USA, 31 January-2 February, 1994
3. Whitman, J., Ramsay, B., Hirose, T., McCully, P., Lapp, D., Zilinskas, V.: "Simulation of Ice Applications Requirements and Ground Segment Performance", Canadian Journal of Remote Sensing, Volume 19, No. 4, pp 363-371, November -December, 1993
4. Ramsay, B., Hirose, T., Heacock, T. and Walton, A.: "Automatic Synthetic Extraction Algorithms for Sea Ice Applications", proceedings of the International Geoscience and Remote Sensing Symposium (IGARSS)'94, Pasadena, USA, 8-12 August, 1994

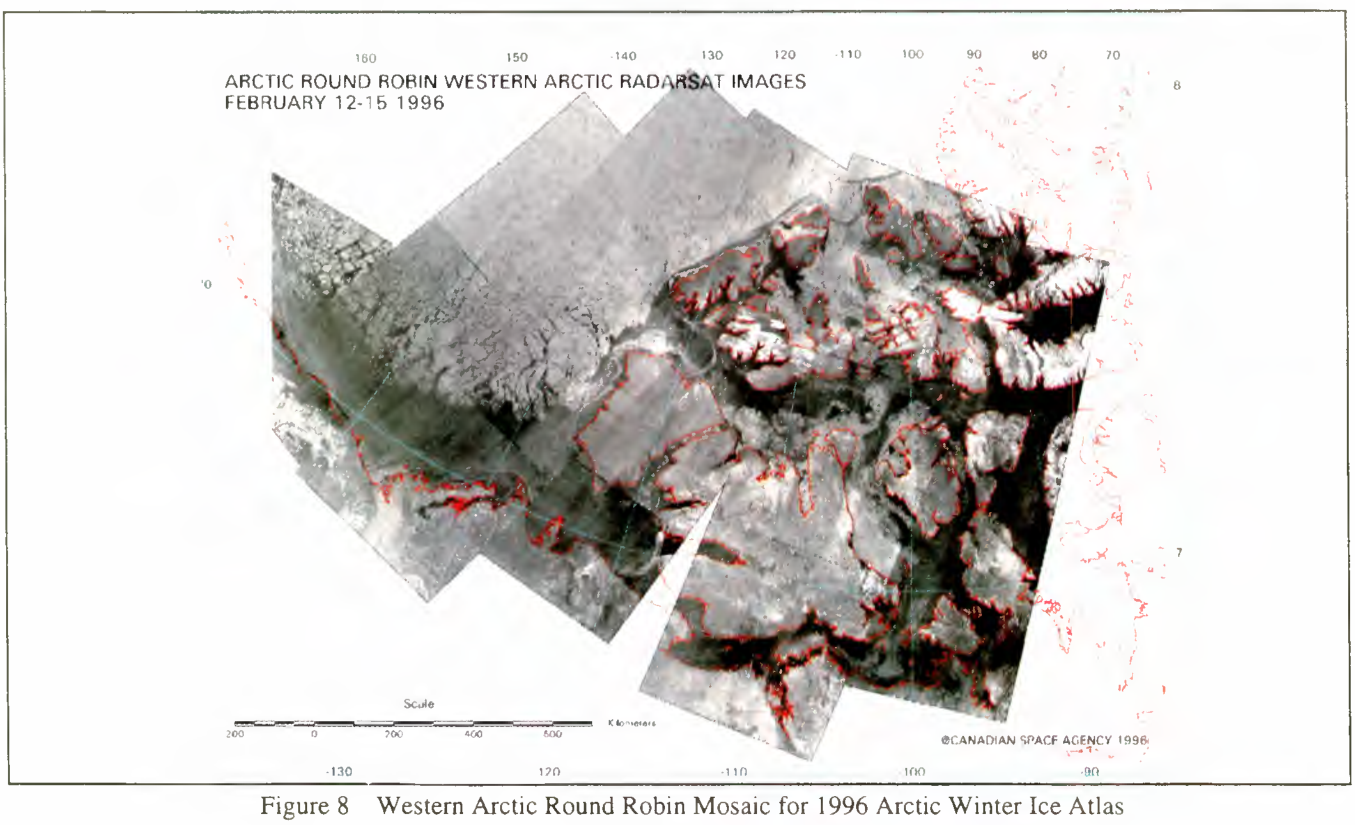

Figure 8 Western Arctic Round Robin Mosaic for 1996 Arctic Winter Ice Atlas

RADARSAT STATUS AND EARLY EXPERIENCE IN SEA ICE APPLICATIONS

Michael Manore[1] and Bruce Ramsay[2]

[1] Canada Centre for Remote Sensing, 588 Booth St., Ottawa, Ontario, Canada, K1A 0Y7
Ph.: +1 613 947 1281, fax: +1 613 947 1385, e-mail: mike.manore@ccrs.nrcan.gc.ca

[2] Ice Services Environment Canada, 373 Sussex Dr., Ottawa, Ont. Canada, K1A 0H3
Ph.: +1 613 996 46 71, fax: +1 613 996 42 18, e-mail: ramsayb@aesott.am.doe.ca

Canadas RADARSAT satellite was launched in November of 1995 and has since been undergoing extensive commissioning. While full operational capability is not expected until the early summer of 1996, the image quality and its suitability to a number of applications has been examined using early commissioning data.The purpose of this paper is to report on the results of RADARSAT system commissioning and early near-operational experience and validation activities for sea ice applications in Canada.

The Canada Centre for Remote (CCRS) and Ice Services Environment Canada (ISEC) are jointly involved in the early qualification of RADARSAT data for operational sea ice reconnaissance in Canada. ISEC has been receiving a limited amount of RADARSAT data in a pre-operational mode, which has permitted the end-to-end testing of fast delivery systems and the examination of the information content of the imagery. CCRS is the lead agency in the RADARSAT Validation Program, which has included two field validation experiments for sea ice applications. A summary of these activities will be provided.

SEA ICE DRIFT IN THE EAST GREENLAND CURRENT

Thomas Martin
Alfred Wegener Institute for Polar and Marine Research
P.O. Box 12 01 61, D-27515 Bremerhaven, Germany
phone: +49 471 4831 501, fax +49 471 4831 425

ABSTRACT

The sea ice drift is one of the key parameters in the fresh water flux of the East Greenland Current. Satellite data are a good data source for monitoring the sea ice drift velocity. An automatic drift algorithm is employed and optimized to work with AVHRR data. This investigation covers the years 1993 and 1994. Seasonal and spatial distributions of the sea ice drift were derived. The maximum drift velocities occur during the period from October until December in the Fram Strait area. The sea ice mass fluxes in the Fram Strait area are twice as large as at $75°N$. The flux has an annual maximum in the time between Oct. and Dec. with approximately 0.1 Sv.

1. INTRODUCTION

Sea ice plays an important role in the climate system. The distribution of sea ice and open water in the polar regions influences the general atmospheric and oceanic circulation. The long-term mean drift in the Eurasian sector of the Arctic is dominated by the Transpolar Drift Stream, motion of ice from along the Siberian coast across the North Pole through Fram Strait. The ice export out of Fram Strait is the most prominent fresh water stream in the Arctic. The ice coverage and the sea ice drift in the Nordic Seas are key parameters for an improved understanding of the convective processes in this region.

Our knowledge of the large-scale motion of Arctic sea ice is largely based on observations from ships, drifting ice stations and arrays of automated buoys. Nevertheless, all these methods provided only a restricted picture of the velocity fields in the Fram Strait area and in the East Greenland Current due to the small number of simultaneous measurements. An extensive number of ice drift buoys was deployed in the central Arctic within the scope of the International Arctic Ocean Buoy Program. A large number of these drifters passed through the Fram Strait. However, these mostly represent conditions in the center of the current. The shear zone and the extended regions of fast ice in the northern part of the East Greenland Current are less represented in this data set. Therefore it could be assumed, that the mean ice velocities with up to 30 cm/s during winter time and 15 cm/s in the summer are overestimating the drifting sea ice in this region (Martin and Lemke, 1995). Remote sensing data are the primary source of information on the high-frequency temporal and spatial variability of sea ice in the polar regions. In this study satellite data are used for ice drift calculations.

During the past, several authors introduced automatical algorithms which derive the sea ice motion from pairs of satellite images. All these algorithms detect the displacement of features in pairs of images. These techniques have been applied to data from different sensor types. The strategy of algorithms like these from Ninnis et al. (1986) or Fily and Rothrock (1987) are based on the calculation of the area cross correlation and were applied to SAR and AVHRR images. It must be emphasized that these techniques are insensitive to rotation and deformation. Kwok et al. (1990) introduced an improved tracking algorithm for SAR images which involves special feature matching routines.

Our goal was to derive the large scale-sea ice drift in the East Greenland Sea for a longer period. Our contribution to the European Subpolar Ocean Programme (ESOP) was the determination of the large-scale sea ice drift from 1993 to 1994. The improved knowledge of the large-scale sea ice drift is utilized to derive the sea ice mass flux and should provide an estimate of the fresh water flux into the East Greenland Sea.

2. ICE MOTION CALCULATIONS

We employed and optimized the sea ice drift algorithm according to Fily and Rothrock (1987) to work with AVHRR data in the area of the East Greenland Current. The Danish Meteorological Institute provide us with daily AVHRR images projected into a Lambert Conformal conic projection (Nielsen and Valeur, 1994 and 1995; Skriever, 1991). To archieve satisfactory results the drift algorithm requires additional information about the locations of cloud-free areas as well as the ice edge position. Information about the ice distribution was prescribed by the 40% isoline derived from ice charts based on SSM/I images. The cloud masks were derived from the AVHRR images by an experienced operator. The algorithm works with the data of the channels in the visible spectral range as well as with the data from the thermal infrared.

A comparison between the results of the automatic drift calculations with the results derived interactively by human eye yields a good agreement. However, the automatic method derives a much more homogeneously distributed drift field. The AVHRR images have a horizontal resolution of 1.1 km. Best results could be archieved with image pairs with a time difference of 24 respectively 48 hours. Assuming no errors in the algorithm and no error in the geocoding of the images, this results in a minimal error in the velocity field of 0.013 m/s (0.006m/s) derived for images with an interval of 24h (48h). An accuracy in

Proceedings of the Fourth Symposium on Remote Sensing of the Polar Environments, Lyngby, Denmark, 29 April – 1 May 1996 (ESA SP-391, July 1996)

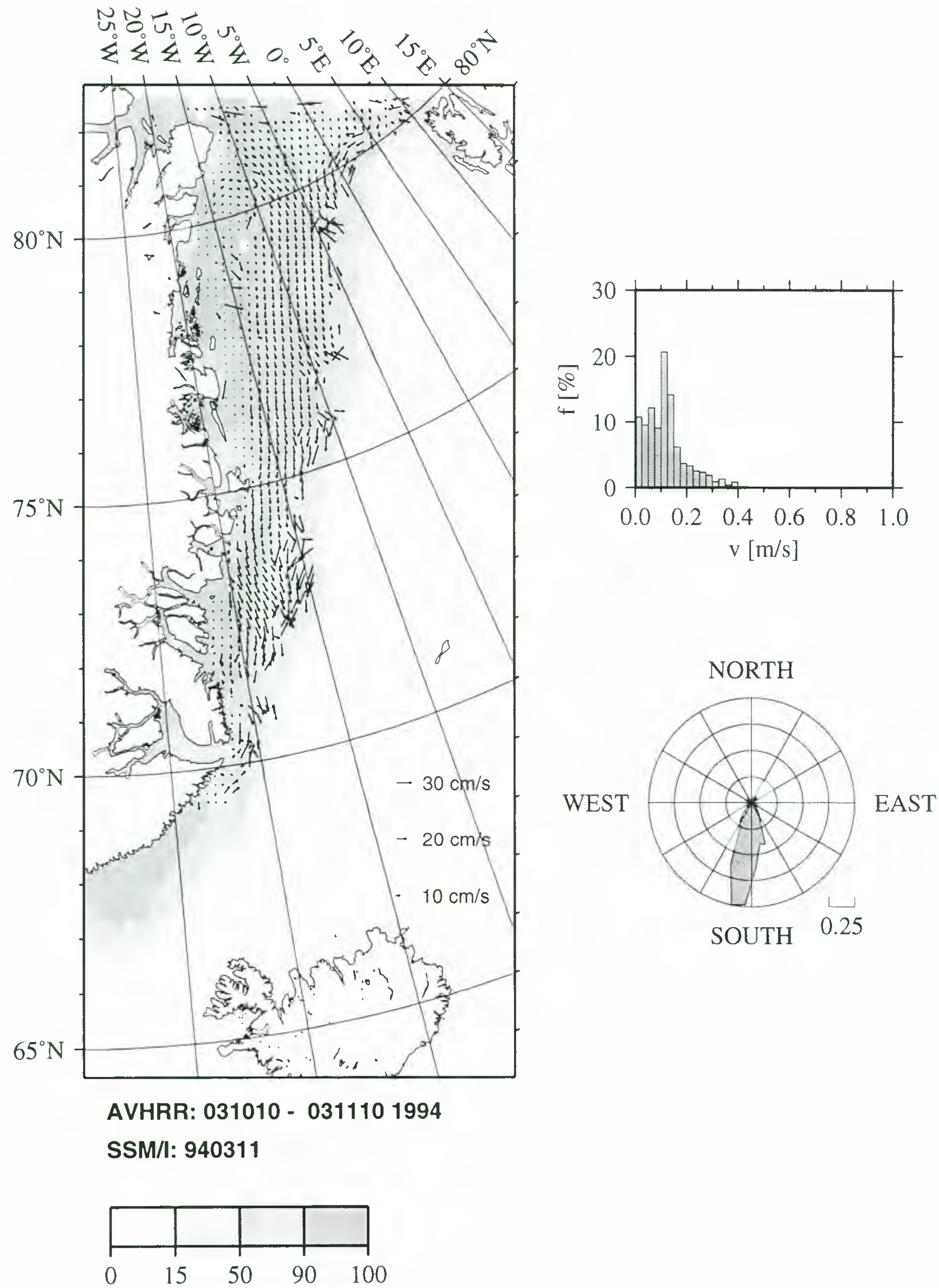

Figure 1: Sea ice drift calculation with two AVHRR images from March 10 and 11, 1994. Left: Sea ice drift field shown as vectors, background - sea ice concentration derived from SSM/I data. Top right: Histogram of the drift velocity. Bottom right: Normalized rose diagram of the drift velocity.

the navigation of the satellite images better than 5 pixels should yield sufficient results for the velocity fields. Contrary to our first tests, we discovered after processing the year 1993 that the accuracy in the satellite navigation was not sufficient to archieve high-quality results. A large number of these images have large errors in the navigation, especially in the northern part in the area of the Fram Strait. To increase the accuracy this error was corrected with a special image processing tool. This tool warps on the basis of tie points one image to a second image. This procedure yields high quality results.

The information on the cloud distribution and ice edge position were derived for the period 1993/94. The drift algorithm was applied to pairs of images covering the whole period of the investigation. Table 1 gives an overview of the amount of the drift calculations. The horizontal coverage of the results for ice drift data is restricted because of the high amount of clouds. It should also be mentioned, that most of these cases represent the sea ice drift in parts of the East Greenland Current. By constructing composites, we can partly overcome this and obtain greater coverage of the velocity fields. Fig. 1 shows an example of a calculated sea ice drift field in the East Greenland Current.

Period	1993	1994
Jan. - Mar.	14	18
Apr. - Jun.	24	38
Jul. - Sep.	21	25
Oct. - Dec.	21	14
Total	80	95

Table 1: Seasonal distribution of sea ice drift calculations in the years 1993 and 1994.

3.RESULTS

The sea ice extent of the East Greenland Current was less developed during 1993 and 1994 as compared to the long-term average. Nevertheless the results of the drift calculations show a number of processes and phenomena. During the winter time extended areas of sea ice with zero or only very small velocities are located along the coast between $75^{\circ}N$ and $81^{\circ}N$. These fast ice regions occur periodically during winter time along East Greenland. The ice drift from different directions converges in the area of the Fram Strait, resulting in a large zones of strong convergence and shear. Between $80^{\circ}N$ and $81^{\circ}N$ in front of the coastline parts of an eddy mark the area of the Northeast Water Polynya with drift directions to the North parallel to the coast and East directed normal to the coast.

As seen in Fig. 1 in some cases single vectors indicate an ice drift contrary to the homogeneous drift field. This may have different causes. Local eddies near the ice edge could force single floes, these drift patterns are often observed near the ice edge and have only a short life time. Test calculations have shown, that ice edge processes are well described by the algorithm. On the other hand, it could be possible, that small cloud and fog patches irritate the algorithm. However, since we are interested in the large-scale sea ice drift field, these local effects have to been neglected by considering merely seasonal means.

Fig. 2 shows the seasonal variability in the zonal structure in the sea ice drift in the northern part of the current. The zonal velocity component shows no significant seasonal and spatial structure. The lateral distribution of the meridional velocity components varies with the distance to the coast as well as with the season. The meridional sea ice drift is smallest during the summer (Jul. - Sept.) and rises to a maximum in autumn (Oct. - Dec.). During the summer, when the fast ice has its smallest extent, a branche of the current directed to the North appears between the coast and $12^{\circ}W$. During onset of the freezing period the fast ice region becomes more solid. To the East follows a zone with a high zonal velocity gradient which results in strong shear. The local velocity maximum lies near the ice edge between $4^{\circ}W$ and $1^{\circ}W$. The absolute velocity maximum occurs during the autumn with near free-drift conditions and strong forcing by northerly winds. These high drift velocities have not been observed during any other season. The zonal distribution of the sea ice drift velocity is transferable to other latitudes, although mostly the fast ice belt along the coast is less developed. The large inhomogeneous ice drift velocity field requires the simultaneous measurement of the current at different locations.

Fig. 3 shows the meridional distribution of the velocity components. The meridional velocity component is at all latitude smallest during the summer and largest during the autumn months. Although the largest individual velocity values are reached in the northern part of the area, the mean velocity increases with distance to Fram Strait and reaches a maximum between $76^{\circ}N$ and $70^{\circ}N$.

4. CONCLUSIONS

To compare the results retrieved from the remotely sensed data, the drift velocities are combined with data of the ice extent and an assumption about the ice thickness to reformulate the results in terms of a mass flux estimate. The retrieved drift data allow a first estimate of the sea ice mass flux. The mass flux is the product of the sea ice drift velocity, the ice extent, the ice concentration and the ice thickness. The ice extent and ice concentration are derived from SSM/I brightness temperatures from CD-ROM data as delivered by the NSIDC. Unknown is the seasonal and local ice thickness distribution. Table 2 gives an overview of the estimated ice mass flux under the assumption of a mean ice thickness of 2.2m respectively 3.0m. The largest ice fluxes occur during the autumn. The flux through $79^{\circ}N$ is approximately twice of the flux through $75^{\circ}N$. During the summer months the flux is reduced by a factor of ten compared to the autumn in the area of Fram Strait.

This investigation has shown, that remote sensing data are a good data source for monitoring the large-scale sea ice drift in the East Greenland Current. Despite the high amount of clouds, the seasonal mean values are reliable over the whole current. The combination with other data sets allows an estimate of the seasonal and local sea ice mass distribution. The next steps should be a combination of the drift data with more realistic sea

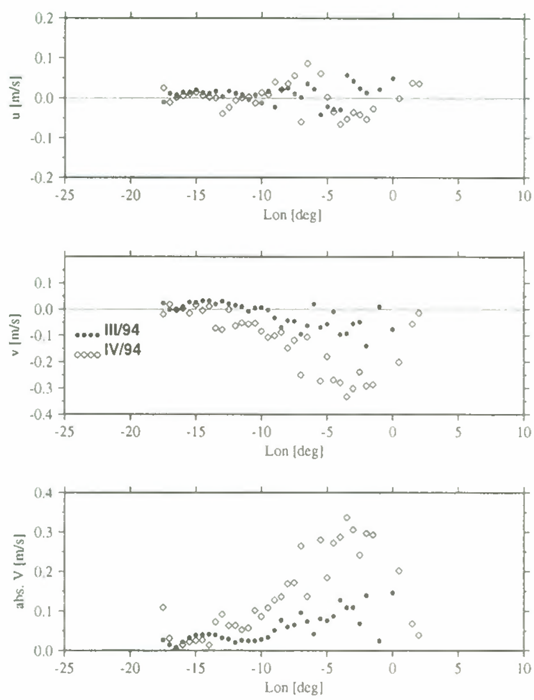

Figure 2: Lateral distribution of the seasonal mean ice drift between $79^o N$ and $80^o N$. Top: Zonal velocity component, positive to East. Middle: Meridional component, positive to North. Bottom: Absolute velocity. III: Jul. - Sept.; IV: Oct. - Dec.

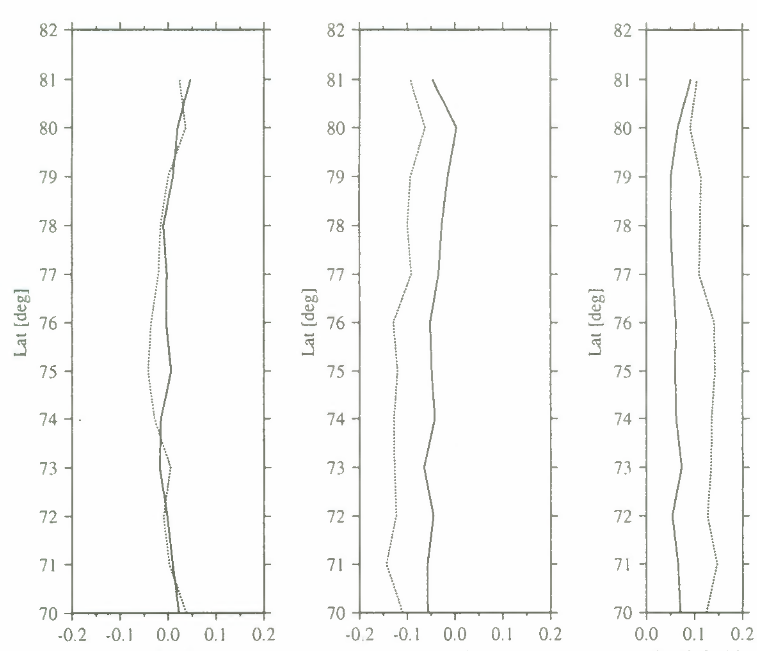

Figure 3: Meridional distribution of the mean drift velocities; solid line: Jul.-Sep.'94, dashed line: Oct.-Dec.'94; u-component positive in eastern direction; v-component positive in northern direction; abs(V) the absolute drift velocity.

	$79°N$ $2.2m(3.0m)$	$75°N$ $2.2m(3.0m)$
	$[Sv]$	$[Sv]$
Jan - Mar	0.08 (0.059)	0.041 (0.03)
Apr - Jun	0.063 (0.046)	0.033 (0.024)
Jul - Sep	0.012 (0.009)	0.012 (0.009)
Oct - Dec	0.116 (0.085)	0.054 (0.04)

Table 2: Seasonal sea ice mass flux in Sverdrup ($1Sv = 10^6 m^3 s^{-1}$)

ice thickness data, to compare these with the ice mass fluxes calculated from numerical models.

5. ACKNOWLEDGEMENTS

The Danish Meteorological Institute provided us with the AVHRR data. The sea ice concentration data were derived with SSM/I data provided by the NSIDC on CD-ROM. This paper was supported by the Commission of the European Communities under contract MAS2-CT93-0057 of the MAST-II Initiative.

6. REFERENCES

Fily, M. and A. Rothrock, 1987; Sea Ice Tracking by Nested Correlations; IEEE Transactions on Geosience and Remote Sensing, Vol. GE-25, No.5, p 570-580.

Kwok, R., J.C. Curlander, R. McConnell and S.S. Pang, 1990: An Ice-Motion Tracking System at the Alaska SAR Facility; IEEE Journal of Oceanic Enginieering, Vol. 15, No. 1.

Martin, T. and P. Lemke, 1995; Sea ice drift and thickness in the East Greenland Current, Proceedings of the Nodic Seas Symposium, Hamburg, March 7-9, p 135.

Ninnis, R.M., W.J. Emery and M.J. Collins; 1986: Automated Extraction of Pack Ice Motion from Advanced Very High Resolution Radiometer Imagery; JGR, Vol. 91, No. C9, p 10725 - 10734.

Nielsen, P. and H. Valeur, 1994; Satellite Based ice charts Greenland Sea; Danish Meteorological Institute, Copenhagen, Data Report 94-2.

Nielsen, P. and H. Valeur, 1995; Satellite Based ice charts Greenland Sea; Danish Meteorological Institute, Copenhagen, Data Report 95-3.

Skriever, H. 1991; The EMI Image Header System for Remote Sensing Images; Electromagnetic Institute, Technical University of Denmark, Version 2, R463.

ICE EDGE DETERMINATION IN THE GREENLAND WATERS USING FIRST ORDER TEXTURE PARAMETERS OF THE ERS.SAR IMAGES.

Rashpal S. Gill.
Danish Meteorological Institute, Lyngbyvej 100, DK 2100 Copenhagen Ø, Denmark.
Tel. (45) 39 157342, Fax. (45) 39 157300

ABSTRACT

The first order texture parameters, power-to-mean ratio (PMR), skewness and kurtosis were computed for regions of openwater, ice (4 - 9/10), fastice and nilas/ice of low concentration (NI) (≤2/10) from the ERS.SAR precision images of the waters around Greenland. The different regions were identified by making near simultaneous observations using aerial reconnaissance. It was found that the water and the fastice regions had the lowest, and almost identical, values of these parameters i.e., these regions were most homogeneous, least skewed (≥0 i.e., all skewed to the right) and had the lowest kurtosis (≥0 i.e., leptokurtic), followed by ice and NI. Filtering based on the PMR values was found to be fairly efficient at discriminating between these regions. Skewness and kurtosis parameters gave similar results. These parameters were also compared with those given by the most commonly used theoretical probability distribution functions (pdf's) such as the log - normal, Rayleigh, gamma and the k - distribution. The comparison showed that the values for openwater, fastice and ice regions were in good agreement with those given by the k - pdf with the values for water approaching those from the gamma pdf (limiting case of k - pdf). NI regions which were most heterogeneous and had the largest variability did not fit any of the above pdfs. The shape parameter of the gamma function used to model the textural variations in the k - pdf model was also found to be a good discriminator.

1. INTRODUCTION

The main problem with using ERS.SAR images in the operational mapping of sea ice in the Greenland waters is in many cases not being able to discriminate between regions of open water and ice. This is due to the large variability of the backscatter from these regions. In particular, the backscatter from the water regions are dominated by the local wind conditions and those from the ice regions are dependent on the ice type, level of melting (if any) and geometrical features such as pressure ridges. Thus, in terms of the grey values, water areas appear black when there is no wind and with the wind ≥2 - 3 m/s, which is required for capillary waves to form, it can appear white. Ice appear greyish - black when there is no melting and during melting it appear black when there is no wind and nearly white when there is a light wind or if there are pressure ridges. Areas of nilas appear black but can also appear nearly white if as a result of winds and currents, which are strong and frequent in these waters especially off Kap Farvel, they are interlocked into each other ("finger rafting"). Thus in many cases it is not possible to state whether the light grey regions are areas of ice or capillary infested waters, or whether the dark regions are areas of calm water or nilas or ice.

In this paper the first order statistical parameters based on the second, third and fourth moments, PMR, skewness and kurtosis, respectively, are computed to determine their efficiency at discriminating between the regions of water, fastice, ice and nilas/ice. PMR, which is a measure of heterogeneity, has been found to be a good measure of scene texture [1]. It has also been used for speckle reduction and terrain classification [2, 3]. For sea ice applications, it has been suggested [4] that PMR values can be used to differentiate between regions of water (most homogeneous) and ice. Skewness and kurtosis, which measures the asymmetry and the degree of flattening of the distribution, respectively, have so far been used for terrain [2] and sea ice type (first- or multi-year) [5] classifications and have produced unsatisfactory results.

To estimate the distributions associated with the different ice regions, the above named statistical parameters of these areas are compared with those of the commonly used pdf's such as log-normal, Rayleigh, gamma and k - distribution. The comparison is carried out on Pearson diagrams [5 - 7] which consists of plots of skewness and kurtosis against PMR. Furthermore, it has been suggested that the shape parameter of the gamma function used to model texture in the k- pdf model can be used for sea states [6, 7] and terrain [8] classifications. The ability of this parameter to discriminate between the different regions of ice is also assessed.

In the next section the data used in the evaluation are discussed. In section 3 the method used to evaluate the statistical parameters is outlined. Also in this secton the method used to compare these parameters with those from the theoretical pdf's, in particular the k - distribution and together with shape parameter mentioned above are described. The results are discussed in section 4 and finally, in section 5 the conclusions are given.

2. DATA SET

Proceedings of the Fourth Symposium on Remote Sensing of the Polar Environments, Lyngby, Denmark, 29 April – 1 May 1996
(ESA SP-391, July 1996)

The data set used in this evaluation consists of six ERS.SAR high resolution precision images and near simultaneous observations made using aerial reconnaissance. Of the six SAR images four (30th May, 1st, 10th and 13th June, 1994) are of the waters off Kap Farvel (the southern most tip of Greenland) and the remaining two (2nd May, 1994) are from Baffin Bay (lat. 70°N, 55°W). These two regions are the most important for shipping. Underflights data consists of aerial photographs, video recordings, visual observations and ice charts produced by the ice patrol using 360° mapping radar.

Qualitative evaluation of all of these data and others have been carried out in [9 - 11].

3. EVALUATION METHOD

3.1 First order statistical parameters

The first order statistical parameters are defined in standard texbooks on statistics [e.g., 12] and are given by the following expressions:

$$PMR = \frac{\mu_2}{\bar{x}^2} + 1 \ , \quad skewness = \frac{\mu_3}{\mu_2^{3/2}} \ ;$$

$$kurtosis = \frac{\mu_4}{\mu_2^2} - 3 \ , \quad where \ \mu_n = \frac{1}{N}\sum_{i=1}^{N}(x_i - \bar{x})^n \ ,$$

$$standard\ dev. = \sqrt{\mu_2} \ , \quad mean\ (\bar{x}) = \frac{1}{N}\sum_{i=1}^{N} x_i \ .$$

PMR has value of 1 for homogeneous areas, skewness and kurtosis are both 0 for the normal distribution.

The above parameters were computed from the images using different size windows (e.g., 32*32, 40*40 pixels, etc.). From these values, the means and standard deviations for the different regions were computed.

3.2 Comparison with theoretical probability distributions

The theoretical distributions used in the comparison are; log - normal, Rayleigh, gamma and the k - distribution. The log - normal is used to represent very heterogeneous urban areas in terrain classification [8]. The Rayleigh distribution is valid for 1-look homogeneous (i.e., fully developed speckle, and no texture) amplitude image. The gamma distribution is valid for multi- look homogeneous images. The only distribution, that takes the texture of the image into consideration is the k - distribution. This distribution results, by assuming the speckle variations to be described by one gamma function and the texture variations to be described by another, slow varying, gamma function [13, 14, 7, 3]. The multi - look amplitude (since the high resolution ERS.SAR product consists of 3-look amplitude values) k - distribution, in the notation of ref. [3] is given by the following expression:

$$P_k(A) = \frac{4A^{\alpha - L - 1}}{\Gamma(\alpha)\Gamma(L)} \left(\frac{\alpha L}{<R>}\right)^{\frac{\alpha + L}{2}} K_{\alpha - L}\left(2A\sqrt{\frac{\alpha L}{<R>}}\right)$$

where $<R>$ is the scale factor, $K_{\alpha-L}$ is the modified Bessel function of the second kind, A is the image amplitude, L is the number of looks, and α is the shape parameter of the gamma function used to model texture. Like the PMR, α is a measure of the scene heterogeneity. $\alpha \rightarrow \infty$ and $\rightarrow 0$ for homogeneous and very heterogeneous scenes, respectively. It is given by the following equation which is obtained by taking moments of the above pdf:

$$\alpha = \frac{1}{\frac{L}{L+1}\frac{m_4}{m_2^2} - 1}$$

where m_n is the nth moment of the k - distribution. The skewness and the kurtosis of each of the pdf's can also be determined by taking moments. These theoretical parameters can then be compared with the values computed for the different regions from the SAR images on Pearson diagrams [5 - 7] to determine which of these pdf's (if any) best fit the data values.

As mentioned in the introduction, α has been used for terrain and sea state classifications. When it was computed for different size windows, as outlined above for the other parameters, it was found that for some regions $\alpha \rightarrow -\infty$ for window sizes $\leq 160 * 160$. This can be seen from the above equation i.e., as $m_4/m_2^2 \rightarrow 4/3$ (L=3 for ERS.SAR), $\alpha \rightarrow +\infty$ and when this ratio is slightly $< 4/3$ $\alpha \rightarrow -\infty$. Negative values of α are not allowed in the gamma and the k - distribution models. Thus these distributions are only valid for those parts of the images where $m_4/m_2^2 \geq 4/3$. To avoid this problem of $\alpha \rightarrow \pm\infty$ it was found more convenient instead to compute α^{-1}.

4. RESULTS AND DISCUSSION

From the data set, 6 regions of openwater; one from each image, 3 of fastice, 5 of ice (from open to consolidated pack ice with concentration of 4 → 9/10) and 5 areas containing nilas or ice of low concentration ($\leq$2/10) or a mixture of both, were identified. The size of the regions ranged from ½ to 20 million pixels, out of the total 64 million, in the original high resolution images. Then for each of these regions, as outlined in the last section, the values of PMR, skewness and kurtosis were computed by averaging different size windows. For presentation, all the figures were produced by using windows of size 32 * 32. Other size windows, of reasonable size to ensure statistical validity of the computed parameters, gave similar results.

Figures 1, 2 and 3, respectively, shows the means and the standard deviations of the PMR, skewness and kurtosis, of the different regions, computed from each of the images. As can be seen from the figures, all the three parameters have the same behaviour i.e., they have the smallest means and standard deviations for the water and the fastice regions, followed by ice and NI. In particular, taking the PMR values; the water regions have values $\leq 1.1 \pm 0.01$, the fastice have similar mean values but slightly higher standard deviations, the ice have values in the range $(1.12 \rightarrow 1.17) \pm (0.02 \rightarrow 0.03)$ and NI have values ranging from $(1.2 \rightarrow 1.37) \pm (0.07 \rightarrow 0.25)$. Based on these values, and those on skewness and kurtosis, it should certainly be possible to discriminate between NI regions, on the one hand, and water, fastice and ice on the other. Discrimination between water and the ice regions is likely but will be less certain especially those based on mean kurtosis. No discrimination is possible between water and fastice. However, this is not likely to be a major problem as most of fastice tends to lie along the coast in fjords. Furthermore, fastice boundaries tends to be easily discernible from the surrounding regions which helps the discrimination task.

Figure 4 shows an example of the filters based on the above parameters. In particular, figure 4a shows the original SAR image after 32 *32 pixel averaging (so that it has the same size as the filter images). This image is from the Baffin Bay (part of the island Disko can be seen on the right hand side of the image). The interpretation of the low resolution image product, of the same frame, has been carried out in [9] where aerial photographs of the different regions can be found. This particular SAR image was chosen because it contains all the four regions (openwater, fastice, ice and NI) which are also indicated. Figures 4b - 4d are the filter images based on PMR, skewness and kurtosis, respectively. As can be seen from these figures they look very similar but the PMR values are the most (the kurtosis least) sensitive to the different regions. Compared to the PMR values (fig. 4b), there is no additional information in the skewness and the kurtosis images (figures 4c and 4d, respectively). This trend is repeated in the other SAR images (not shown in this paper). In the images, the most homogeneous (lowest PMR values), least skewed and lowest kurtosis values regions, appearing dark grey/black, are the open water and the fastice areas. This is in contrast to the most heterogeneous, most skewed, largest kurtosis, namely the areas covered with nilas, appear nearly white. The ice regions have the grey values in between these two extremes. This interpretation agrees very well with the

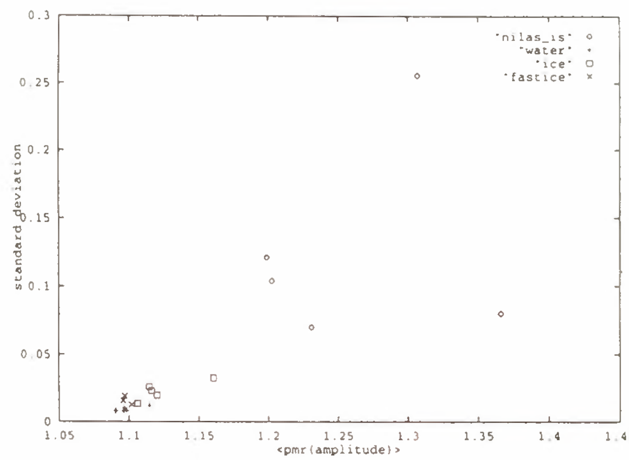

FIG. 1. Mean and standard deviations of PMR values.

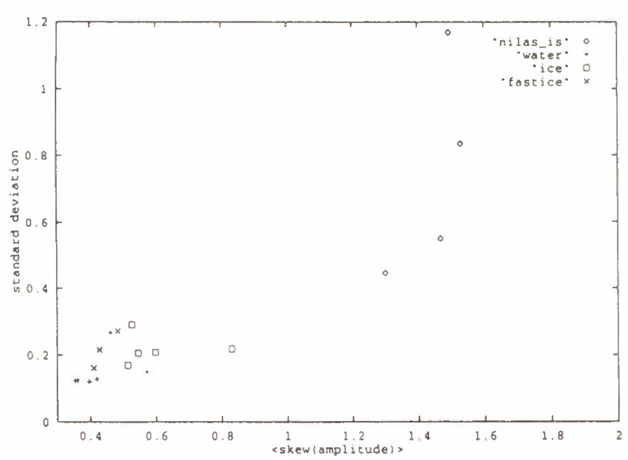

FIG. 2. Mean and standard deviations of skewness values.

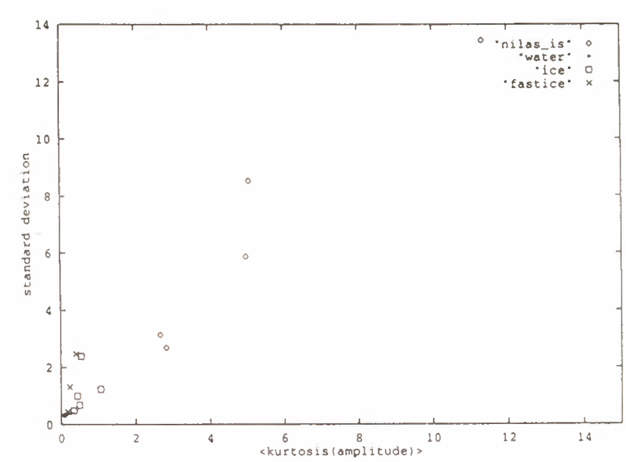

FIG. 3. Mean and standard deviations of kurtosis values.

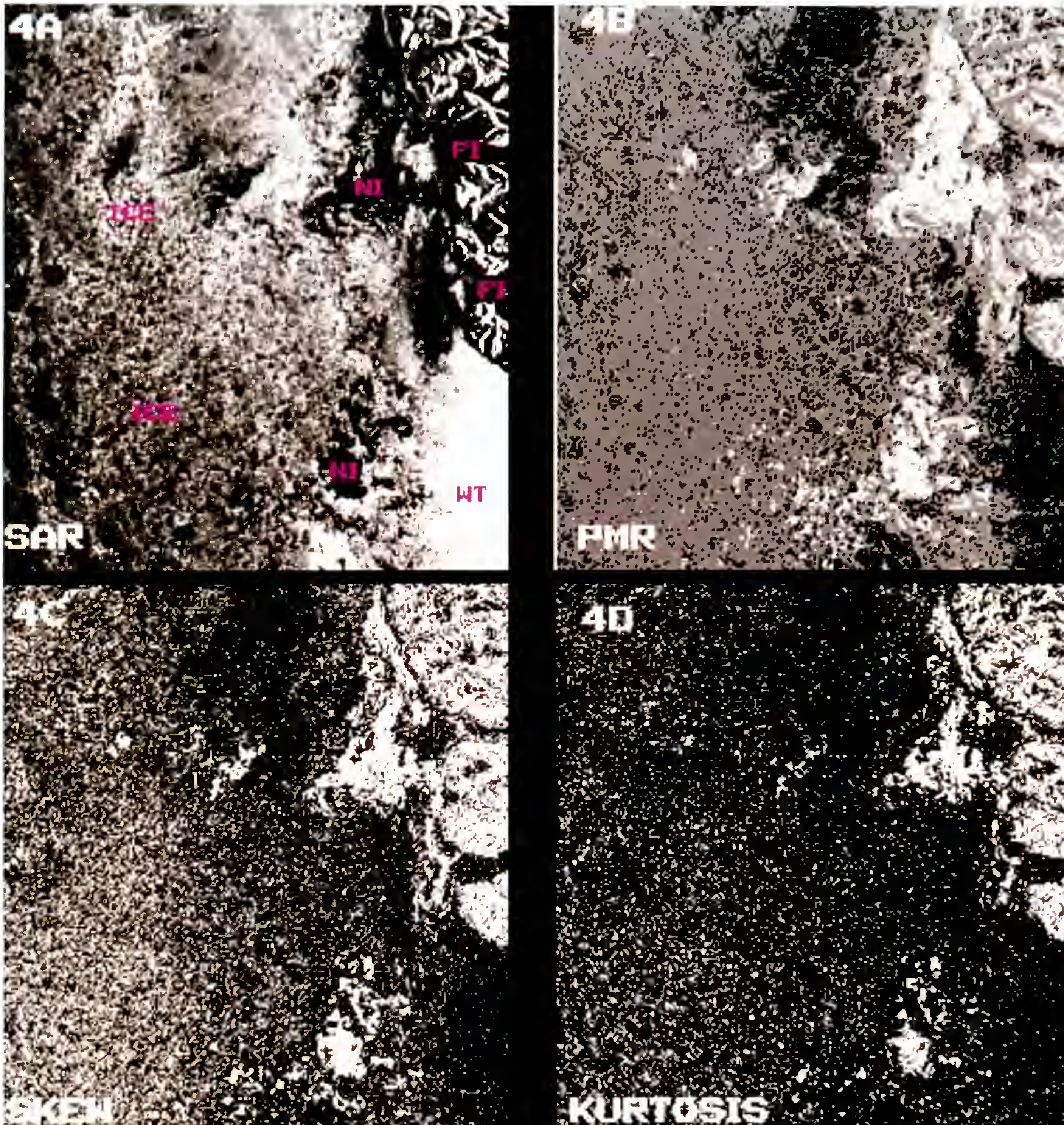

Figure. 4. Comparison between the original SAR image (top left ➜ fig. 4a) and the filter images based on PMR (top right ➜ fig. 4b), skewness (bottom left ➜ fig. 4c) and kurtosis (bottom right ➜ fig. 4d). Size of each image is ~ 100 km * 100km. In the SAR image FI, NI and WT denotes fastice, nilas and openwater regions, respectively.

aerial observations. However, it is also clear from this that mis-interpretation between the openwater and the ice regions is likey. Nevertheless, the images based on these statistical parameters contain very useful additional informations which should be used in conjuction with the SAR images.

To estimate which of the theoretical pdf's best describe the statistics of the different regions, plots of skewness and kurtosis against PMR of the theoretical and those deduced from the data were made and are shown in figures 5 and 6, respectively. These figures shows that the values for water, fastice and ice lie on the k - pdf while those of NI do not fit any of the above theoretical pdf's. Furthermore, the values for water and fastice approach those characteristic of the gamma distribution which imply that these regions are almost totally homogeneous. Infact the amount of these values lie away from the gamma curve is an indication of the amount of heterogeneity of the particular region (assuming the assumptions made to derive this distribution are applicable for these ice conditions i.e., strong scattering, uniform phase variations etc.). From these figures it can be concluded that discrimination between the openwater and the ice regions is not possible based on these Pearson diagrams. However, since the values for water/fastice are approximately given by the gamma distribution, it should be possible to use this information to carry out image classification. For example, if the observed PMR (or one of other parameters) ≈ 1.1 (the value from the gamma distribution = 1.087), then the region can be classified as water/fastice, values > 1.15, say, can be considered as ice infested. This needs further validation under different wind conditions and temperatures.

There are a number of other features of the theoretical distributions which are worth noticing; (a) for L=1, the k - pdf (designated by k_pdf_11 in the figures) and the values from gamma distribution approach the Rayleigh distribution (if the intensity values are plotted then they tend to the negative exponential distribution), (b) for multi- look data the minimum values for the k - distribution tends to those given by the gamma distribution, for example, for L=3 the gamma distribution give PMR=1.087 and this is also the minimum value obtained from the k - distribution.

Figure 7 shows the mean of α (defined in the last section) of the different regions plotted against their mean PMR values. In the figure the limiting value of the PMR from the gamma distribution, at which $\alpha \to \infty$, is also shown. From this figure, $\alpha \to \infty$ for the water and fastice regions and $\alpha \to 0$ for the NI regions. The ice regions have α values between these extremes. However, the information in this plot is very similar to that avaliable in figures 1 - 3. This can be seen in figure 8 in which the standard deviations are plotted against the means of α^{-1}.

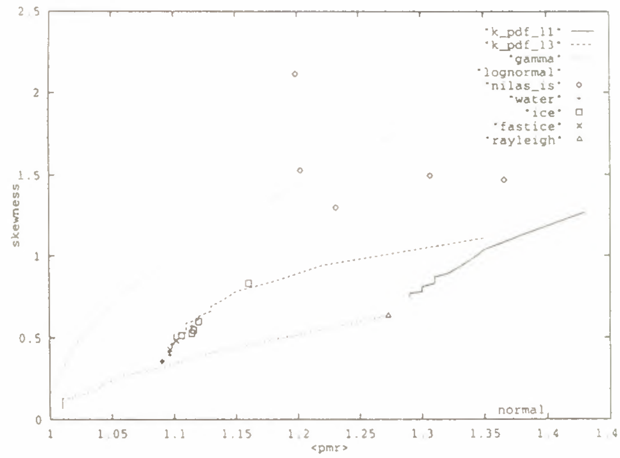

FIG. 5. Skewness against PMR.

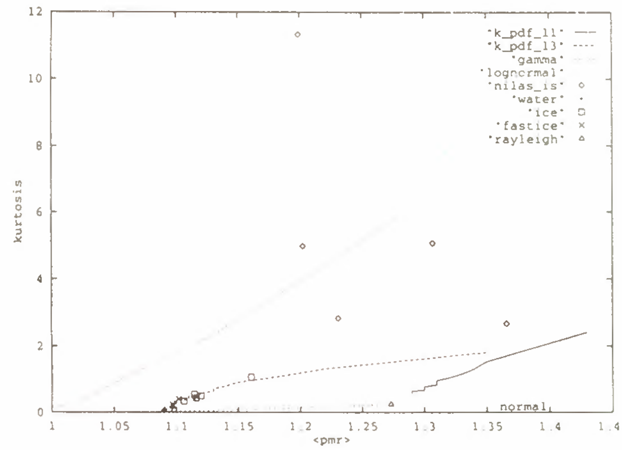

FIG. 6. Kurtosis against PMR.

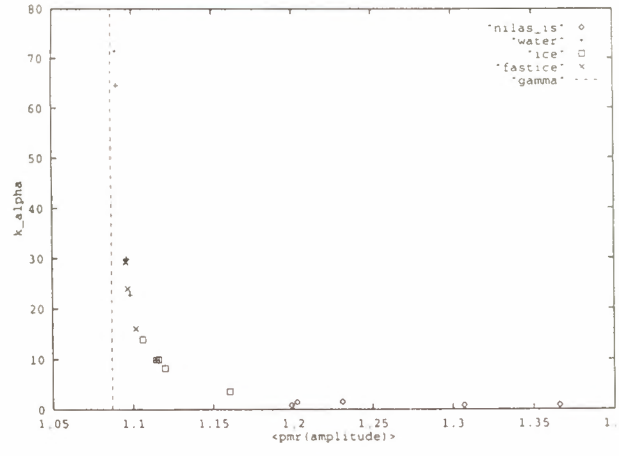

FIG. 7. α against PMR.

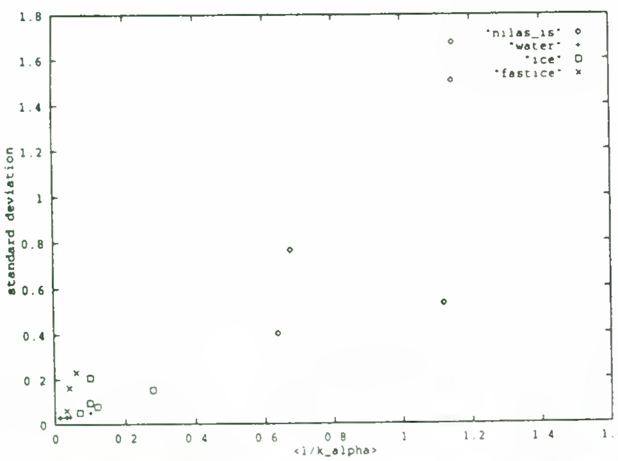

FIG. 8. Means and standard deviations of α^{-1}.

FIG. 9. Filter image based on α^{-1}.

Figure 9 shows the filter image based on α^{-1} of figure 4a. Comparing this filter image with the others given in figures 4b - 4d, it can be seen that they are very similar. In fact, analysis of some of the other SAR images showed that, compared to the PMR values, the α^{-1} values were relatively, less sensitive to the variations within the different regions. This needs to be further investigated using different data.

5. CONCLUSIONS

The first order statistical parameters, PMR, skewness and kurtosis were evaluated in terms of their ability to discriminate between the regions of openwater/fastice, ice and NI. The different regions were identified by making near simultaneous underflights. Based on the limited data set used in this evaluation, it was found that the filtering based on the PMR values was very helpful in determining the ice edge. Filtering based on the more complex parameters; skewness, kurtosis and α^{-1}, did not provide any significant additional information to that already avaliable from the PMR values.

The statistics of the openwater, fastice and ice were well described by the k - distribution with the values for water and fastice having a very nearly a gamma distribution.

6. ACKNOWLEDGEMENTS

The author wishes to thank H. H. Valeur for useful comments, P. Nielsen for developing some of the software and K.Q. Hansen for his help in processing the images.

7. REFERENCES

[1] Ulaby F. T, Kouyate F, Brisco B & Lee Williams T; "Textural Information in SAR Images", IEEE Trans. Geosc. Remote Sensing, Vol. GE-24, no.2, p235, 1986.

[2] Laur, H., T. Le Toan and A. Lopes; "Textural Segmentation of SAR Images using First Order Statistical Parameters", IGARSS Symposium, p1463, 1987.

[3] Lopes A., Laur H. & Nezry E; "Statistical dist. and texture in multilook and complex SAR images", IGARSS Symposium, vol. 3, p2427, 1990.

[4] Skriver H., "On the accuracy of estimation of ice type concentration from ERS-1 SAR images", Proc., 14th EARSeL Symposium, Gotenborg, 1994.

[5] Lyden J. D., Burns B. A., and Maffet A., L.,"Charaterisation of Sea Ice Types Using Synthetic Aperature Radar", IEEE Trans. Geosci. Rem. Sens., GE-22,p 431, 1984

[6] Chapron B., Garello R., Kerbaol V., Lefevre J. M., "Nonlinear Theory of Ocean-SAR Transformation and Statistical Analysis of ERS-1 Wave Mode Imagettes", Proc. 2nd ERS-1 symposium, Hamburg, p247, 1993.

[7] Delignon Y., Garello R., and Hillion A., "Parametrization of sea-state from SAR images", Proc. Of ICASS symp., vol. 3,p 29, 1992.

[8] Liu G., Huang S., Torre A., and Rubertone F., "Statistical analysis of multilook poraimetric SAR data and terrain classification with adaptive distribution", SPIE vol, 2584, p212, 1996.

[9] Nielsen P., Pedersen F.B. and Valeur H.H., "ERS-1 SAR images and operational mapping of sea ice in the Greenland waters. preliminary results of a pilot project", Proceedings of the First ERS-1Pilot Project Workshop, Toledo, Spain, pp 175- 182, 1994.

[10] Gill R.S., Valeur H.H. & P. Nielsen, "Evaluation of the ERS.SAR images in the operational mapping of sea ice in the Greenland waters", European symposium on satellite remote sensing II, Paris, 2586-16, 1995.

[11] Gill R.S., Nielsen P. & Valeur H.H., "Evaluation of the ERS.SAR high resolution images in the operational mapping of sea ice in the Kap Farvel waters", Second ERS Application workshop, London, Dec., 1995.

[12] Croxton F., E., Cowden D. J., & Klien S., "Applied General Statistics" publ. Pitman, 1968.

[13] Jakeman E. and Pusey P.N.,"A model for non-Rayleigh sea echo " , IEEE Trans. Antenna propag., vol., 24, no. 6, p806, 1976.

[14] Jao K. J.,"Amplitude distribution of composite terrain radar clutter and the K-distribution", IEEE Trans. Antenna propag., Vol. AP-32, no. 10, p1049, 1984.

SEA ICE CHARACTERISTICS AND BACKSCATTER VARIABILITY IN THE BELLINGSHAUSEN SEA, ANTARCTICA

Kim Morris, Martin Jeffries and Shusun Li

Geophysical Institute, University of Alaska,
903 Koyukuk Drive, P. O. Box 757320, AK 99775–7320, U.S.A.
Phone: 1-907-474-6522; Fax: 1-907-474-7290
kmorris@images.alaska.edu,

ABSTRACT

Radiometrically-corrected ERS-1 SAR data have been used to document the backscatter (σ^o) variability of sea ice in the Bellingshausen Sea in winter (August and September, 1993) and summer (January, February and March, 1994). There is no definitive winter multiyear (MY) σ^o signature in the Bellingshausen Sea. The similarity between the winter first-year (FY) and MY ice σ^o values may be due to similar surface properties, particularly roughness, seawater flooding and iciness of the snow cover. These factors may explain why these antarctic FY ice σ^o values are higher than those in the Arctic in winter. Antarctic winter MY ice σ^o values are similar to those in the Arctic. Antarctic summer MY ice σ^o values are higher than the winter values, and significantly greater than those in the Arctic, probably due to some snow metamorphosis and increased snow surface roughness. The greatest contrast in antarctic sea ice backscatter signatures is between new/young ice and the older, thicker ice types, a contrast also seen in Arctic σ^o values. This is a consequence of the similar influences new/young ice surfaces are subject to at these early stages of ice development. At later stages of ice development such phenomena as floe surface flooding and a perennial snow cover affect Antarctic, but not Arctic, sea ice.

1. INTRODUCTION

Active microwave remote sensing has a distinct advantage over passive microwave and other remote sensing instruments for sea ice studies because of its high spatial resolution and all–weather, all-season capability to obtain earth surface data. Active microwave remote sensing of Antarctic sea ice has been possible only since the launch of the first European Remote Sensing Satellite (ERS-1) in July 1991.

There are some fundamental differences in Arctic and Antarctic sea ice properties and processes that are relevant to the understanding of remotely sensed data. These include the maintainence of at least part of the snow cover and lack of melt pond formation on the sea ice during the Antarctic summer and the flooding of large areas of the surfaces of Antarctic floes with seawater which soaks the base of the snow cover. In the Arctic, the snow cover is completely removed and melt pond formation, which is extensive, plays a key role in changing the near-surface ice properties enabling the differentiation of multiyear (MY) ice from younger ice types by all microwave sensors. Seawater flooding of Arctic ice floes has not been documented. Field investigations in Antarctica using ship-mounted radar scatterometers indicate that thick snow and seawater flooding significantly affect active microwave sea ice signatures [Lytle et al., 1996; Drinkwater et al., 1995].

Since 1991, ERS-1 SAR data have been used primarily to study the Weddell Sea ice cover [Drinkwater and Kottmeier, 1994; Drinkwater et al., 1994; Drinkwater et al., 1995]. This paper presents the results of an investigation of ERS-1 SAR backscatter variability in the Bellingshausen Sea.

2. SAR DATA ACQUISITION AND PROCESSING

One hundred and four SAR Precision Images (PRI) from 11 different orbits, covering the area between 65°S-74°S and 70°W-105°W and acquired between 21 August and 10 September 1993, were analysed for winter backscatter variability. Seventy nine SAR PRI images from 17 orbits, covering the area between 70°S-73°S and 89°W-98°W and acquired between 22 January and 20 March 1994 during the 3 day repeat cycle/Ice Phase of the satellite, were analysed for summer backscatter variability.

Zones of homogeneous tone and texture were sampled and σ^o statistics (mean and standard deviation) were calculated. Individual samples ranged from 6 pixels to 772,000 pixels. The number of samples per image ranged from 5 to 55, depending on the complexity of the sea ice cover. Samples of similar tone, texture and location in the pack were grouped and "global" statistics were calculated.

3. SEA ICE CHARACTERISTICS

3.1 Winter sea ice

The SAR mosaic in Figure 1 illustrates the general sea ice conditions in the Bellingshausen Sea during late winter 1993. On the basis of sea ice features and variations in tone and texture, three zones are identified: the coastal zone, the perennial ice zone and the annual ice zone.

The coastal region lies within approximately 50 to 60 km of the coast and is dominated by flaw leads and polynyas. Two ice types are identified. First, there are extensive areas of very dark tone with a near uniform texture which are probably relatively undeformed nilas. Second, there are extensive areas of brighter tone with a much stronger texture which are probably areas of moderately to strongly deformed new and young ice.

The boundary between the annual and perennial ice coincides closely with the previous summer's ice edge and generally lies near 70°S. Three main winter ice types (W1, W2, and W3) have been identified according to their tone and form in this zone. Type W1 ice is the dominant ice type and is characterized by mid-range gray tones which form the "background" from which the other two

Proceedings of the Fourth Symposium on Remote Sensing of the Polar Environments, Lyngby, Denmark, 29 April – 1 May 1996 (ESA SP-391, July 1996)

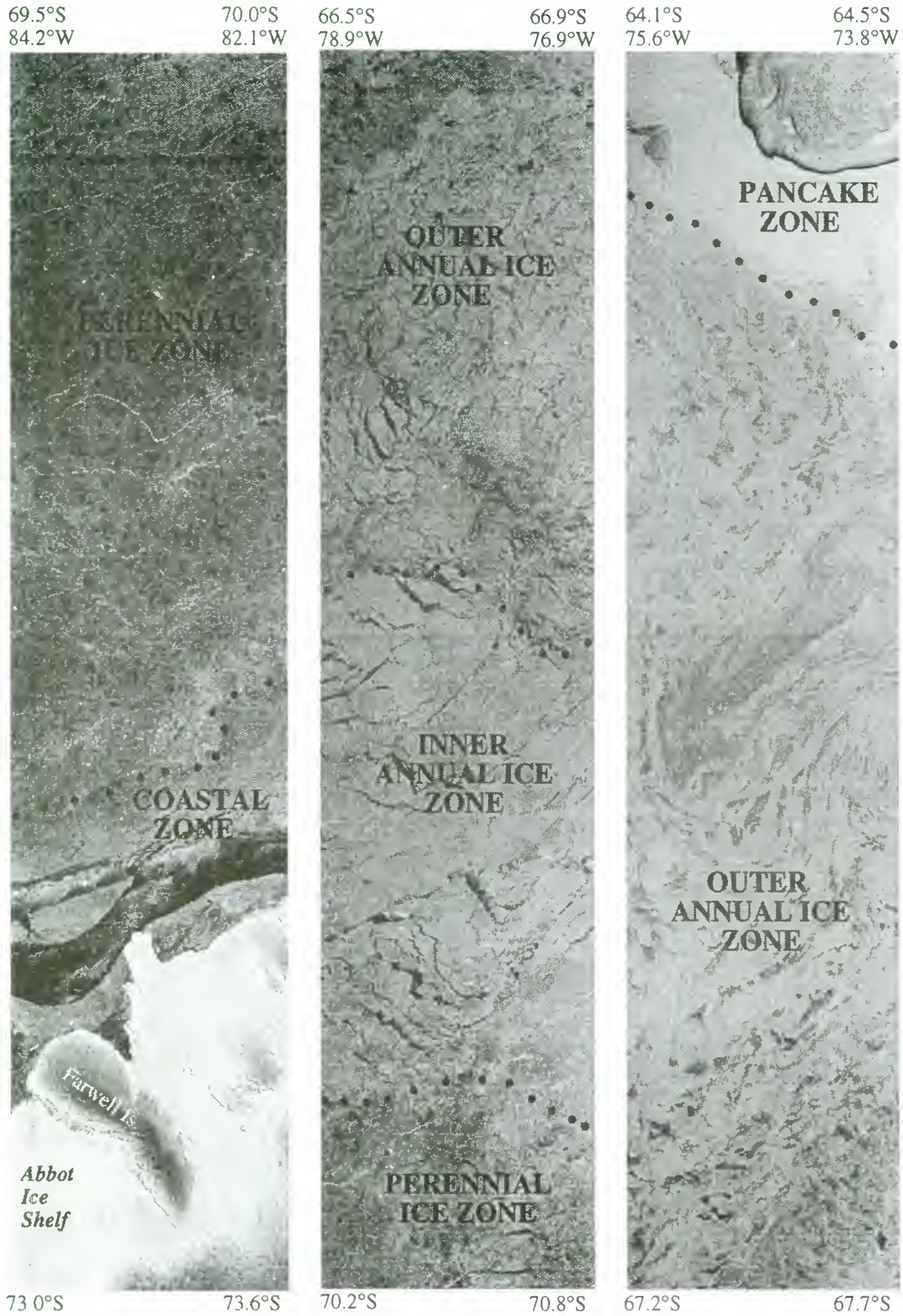

Figure 1. Mosaic of ERS-1 SAR orbit 11019 (24 Aug. 1993) illustrating winter sea ice conditions in the Bellingshausen Sea. The three main ice regimes are: annual pack (subdivided into inner and outer); perennial pack and coastal zone. Each image swath has surface dimensions of 100 by 445km. ERS-1 data are © ESA.

ice types are distinguished. Type W2 ice appears darker than Type W1 ice and takes the form of rounded, floe-like structures that are found throughout the perennial pack ice. Type W3 ice is brighter and occurs in much smaller quantities than Types W1 and W2. It has a small, floe-like structure.

The annual pack ice can be divided into two zones: the inner and outer annual pack ice. The inner annual pack ice is not significantly different from the outer annual pack ice in terms of gray tones; rather, they differ in general appearance and texture. The outer pack ice has a more broken and chaotic appearance than the inner annual pack ice. The inner annual pack ice, which is spatially less extensive than the outer annual pack ice, has a more massive and consolidated appearance.

3.2 Summer sea ice

The SAR mosaic in Figure 2 illustrates the general sea ice conditions and backscatter variability in the Bellingshausen Sea during summer 1994. In contrast to the winter perennial sea ice, the summer perennial sea ice tones appear more uniform with only minor variability, and little in the way of large-scale floe structure is evident. The ice pack was divided into coastal and perennial pack ice zones.

The polynya in front of Farwell Island (Fig. 2) was the sole coastal zone location from which backscatter values for the new and young ice types were derived. While the SAR image mosaic in Figure 2 gives the impression of minimal backscatter variability in the perennial ice pack,

Figure 2. Mosaic of ERS-1 SAR orbit 13650 (24 Feb. 1994) illustrating typical summer sea ice conditions in the Bellingshausen Sea. The two main ice regimes are: perennial pack and coastal zone. The mosaic has surface dimensions of 100 by 440 km. ERS-1 data are © ESA.

a closer examination reveals greater complexity. Three summer ice types (S1, S2 and S3) have been identified and their backscatter determined. Type S1 ice, the dominant ice type, is composed of mid-range gray tone and forms the "background" from which the other two ice types are distinguished. Type S2 ice is darker than Type S1 and primarily takes the form of small, rounded, floe-like structures. Type S3 ice is brighter than Type S1 and Type S2 ice and appears as small floe-like structures of variable definition.

4. BACKSCATTER VARIABILITY

4.1 Probability density functions of winter ice σ^o

In the coastal and perennial ice zones, the probability density functions (PDF) for each ice type within each zone are significantly different each other (Fig. 3). The PDF for the undeformed new ice in the coastal zone has a very narrow range of low values which reflects the nearly uniform texture and limited deformation of this ice type. The PDF for the deformed new and young ice has a very broad base, which is a consequence of the variation in the degree of deformation and surface characteristics. The Type W2 ice distribution in the perennial ice zone falls between each of the coastal ice distributions, while the PDFs for W1 and W3 show much higher σ^o values. Within the annual ice there is no significant difference between the outer pack ice and inner pack ice. The annual ice σ^o distributions are very similar to that of the Type W1 perennial ice.

4.2 Probability density functions of summer ice σ^o

The PDF for the new ice has a very narrow range of values (Fig. 4), similar to the winter new ice (Fig. 3). The PDF for the deformed new and young ice might be described as bimodal and it covers a similar range of values as its winter equivalent (Fig. 3). The mean σ^o values for the perennial ice types are distinct from eachother (Fig. 4b). The extent of overlap between the tails of the distributions, particularly between Type S1 and Type S3 ice, demonstrates a greater ambiguity in the nature of the radar backscatter from summer sea ice. Nevertheless, the backscatter signatures of the three summer perennial ice types are higher than those observed in the winter perennial ice zone.

5. DISCUSSION

5.1 Winter annual ice

The backscatter from the annual ice in the Bellingshausen Sea is roughly 4dB and 7dB higher than that of deformed and undeformed ice first–year (FY) ice respectively in the Arctic, and almost identical to that of deformed and undeformed Arctic MY ice [Kwok and Cunningham, 1994]. The backscatter signatures of the Bellingshausen annual ice are almost identical to those of rough FY ice in the Weddell Sea [Drinkwater et al., 1994; Drinkwater et al., 1995].

Sources of the high backscatter values are: widespread deformation and rough ice throughout the annual ice cover which cause strong scattering from the angular, tilted surfaces [Drinkwater et al., 1995]; seawater flooding of the ice surface and the resultant slush and brine wicking [Lytle et al., 1996] which creates a high dielectric contrast between the dry snow and the slush; and extensive ice layers within the winter snow cover which cause strong backscatter in a similar fashion to ice features in the snow cover on glaciers and ice sheets [Zabel et al., 1995].

5.2 Winter perennial ice

5.2.1 Type W1 ice

On the basis of National Ice Center antarctic ice charts for the end of summer 1993, we conclude that the 1993

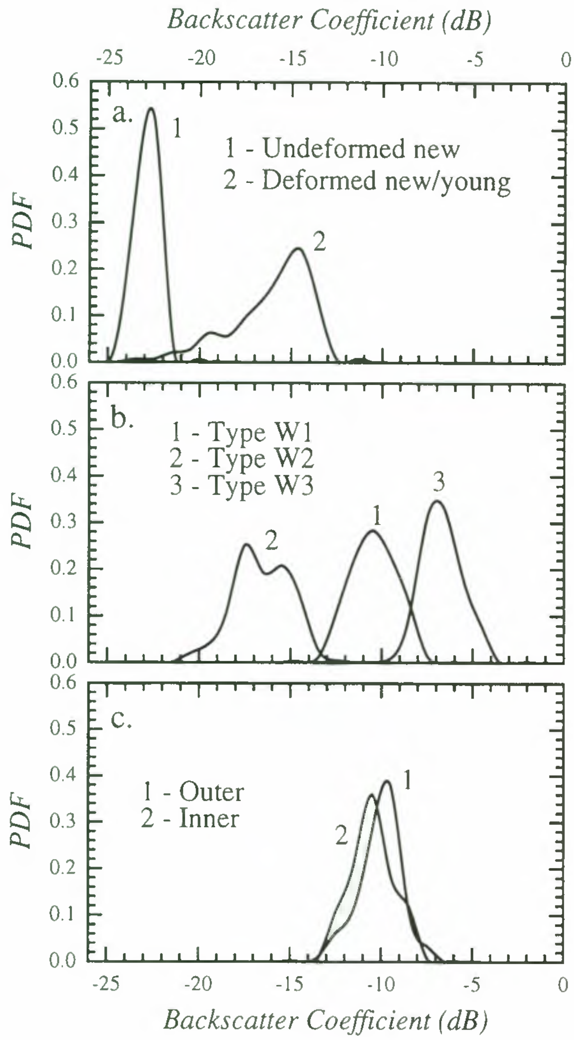

Figure 3. Probability density functions of σ^o values from the winter ice types in (a) the coastal zone, (b) the perennial pack ice, and (c) the annual pack ice.

winter perennial ice zone contained a large amount of MY ice. Since the Type W1 ice is the most common in the winter perennial ice zone, it probably represents MY ice.

The thick snow cover on old floes increases backscatter due to volume scattering [Lytle et al., 1996]. The multiyear snow cover on those few old floes investigated in the Bellingshausen Sea was very hard and icy and composed of melt clusters with dimensions of 5–10mm across [M. Sturm, pers. comm., 1995] and are probably a source of volume scatter.

The amount of flooding on the few MY floes investigated in the Bellingshausen Sea is comparable to FY floes in the same region. This flooding, together with the melt clusters and deformation features, contribute to the high MY ice backscatter signature. The Type W1 MY ice backscatter signature is, however, 3–4dB lower than that in the Weddell Sea in winter 1992 [Drinkwater, pers. comm., 1995]. This might be due to some combination of more extensive flooding, a more icy snow cover and rougher ice in the Weddell Sea at that time compared to the Bellingshausen Sea one year later. The backscatter

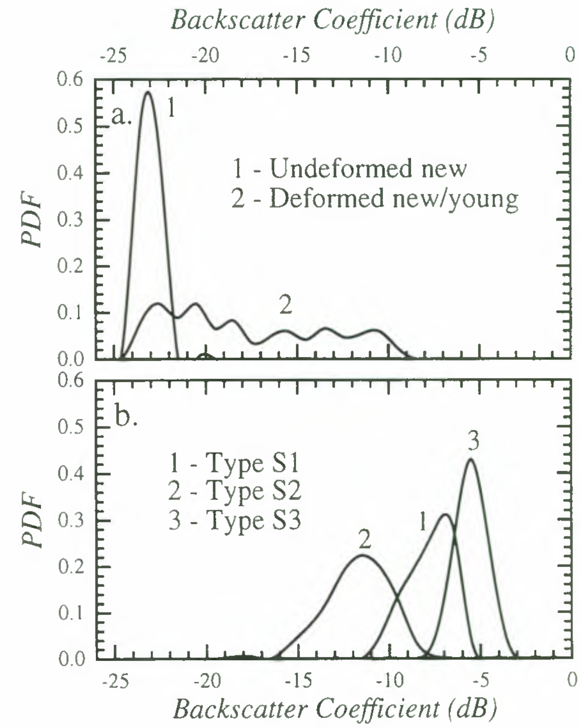

Figure 4. Probability density functions of σ^o values from the summer ice types in (a) the coastal zone and (b) the perennial pack ice.

signatures of the Type W1 MY ice are similar to those of deformed and undeformed Arctic MY ice, which have PDF peaks at roughly −11 to −10dB [Kwok and Cunningham, 1994].

5.2.2 Type W2 ice

Although its appearance of small, rounded floes, suggests that Type W2 ice might be old floes, its backscatter indicates that it is more likely FY ice at an early stage of development. Its backscatter PDF is intermediate between that of the relatively undeformed nilas and deformed new/young ice in the coastal zone (Fig. 3) suggesting that Type W2 ice is young, relatively thin FY ice that has not been extensively deformed. The occurrence of extensive areas of Type W2 young ice at all times during the study period suggests that there may be considerable new and young ice growth, and thus significant heat and salt fluxes, in leads that open frequently in the perennial ice cover on the continental shelf.

5.2.3 Type W3 ice

Type W3 ice occurs in much smaller amounts than the other winter perennial ice types. Its high backscatter signature suggests that it is either completely flooded and/or extremely deformed. Thus, it might represent either occasional rubble fields or remnants of the very oldest MY ice.

5.3 Summer perennial ice

The Type S1 ice is the most common of the summer perennial ice types and so is probably MY ice. The backscatter signature of this ice is almost identical to that of second–year (MY) ice in summer 1992 in the western Weddell Sea, where rough surface scattering from a wet snow cover increased the backscatter [Drinkwater et al., 1994]. This probably accounts for the increased backscatter from the Type S1 ice. The same explanation can also be applied to the Type S2 and S3 ice types which might be the same ice types as the Type W2 and W3. Thus, the Type S2 ice is probably FY ice undergoing the transition to MY ice.

An increase in backscatter from winter to summer in the Antarctic sea ice is the opposite of what occurs in the Arctic. There, the ice is a complex of melt ponds and wet, bare ice, resulting in relatively low backscatter due to signal loss that occurs under those wet conditions.

5.4 Coastal ice

The identification and sampling of backscatter variability of new and young ice types is easier and more reliable in the coastal zone. This is because these ice types dominate this zone. New and young ice types also occur in leads in the pack ice, but are more difficult to sample because of the size of the leads. The backscatter signatures of the summer coastal ice types are not significantly different from those in winter. The minor differences that do exist are probably more a function of the dynamic nature of this environment and resultant deformation and effects on surface roughness than they are due to other environmental influences such as temperature effects on snow and ice properties.

The backscatter signatures of the Bellingshausen Sea coastal ice types are probably an accurate representation of ice in leads in the perennial and annual ice and thus can be compare with the generic Arctic lead ice described in Kwok and Cunningham [1994]. The peak of the backscatter PDF for Arctic lead ice is –17dB. The Antarctic winter undeformed new ice and deformed new/young ice categories bracket the Arctic lead ice backscatter distribution. The similarity between the Arctic and Antarctic backscatter signatures at these early stages of ice development is due to the ice surfaces being subjected to similar influences.

6. SUMMARY AND CONCLUSION

The seasonal variability of spaceborne radar backscatter from sea ice in the Bellingshausen Sea has been described and compared with those available for Weddell Sea ice and Arctic sea ice. The results have been explained on the basis of the current understanding of differences between Arctic and Antarctic sea ice and snow cover properties and processes and their role in affecting backscatter. The main findings are:

1. Backscatter signatures from FY ice in the Bellingshausen and Weddell seas are similar. Both are higher than that of winter FY ice in the Arctic Ocean.

2. MY and FY sea ice winter backscatter signatures are similar in the Bellingshausen Sea. The lack of a definitive MY ice signal in this region differs from Arctic MY ice. Thus SAR may have limited application to studies of the snow and ice thickness distribution and the mass balance of the pack ice in the Bellingshausen Sea.

3. Backscatter signatures of summer MY ice in the Bellingshausen and Weddell seas are similar, probably due to partial melting of the snow cover and increased snow surface roughness and iciness. Backscatter from the antarctic summer MY ice is much higher than that in the Arctic.

4. On average, antarctic summer backscatter signatures of all the perennial ice types are higher than the winter signatures.

5. The backscatter signatures of new and young ice in antarctic polynyas, and by implication those in leads in the pack ice, are similar in winter and summer and quite different from the older, thicker ice types. Consequently, SAR data have potential for use in studies of the heat and salt fluxes associated with ice growth on polynyas and leads, as is currently the case in the Arctic.

Acknowledgements. This work was supported by the National Science Foundation grant OPP-9117721. We thank Chuah Teong Sek, Mark Drinkwater, Vicki Lytle, Rob Massom, Klaus Reiniger and Willy Weeks for their valuable comments and assistance.

7. REFERENCES

Andreas, E. L. and S. F. Ackley, On the differences in ablation seasons of Arctic and Antarctic sea ice, *J. Atmos. Sci., 39*, 440-447, 1982.

Drinkwater, M. R. and C. Kottmeier, Satellite microwave radar– and buoy–tracked ice motion in the Weddell Sea during WWGS"92, in *Proceedings of the 1994 International Geoscience and Remote Sensing Symposium (IGARSS"94),* Catalog No. 94CH3378–7, pp. 153–155, Inst. of Electr. and Electron. Eng., New York, 1994.

Drinkwater, M. R., D. S. Early and D. G. Long, ERS–1 investigations of Southern Ocean geophysics using combined scatterometer and SAR images, *Proceedings of the 1994 International Geoscience and Remote Sensing Symposium (IGARSS"94),* Catalog No. 94CH3378–7, pp. 165–167, Inst. of Electr. and Electron. Eng., New York, 1994.

Drinkwater, M. R., R. Hosseinmostaffa and S. P. Gogineni, C–band backscatter measurements of winter sea ice in the Weddell Sea, *Int. J. Rem. Sens., 16*, 3365–3389, 1995.

Kwok, R. and G. F. Cunningham, Backscatter characteristics of the winter ice cover in the Beaufort Sea, *J. Geophys. Res.*, *99*, 7787–7802, 1994.

Lytle, V. I., K. C. Jezek, S. Gogineni and A. R. Hosseinmostafa, Field observations of microwave backscatter from Weddell Sea ice, *Int. J. Remote Sensing, 17*, 167-180, 1996.

Zabel, I. H. H., K. C. Jezek, P. A. Baggeroer and S. P. Gogineni, Ground–based radar observations of snow stratigraphy and melt processes in the percolation facies of the Greenland ice sheet, *Ann. Glaciol.*, *21*, 40–44, 1995.

MULTIFREQUENCY SCATTEROMETER MEASUREMENTS OF BALTIC SEA ICE DURING EMAC '95

M. Pettersson, W. Dierking and J. Askne

Department of Radio and Space Science, Chalmers University of Technology
S-412 96 Göteborg, Sweden
Ph.: +46 31 772 18 83, fax: +46 31 16 45 13, e-mail: mats@rss.chalmers.se

As part of the European Multi-Sensor Airborne Campaign 1995 (EMAC'95), the Microwave Airborne Campaign on Snow and Ice (MACST '95) took place in Finland and the Baltic Sea. Parallel to the acquisition of satellite and airborne sensor data from sea ice in the Baltic, various ground measurements were carried out during March and April, using the Finnish research vessel Aranda as an operational platform. The Swedish Remote Sensing Group from Chalmers University of Technology investigated the radar response of Baltic sea ice using a ship-based multifrequency scatterometer. The backscattering was measured at L-, S-, C- and X-band for all polarimetric combinations. In addition, we measured ice surface roughness and snow parameters. Ice volume parameters as density, salinity and air bubble size were analysed by the Finnish Institute of Marine Research. The objective of our investigations was to analyse the contribution of different scattering sources to the measured radar signal at various frequencies.

In order to separate the different scattering contributions we used the Integral Equation Method (IEM) for the ice surface and interfaces within the ice, and a model of independent Rayleigh scattering for inhomogeneities in the ice volume. In addition, the travel time of the radar waves is used to identify the sources of dominant scattering. We will present the results of our scatterometer measurements and the theoretical models. For wide area coverage other airborne and spaceborne sensors images will be analysed.

AIRBORNE LINE SCANNER MEASUREMENTS FOR ERS-1 SAR INTERPRETATION OF SEA ICE

Axel Bochert

Alfred-Wegener-Institut für Polar- und Meeresforschung
Columbusstrasse, D-27568 Bremerhaven, Germany
fax: +49 471 4831 149; e-mail: abochert@awi-bremerhaven.de

ABSTRACT

The potential of Synthetic Aperture Radar (SAR) images recorded with the First European Remote Sensing Satellite (ERS-1) for sea ice classification is investigated. The classification strategy employed is a region-based segmentation with subsequent interpretation of the segments. The formation of homogenious regions allows for a characterization by texture parameters besides backscatter coefficients.

To avoid a subjective selection and characterization of training segments two airborne line scanner systems, one for visible and the other for infrared digital images of the ice surface, are utilized for validation measurements. After the correction of the radiometric and geometric distortion of the line scanners the image data are classified in a two-dimensional feature space. After the co-location of the line scanner images with the segmented SAR data it is possible to derive the characteristics of different ice types from the radar signatures.

1. INTRODUCTION

Monitoring the ice covered seas is essential for the understanding of climate processes. Particularly the ice concentration and ice thickness are of interest for energy exchange between the ocean and the atmosphere. Since ice thickness cannot be monitored from satellites, the identification of sea ice types plays an important role in remote sensing of the polar environment.

Spaceborne multichannel passive microwave radiometers perform global monitoring of the sea ice coverage. For the validation of these data as well as for the study of small-scale processes ice maps of high spatial resolution and accuracy are necessary. The desired resolution is provided by the SAR of the ERS-1. The accuracy of the determination of different ice types can be examined through a validation with airborne line scanner measurements.

2. SENSORS

Two sensor systems are used in the presented work: the airborne line scanners, for visible and for infrared digital images of the surface, and the SAR carried by the ERS-1.

2.1 Line Scanner Systems

Essentially for the validation of satellite data, at the Alfred-Wegener-Institute different airborne line scanner systems were developed, which are sensitive in the visible spectral range and in the thermal infrared range [Bochert and Wamser, 1994]. Both systems consist of cross-track scanners which measure the intensity of surface signals perpendicularly to the flight track. The image lines consist of 512 pixels and are sampled with a frequency of 50 Hz. The image lines are continuously digitally converted and stored on the disk drive of a personal computer. When operated aboard a fast wing or helicopter aircraft, the line scanners are moved relatively to the ground. Due to the continuous recording of scans the second image dimension is achieved.

The Visible Line Scanner (VLS) measures the reflection of the solar radiation at the surface in the spectral range from $0.4\,\mu$m to $1.1\,\mu$m. A linear CCD-array (Charge Coupled Device) is used as detector. Generally it is possible to distinguish between three surface types with this camera: open water, snow covered ice and either melt ponds in summer or new ice in winter. In 1992 an Infrared Line Scanner (IRLS) was developed to improve the distinction of sea ice of different ages, which varies in thickness. The Infrared Line Scanner measures the surface temperature in a spectral range from $8\,\mu$m to $12\,\mu$m. From a technical point of view the Infrared Line Scanner is much more sophisticated than the Visible Line Scanner. The detector, which is a single element semiconductor, is cooled down to $-190°$C by a Stirling-cooler in order to improve the signal-to-noise ratio. Scanning is carried out by means of a mirror optic which consists of a fast rotating tetragon-mirror. During recording of the ground data the radiation of two temperature controlled plates is measured additionally as reference to achieve an absolute accuracy of about ± 1 K with a resolution of 0.1 K.

The two line scanners were mechanically and electrically connected for the combined operation. This

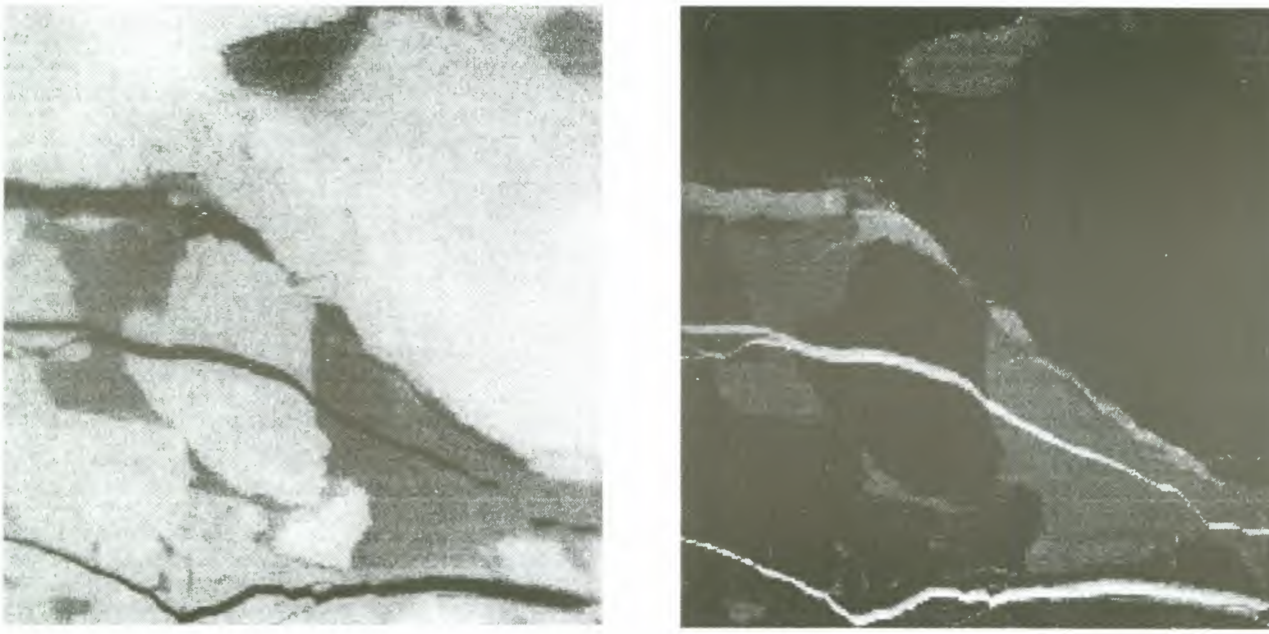

Figure 1: Image segment covering an ice area of 4 km x 4 km. The light areas represent high radiation intensities in both images. On the left hand side the intensity of the reflected sunlight is displayed uncalibrated. The temperature image on the right hand side shows temperatures between −25°C and −2°C.

enables the recording of the same field of view with both systems. For the validation with satellite data the system supports the storage of user comments and navigation data.

2.2 ERS-1 SAR

The ERS-1 was launched by the European Space Agency (ESA) in July 1991 [ESA, 1992]. The satellite payload includes an Active Microwave Instrument (AMI) with a Synthetic Aperture Radar (SAR). The SAR operates at a frequency of 5.3 GHz (C-band), at an incidence angle around 23° and with VV-polarisation (vertical on transmit, vertical on receive). In the image mode the SAR provides two-dimensional images with a high spatial resolution of about 30 m. During data acquisition the pixel spacing of the images is 12.5 m. The SAR obtains strips of 100 km in width to the right of the satellite track. For scientific use the strips are divided in subscenes of 100 km in length. The images are built up from the strength of the return signals of the radar, which primarily depends on the roughness and dielectric properties of the ground.

For this work Precision Images (PRI) are used, which are speckle reduced (multi-look) and system corrected. It is easy to geocode these images, a terrain distortion does not appear in ice covered seas.

3. PROCESSING THE LINE SCANNER IMAGES

Figure 1 shows an image segment covering an area of 4 km × 4 km. In both images the light areas represent high radiation intensities. The infrared image on the right hand side covers a temperature range between −25°C and −2°C. The image of the Visible Line Scanner on the left hand side is not calibrated. Comparing the images of the two spectral ranges the advantage of the Infrared Line Scanner becomes obvious: the image shows more distinct differences between various ice thicknesses and a better resolution of the boundaries from one ice type to another.

After the correction of the radiometric and geometric distortion of the line scanners the data are classified with the use of a two-dimensional feature space.

3.1 Visible Line Scanner

The data of the Visible Line Scanner are corrected with respect to the erratic disturbance, sensitivity variations along the image lines and variations of the illumination during a measuring flight.

Sensitivity variations in the cross-track direction derived from sensor inhomogeneities, vignette of the optic device, extinction of the atmosphere and angle dependent reflection of the solar radiation at the surface. Since the distortions have related effects and the measurements are in relative units, they were corrected simultaneously by an automatic data-derived correction function.

The variations of illumination during a measurement depend on the variable cloud conditions and sun elevation. For subsequent processing it is necessary to compensate this influence. This is done by his-

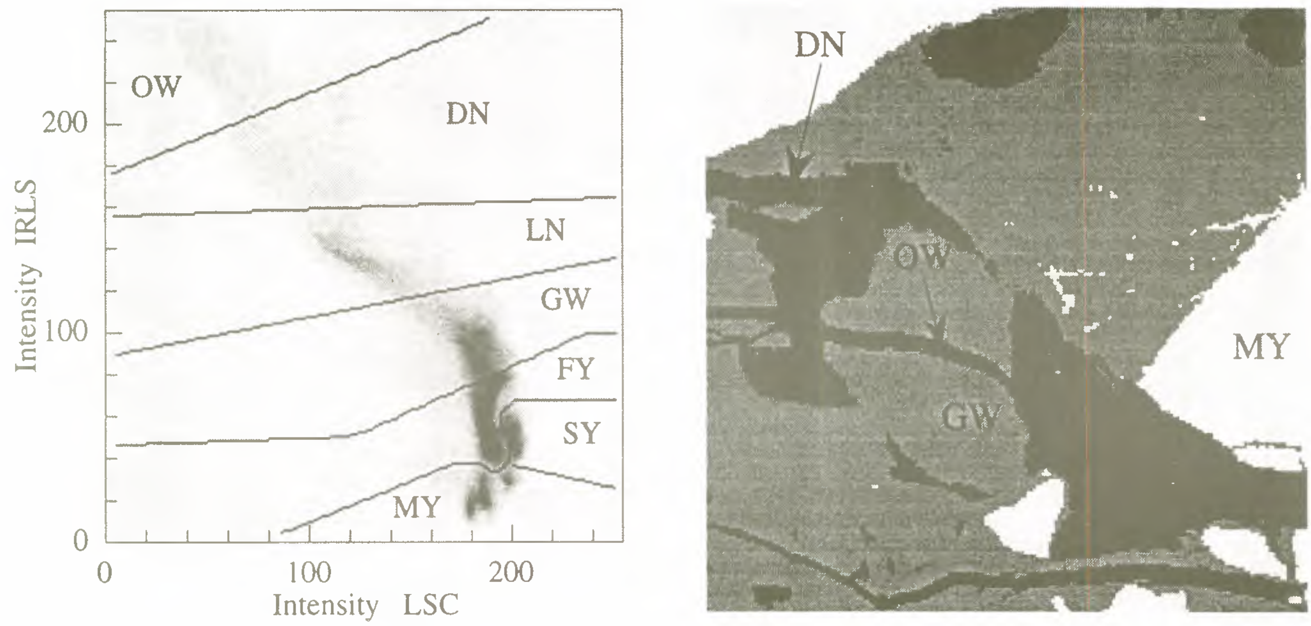

Figure 2: Two-dimensional histogram from an image of a long flight path. Figure 1 shows a subscene of this flight path. On the right hand side the classified line scanner subimage is shown. (OW - open water; DN - dark nilas; LN - light nilas; GW - gray-white ice; FY - first-year ice; SY - second-year ice; MY - multi-year ice

togram correlation of different image segments and interdependent scaling of the intensities.

3.2 Infrared Line Scanner

The radiometric measurement of absolute temperatures requires permanent calibration of the sensor signal. The Infrared Line Scanner contains two temperature controlled plates for reference measurements with different temperatures. These measurements result in a linear calibration function and allows for an accurate temperature computation at each image line.

Opto-mechanical cross-track scanners produce a characteristic geometric distortion of the images. The distance from the scanner to the ground is greater at either end of the scan line than at the nadir. As the scanner mirror rotates at a constant angular velocity, but the pixels are recorded at a constant linear rate, the sampling varies along the image line. This causes a compression toward the margin of the images, which is rectified.

Concerning the sea ice classification it is not necessary to achieve accurate absolute temperature images. But the temperature error should not be a function of the image coordinates, specially the angle of measurement. With the increased angle to the margins of the image the distance through the atmosphere increases and thus the atmospheric influence too. Furthermore the emissivity of the ice surface depends on the angle of view. These influences are corrected with a model of radiation transfer through the atmosphere and angle dependent emissivity.

3.3 Derivation of Sea Ice Maps

According to the different scanning principles and the mechanical adaption of the two systems, the images of the Visible Line Scanner and the Infrared Line Scanner have to be adjusted to each other. An example of a pair of combined images is shown in Figure 1. Each pixel of the images, i. e. each location on the ground contains the information of the visible spectrum and the thermal infrared spectrum. With the transformation of the image data into a two-dimensional histogram, it can be seen in Figure 2 that the intensity pairs of both spectral ranges accumulate in certain areas. This histogram allows to distinguish different ice types because it is possible to refer to the various surface temperatures in an area of homogeneous reflection or to different reflection characteristics in another area of equal temperature. In this way areas with the same type of ice can be recognized and ice charts of high spatial resolution and sufficient coverage can be achieved.

Due to the changing light conditions, air temperatures, and wind speeds it is not possible to achieve an automatic classification algorithm. For the present work an interactive classification algorithm has been established. As an example Figure 2 shows the result of an ice map of the region from Figure 1.

4. RADAR IMAGES

Radar images are of importance for small-scale process studies, and sensor intercomparisons due to the fact that radar signals are largely independent of daylight and weather conditions. Different parameters may be derived from radar images. These are mainly sea ice motion and ice concentration.

4.1 Processing the Radar Images

The first step of processing the PRI images is to derive backscatter coefficients. Although the radar images are system corrected, the measurements depend upon the incidence angle. The dependency arises from the physical projection of the radar signal upon the surface which is imaged. Thus derivation of backscatter coefficients which are dependent on the incidence angle have to follow the remarks from LAUR [1992]. His extreme low pass filtering for speckle reduction decreases the desired resolution of the SAR images. This prevents the analysis of the small-scale spatial variations in the backscatter coefficient from which the texture parameters are calculated. On the other hand texture analysis improves SAR image interpretation compared with the exclusive use of backscatter coefficients [NYSTUEN and GARCIA, 1992; SHOKR, 1991; SMITH *et al.*, 1995]. For texture analysis it is necessary to use as large areas of the images as possible to estimate the mean backscatter coefficient and the texture parameters for the reduction of the influence of speckle noise.

For the presented work a region-based parameter retrieval algorithm is implemented. This algorithm was introducted by SKRIVER [1989 and 1994] . The segmentation algorithm is based on an edge detection and a region growing technique. This algorithm is adapted to the low contrast edges and missing edge points of SAR images of sea ice.

The segmentation is carried out by in following steps. The edge detection delineates the segments of homogeneous backscatter coefficients. Due to the multiplicative nature of speckle noise it is not successful to use common difference-based methods. But the gamma ratio edge detector [MADSEN, 1986] generates an edge image independent of the intensities of the bordering areas. The gamma ratio edge detector generates very broad edges, but in addition a gradient direction image which supports an edge thinning to a width of one pixel [SKRIVER, 1994]. Due to speckle noise this image contains a large number of missing edge pixels and thus no completely separated segments.

Now a region growing algorithm is applied. The regions are growing simultaneously in gradient direction from kernel points until an edge pixel or another growing segment is reached. The kernels are derived from the maxima of the edge distance transformed edge image. To avoid multiple kernels for the same segment, close neighbouring maxima are merged to a single kernel.

The result of the region growing algorithm includes a large number of small segments which are unusable for a statistical segment interpretation. These small segments where merged to neighbouring segments by an iterative procedure. With each iteration the merging segment size increases and the test ratio of mean backscatter coefficients decreases. Normally with three iterations the radar image is segmented into useful segment sizes bigger than 500 pixels.

The segmented radar images are now available for parameter retrieval and with these parameters for the segment interpretation. In this work different parameters for each segment were calculated. The mean backscatter coefficient σ^o is determined by the average of the backscatter coefficient σ^{o*} of all single pixels

$$\sigma^o = E\Big[\sigma^{o*}(i)\Big]. \qquad (1)$$

The values of the property density function namely the normalized second-order moment (power to mean ratio) β_2, and the third-order central moment (skewness) γ_3 have devoted good results in the work of SKRIVER [1989].

$$\beta_2 = \frac{E\left[\left(\sigma^{o*}(i)\right)^2\right]}{\left(E[\sigma^{o*}(i)]\right)^2} \qquad (2)$$

$$\gamma_3 = \frac{E\left[\left(\sigma^{o*}(i) - E[\sigma^{o*}(i)]\right)^3\right]}{\left(E\left[\left(\sigma^{o*}(i) - E[\sigma^{o*}(i)]\right)^2\right]\right)^{\frac{3}{2}}} \qquad (3)$$

Three texture parameter are derived from the cooccurrance matrix introduced by HARALICK [1973]. SKRIVER [1994], SHOKR [1991] as well as NYSTUEN and GARCIA [1992] worked out that the contrast ξ_{CON}, the inverse difference moment ξ_{IDM} and the entropy ξ_{ENT} are of high potentional for sea ice discrimination in SAR images.

$$\xi_{CON} = \sum_i \sum_j \Big((i-j)^2 p(i,j)\Big) \qquad (4)$$

$$\xi_{IDM} = \sum_i \sum_j \frac{p(i,j)}{1+(i-j)^2} \qquad (5)$$

$$\xi_{ENT} = -\sum_i \sum_j \Big(p(i,j) log\big(p(i,j)\big)\Big), \qquad (6)$$

where $p(i,j)$ is the co-occurrance matrix with the dimensions i and j. These values are the average values of the different directional calculations with a fixed displacement of three pixels [HARALICK, 1973].

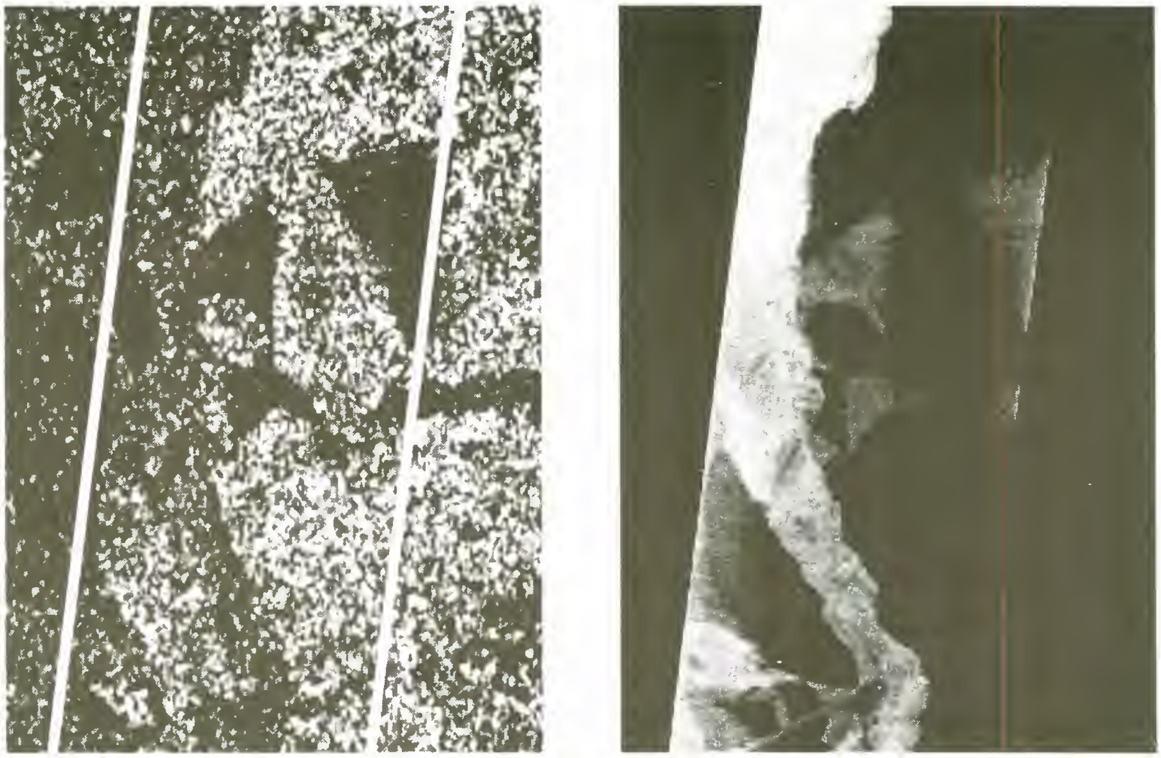

Figure 3: Subscene of a matched image pair with a size at ground of 3.7 km × 2.7 km. In the ERS-1 SAR image (©esa) on the left hand side the line scanner coverage is pointed out by two lines. The right image shows the data of the Infrared Line Scanner.

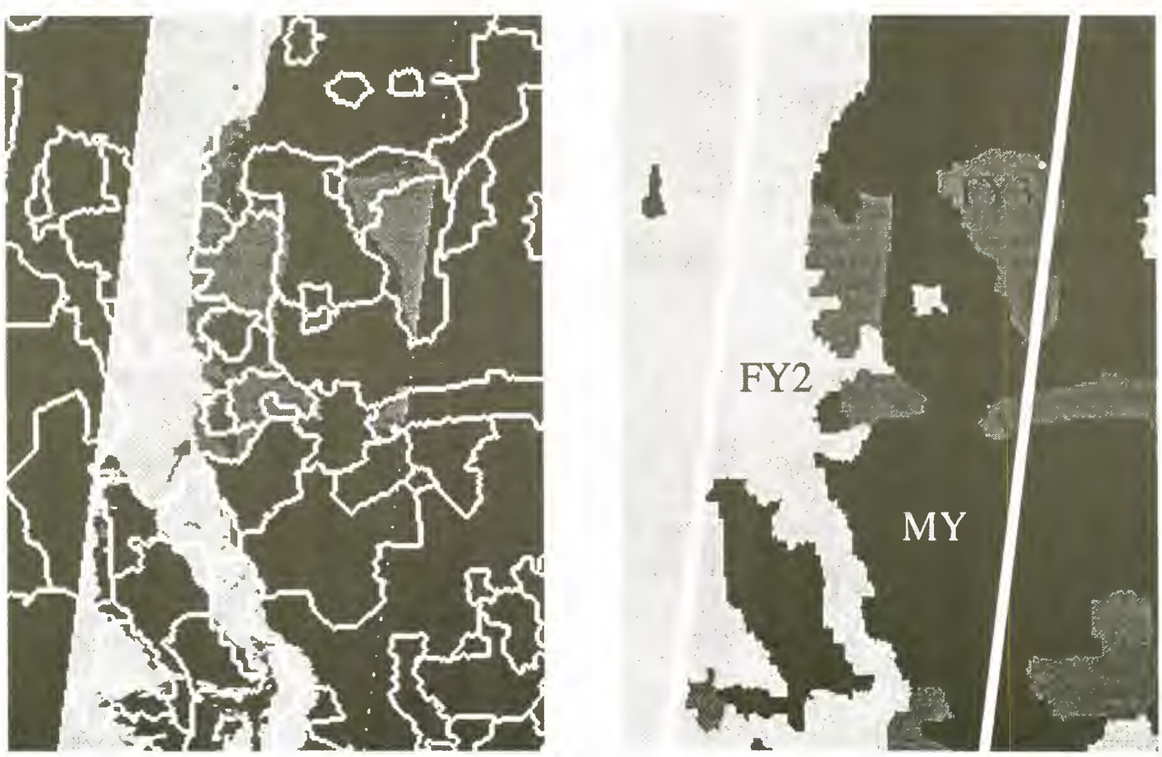

Figure 4: The left image shows the classified line scanner image overlain by the edges of the segmented radar image. The classified radar image is shown on the right. The images show a region of 3.7 km × 2.7 km. (FY2 - medium first-year ice; FY3 - thick first-year ice; MY - multi-year ice)

			line scanner classes in %		
			FY2	FY3	MY
			33,6	9,6	56,8
radar	FY2	32,4	95,3	0,0	0,7
classes	FY3	12,4	4,6	100,0	2,2
in %	MY	55,2	0,1	0,0	97,1

Table 1: Coverage of the ice types in the image of the line scanner and of the radar from Figure 4. The accuracy matrix shows a mean classification accuracy of 97.4%. (FY2 - medium first-year ice; FY3 - thick first-year ice; MY - multi-year ice)

The processing of the radar images results in a segmented image where each segment is represented with its mean backscatter coefficient and the mentioned texture values.

4.2 Fitting the Line Scanner Images

In order to enable the interpretation of the radar image with regard to the classified line scanner data these two data sets have to be matched. Due to the duration of the data acquisition with the line scanner the sea ice situation has changed in comparison with the radar image. Therefore the data sets cannot be matched with regard to the navigation data recorded by the aircraft. Two-dimensional correlation technique fails in spite of the different signatures of the images. Interactive fitting of subimages of the line scanner data proved to be a successful technique. Figure 3 shows a matched subimage with the radar image and the image of the temperature of the Infrared Line Scanner as it will be used for the interpretation of the radar image.

4.3 Procedure of Interpretation

The interpretation of the radar segments starts with the analysis of the region covered by the line scanners. Figure 4 contains on the left hand side the classified line scanner data overlain by the edges of the radar segments. We can see fairly good matching between these two data sets. Only at the edges of the segments a displacement of some pixels can be observed. The radar segments which are covered by the line scanner data serve as training regions to calculate the radar signatures for each ice type. To avoid the influence of the small displacement the radar segments are interpreted as the dominant ice type in the respective segment, derived from the line scanner image.

In the presented image we have three ice types, medium first-year ice (FY2), thick first-year ice (FY3) and multi-year ice (MY). Table 1 shows the coverage of these ice types in the line scanner image as 33.6%, 9.6% and 56.8% respectively. With a trained minimum distance classifier the radar segments are classified to the relevant ice types. This classifier works out the significant texture parameters of the radar images and applies them for the subsequent classification. In the small example image beside the backscatter coefficient σ^0 only the normalized second-order moment β_2 and the inverse difference moment ξ_{IDM} are used. The left side of Table 1 contains the coverage of the ice types in the radar image. The other part of the table serves as a accuracy matrix which shows the correspondence of the classified radar segments with the line scanner data.

5. CONCLUSION

With the introduced line scanner systems installed on research aircrafts it is possible to record images for the interpretation of satellite data. The spatial resolution of these systems is approximately the same as of the SAR, the covered area is sufficient for the validation of SAR data of the ERS-1. Beside the validation a measure for the significance of the classification parameter is obtained. These are the backscatter coefficient and texture parameters. The analysis of a test region with the size of 2.7 km × 3.7 km shows a good result of the radar classification with a mean classification accuracy of 97.4% (see Table 1). This implies that the introduced method is capable of interpretating ERS-1 SAR images, which allows for a large scale validation.

6. REFERENCES

BOCHERT, A.; WAMSER, CH.: *New Airborne Line Scanner Systems for High Resolution Sea Ice Observation.* The Global Atmosphere and Ocean System. Vol. 2. pp. 247–251. 1994

BOCHERT, A.: *Klassifikation von Radarsatellitendaten zur Meereiserkennung mit Hilfe von Line-Scanner-Messungen.* Berichte zur Polarforschung. Alfred-Wegener-Institut. Bremerhaven. In preparation.

ESA: *ERS-1 System. ESA SP-1146.* European Space Agency. 1992

HARALICK, R.M.; SHANMUGAM, K.; DINSTEIN, I.: *Textural features for image classification.* IEEE Trans. Syst. Man Cybern.. Vol. 3. pp. 610–621. 1973

LAUR, H.: *Derivation of Backscatter Coefficient σ° in ERS-1.SAR.PRI Products.* ESA. 1992

MADSEN, S.N.: *Speckle Theory. Modelling, Analysis and Applications related to Synthetic Aperture Radar Data.* Ph. D. Thesis. LD 62. Electromagnetics Institute. Technical University of Denmark. 1986

NYSTUEN, J.A.; GARCIA, F.W.: *Sea Ice Classification Using SAR Backscatter Statistics.* IEEE Transactions on Geoscience and Remote Sensing. Vol. 30. No. 3. 1992

SHOKR, M.E.: *Evaluation of Second-Order Texture Parameters for Sea Ice Classification from Radar Images.* J. Geophys. Res.. Vol. 96. No. C6. pp. 10625–10640. 1991

SKRIVER, H.: *Extraction of Sea Ice Parameters from Synthetic Aperture Radar Images.* Ph. D. Thesis. LD 74. Electromagnetics Institute. Technical University of Denmark. 1989

SKRIVER, H.: *On the Accuracy of Estimation of Ice Type Concentration from ERS-1 SAR Images.* Proceedings 14th EARSel Symposium. Gothenborg. 1994

SMITH, D.M.; BARRETT, E.C.; SCOTT, J.C.: *Sea-Ice Type Classification from ERS-1 SAR Data based on Grey-Level and Texture Information.* Polar Record 31 (177). pp. 135–146. 1995

ARCTIC OCEAN MELT SEASON CHARACTERISTICS AND SEA ICE MELT POND FRACTIONS USING ERS–1 SAR

M. O. Jeffries, K. Schwartz and S. Li

Geophysical Institute, University of Alaska Fairbanks
903 Koyukuk Drive, P.O. Box 757320
Fairbanks, AK 99775–7320, U.S.A.
phone: 1–907–474–5257, fax: 1–907–474–5257
martin.jeffries@gi.alaska.edu, sli@iias.images.alaska.edu

ABSTRACT

Variations in multiyear sea ice backscatter in ERS–1 SAR images are interpreted in terms of spring melt onset, autumn freeze–up, and duration of the snow decay period, the melt season and the melt pond season in the north–eastern Beaufort Sea adjacent to the Queen Elizabeth Islands in the Canadian High Arctic and in the western Beaufort Sea north of Alaska. The melt season characteristics of each area are consistent with previous observations that the north–eastern Beaufort Sea has one of the most severe summer climates in the entire Arctic Ocean. A model, which assumes that the backscatter from multiyear floes is the sum of backscatter from bare ice and melt ponds, is used to derive the melt pond fraction during the summer. Melt pond fractions decrease from an early summer maximum of about 60% to a late summer minimum around 20%. The decline in melt pond fraction is consistent with previous, more qualitative, observations and there is reasonable agreement between the SAR–derived values and previous estimates.

INTRODUCTION

ERS–1 SAR data have been used primarily for studying the winter Arctic sea ice cover, since winter ice dynamics and growth play a key role in air–ice–ocean interactions that affect the regional and global climate. There have been fewer studies of the summer sea ice cover with ERS–1 SAR data. Winebrenner et al. (1994) determined that spaceborne SAR data can be used to identify the onset of melt in spring, and noted that this might serve as a useful indicator of climate change at high latitudes. The onset of freeze–up at the end of summer has also been documented with ERS–1 SAR data (Holt et al., 1993; Schwartz, 1994). This too might be a useful climatic indicator and together with melt onset data would give the duration of the melt season.

During much of the melt season the sea ice surface in the Arctic is a mixture of melt ponds and bare ice. Quantitative data on the spatial and temporal variability of the fractional coverage of melt ponds on the ice surface are required to improve albedo parameterization and the performance of numerical thermodynamic models that are used to investigate air–ice–ocean interactions and the sensitivity of the sea ice to climate change. (Ebert and Curry, 1993).

Most of the currently available data on melt pond fractions appear to have been acquired by qualitative, visual estimates made in different years in different parts of the Arctic Ocean and they do not cover an entire melt season (Grenfell and Maykut, 1977; Maykut, 1986). Using aerial photography, only Langleben (1971) appears to have produced a more quantitative data set on the temporal variability of the melt pond fraction. Askne et al. (1994) used ERS–1 SAR data to determine melt pond fractions in late August in the eastern Arctic.

In this paper we discuss the spring to autumn ERS–1 SAR signatures of multiyear ice, melt season characteristics and melt pond fractions for two different regions of the Beaufort Sea, Arctic Ocean. Backscatter time–series for each region are interpreted in terms of changes in the state of the surface of the sea ice, including the onset of melt, the removal of the winter snow cover, and the onset of freeze–up. These are then used to define the duration of the melt season and the melt pond season. A model to derive melt pond fractions is described and the resultant data are discussed with respect to currently available data.

STUDY AREAS AND ANALYSIS

Two small regions of the Beaufort Sea were selected for this study: (1) an area of the western Beaufort Sea between latitudes 71°N and 77°N, and longitudes 154°W and 164°W, about 450km north of Barrow, Alaska; and (2) an area of the north–eastern Beaufort Sea between latitudes 80°N and 81°N, and longitudes 100°W and 110°W immediately adjacent to the Queen Elizabeth Islands, Canadian High Arctic. These regions were chosen because of their contrasting ice and summer climate conditions; in the north–eastern Beaufort Sea, the sea ice is older and thicker, and the summers shorter and more severe than those elsewhere in the Canada Basin of the Arctic Ocean (Alt and Edlund, 1989; Bourke and Maclaren, 1992).

Proceedings of the Fourth Symposium on Remote Sensing of the Polar Environments, Lyngby, Denmark, 29 April – 1 May 1996
(ESA SP-391, July 1996)

The ERS–1 backscatter data, σ°, were derived from radiometrically corrected Standard Low Resolution SAR images from the Alaska SAR Facility. Each image has a spatial resolution of 240m, a pixel size of 100m and ground dimensions of 100km by 100km. The absolute calibration of the ASF ERS–1 data is better than ± 1 dB (A. Freeman, pers. comm., 1994). Therefore, changes in backscatter of more than 1 dB can be assumed to be caused by changes in the physical properties of the surface being examined, and not by changes in the instrument.

Period 2 begins in late May and ends in mid–June; σ° fluctuates between -9 and –12 dB and air temperatures oscillate about 0°C. Such fluctuations in backscatter are probably the result of freeze/thaw cycles and their effects on snow wetness (Winebrenner et al., 1994; Drinkwater, 1995).

Period 3 lasts from mid–June, when there is an initial sharp decrease in σ° from –12 dB to –19 dB in only three days,

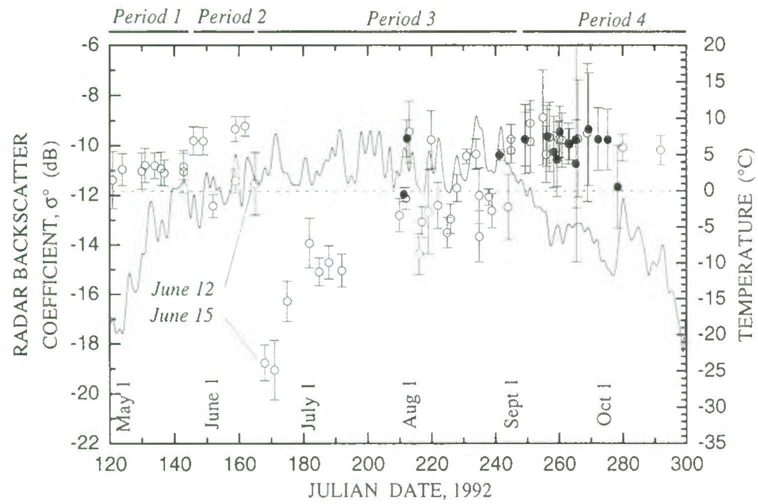

Fig. 1. Multiyear sea ice SAR backscatter (circles) and daily mean temperature (solid line) variability from spring to autumn 1992 in the western Beaufort Sea. The open and closed circles are for data derived from ascending and descending orbits respectively. Each circle represents the mean ± 1 standard deviation of the backscatter of multiple floes in SAR images on a given date. The broken horizontal line represents a temperature of 0°C. Periods 1 to 4 are discussed in the text.

A total of 88 and 40 images of the western and north–eastern Beaufort Sea study areas respectively were analyzed on a computer for the period spring to autumn 1992. Image analysis focussed on obtaining σ° statistics for individual ice floes. Most of the floes that were chosen had a diameter of at least 1km, were relatively homogenous and contained as few ridges (sources of strong backscatter) as possible. A mean σ° value was computed for rectangular areas outlined within each floe. Typically, 20 large floes were selected for measurement in each image and a mean and standard deviation σ° value was calculated for all those floes. The average number of pixels analysed in each image was 14,000±4000.

SAR SIGNATURES

The time–series of backscatter variability for the western Beaufort Sea and a temperature record for Barrow, N.W. Alaska, from spring to early autumn are presented in Figure 1. Four periods of backscatter variability are identified.

Period 1, corresponding to late winter, lasts until late May. The typical backscatter is –11 dB, with little day to day variation, and temperatures are 0°C. The σ° values are typical of those for multiyear sea ice in this area in late winter when the snow cover is dry (Kwok and Cunningham, 1994).

until late August, when σ°primarily is in the range –10 to –14 db. With few exceptions, air temperatures during this period are >0°C.

The precipitous decline in backscatter occurs when temperatures rise above 0°C and there are no further freeze/thaw cycles. This represents the onset of the melt season when significant moisture in the snow cover attenuates the radar signal and greatly reduces the returns (Winebrenner et al., 1994).

After the steep decline associated with the onset of melt, σ° values recover to about –14 dB in early July. This backscatter recovery period represents the time when the snow cover is decaying. As the snow decays its wetness increases significantly and together with the surface roughness this increases the backscatter (Shi and Dozier, 1996). Late in the snow decay period, when much of the snow cover has melted, backscatter can increase due to the existence of a short–lived, rough superimposed ice layer at the ice floe surface (Onstott et al., 1987).

There is a slight decrease in σ° values in mid–July, from –14 to –15dB, which might represent the final disappearance of the saturated snow cover and any superimposed ice layers. At this time the ice surface becomes a mixture of melt ponds and bare sea ice, except for occasional summer snowfalls. From early July to late August there is a trend to higher σ° values.

Period 4 begins in early September when temperatures fall and remain below 0°C and $\sigma°$ values increase by about 2 dB. The backscatter drop coincides with the end of the melt season and the onset of freeze–up when the melt ponds freeze over (Schwartz, 1994). As the sea ice surface begins to cool, the free water on the bare ice surface freezes, and the dominant scattering mechanism changes from surface to volume scattering and there is an overall increase in backscatter (Carlström and Ulander, 1993; Beaven and Gogineni, 1994).

The backscatter record for the north–eastern Beaufort Sea is similar to that in the western Beaufort Sea, with distinct changes in backscatter in spring and autumn associated with temperatures rising above and falling below 0°C respectively.

MELT SEASON CHARACTERISTICS

The steep decline in backscatter in spring marks the onset of the melt season (Winebrenner et al., 1994). This occurs 9 days later in the north–eastern Beaufort Sea than in the western Beaufort Sea (Fig. 2). The date of melt onset in the north–eastern Beaufort Sea is only one day later than the long–term average for this region (Edlund and Alt, 1989). This, and the longer period of snow cover decay in the north–eastern Beaufort Sea (Fig. 3) are consistent with a climate that is cooler than elsewhere in the N. American Arctic (Edlund and Alt, 1989). The duration of snow cover decay in the western Beaufort Sea (Fig. 2) is typical of this region of the Arctic Ocean where snow cover removal generally takes 22 days (Barry et al., 1993).

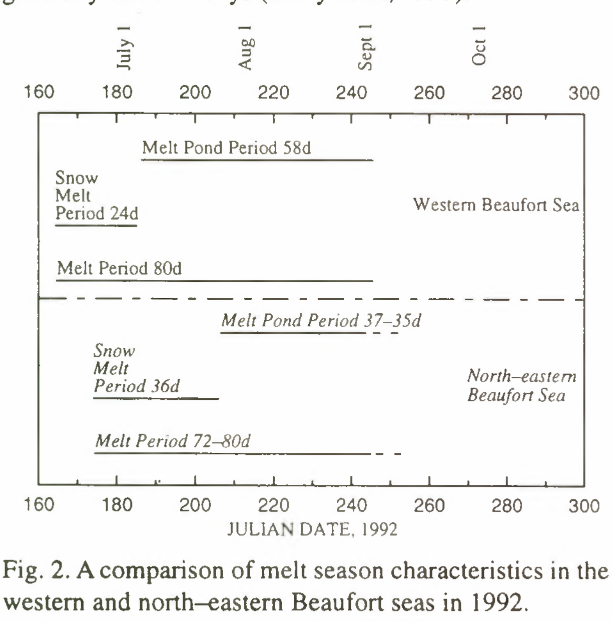

Fig. 2. A comparison of melt season characteristics in the western and north–eastern Beaufort seas in 1992.

In the north–eastern Beaufort Sea we have defined an 8–day period during which freeze–up must have occurred, as there are insufficient SAR data available to be more accurate. We define the melt season as being from the onset of melt in June to the onset of freeze–up in late August/early September. Thus the melt season is as much as 8 days shorter, and certainly no longer, in the north–eastern Beaufort Sea than in the western Beaufort Sea (Fig. 2).

We define the duration of the melt pond season, or snow–free period, as being from the time the previous winter's snow cover is completely removed until the onset of autumn freeze–up. The melt pond season in the north–eastern Beaufort Sea is significantly shorter than in the western Beaufort Sea (Fig. 2), and 20–28 days shorter than the long–term average for the region (Edlund and Alt, 1989). This very short melt pond season in 1992 is consistent with a Canadian Arctic summer that was as much as 2°C cooler than normal and resulted in a difficult shipping season (Environment Canada, 1992).

In the western Beaufort Sea, once the snow has been removed from the ice surface in the early part of Period 3, the remainder of the period is characterized by a trend to higher $\sigma°$ values. In the north–eastern Beaufort Sea, the trend to higher $\sigma°$ values begins in early August. We interpret this trend to be due to the gradual drainage of melt ponds and the exposure of additional bare ice during the course of the summer; a phenomenon reported by Grenfell and Maykut (1977).

MELT POND FRACTIONS

Even though the melt ponds can not be resolved in the ERS–1 SAR images used for this investigation, as the size of a pixel is large compared to the size of the melt ponds, their presence has an effect on the backscatter. The backscatter of a pixel can be considered to be the sum of the energy returned from all of the scatterers within the pixel. In this model a large multiyear floe is considered to be composed of bare ice and melt ponds.

If the backscatter value, $\sigma°$ in dB, measured for a floe in a SAR image is the sum of the backscatter from melt ponds and bare ice, and P_0 is the reference power which would be received from a Lambert reflector, then the power, P, received from a target equals

$$P_o\, 10^{(\sigma°/10)} \qquad (1).$$

If σ_m is the estimated backscatter coefficient for melt ponds in dB, σ_i is the estimated backscatter coefficient for bare ice in dB, f_m is the areal fraction of the floe covered with melt pools, and $1-f_m$ is the bare ice fraction, then the backscatter coefficient, $\sigma°$, equals

$$10\cdot\log_{10}\left[f_m\cdot 10^{(\sigma m/10)} + (1-f_m)\cdot 10^{(\sigma i/10)}\right] \qquad (2).$$

i.e., $\sigma° = 10\cdot\log_{10}$ [(energy from melt pools) +(energy from bare ice)]

When solved for f_m, the areal fraction of melt ponds is

$$\frac{10^{(\sigma^\circ/10)} - 10^{(\sigma i/10)}}{10^{(\sigma m/10)} - 10^{(\sigma i/10)}} \qquad (3).$$

A value of –14 dB is used for σ_i (Carlström and Ulander, 1993). A value of –25 dB, the backscatter measured for wind–free leads between floes in the ERS–1 SAR images, is used for σ_m. With these values, equation (3) gives the melt pond coverage of floes as a function of backscatter (Fig. 3). The computation of the areal fraction of melt pools is more sensitive to the estimate of σ_i than it is to the estimate of σ_m.

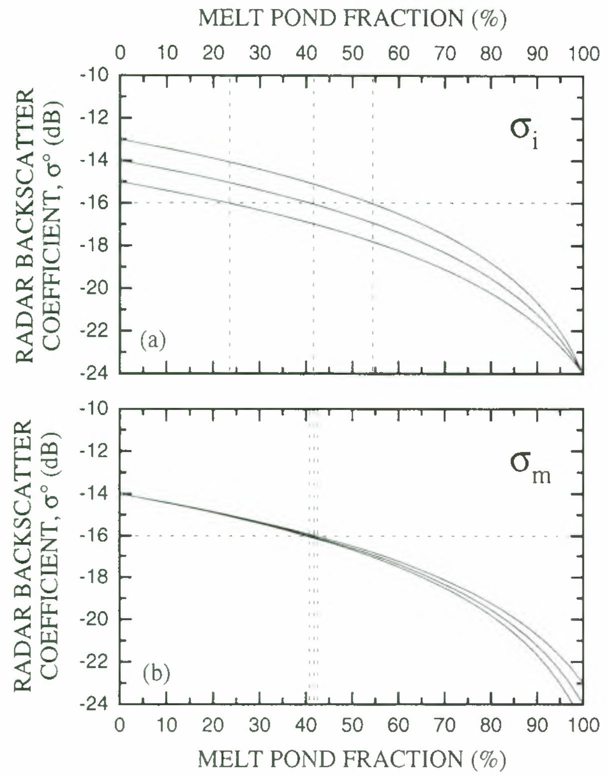

Fig. 3. The melt pond fraction of ice floes derived using equation 3. The broken horizontal line shows that a backscatter value of –16 dB, for example, corresponds to a 42% melt pond fraction. The graphs indicate the sensitivity of the melt pond fraction estimates to (a) a ±1dB variation in the estimate of the bare ice backscatter (σ_i) and (b) a ±1 dB variation in the estimate of the melt pond backscatter (σ_m). The three broken vertical lines in each graph indicate the melt pond fractions arising from the choice of σ_i ± 1 dB and σ_m ± 1 dB.

Using equation (3), the melt pond fraction of floes has been derived from the σ° values for the melt pond season in each study area (Fig. 4). In the western Beaufort Sea, melt pond coverage is highest immediately after the disappearance of the snow cover, and then declines steadily during the summer, reaching a minimum immediately prior to freeze–up. In the north–eastern Beaufort Sea, the maximum melt pond coverage does not occur until early August. Prior to that, melt pond fraction values are relatively low. A different pattern of melt pond cover development during July in the north–eastern Beaufort Sea might reflect differences in ice surface characteristics and melt pond evolution in this area where the ice is extremely deformed. This might have been enhanced by high air temperatures during this interim period and their effects on ice surface properties and backscatter characteristics.

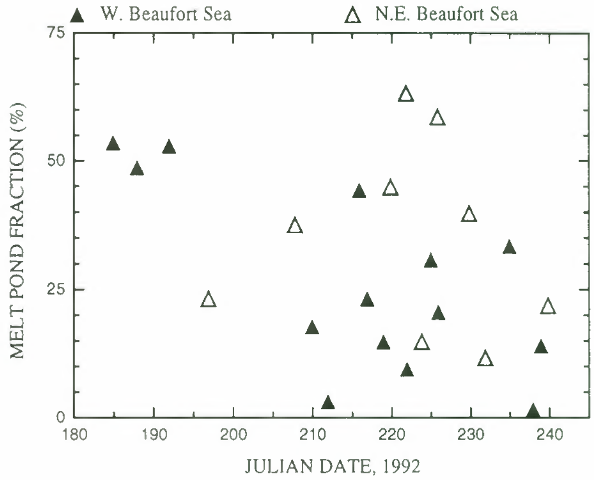

Fig. 4. Melt pond fraction of ice floes as a function of time in the western Beaufort Sea and the north–eastern Beaufort Sea. The data are calculated using equation 3 to convert the mean backscatter values during the melt pond season to melt pond fractions.

Some sense of the reasonableness of these melt pond fractions and their temporal change can be obtained by examining data available in the sea ice literature, such as it is. Early in the melt season, melt pond fractions of 80% have been measured in aerial photographs of the southern Beaufort Sea ice (Langleben, 1971). Visual estimates of melt pond fractions in the pack ice indicate that they reach a maximum of >50% immediately after the disappearance of the snow cover, and as summer progresses and the ponds drain and additional bare ice is exposed, the fraction decreases to about 30% in mid–summer and reduces to about 10% by the end of summer (Grenfell and Maykut, 1977; Maykut, 1986). However, even late in the melt cycle, melt ponds may account of 60% or more of the surface area of floes (Maykut, 1986).

The SAR–derived data follow this general pattern of a decreasing melt pond fraction and there is reasonable agreement between these data and previous observations and estimates. Locally high melt pond fractions might explain some of the variability observed in the SAR–derived data. Differences between previous observations and the SAR–derived melt pond fractions might also be due to the somewhat qualitative nature of the former, and the effects of environmental factors (temperature, snow cover, wind) on the latter. The SAR–derived melt pond fractions immediately prior to freeze–up (Figure 4) are similar to those determined from SAR data for the late melt period in August 1991 in the area north of Svalbard (Askne et al., 1994).

DISCUSSION AND CONCLUSION

Spaceborne SAR backscatter data of multiyear sea ice from spring to early autumn in two regions of the Beaufort Sea, Arctic Ocean, have been presented. Backscatter variability has been interpreted in terms of melt season characteristics. The information contained in the backscatter records provides some insight into the temporal and spatial variability of the nature of the melt season in the Arctic Ocean, and suggests that SAR data could be used for long-term monitoring of summer environmental variability and its effects on much larger areas of the pack ice.

Improvements to the description of the melt season characteristics and parameters would include more frequent SAR data coverage and availability. More frequent data acquisition would improve the identification of the timing of significant melt season events and the determination of the duration of the different melt season periods.

A model for the calculation of melt pond fractions on sea ice floes using SAR backscatter variability has been presented. The melt pond fractions, their variability at any given time, and their temporal change determined in this study appear to be reasonably close to observed values and patterns. Differences between the calculated and observed values may be due more to the qualitative nature of most previous melt pond estimates rather than any significant errors in the SAR model estimates.

Given the limited understanding of the factors affecting backscatter from summer sea ice, the results of this study suggest that there is some potential in the use of SAR to derive spatial and temporal statistics of melt pond fractions for much larger areas of the Arctic Ocean. Such data would be beneficial for understanding the heat and mass balance of the ice cover, and for numerical modelling of sea ice growth and decay and its sensitivity to climate change.

ACKNOWLEDGEMENTS

This work was supported by Grant No. DPP–9122948 from the Office of Polar Programs at the National Science Foundation.

REFERENCES

Askne, J., L. M. H. Ulander, A. Carlström, Yan Sun and M. Pettersson. 1994. Validation of ERS–1 SAR for Arctic ice properties from ARCTIC–91. In: *Proceedings of the second ERS–1 symposium; space at the service of our environment, 11–14 October 1993, Hamburg, Germany*. Paris; European Space Agency (ESA SP–361): 257–262.

Beaven, S. G. and S. P. Gogineni. 1994. Shipborne radar backscatter measurements from Arctic sea ice during the fall freeze–up. *Remote Sens. Rev.*, 9, 3–25.

Bourke, R. H. and A. S. McLaren. 1992. Contour mapping of Arctic Basin ice draft and roughness parameters. *J. Geophys. Res.*, 97, 17,715–17,728.

Carlström, A. and L. M. Ulander. 1993. C–band backscatter of old sea ice in the central Arctic during freeze–up. *IEEE Trans. Geosci. Remote Sens.*, 31, 819–829.

Drinkwater, M. 1995. Airborne and satellite SAR investigations of sea–ice surface characteristics. In: Ikeda, M. and F. W. Dobson (eds). *Oceanographic Applications of Remote Sensing*. Boca Raton, Florida: CRC Press, 339–357.

Ebert, E. E. and J. A. Curry. 1993. An intermediate one–dimensional thermodynamic sea ice model for investigating ice–atmosphere interactions. *J. Geophys. Res.*, 98, 10,085–10,109.

Edlund, S. A. and B. T. Alt. 1989. Regional congruence of vegetation and summer climate patterns in the Queen Elizabeth Islands, Northwest Territories, Canada. *Arctic*, 42, 3–23.

Environment Canada. 1992. *Climate Perspectives: A Weekly Review of Canadian Climate and Weather* 14 (14–20 September):1.

Grenfell, T. C. and G. A. Maykut. 1977. The optical properties of ice and snow in the Arctic Basin. *J. Glaciol.*, 18, 445–463.

Holt, B., G. Cunningham and R. Kwok. 1993. Sea ice radar signatures from ERS–1 during late summer and fall in the Beaufort and Chukchi Seas. In: *Proceedings of the first ERS–1 symposium; space at the service of our environment, Cannes, France*. Paris: European Space Agency (ESA SP–359). pp.339–342.

Kwok, R. and G. F. Cunningham. 1994. Backscatter characteristics of the winter sea ice cover in the Beaufort Sea. *J. Geophys. Res.*, 99, 7787–7802.

Langleben, M. P. 1971. Albedo of melting sea ice in the southern Beaufort Sea. *J. Glaciol.*, 10, 101–104.

Maykut, G. A. 1986. The surface heat and mass balance. In: Untersteiner, N. (editor). *The Geophysics of Sea Ice*: New York and London: Plenum Press. pp.395–463.

Onstott, R. G., T. C. Grenfell, C. Mätzler, C. A. Luther and E. A. Svendsen. 1987. Evolution of microwave signatures of sea ice signatures during early summer and midsummer in the marginal ice zone. *J. Geophys. Res.*, 92, 6825–6835.

Schwartz, K. 1994. Variations in the state of the Arctic Ocean sea ice surface from late winter to fall determined from ERS–1 SAR data. *MS Thesis*, University of Alaska Fairbanks.

Shi., J. and J. Dozier. In press. Inferring snow wetness using C–bands data from SIR–C's polarimetric synthetic aperture radar. *IEEE Trans. Geosci. Remote Sens.*, 1996.

Winebrenner, D. P., E. D. Nelson and R. Colony. 1994. Observation of melt onset on multiyear Arctic sea ice using ERS–1 SAR. *J. Geophys. Res.*, 99, 22,425–22,441.

AIR MONITORING OF ICE CONDITIONS IN THE ARCTIC SEAS

Vladimir I. Chernook, Vladimir B. Zabavnikov

Knipovich Polar Research Institute of Marine Fisheries and Oceanography (PINRO)
6, Knipovich Street, Murmansk, 183763 Russia
phone: +47-789-10 423 —fax: +47-789-10 518 — e-mail: pinro@imr.no

ABSTRACT

The development of the Arctic relies on active navigation in the seas surrounding this region. To increase ship speed and ensure navigation safety, a good knowledge of ice conditions is required. The relevant information can be obtained with high efficiency by airborne surveys.

To get the maximum possible of high-quality information and an efficient interpretation of data on ice conditions, remote sensing must be carried out in several spectral ranges of the electromagnetic waves using complex equipment operating in the whole spectrum.

Processing of radar, IR and video-images is performed operatively on board the aircraft as well as thematically in coastal centres. For automatic control of data acquisition, real-time integration and processing, an onboard computer system is used. For communication and exchange of information with vessels and coastal centres, the aircraft is equipped with AM and FM radios. Besides the transfer of data may be executed through Inmarsat satellites.

INTRODUCTION

The development of a vast Arctic region of Russia requires development of active navigation in the seas of the Arctic Ocean. To ensure safe navigation, it is necessary to have, on the one hand, qualitative meteorological, hydrological and ice forecasts, and, on the other hand, reliable knowledge and data on the ice conditions; this information can be obtained by surveys from coastal stations, ships and remote-sensing platforms.

Long experience of marine drifting ice and practice in the so-called marine Arctic operations have shown that efficient and high-quality information can be obtained from airborne and space-borne platforms. The preference is given to air-survey data since the information here has more authentic, operative character and higher resolution.

The first regular air surveys of marine drifting ice started in 1930 with the active development of a line in the Northern Sea Route (NSR). In that time air surveys were performed only by visual observations.

For more than 60 years, air researches on marine drifting ice in the Arctic pool have been going from simple visual air surveys to complex technologies based on multiband instrumentation and modern onboard computer systems (PC's...)

To obtain the maximaum possible volume of high-quality information and an efficient interpretation of data on ice conditions, it is necessary to perform remote sensing of marine surface in several spectral ranges of the electromagnetic waves.

An urgent problem is the rational organisation and optimisation of airborne surveys, which permit to receive, at minimum costs, qualitative information on the characteristics and distribution of marine ice.

Air surveys of the seas of the Arctic pool using multiband remote sensing is regularly and successfully performed during recent years by experts of PINRO on board a laboratory aircraft (IL-18 D 'Pomor') equipped with visible, IR and radio instruments. A wide range of applied sciences problems is addressed, mainly airborne research on ice conditions of the Arctic seas.

The main purpose of this work is to provide:
- navigation safety for Murmansk Shipping Company's ships to Northern Pole and on a line of NSR;
- navigation safety for fishing vessels at the edge zone of marine drifting ice;
- information service in support to the Defence Ministry;
- safety for oil and gas extraction and transportation of raw materials in outlying seas of the Russian North.

Information processing is performed on board the aircraft laboratory as well as on the ground using modern computer systems and software in real coordinates and time.

Proceedings of the Fourth Symposium on Remote Sensing of the Polar Environments, Lyngby, Denmark, 29 April – 1 May 1996
(ESA SP-391, July 1996)

REMOTE SENSING MEANS AND METHODS FOR MARINE DRIFTING ICE

Originally ice investigations from aircraft had visual character. Due to the high resolution obtained and the large experience of hydrologists/observers, visual surveys are still carried out presently as an element of ice aerial survey. Visual surveys are carried out from 200-300 m height or below the bottom layer of clouds. No significant aircraft re-equipment is required. During the visual survey the observers can determine all main characteristics of ice cover.

Together with this, visual aerial survey of marine ice is performed in a comparatively narrow strip of view, from 2 up to 20 heights of flight, at minimum distance between surveying tacks of 30 km. This results in significant errors of interpolation between them and miss of those or other objects, describing condition of the ice cover. Besides, visual survey depends to a large extent on light and weather conditions, subjectivism and experience of the observers, as well as on errors in the quantitative evaluations of ice conditions.

For these reasons, visual ice aerial surveys cannot yet fully satisfy the increasing operation requirements. Thus for the last 30-35 years, instruments and methods for ice condition determination have received a substantial development.

To get complex and detailed information on ice cover, it is necessary to operate remote sensing instruments in various areas of the electro-magnetic spectrum. For this purpose, in recent years, equipment working in the visible, IR and radio wavelengths is applied.

First of all, the following measuring complexes are required:
- Visible range – photo and video equipment of various systems;
- IR range – IR radiometers and thermovisions of various types and systems;
- Radio range – radiometers, side-looking air-borne radars (SLAR) and synthetic aperture radars (SAR), ice thickness meters.

The aerial photography is conventional and rather precise method of reception of information about the ice cover condition. The main advantage of aerial photography is high resolution and affinity of the image to the natural one, perceived by human eye. But its essential defects are duration and complexity of processing of the photos that sharply reduces effectiveness of work, dependence on weather conditions.

Various video equipment finds growing application at ice aerial surveyes. In the last years their resolution has considerably increased, colour transfer has improved, weight and dimensions have decreased, management simplicity and operation reliability have increased.

The advantage of video survey as compared with aerial photography consists in the opportunity of recording images on magnetic tapes, operative inputing in onboard computer and automated processing.

For navigation safety among marine drifting ice it is necessary to know the characteristics of ice-hummocks, which are determined on photo-, video- and IR-images and with the help of laser profilemeter.

Data on space distribution of temperature of ice and water surface are received with the help of thermovisions. This permits to predict the terms and centres of ice forming and natural thawing, as well as the position of an ice edge.

Thermal aerial survey in the wavelength of 8-14 μm allows ice exploration in a dark time of the day and in the polar night, thus determining, with a sufficient degree of reliability, presence of cracks and fractures, hummocking and condition of snow-and-ice cover, as well as age characteristics of ice.

In the last years, for determination of radio brightness temperature of natural objects, passive UHF-radiometers have been used; their advantage is small depending on weather conditions, while their drawback is considerable due to large error in temperature determination as compared to IR equipment.

However, among the listed remote-sensing equipment the leader is a complex of multiband Side-Looking Airborne Radar (SLAR) stations, which permit essentially to increase the width of a strip of view and, hence, to survey an area up to dozens of times. Being weather-independent and operating at 1000-9000 m height, this ensures higher economic efficiency.

In comparison with panoramic plane radar stations, the SLAR presents the following advantages:
- higher resolution
- considerably larger range of detection of objects
- opportunity of reception of the images in a rectangular coordinates system, thus facilitating comparison with video and photo images.

The one-frequency radar surveys have restrictions related to ambiguity of signal decoding; it is expedient to use a complex of multiband SLAR.

SLAR data are processed and displayed onboard and registered for subsequent processing in an analog and digital form. Thus the information contents of radar images are rather great and characterised by large volumes of data. Automated processing in real coordinates and time is thus necessary, this can be done successfully by the use of personal computers (PC's).

To measure the thickness of marine ice, a special radar instrument is used, the principle of which is based on irradiation of ice with probing radio impulses and measurement of a time interval between the signals, reflected from the top and bottom borders of the ice. It also assists the instrumental evaluation of ice concentration.

The specified principle is successfully realised by PINRO experts on board the plane-laboratory IL-18 D 'Pomor', which is equipped with some of the above listed measuring complexes.

THE PLANE LABORATORY IL-18D 'POMOR'

The plane-laboratory IL-18D 'Pomor' has the following main specifications:

– maximum flight range	5500 km
– maximum flight duration	up to 12 hr
– speed range	300-700 km/h
– range of flight heights	100-7500 m

The plane-laboratory has four places for visual observations, equipped with blisters.

Accuracy of navigation, determination of the position of a plane and objects on a sea surface are obtained with the help of a navigation complex, which gives data about time and coordinates, as well as about speed, course and height of flight.

The complex consists of:
- positioning system of precise navigation GPS R-900 or MX-200
- Altimeter
- Navigator.

GPS permits to determine coordinates with 100 m accuracy minimum, 1 m/s speed and 10 m height of flight. The system stores in memory 999 points of a scheduled route and specifies the deviations.

The navigator is realised on a PC and displays on a screen the flight route, the coastal line, all navigation parameters and current results of discrete sensing of marine surface, simultaneously recording them on a magnetic carrier.

The photo cameras (AFA-41/10, AFA-41/20, RA-39 and A-39) working in the visible range are used on 'Pomor' for close-up and perspective photography; the video cameras (VHS and SVHS) are used for observation and perspective survey.

To operate in the IR spectral range, the plane-laboratory is equipped with IR-radiometer and thermovision AGA-780. The specified equipment works in the 3-5 μm and 8-14 μm ranges, respectively, at viewing angles of 7° and 20°.

As a measuring equipment at microwave sensing (radio range) on 'Pomor' a multiband SLAR complex is used, consisting of SLARs and SARs. The SLARs includes RBO-0.8 (sensing to one side) and RBO-3 (sensing to both sides), possessing radiation wavelengths of 0,8 cm and 3 cm, respectively, and the space resolution 30×30 m and 20×50 m and strip of view of 15 km and 2×40 km respectively. The SAR senses to one side and has radiation wavelengths 23 cm and 180 cm, and strips of view of 15-120 km and 45 km and space resolution 20×50 m and 100 m, respectively.

Besides, on the plane-laboratory there are all opportunities for installation and operation of the additional equipment necessary at realisation of ice aerial surveys (ice thickness metres, profilemetres, scanners etc.).

For operative communication and information exchange between the vessels and coastal centres, as well as for data file transfer. including image files, 'Pomor' is equipped with a complex of radio communication equipment of SW and USW ranges.

The onboard processing of SLAR, IR and video images is carried out using a specialised hardware-software complex, consisting of:
- Personal computer;
- Device for image input;
- Standard and specially developed software, depending on specific character of the problems to be solved.

For automatic control of the data acquisition, integration and processing in real coordinates and time, the onboard operative informative system (BOIS) is used. The hardware basis of BOIS is a PC and a set of communication device with a measuring equipment. The advanced software permits to execute the most diverse functions depending on problems to be solved.

ORGANIZATION & REALIZATION OF AIR MONITORING IN THE ARCTIC SEAS

For complex aerial survey of ice condition, first of all, technical specifications of plane-laboratory, synoptical situation, time of day and season of a year are to be taken into account.

Three last circumstances are caused by the fact that, along with all-weather SLAR and SAR systems, an IR equipment is used, which is limited by meteorological conditions (clouds, mists, fogs, deposits etc.), as well as various photo and video surveys, visual observations, which can be successfully and qualitatively conducted only at favourable weather conditions and in daylight time.

Thus, before the beginning of the work, the analysis of meteorological situation is executed and synoptical forecast on a region of aerial survey is accepted with prospect from a day and under. Thus the flight takes place during day time with a general direction, taking into account the Earth's rotation, i.e. from East to West.

The air survey route is created so that within minimum flight time one could determine the ice conditions with maximum reliability and authenticity. The character of the route depends on the goals of the flight, expected ice and meteorological conditions and features of the region covered. Some variants of tasks are thus applied: P-shaped, oblique-angled, fan-shaped and spiral. However, the main are the first two; the others are applied as auxiliary. The operating height of flight is chosen proceeding from technical possibilities of the equipment, mission tasks and real meteorological conditions of the surveyed region and can make 100-7000 m.

Data acquisition is done along the whole route from the moment of arrival in a given region up to the departure. Thus the periodicity of sensing of sea surface by means of equipment working in discrete mode is chosen from the features of a region of research. Visual observations, aerial photography and video survey are executed continuously on the flight route as long as light conditions, visibility and meteorological conditions permit it. The radar sensing during aerial photography is carried out continuously. All the data output is provided on computer display and printer, as well as recorded on a disk for the subsequent ground processing.

Processing of the survey results is done in two stages:
- preliminary processing to correct the primary information and presentation in a form convenient for subsequent analysis;
- thematic processing to analysee and interpret aerial survey materials with the subsequent synthesis of maps for the consumers.

Both stages are based on automated processing with a computer in an interactive mode, assuming the participation in this process of an applied expert-researcher (hydrologist or physicist). The majority of procedures of preliminary processing of the information is reasonably well formalised and logically programmed. Thus, by now, the methods and software, enabling to decide the following problems, were developed:
- Correction of instrumental and other distortions;
- Calibration or normalization of the images;
- Geographical binding of remote data;
- Transformation of the images into a cartographical projection.

The preliminary processing should be made on the ground stations of the information consumers. Thus for effective use of the remote sensing information the operators of receiving station dispose advanced and adequate functional-and-service environment, which is maintained by the necessary software.

Then, the thematic processing, including data decoding and interpretation, is made, that is determination of ice concentration, age structure and other characteristics of ice cover.

Radar images and 'visible' images are subjected to decoding. Decoding of radar images can be direct or indirect. The tone and tone structure of the object image, its form and size belong to direct attributes. Thus the texture of the image is frequently used, for it is a subclass of a tone structure.

The tone of radar images depends on the ice electrical and physical properties, the surface roughness and humidity, the inclination angle and irradiation direction of the area studied. During the decoding and interpretation process, the attribute of form is applied.

The position, the mutual connection of objects, and also the traces of their activity belong to indirect decoding attributes. For example, typical indirect attributes are: polynias on the lee side of grounded hummocks, channels formed by icebreakers.

Except for the direct and indirect decoding attributes, sometimes logic ones, imposing space and temporary restrictions, are used. A characteristic example is the impossibility of young ice during the summer.

Radar image of each kind of ice has specific features due to the surface of the ice cover, its formation conditions, its duration and development phase, resulting in a wide range of roughness and physical properties. Therefore radar detection of marine ice of all aging stages, from shuga and nilas up to long-term ice is possible. However, the selection in a mass of one-year ice of intermediate stages is a very difficult problem.

The unequivocal interpretation of radar information about ice cover is not always possible. To eliminate this defect additional data, visual observation and other remote-sensing methods are necessary.

Interpretation and decoding of photo images are subjective, depending on personal experience and knowledge of the expert-interpreter (hydrologist, physicist); it is in many respects similar to visual observation.

The processed materials are prepared and presented to the consumers, often as maps of various scale displaying ice conditions with accepted international designations and symbols. Besides, photo, video, thermal and radar images are added to the maps with details of the ice conditions on the most interesting areas of research.

There is an additional opportunity of reception of thematic electronic maps for direct perception or inclusion in other processing systems. The resulting electronic maps can be displayed in various cartographic projections with any degree of detailed elaboration. The presentation format allows further thematic processing in order to obtain various parameters, for example, quantity and distribution of objects of a given type, perimeters and areas of given zones.

The principles and methods described above, as well as the acquisition, processing, analysis methods, the data interpretation and presentation, permit to have the characteristics and parameters of the ice cover, necessary for effective and safe navigation.

CONCLUSIONS

The development of navigation on the NSR line requires more safety for navigation among marine ice. This problem can be successfully solved only at comprehensive perfection and development of technical means and methods of marine ice remote sensing, particularly automation of processes of data processing, joint interpretation and decoding of the images and discrete data in various parts of the electro-magnetic spectrum.

The specified problems during recent years are being successfully solved by PINRO experts. The results obtained heve passed check and tests at realisation of air surveys.

Our own experience, the modern world practice and the development of airborne remote-sensing techniques have shown, the best efficiency of ice conditions monitoring can be achieved through surveys from small- and medium-size planes providing low-cost services, with low fuel consumption and capable of landing on standard airfields.

GEOLOGY & VOLCANOLOGY

LITHOLOGIC MAPPING BY FIELD AND SATELLITE MULTISPECTRAL DATA, TARN FLAT, ANTARCTICA

Ruggero Casacchia, Rosamaria Salvatori

C.N.R./ARF c/o Progetto Antartide
Via Tiburtina 770, 00159 Roma Italy
phone: +39 6 4075819, fax: +39 6 4075807, e-mail: rosas@gioconda.ced.rm.cnr.it

Francesco Mazzarini

C.N.R. CSGSDA
Via S. Maria, 53, 56100, Pisa, Italy
phone: +39 50 847111, fax: +39 50 500932, e-mail: ross@mailbox.dst.unipi.it

Francesco Salvini

III Universita' degli Studi di Roma, Dipartimento di Scienze Geologiche
Viale Ostiense, 169, 00154 Roma, Italy
phone: +39 6 57372828, fax: +39 6 57372827

ABSTRACT

A lithologic investigation has been performed on the Tarn Flat area, Antartctica, based on Landsat TM and SPOT-XS processed images and on radiometric field data acquired by an EXOTECH radiometer. Results from the field survey, performed during the austral summer 1994/95 expedition, were used to verify the ability of satellite images in discriminating among the main rock units. Principal Component transformation allowed to enhance spectral information of rock units, despite the high band correlation of TM data, while high-pass filtering and TM-SPOT merging allowed a fairly accurate detection of morphologic features. A supervised classification has been carried out on the processed satellite images, as a further demonstration of the utility of remote observation to investigate extreme environments.

1. INTRODUCTION

In remote areas geologic mapping is one of the most important application of satellite data. In Antarctica field work is difficult to be carried out and it can be performed only in a restricted period of time. For this reason the morphologic pattern and the spectral response derived from multispectral TM and SPOT-XS images can be useful to discriminate between the different rock units.

The work presented in this paper has been performed in the framework of the Italian National Research Programme in Antarctica and it is based on the comparison between field data acquired over rock surface, by a portable spectrometer, during the austral summer 1994/95 and the results obtained by Landsat

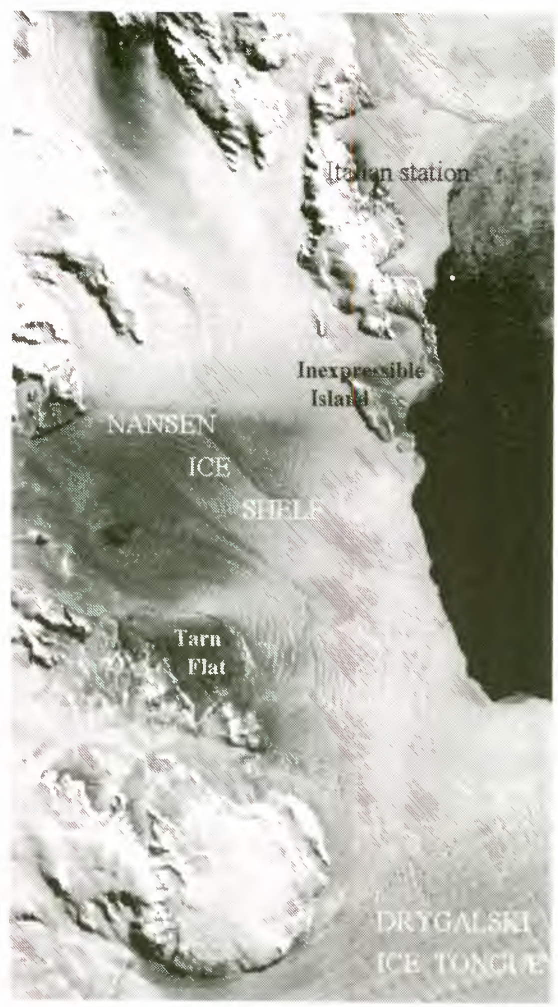

Figure 1. Location of the study area in Terra Nova Bay, North Victoria Land, Antarctica. The image covers an area of about 112x64 km.

Proceedings of the Fourth Symposium on Remote Sensing of the Polar Environments, Lyngby, Denmark, 29 April – 1 May 1996
(ESA SP-391, July 1996)

TM (acquired on January 1990) and SPOT-XS (acquired on December 1988) data processing.
The study area is Tarn Flat, a small plateau of about 14 km across (Figure 1) located in the proximity of the Nansen Ice Sheet, at about 80 km from the Italian base. Elevations range from 200 m to approximately 600 m and, during the austral summer, this area is almost ice-free, thus allowing to sample a statistically meaningful number of pixel on rock surfaces.
At Tarn Flat, the main outcrops are represented by granitoids belonging to the Early Ordovician intrusive sequences including granites, granodiorites, diorites and gabbros [Ref. 1]; however, most of the ice-free areas are strongly affected by periglacial processes that produced blockfields, blocksheets and debris [Ref. 2]. Other consistent deposits such as glacial drifts, morains and raised beaches are due to glacial processes. Among these surfaces, the rock units that can be better identified in terms of surface extension at the resolution of satellite data, revealed to be glacial drifts and granitoid rocks; mafites mainly occur on a small area in the North-West part of Tarn Flat.

2. FIELD DATA ACQUISITION

Field data consisted of spectral measurements, GPS data and field description of the textural and compositional characteristics of the rock targets. The instrument used during the survey was a *EXOTECH 100 AX* radiometer, operating in four channels at the wavelength range shown in table 1.

Ch	bandpass (nm)	GAINx1 $x10^{-3}$	GAINx5 $x10^{-3}$	GAINx25 $x10^{-3}$	GAINx125 $x10^{-6}$
A	502-609	4.09	.818	.164	32.7
B	600-698	4.00	.800	.160	32.0
C	698-800	4.04	.808	.162	32.3
D	805-980	4.04	.807	.161	32.3

Table 1. Source equivalent radiant emittance within the specified spectral bandpass (watts/cm^2/volt): 15° FOV (plane glass).

The spectroradiometer allows to take data by three different optics (2π steradian, 1° and 15°), the choice of which determines the dimension of the surface area that contributes to the measured source equivalent radiant emittance. For each channel, the recorded values, were amplified and then displayed in digital number format; the conversion into radiant emittance and into radiation power incident values were carried out by the values listed in table 2.
In each session of field data acquisition, the first measure concerned the spectral irradiance, and it was carried out by mounting the 2π steradian optics, with the instrument in zenithal position. This operation was repeated every 30', or more frequently if stable meteorological condition did not occur. The exitance of the rocky surface was measured with the intrument in nadir position, at about 1-1,5 m above the target and mounting the 15° optics (plane glass); the reflectance was computed as the ratio of measured surface exitance to spectral irradiance.

Ch	bandpass (nm)	GAINx1 $x10^{-3}$	GAINx5 $x10^{-3}$	GAINx25 $x10^{-3}$	GAINx125 $x10^{-6}$
A	502-609	7.87	1.57	.315	62.9
B	600-698	8.59	1.72	.344	68.7
C	698-800	7.01	1.40	.280	59.0
D	805-980	6.72	1.34	.269	53.8

Table 2. Radiation power incident on the optical element within the specified spectral bandpass (watts/cm^2/volt): 2π steradian FOV (diffuser).

At Tarn Flat, 14 sites were visited and outcropping granites, mafites, detritus and glacial drift were sampled; the rock targets were then classified according to lithology, alteration degree, tectonic deformation and to their small scale textural parameter variations (grain size, packing, sorting).
Moreover, in order to take into account the overall spectral behaviour of the targets, different measurements were taken at each site. In this way we tried to make the field data comparable to the satellite ones. In fact, when comparing field and satellite data, a good correlation exists mainly for surfaces showing a regular texture. In Antarctica this aspect is particularly relevant in mapping glacial drift units that may be characterized by material from very fine to boulders of few meters across.

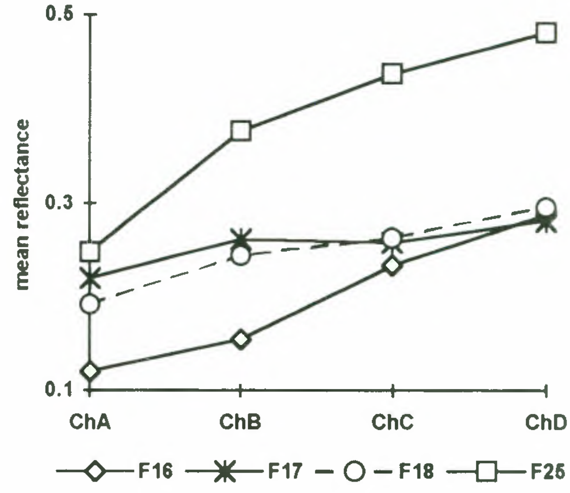

Figure 2a. Mean reflectance of granitoid samples
F16 = highly oxidized granite, F17, F18 = oxidized granite; F25 = unaltered granite

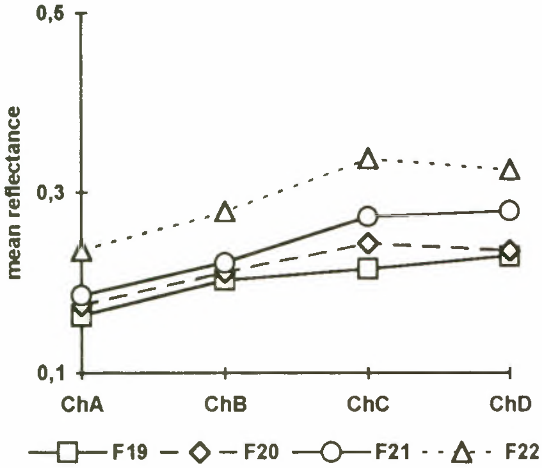

Figure 2b. Mean reflectance of glacial drift samples. F19 = glacial drift (fine sand), F20 = glacial drift (conglomerate), F21 = glacial drift, F22 = glacial drift (boulders).

In figure 2 field spectral data recorded on granitoids (fig. 2a) and glacial drifts (fig. 2b) are shown. Granitoid rocks appear to be well discriminated according to their weathering degree (oxidation), while for glacial drifts the discriminating factor is the occurrence of the finer component along with the dimension of the rock blocks.

3. SATELLITE DATA PROCESSING

Satellite data processing was performed both on selected TM spectral channels and on a SPOT-XS image in order to increase the spectral contrast among the main lithologies, to improve texture patterns and unit boundaries detection.
Five TM spectral channels were used, excluding TM6 beacuse of its spatial resolution and TM1 because of the high saturation of the snow surfaces, that modifies the brightness of the scene, also reducing the information about rock units.
TM spectral channels of the Antarctic scene analysed in this study show to be highly correlated and affected by horizontal radiometric noise, thus constraining data interpretation and image classification. Among the methods to improve features detection within a scene, we found that, in the case of regions where strong brightness differences are present, good result are provided by the Principal Component transformation. In addition to PCA, high-pass filtering and BGR-IHS transformation contributed to substantially increase the ability of detecting textural and morphological variations.

3.1 Principal Component

The principal component transform (PCT) is a widely applied method for image enhancement prior to visual interpretation of the data, or as a processing procedure prior to automated classification of the data [Ref. 3]. From the application of this method, it results that the largest amount of total variance is mapped into the first PC, while a decreasing amount of data variance is mapped into successive PCs; for this reason, the first transformed picture has the greatest spread in data or the greatest contrast among terrain units and is actually an albedo picture, which depicts the average brightness of the scene [Ref. 4,5]. When this processing technique is applied to correlated spectral bands affected by striping or banding (such as those of TM), the radiometric noise can be confined to the higher PC images, thus being less pronounced in the first PC image.
In this study PCT was applied to TM bands from 2 through 7 and to a data set constituted by the infrared bands TM5 and TM7 in order to further strengthen the information pertaining rock outcrops. PCT was applied also to SPOT data in order to merge the information contained in the three individual spectral channels.

To the purpose of geologic mapping the best results, in enhancing the spectral differences between the rock units, were obtained by merging into a RGB display PC1 from TM5 and TM7, PC1 from all the five TM bands and TM4 [Ref. 6]. A useful result obtained by the selection of these images is the possibility of interpreting and mapping features occurring on both rock and snow/ice surfaces. This is particularly important for those units like morainic deposits often characterized, in satellite data, by a high number of mixed pixel [Ref. 7], because this method does not introduce masking effects.

3.2 High-pass filtering

The PC images (both TM and SPOT) were high-pass filtered by a 3x3 Laplacian kernel (Tab. 3). This technique is particularly effective in making sharper the fine detail of a scene, usually pertaining areas with a high density of morphologic features, or patterns of limited extension. By applying this convolution filter it has been possible to better delineate the boundaries of each rock unit and to increase the visual interpretation of their geometric patterns.

0	-1	0
-1	5	-1
0	-1	0

Table 3. Weights used in the high-pass Laplacian kernel.

3.3 RGB-IHS transformation

This technique was applied to the selected PC images derived from TM bands and to PC1 from SPOT channels, in the attempt of producing a false color image with the spectral information of the TM, but displayed at the spatial resolution of SPOT. Before the

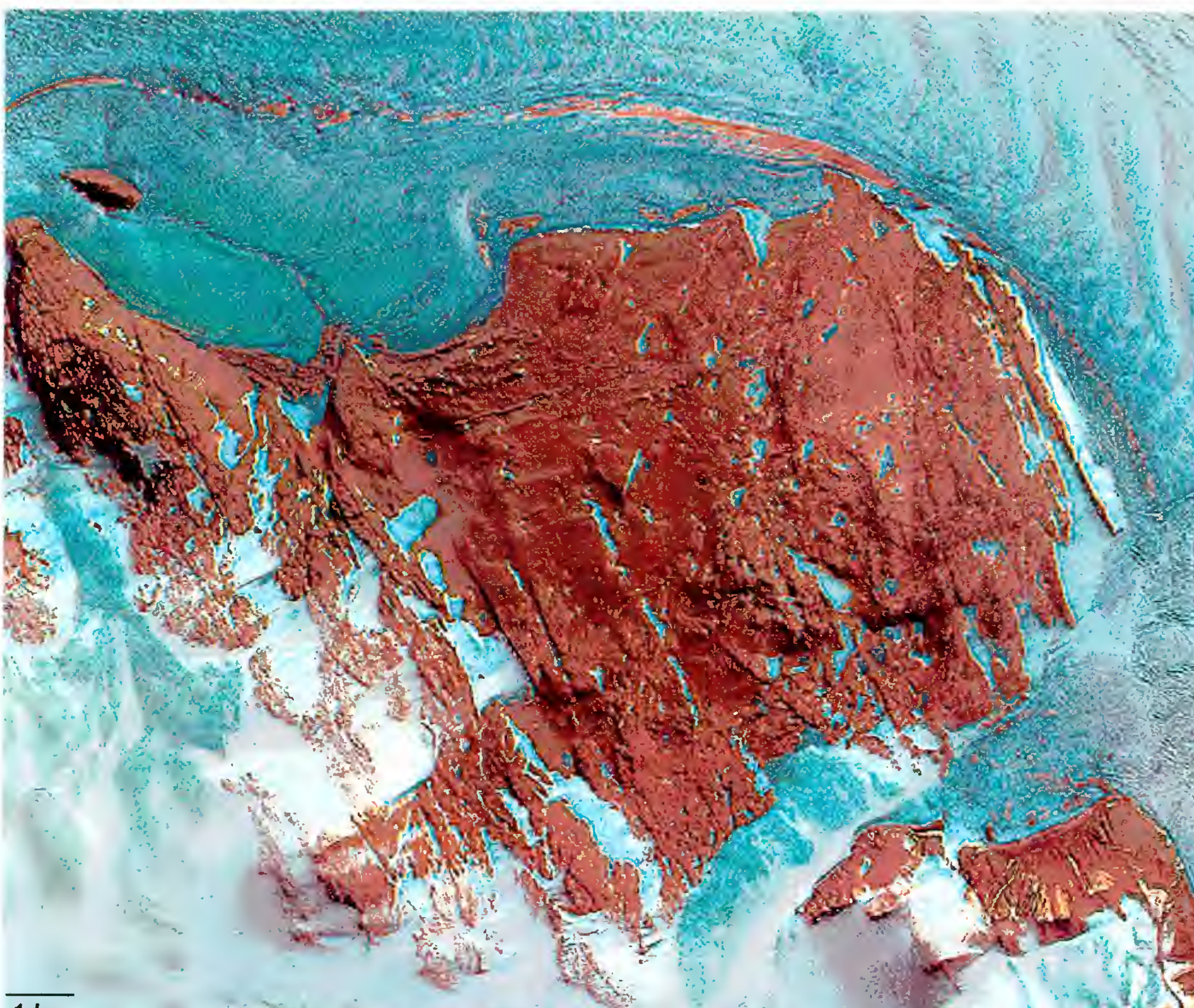

Figure 3. The Tarn Flat area in North Victoria Land. The image obtained from merging of TM and SPOT-XS processed images, covers a surface area of about 16x13 km. Smooth light brown areas correspond to fine-grained glacial drift (sands); dark brown at the center of the image is glacial drift with blocks of a few tens of cm across. Rough light brown areas (south and east) correspond to a unit including hard rock, boulders of a few meters and glacial drift..

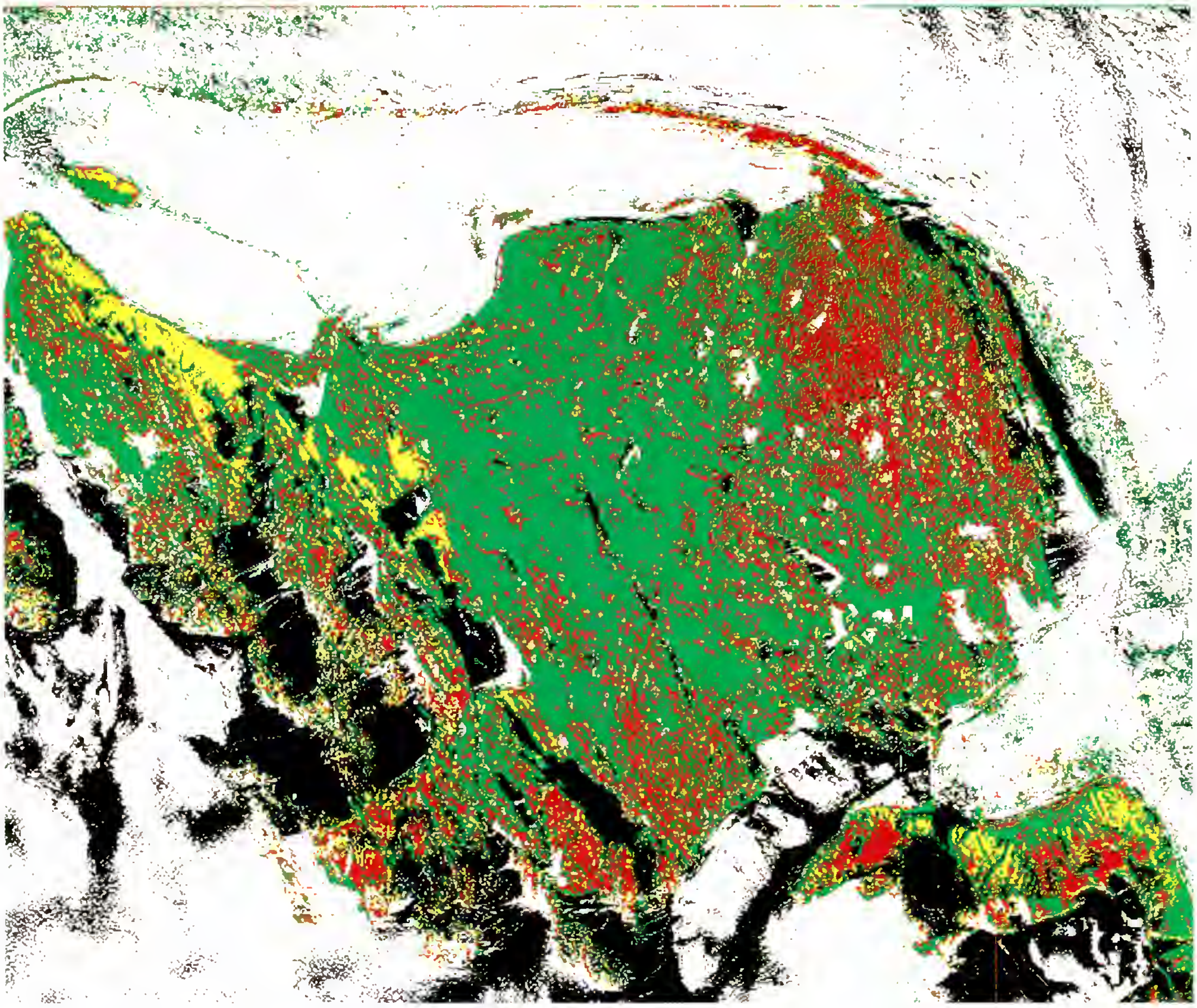

Figure 4. Same area as in figure 3, classified according to field spectral measurements and textural information derived from satellite data processing.
Yellow = Glacial drift, smooth (sands); *light brown (smooth) in fig.3.*
Green = Glacial drift, fine (sands and blocks up to 50 cm), *dark brown (smooth) in fig .3.*
Red = Block field, hard rock and glacial drift; *light brown (rough) in fig.3.*
White = Ice.
Black = Unclassified.

transformation, TM data were coregistered to the SPOT scene. In the first transformation (RGB=>IHS) input channels were the above mentioned TM selected images; in the second step (IHS=>RGB) the intensity component was PC1 from SPOT bands. The resulting image is that of Figure 3, showing, according both to the different brown tones and to the different surface texture, three major rock units. These surfaces represent respectively a glacial drift unit with a relatively high fine sand component, a glacial drift also including heterogeneous blocks of a few tens of cm and a unit constituted by hard rock and glacial drift with boulders of 2-3 m across.

3.4 Classification

A supervised classification (Figure 4) was performed on the image displayed in Figure 3. The regions of interest were selected on the satellite images and the data acquired by the field survey, both visual and spectral. An average number of about 800 pixel was selected for each class and a minimum distance classifier was adopted. Of all the pixels related to rock material about 83% resulted classified. This result is in good agreement with field survey, and describes in fairly good detail the main lithological and textural differences among the rock surface units.

4. RESULTS

The methodology adopted in this study allows a fairly accurate mapping of the main rock units of the Antarctic territory. The comparison between satellite processed images and field data shows that at Tarn Flat, where the mapped deposits are mainly granitoids or glacial drifts, discrimination of rock unit can be performed according to textural and morphological differences. To this purpose a major contribution derives from TM/SPOT merging and to high-pass convolution filtering.

Principal Component transform has proven to be a technique reliable to reveal the information within a set of correlated multispectral data. In applying this technique, however, it must be taken into account that it is extremely scene-dependent and that best results are obtained for scene characterized by a large statistical variability.

The detected textural differences are linked to different types of glacial deposits, from glacial till (smooth texture) to blockfield (coarse texture), probably reflecting different depositional facies. Therefore, discrimination between outcropping rock (granitoids) and coarse deposits (blockfield with boulders) is still critical. A detailed mapping of surface glacial deposits bear information on the real distribution of rocky outcrops, and allow a better understanding of the most widespread surface rock unit in Antarctica.

5. ACKNOWLEDGEMENTS

This work was supported by the Italian National Research Program in Antarctica, Project "Remote Sensing, G.I.S. and Data base".

6. REFERENCES

1. Carmignani L. , C. Ghezzo, G. Gosso, B. Lombardo, M. Meccheri, A. Montrasio, P.C. Pertusati and F. Salvini 1987, Geology of the Wilsone Terrane in the Area between David and Mariner Glaciers, Victoria Land (Antarctica). *Mem. Soc. Geol. It.*, 33, 79-99.

2. Baroni C., and G. Orombelli 1989, Glacial geology and geomorphology of Terra Nova Bay, Antarctica. *Mem. Soc. Geol. It.*, 33, 171-193.

3. Lillesand T.M. and R.W. Kiefer 1987, *Remote Sensing and Image Interpretation,* John Wiley & Sons, Inc.

4. Chavez P.S. and A.Y. Kwarteng 1989, Extracting Spectral Contrast in Landsat TM Image Data Using Selective Principal Component Analysis. *Photogram. Engineering and Remote Sensing*, 55, 3, 339-348.

5. Sabins. F.F. 1986, *Remote Sensing: principles and interpretation*, W.C. Freeman and C., New York.

6. Casacchia R., R. Salvatori, & A.B. Petrangeli 1995, Geologic Mapping in Victoria Land, Antarctica, based on multispectral satellite data, *Proc. Geographic Information Systems, Photogrammetry, and Geological/Geophysical Remote Sensing,* 25-27 Sept. 1995, Paris, France, EUROPTO Series, vol.2587, 2-9.

7. Salvini F., R. Della Maggiore, L. Fortunati and F. Mazzarini 1994, "Rock mapping of glaciated areas by satellite image processing". *Polar Research,* Vol.13, No.1, 23-34.

QUANTITATIVE MAPPING OF ACTIVE AEOLIAN SURFACES IN NORTHERN FENNOSCANDIA - LANDSAT TM HYBRID CLASSIFICATION

Jukka Käyhkö*, Ken Pye & Peter Worsley

Postgraduate Research Institute for Sedimentology, The University, Whiteknights, P.O.Box 227, Reading RG6 6AB, England
phone: +44 1734 316 713, fax: +44 1734 310 279

**Present address: Department of Geography, University of Turku, FIN-20500 Turku, Finland*
phone: +358 21 633 5580, fax: +358 21 633 5896

ABSTRACT

Hybrid classification of 11 Landsat TM quarter images (*circa* 81,000 km^2) was performed in an attempt to locate and quantify areas of aeolian activity in northern Fennoscandia. Three- and four-band combinations 1, (3), 5, 7 of Landsat TM data were employed in the *k-means* minimum Euclidean distance clustering algorithm after grey-level thresholding. The normal distribution parameters of the created clusters were used to classify the entire image with a Gaussian maximum likelihood classifier. Reference data for the deflated areas were calculated using scanned aerial photographs from seven localities. Aeolian activity was mostly found on early Holocene anchored inland dunes, glaciofluvial and glaciolacustrine deposits, and in localised areas on fell slopes, almost exclusively either to the north of or vertically above the Scots Pine tree line. The total area of deflated surfaces in the study region was circa 1000 ha (10 km^2).

1. INTRODUCTION

Previously, mapping of aeolian processes in northern Fennoscandia has been mainly undertaken on a national basis, as part of wider context *(e.g.* general geological/ geomorphological mapping), or restricted to dune fields only *(e.g.* Klemsdal 1969, Seppälä 1972, Sollid et al 1973, Aartolahti 1976, Bergqvist 1981, Tikkanen & Heikkinen 1995). The use of satellite imagery in this study provided the means to cover a wide area across the national borders in northern Fennoscandia, and also allowed areal estimates of aeolian activity.

2. MATERIAL AND BAND SELECTION

One full system corrected Landsat TM scene and seven quarter scenes were interpreted in this study (Table 1, Fig. 1). The areal coverage of the images is approx. 81,000 km^2. Of the total coverage, 60% lies in Finland, 14% in Norway, 10% in Russia and 16% in Sweden. All images were cloud-free and acquired in summer.

Table 1. List of the TM scenes used in the study

Path	Row	Quarter	Date acquired
191	11	C	87-07-20
191	12	A, B, C, D	87-07-20
193	11	b, d (floating)	87-07-18
194	12	full image	92-06-04

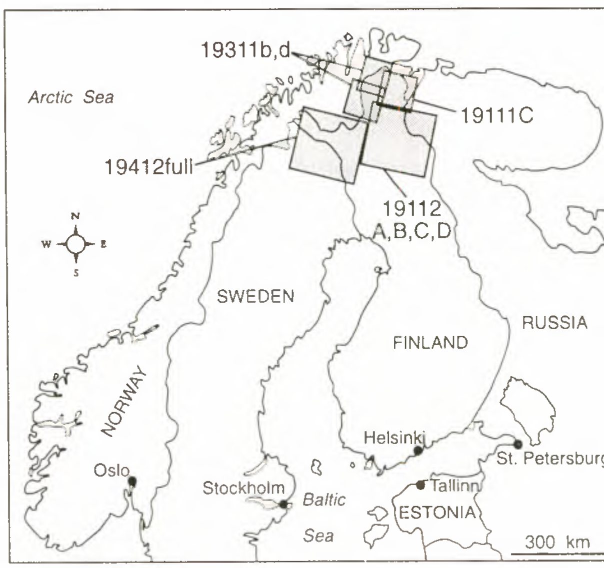

Figure 1. The areal coverage of the Landsat TM data used in the study.

The research objectives of this study were to separate barren surfaces from the green vegetation, and active aeolian surfaces from other types of barren ground like boulder fields and lichen heaths. Finally, some subdivision amongst aeolian surfaces with respect to sediment texture and moisture content was attempted. Visible wavelengths are powerful in separating green vegetation from sandy surfaces due to the higher energy absorption by plants. Also, the middle-infrared region can be used, if the sand surface is dry, as green vegetation appears dark due to water absorption (Hoffer 1978). Lichens and barren sand are best separated using visible wavelengths also, and because of the small step at the red edge, the shorter the wavelength the better. The infrared region is not as useful, because of the high reflectance of lichens due to lack of water absorption (Petzold & Goward 1988), whereas the middle infrared region is the only useful wavelength region for distinguishing sediment spectral properties due to texture, moisture and mineralogy (Drury 1993).

Initially, a three-band combination TM1, TM5, TM7 was chosen for classification (scenes 193 11d and 194 12). From the visible wavelength bands, TM1 was selected because of the best separation potential between lichen and sand. TM5 was chosen in order to differentiate deflation from snow patches, and together with TM7, to interpret sediment textural and soil moisture properties. Later, a fourth band, TM3, was added to the combination, as subsequent histogram evaluation showed that this band has slightly more deviation - and thus potentially more information - amongst the brightest deflation pixels than the other visible wavelength bands. On TM4, deflated areas manifested only minor differences in reflectance pattern compared with that of green vegetation.

3. THE CLASSIFICATION PROCEDURE

The image interpretation was performed at the Satellite Image Centre of the National Land Survey of Finland (NLSF), Helsinki. The software used for the interpretation was DISIMP Version 5.3 (DISIMP 1990), in the Hewlett-Packard Apollo environment. Within the system configuration used at NLSF, the DISIMP software offers the subroutines for image processing, while some of the actual classification programs have been developed at NLSF, VTT Technical Research Centre of Finland, and the Finnish Environment Agency.

The mapping of aeolian activity could not be undertaken purely with automated spectral pattern recognition. This is because many non-aeolian features possess spectral characteristics identical to deflated surfaces. These include man-made features like gravel roads and dumping-grounds, as well as natural features like river bars and beaches. Thus, rather than trying to detect aeolian activity *sensu stricto*, a broader approach of detecting areas of bare sandy surface was put into practice. A subsequent spatial pattern recognition procedure was undertaken after the classification process. Here, the classification result was remedied manually, examining features classified as bare sand surfaces with the aid of aerial photographs, maps and field checks.

The supervised approach for mapping the deflated areas was first experimented with. Training areas were carefully delineated with the aid of large-scale aerial photography. Care was taken that the data set was both adequate and representative for use in the classification stage. The classifiers used in the procedure were a Gaussian maximum likelihood classifier *allocn* (DISIMP 1990, Foody et al 1992) and a linear discriminant function classifier *cldcf* developed at VTT (see Fukunaga 1990: 131-138, Hardin 1994). The supervised approach proved, however, to be unsuitable for mapping aeolian activity. The main reason for the unsatisfactory classification result was the reasonably small size of the identified deflation features (often approx. 1 pixel), and the resulting mixed pixel problem. The complex nature of mixed pixels made it impossible to produce spectral classes that would represent narrowly defined information categories (land cover types), which is the key factor in supervised classification (Lillesand & Kiefer 1994).

After the supervised classification proved to be unsatisfactory for mapping aeolian activity, an alternative approach was established using hybrid classification. An overview of the classification procedure is presented in Fig. 2.

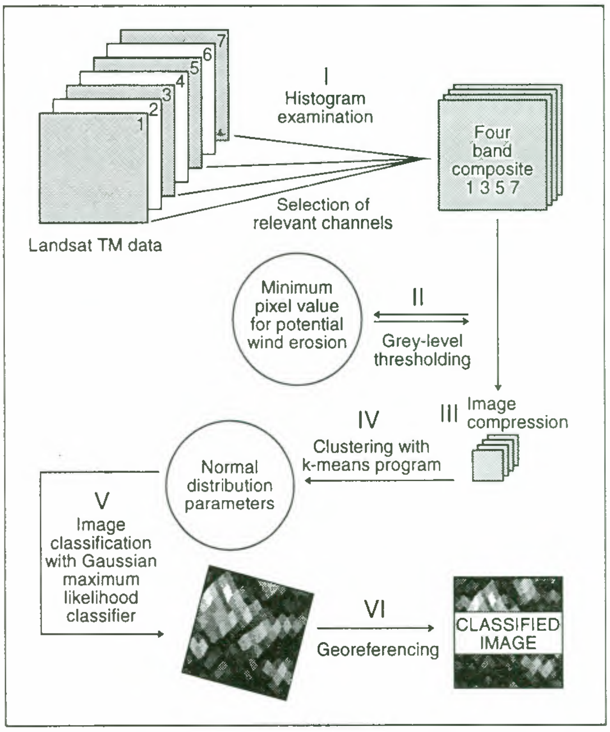

Figure 2. The hybrid classification procedure employed in the study

The unsupervised classification procedure was preceded by grey-level thresholding to pixels that potentially represent deflation areas, and to pixels that cannot represent deflation, using band TM7. However, after a thorough histogram evaluation at a later stage, it appeared that rock outcrop and boulder field pixels on the fells formed a tail at the bright end of TM7 histogram, probably due to extensive crustose lichen cover on the rock surfaces. To exclude these unwanted land cover types from the classification procedure, a subsequent histogram evaluation on different bands was undertaken, covering a large variety of environments. TM2 appeared to manifest the most peaked histogram pattern of all, hence narrowing down the amount of surplus pixels. The grey-level thresholding result is summarised in Table 2.

Table 2. Summary of the grey-level thresholding

Scene	TM band	Threshold DN	The % of pixels exceeding the threshold
191 11C	2	30	0.253
191 12A	2	32	0.345
191 12B	2	32	0.738
191 12C	2	32	0.245
191 12D	2	32	1.472
193 11b	2	32	0.574
193 11d	7	35	3.009
194 12full	7	42	3.416

A compressed multi-band image was next formed of each scene using the *cmpuns* program (NLSF, Vuorela 1992), by selecting from different bands only the pixels whose DN on the threshold band (TM7 or TM2) exceeded the threshold value. The unsupervised classification was next carried out using the *k-means* minimum Euclidean distance clustering algorithm, programmed at the Finnish Environment Agency. The created clusters were subjected to pooled statistical analysis to determine their spectral separability. Similar clusters representing similar land cover types were combined, and the final number of clusters on various images was smaller (28-33) than the analyst-defined maximum of 40.

With *mskdtv* program (VTT, DISIMP 1990), a new multi-band image was created by masking the selected bands of the image with the band used in the grey-level thresholding, and using its threshold value. The background pixels were given a null value (0) on all bands. The normal distribution parameters (mean vectors and covariance matrices) of the created clusters were used to classify the newly formed entire image. This was carried out using Gaussian maximum likelihood classifiers *allocn* (in the early stage) and *clmxl* (in the later stage). Both of these are DISIMP (1990) programs, and work with similar algorithms. After the classification, the images were geocorrected to the uniform co-ordinate system Finnish national grid using GCP files made at NLSF. The output pixel size was determined as 25 m. The RMS of the rectified images was in all cases less than 0.5 pixels.

Next, the information classes of the spectral classes were examined manually with the aid of ground data. As the reflectance of bare sand is higher than that of vegetation on the bands employed, the most distinctive bare sand classes will, in general, show the highest mean vector values in the normal distribution parameters. When the proportion of vegetation or other land cover type increased in a mixed pixel, this resulted in lower mean vector values. Hence, by examining the mean vector values of different classes and evaluating the corresponding ground data, it was possible to include classes one by one, and select a set of classes that best delineated deflation

To aid the class selection, deflated areas in seven localities across Lapland were traced from aerial photographs, scanned at 300dpi resolution and imported to IDRISI. Having now obtained the approximate sizes of the selected deflated areas, corresponding sub-images from the classified TM scenes were viewed. Using the ERDAS raster attribute editor (ERDAS 1994), the classes with highest mean pixel values were added one by one on the scene, and the resulting growth in area was observed. Because of the difference in the scale factor between the scanned binary mask and the TM data (approx. 1 m vs. 25 m) no complete match should be expected in the comparison even if the inspected areas *were* truly identical *(i.e.* no classification errors) *(c.f.* Woodcock & Strahler 1987; Marceau et al 1994a,b). The appropriate classes determined as aeolian activity were at this stage aggregated into four "ecological" classes. De Jong (1994) concluded that such a recoding approach can be used area-specifically and that the optimal solution has to be chosen by the researcher. The four classes can be described as follows:

I Pure sand surface (high reflectance values across the spectrum)

II Sand with lichen or some green vegetation (intermediate reflectance in the visible, high values allowed in the IR)

III Sand or gravel with an 'edge effect', *i.e.* mixed sand/green vegetation (low reflectance values in the visible, high values allowed in TM5, intermediate in TM7)

IV Dismissed classes (values below or above the analyst-defined threshold for the class mean vector values, which varied from scene to scene)

The manual approach was a critical stage of the work, as the area figures for bare sand across the entire scene varied markedly in response to the employed class selection. In general, the localities with large blowouts provided the closest match in the comparison, whereas areas of small blowouts were strongly underestimated due to inadequate spatial resolution. The best class combination resulted in an average 20% under-estimate of the TM areas compared with the aerial photograph scanning results.

4. RESULTS

Altogether 928 ha of land surface with aeolian activity were found in the study region. Fig. 3 shows the areal distribution of the active surfaces within the study region, and Table 3 summarises the areal occurrence of aeolian processes in different environments and countries. The current nomenclature divides the area into 63 sites with active aeolian processes. Aeolian features occurred basically in three different environments:

1. On fine grained glaciofluvial deposits, in the form of deltas or glaciolacustrine beds, which usually also have dune forms.
2. On coarse-grained glaciofluvial formations, mostly eskers, with indistinctive primary aeolian deposits.
3. On the fells, without distinctive aeolian deposits. In many instances, these features are primarily of glaciolacustrine origin

There are no previous estimates of the total area of aeolian activity for the whole of the study region. The only available figure (280 ha) is for Finnish Lapland, and for dune deflation only (Tikkanen & Heikkinen 1995), based on interpretation of maps and aerial photographs. The equivalent figure of 430 ha reported here (Table 3) is 54 % larger. Three quarters of the total active surfaces was found in Finland, 15% in Norway, 7% in Sweden and 1.5% in Russia. Compared with the countries' areal proportions in the study region, Finland has more active surfaces than would be expected, Norway a proportional amount, whereas Sweden and, especially Russia, have much less activity than would be anticipated. In Sweden and, particularly in Finland, most of the activity occurs on aeolian and glaciofluvial sediments. In Norway, on the other hand, fell deflation is the largest class, as it is in Russia, where neither of the other two types is found at all. Figure 3 shows clearly how aeolian processes tend to occur outside the pine forest zone. With few exceptions the localities that seem to occur within the pine forest zone (*c.f.* Fig. 3) are actually located in high-ground areas vertically above the continuous pine limit. The pine forest limit should, however, be regarded as indicative only, as it is a gradual transition zone rather than a distinct line.

In order to unravel the immediate vegetational environment adjacent to the aeolian activity, a simple 100 metre buffer method was used to overlay the classification with a digital vegetation map (Käyhkö 1996).

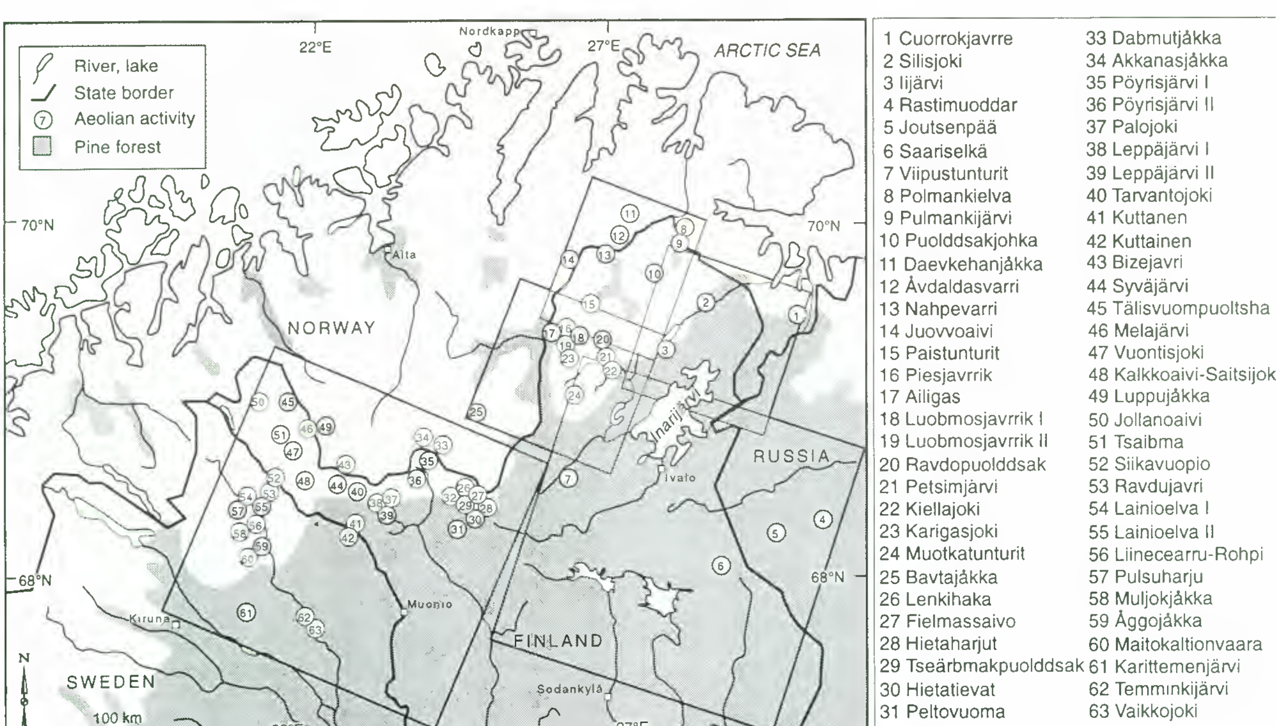

Figure 3. The areal distribution of aeolian activity within the study region. Pine-free enclaves within the pine forest zone are not shown on the map

Table 3. Summary of the area (ha) of aeolian activity in those parts of the countries which were included in the study, and among three different sedimentary environments (see text). The table is based on the raw data, calculated using the 0.0625 ha pixel size.

Environment	Finland	Norway	Russia	Sweden	Row-total, ha
Aeolian & glaciofluvial	430.5	39.8125	-	41.375	511.6875
Glaciofluvial	19.125	34.6875	-	9.75	63.5625
High ground (fells)	263.875	61.125	14.875	12.625	352.50
Column-total, ha	713.5	135.625	14.875	63.75	927.75

The vegetation map utilised was the ungeneralised version of the *Satellite Image Based Land Cover and Forest Classification of Finland*, processed at the NLSF. The buffer study suggests that 15-20 % of pine forest coverage in the near vicinity of the aeolian activity is enough to substantially slow down the sand transport process in the study area. Aeolian activity is concentrated in NW Finland, on glaciofluvial and glaciolacustrine sediments which were deposited between the SSW trending ice margin (Kujansuu 1967) and the watershed, which the Finnish-Norwegian border loosely follows. The largest active area is located adjacent to a glaciofluvial unit around Lake Pöyrisjärvi (locations 35-36), sustaining approx. 200 ha of active aeolian surfaces, and also the largest single deflation basin in Lapland, approx. 14 ha in area. The three largest locations sustain circa 90% of all category 1 (aeolian & glaciofluvial) activity in Finland. This is not a coincidence, however, as these are the three conspicuous glaciofluvial-glaciolacustrine areas north of the pine forest limit in the study region.

The largest concentration of activity in Norway lies in northernmost part of the study region (sites no. 11 and 12), and covers 40 ha. This area consists of well developed parabolic dunes adjacent to glaciofluvial areas just inside the Tromsø-Lyngen substage end moraines (*c.f.* Klemsdal 1969; Sollid et al 1973). In Sweden, the largest area of aeolian activity occurs in the vicinity of the river Lainioelva (sites no. 52-58), approx. 44 ha, almost half of which is found on the Pulsuharju esker. On the fells of the study region, altogether 350 ha of aeolian activity was detected. The largest concentration of deflated surfaces was found in the Saariselkä fell region in the eastern Finland, representing just over 100 ha (site no. 6).

5. DISCUSSION

It is difficult to estimate the accuracy of the Landsat TM mapping results. The main factor to be considered is, whether the technique applied here has been able to determine *all* locations with aeolian activity in the study area, without any significant areal misinterpretation arising from erroneous classification. In principle, the classification accuracy could have been estimated with the aid of a confusion matrix (*e.g.* Dymond 1992). However, because of the large number of classes with such subtle spectral differences between them, and the fact that the corresponding land type classes appeared impossible to describe unambiguously in the field, this would have been an enormous task. Also, owing to the fact that the aeolian features *are* spectrally identical to some other features of different origin, and thus impossible to distinguish even in theory, the accuracy estimation was not considered essential at this stage.

The mixed pixel problem (see, for example Price 1992; Foschi 1994) and scale factor questions (see Woodcock & Strahler 1987; Raffy 1992; Marceau et al 1994a, b) are widely acknowledged. According to Marceau et al (1994a) there is no unique best spatial resolution for detection of all geographical entities on a heterogeneous image. Woodcock & Strahler (1987) concluded in their paper that the local variance in images is related to the relationship between the size of the objects in the scene and the spatial resolution of the sensor, being largest when the objects and the resolution cells are of the same size. Marceau et al (1994b) came to the same conclusion, and implied that the minimum variance is an indicator of the optimal spatial resolution for the particular parameters under consideration. In general, coarser resolution tends to result in an underestimate of the areal coverage of scattered features.

Since the areal measurements of aeolian activity in the training areas determined from the TM images were some 20% lower than those determined from aerial photography, the total figure of 928 ha of aeolian activity in the study area is probably an underestimate rather than an overestimate. However, as the underestimated areas are the smallest ones, the resulting error is believed to be minor.

6. CONCLUSIONS

With the aid of the Landsat TM hybrid classification and a subsequent GIS approach, the following can be concluded:

1. Approximately 1000 hectares (10 km^2) of active aeolian surfaces are to be found in the study area.

2. With few exceptions, active aeolian surfaces were found on aeolian/glaciofluvial sediments outside the pine forest zone.
3. The largest concentration of active aeolian surfaces was in NW Finland adjacent to the watershed along the Norwegian border. This is due to the current absence of pine forest, and, more importantly, due to the widespread occurrence of glaciolacustrine sediments in the region.
4. The GIS approach supported the idea of a link between absence of pine and aeolian activity: the critical pine coverage to substantially decrease aeolian activity in the study region was estimated at 15-20 %.

7. ACKNOWLEDGEMENTS

This work was undertaken as part of Ph.D. research by JK at the University of Reading. It was funded by The British Council, The ORSAS, Emil Aaltonen Foundation, The Academy of Finland (projects 1012238 and 2247), Maj and Tor Nessling Foundation, University of Helsinki. and Alfred Kordelin Foundation. Invaluable help in the data manipulation, and fruitful comments on the manuscript, were given by Mr. Arto Vuorela (NLSF). Mr. Tapio Siltala (NLSF) made the data accessible for the study. Mr. Sakari Palo tirelessly assisted in the long field sessions. University of Reading PRIS contribution no. 512.

8. REFERENCES

Aartolahti T 1976, Lentohiekka Suomessa. *Suomalainen Tiedeakatemia. Esitelmät ja pöytäkirjat,* 83-95.

Bergqvist E 1981, Svenska inlandsdyner. Översikt och förslag till dynreservat. *Naturvårdsverket Rapport* 1412. Solna, Sweden. 103 pp.

De Jong S M 1994, Derivation of vegetative variables from a Landsat TM image for modelling soil erosion. *Earth Surf. Proc. & Landf.* 19, 165-178.

DISIMP 1990, *Device Independent Software for Image Processing, Version 5.1. Updates to Utilities Reference Manual.* CSIRO, Canberra.

Drury S A 1993, *Image Interpretation in Geology.* Chapman & Hall, London. 283 pp.

Dymond J R 1992, How accurately do image classifiers estimate area? *Int. J. Rem. Sens.* 13, 1735-1742.

ERDAS 1994, *ERDAS IMAGINE v. 8.1.* ERDAS Inc. Atlanta. USA.

Foody G M, N A Campbell, N M Trodd & T F Wood 1992, Derivation and applications of probabilistic measures of class membership from the maximum-likelihood classification. *Phot. Eng. & Rem. Sens.* 58, 1335-1341.

Foschi P G 1994, A geometric approach to a mixed pixel problem: Detecting subpixel woody vegetation. *R. Sens. of Env.* 50: 317-327.

Fukunaga K 1990, *Introduction to Statistical Pattern Recognition.* 2nd ed. Academic Press, San Diego. 591 pp.

Hardin P J 1994, Parametric and nearest-neighbor methods for hybrid classification: a comparison of pixel assignment accuracy. *Phot. Eng. & Rem. Sens.* 60, 1439-1448.

Hoffer R M 1978, Biological and physical considerations in applying computer-aided analysis techniques to remote sensor data. In Swain P H & S M Davis (eds.): *Remote sensing: The quantitative approach*, 227-289. McGraw-Hill, New York.

Käyhkö J 1996. Mapping of aeolian activity in Lapland using Landsat TM hybrid classification and GIS (in prep.).

Klemsdal T 1969, Eolian Forms in Parts of Norway. *Norsk Geogr. Tidsskr.* 23, 49-66.

Kujansuu R 1967, On the deglaciation of western Finnish Lapland. *Bull. Comm. Géol. Finl.* 232. 98 pp.

Lillesand T M & R W Kiefer 1994, *Remote sensing and image interpretation.* Wiley, New York. 750 pp.

Marceau D J, P J Howarth & D J Gratton 1994a, Remote sensing and the measurement of geographical entities in a forested environment 1. The scale and spatial aggregation problem. *Rem. Sens. Env.* 49, 93-104.

Marceau D J, D J Gratton, R A Fournier & J-P Fortin 1994b, Remote sensing and the measurement of geographical entities in a forested environment 2. The optimal spatial resolution. *Rem. Sens. Env.* 49, 105-117.

Petzold D L & S M Goward 1988, Reflectance spectra of subarctic lichens. *Rem. Sens. Env.* 24, 481-492.

Price J C 1992, Estimating vegetation amount from visible and near infrared reflectances. *Rem. Sens. Env.* 41, 29-34.

Raffy M 1992, Change of scale in models of remote sensing: a general method for spatialization of models. *Rem. Sens. Env.* 40, 101-112.

Seppälä M 1972. Location, morphology and orientation of inland dunes in Northern Sweden. *Geogr. Ann.* 54A, 85-104.

Sollid J L, S Andersen, N Hamre, O Kjeldsen, O Salvigsen, S Sturød, S Tveitå & T Wilhelmsen 1973, Deglaciation of Finnmark, North Norway. *Norsk Geogr. Tidsskr.* 27, 233-325.

Tikkanen M & O. Heikkinen 1995, Aeolian landforms and processes in the timberline region of northern Finnish Lapland. *Zeszyty Naukowe Uniwersytetu Jagiellonskiego. Prace Geograficzne* - Zeszyt 98, 68-90.

Vuorela A 1992, *On developing the land cover and forest classification in the National Board of Survey* (in Finnish). Unpubl. MSc thesis. Helsinki Univ. of Tech.

Woodcock C E & A H Strahler 1987, The factor of scale in remote sensing. *Rem. Sens. Env.* 21, 311-332.

USE OF SAR DATA TO STUDY ACTIVE VOLCANOES IN ALASKA

Kennesson G. Dean, K. Engle, Z. Lu and J. Eichelberger

Geophysical Institute, University of Alaska Fairbanks
903 Koyukuk Drive, P.O. Box 757320
Fairbanks, Alaska 99775–7320, U.S.A.
phone: 1–907–474–7364, fax: 1–907–474–7290
kdean@gi.alaska.edu

Tina Neal, Mike Doukas

Alaska Volcano Observatory
U.S. Geological Survey
4200 University Drive
Anchorage, Alaska 99508

SUMMARY ABSTRACT

Synthetic Aperture Radar (SAR) data of Westdahl, Veniaminof, and Novarupta volcanoes in the Aleutian Arc of Alaska were analyzed to investigate recent surface volcanic processes. These studies support ongoing monitoring and research by the Alaska Volcano Observatory (AVO) in the North Pacific Ocean Region. Landforms and possible crustal deformation before, during, or after eruptions were detected and analyzed using data from the European Remote Sensing Satellites (ERS), Japanese Earth Resources Satellite (JERS) and the U. S. Seasat platforms. Field observations collected by scientists from the AVO were used to verify the results from the analysis of SAR data.

The SAR data were recorded on multiple dates, from various platforms, at different frequencies and different look directions. Radiometric and geometric processing was required to analyze surface conditions in mountainous terrains on these disparate data sets. The data were filtered and re-sampled to 30 m and 90 m pixel spacing to remove most of the system noise and the large backscatter variability which results in the "salt and pepper" appearance, typical of full resolution SAR images. The data were also merged with a digital elevation model (DEM) to correct for terrain distortions.

To test the effects of resolution on our ability to detect eruption-induced landform changes, we compared analyses derived from both 30 m and 90 m data. Landforms observed on the 30 m data were also detected on the 90 m data with minimal loss of information in most cases. We conclude that SAR data with 90 m pixel size are adequate to investigate gross geomorphic features. However, when fine-scale detail is required, 30 m data are preferred. Use of the 90 m data reduces processing time, optimizes the use of disk space, and makes network transfers of data significantly more efficient.

At Westdahl Volcano, we examined modifications of the land resulting from the 1978 and the 1991-92 eruptions. The source crater of the 1978 eruption was observed on a Seasat image (Fig. 1) as well as three linear structures (prongs) radiating from the crater. Evidence of mudflows observed by field parties who visited the eruption site on 6 & 7 Aug. 1978 (Krafft, 1978) was not observed on the image. By happenstance, the 1991-92 eruption was recorded on a ERS-1 SAR image (Fig. 2) . A new cinder cone and lava flow emanating from a fissure northeast of the 1978 cone are clearly visible. The 1978 crater, now buried by snow, was barely detectable on the 1992 image.

At Veniaminof Volcano, melt pits (Neal et. al., 1996; Yount et. al., 1985) that formed in an intra-caldera ice cap from eruptions in 1983-84 and again in 1993-95 were detected. In addition, we observed changes in the radar signatures of the ice on SAR images recorded during the 1993 eruption. Typically, glaciers have a dark signature in the summer and a bright signature in the winter depending upon the presence of liquid water at the surface. Anomalous radar signatures in the ice cap in November, 1992, August, 1993, and October 1994 may be related to melting from volcanic activity. On one of the images, ash deposits radiating away from the source vent, an intra-caldera cinder cone, are evident (Fig. 3).

At Novarupta Volcano, experimental interferometric SAR (IFSAR) processing techniques were used to measure ground deformation and to generate DEMs. Results to date suggest a ring pattern of deformation over a 5-km region northeast of the Novarupta vent. This surface displacement may be related to approximately 5 cm of up-

Proceedings of the Fourth Symposium on Remote Sensing of the Polar Environments, Lyngby, Denmark, 29 April – 1 May 1996 (ESA SP-391, July 1996)

ward vertical movement over a three year period (Lu et. al, in press), however these results have yet to be verified by other ground- or GPS- based geodetic techniques. A new DEM with 10 m vertical resolution and 30-m spatial resolution have also been generated from the SAR data for this area. Our intent is to refine IFSAR techniques so they may be used routinely by AVO to monitor and study volcanoes, determine the effects of eruptions, and measure crustal deformation that may precede eruptions in this remote region.

References

Krafft, M., 1989. Global Volcanism 1975-1985, The First Decade of Reports from the Smithsonian Institution's Scientific Alert Network (SEAN), L. McClelland, T. Simpkin, M. Summers, E. Nielsen, T. Stein (eds), Prentice Hall, Englewood Cliffs, New Jersey, Am. Geophy. Union, Washington DC, pp. 329-332.

Lu, Z., R. Fatland, M. Wyss, S. Li, J. Eichelberger and K. Dean, (in press). Deformation of Volcanic Vents Detected by ERS-1 SAR Interferometry, Katmai National Park, Alaska, Submitted to Letters Nature. Apr. 1996.

Neal C. A., R. G. McGimsey and M. Doukas, 1996. Volcanic Activity in Alaska: Summary of Events and Response of the Alaska Volcano Observatory, U.S. Geol. Surv., Open File Report 96-24, pp. 7-10.

Yount, M.E., T.P. Miller, R.P. Emanuel, R. and F.H. WIlson, 1985. Eruption in an ice filled caldera, Mount Veniaminof, Alaska Peninsula, in Bartsch-Winkler, Susan and Reed K.M., eds., The U.S. Geol. Surv.. in Alaska, Accomplishments during 1983: U.S. Geol. Surv. Circular 945, p. 58-60.

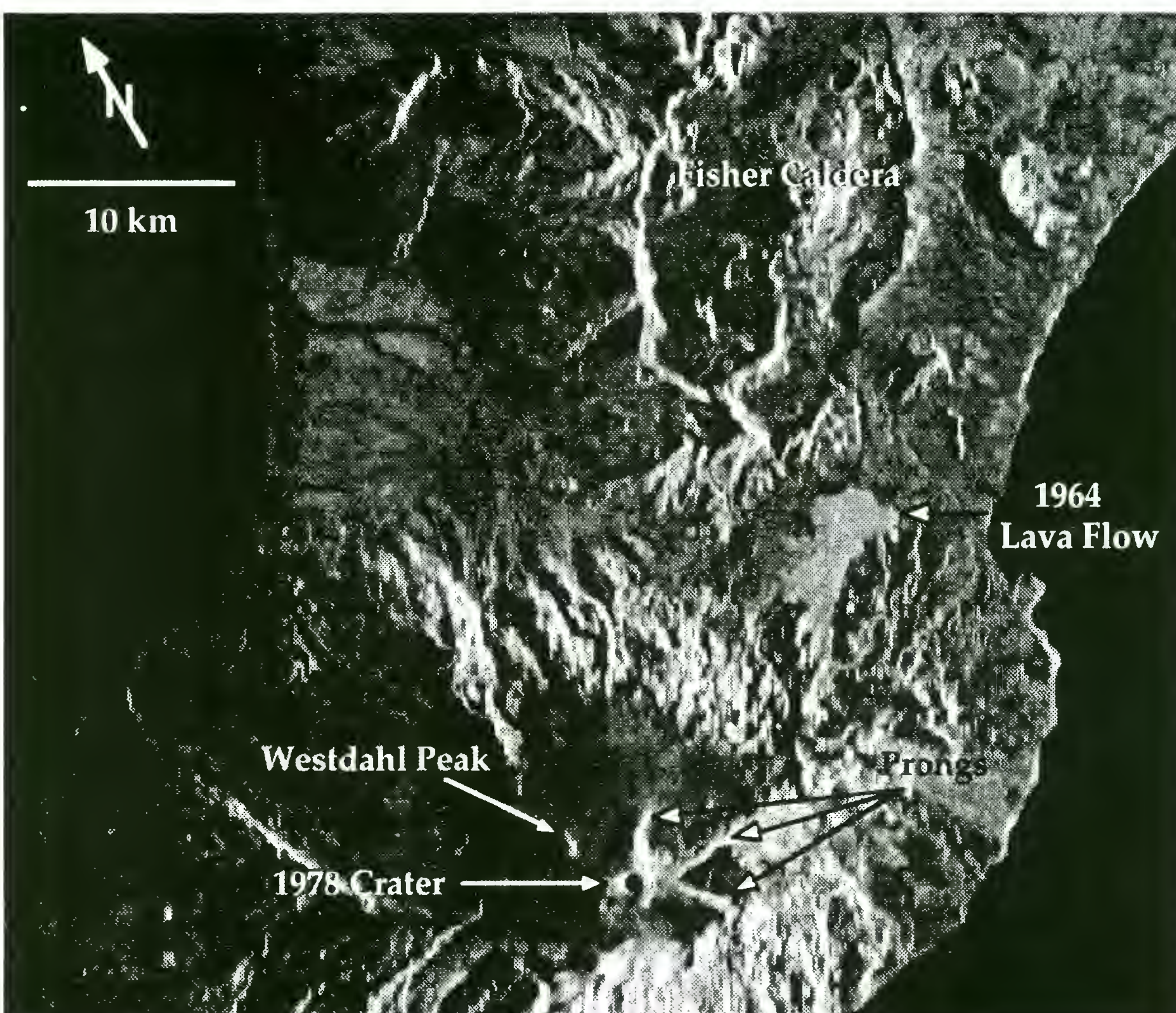

Figure 1. Westdahl Volcano - 1978. An explosive eruption in February formed a crater 500 m deep through glacial ice. This Seasat SAR image was recorded on 7 August 1978, and shows the crater and three prongs readiating from the crater. The 1964 lava flow is clearly visible. The image has been filtered, and resampled to a 90 m pixel spacing. Westdahl Volcano is located on Unimak Island approximately 1000 km southwest of Anchorage, Alaska.

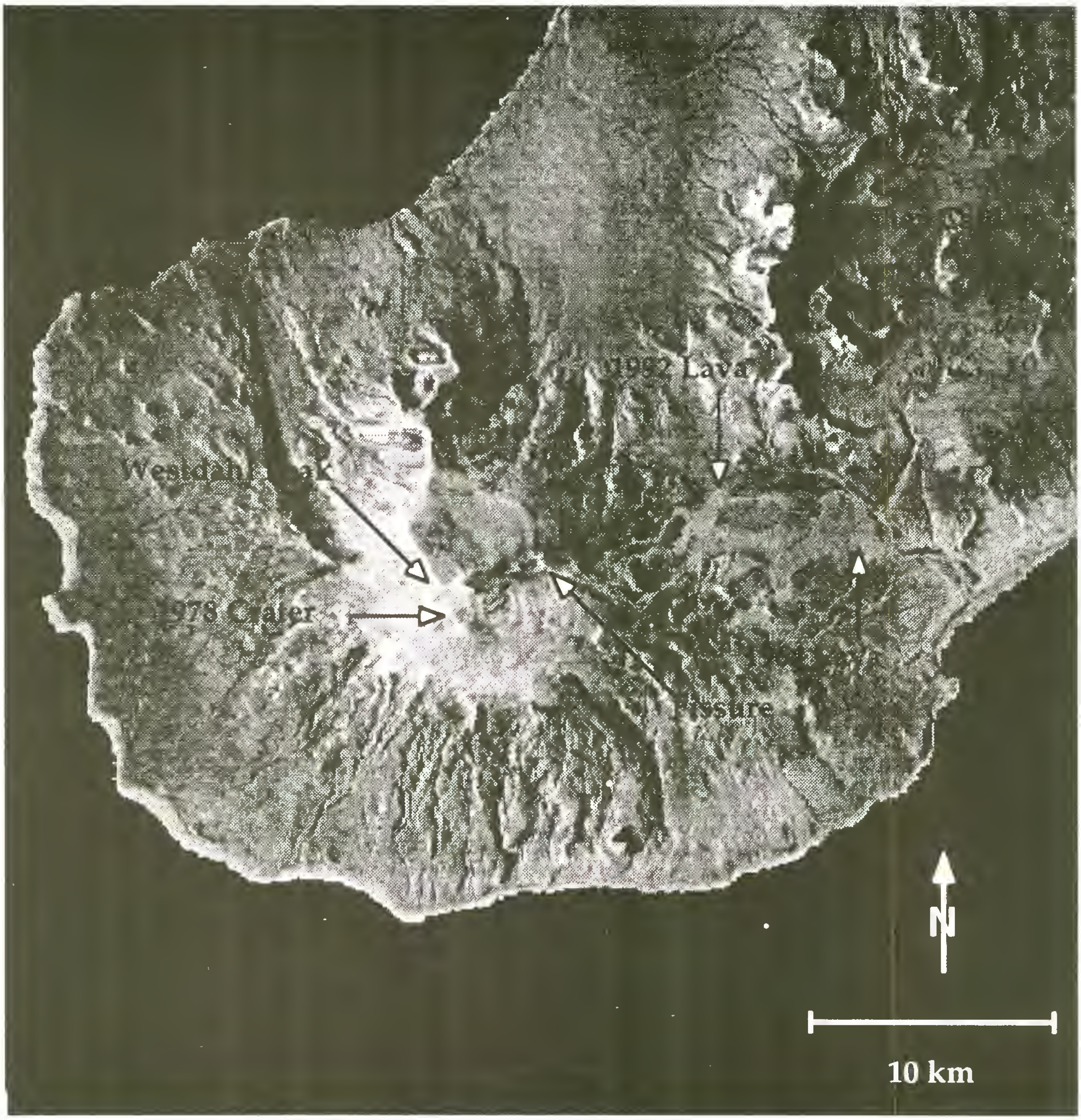

Figure 2. Westdahl Volcano erupted in November 1991. This ERS 1 SAR image was recorded on 19 January 1992, and shows the fissure that resulted from the eruption and a new lava flow. The caldera-end of the fisure is approximately two kilometers north of the 1978 vent. The 1978 vent, clearly seen in figure 1, is buried by snow but is still detectable on the ERS - 1 image. The prongs observed on the 1978 image can not be seen on this SAR image. This image has been filtered, resampled to a 90m pixel spacing and terrain corrected.

Fig. 3. Veniaminof Volcano erupted on 23 July 1993 and continued to be active into 1995 with only periodic observations of hot spots seen on AVHRR data during the later part of this period. A series of ERS and JERS SAR images were used to monitor the eruption and to assess changes in surface morphology. All of the images were filtered, resampled to 90 m pixels and terrain corrected. The ice cap that overlies the caldera has a dark radar signature during the summer months when liquid water is present in the ice cover. During the winter, water is frozen and the ice-radar signature is bright. This ERS SAR image, 24 August 93, shows the dark summer ice cap. The 1983 and 1993 eruption emanated from a cinder cone west of the caldera center. The ice cap adjacent to the south side of the cone melted, forming an ice pit in 1983. During the 1993 eruption additional ice melted along the east side of the cone, enlarging the ice pit in that direction. A v-shaped light area with its apex at the cone and radiating to thesoutheast may be ash on the snow or roughening of the ice surface from fallen ash. Veniaminof Volcano is located on the Alaska Peninsula 800 km southwest of Anchorage.

ENVIRONMENT
VEGETATION
BIOLOGY

MAPPING PLANT COMMUNITIES IN A LOCAL ARCTIC LANDSCAPE APPLYING SCANNED INFRARED AERIAL PHOTOGRAPHS IN A GEOGRAPHIC INFORMATION SYSTEM.

Lennart Nilsen, Institute of Biology and Geology, University of Tromsø, NORWAY. Fax: 47 77 64 56 00. E-mail: lennart@ibg.uit.no.

Thierry Brossard and Daniel Joly, University of Franche-Comté, CNRS, Laboratoire Environnement et Paysage, 30 rue Mégevand, 25030 Besançon, FRANCE. Fax: 33 81 66 54 00. E-mail: tbrossard@univ-fcomte.fr.

ABSTRACT.

A limited area in front of the Midtre Lovénbreen glacier, Northwest Spitsbergen, Svalbard was selected for this large scale study. The central issue were to distinguish plant communities and their distribution in relation to micro-environmental conditions. A procedure for automatic mapping of plant communities and their corresponding environmental features by means of statistic modeling and a geographic information system (GIS) have been developed. Large scale data from different sources such as a scanned infrared(IR)-aerial photograph, information layers derived from a digital elevation model (DEM) and vegetation sampling in the field have been integrated in GIS. Probability models build the links between GIS data layers and plant communities resulting from classification of field data. Based on the probability model maps were produced showing the actual and potential distribution of plant communities. The accuracy of the vegetation map was improved by adding additional information from the DEM. However, separate statistic models have to be developed for periglacial landscapes with immature and unstable vegetation and for stable landscapes with climax vegetation types.

INTRODUCTION.

Remote sensing and GIS have become powerful tools for vegetation mapping, modeling of vegetation distribution (Brown 1994, Goodchild 1994), and ecosystem monitoring in general.
Few studies have been performed in polar regions using remote sensing data for vegetation mapping and mainly at intermediate or small scales with a ground resolution of 20 meters or larger (Craighead et al. 1988, Ostendorf & Reynolds 1993). Digitized aerial photographs have also been applied (Frank & Thorn 1985) and compared with satellite data (Mosbech & Hansen 1994). Evans et al. (1989) made a large scale study using GIS, DEM and aerial photographs to analyse relationships between vegetation pattern, terrain and snow distribution.

Some studies have also been performed on Svalbard using remote sensing data monitoring different aspects of vegetation (Øritsland & Ødegaard 1980, Elven et al. 1990, Nilsen 1992, Brossard et al. 1993, Spjelkavik 1995). However, problems arise when trying to distinguish vegetation units on Svalbard at a large scale.

First; investigations so far has shown that it is difficult to detect phytososiological units by means of traditional remote sensing sources like Landsat 5 TM. Spjelkavik (1995) concluded that individual vegetation stands can not be obtained by Landsat TM due to the spatial resolution of the satellite data. Second; there is no agreement about a standard set of mapping units on Svalbard. This is reflected in the inconsistent application and wide range of used names. Elvebakk (1994) has made a syntaxonomical survey which can act as a guide to valid names used for Svalbard vegetation types. Third; few plant communities have been studied comprehensively to establish them within a phytososiological system. Fourth; The Svalbard archipelago has few species and they have a broad ecological amplitude which makes it difficult to detect character species of certain habitats (Elven et al.1990).

The judgment of scale and criteria for vegetation mapping is subjective and is often guided by management purposes. In this study the plant community is the mapping unit. The plant community concept is applied referring to a homogeneous vegetation within a restricted area with an aggregation of certain plant species. The classification of vegetation is performed with a phytosociological system as a framework. From the botanical point of view this is favorable as it provides the most complete information regarding species composition.

This study deals with large scale vegetation mapping of a small high-arctic area in front of a glacier near Ny-Ålesund, arctic Norway. The main problems addressed are: Can we distinguish plant communities and their spatial distribution in relation to micro-environmental conditions using classification algorithms on scanned IR-aerial photosgraphs? Can the vegetation classification be improved by using additional environmental information?

In order to answer these questions data from multi-disciplinary sources were integrated in a GIS database. The GIS database makes it possible to model, combine and analyse spatial relationship between the data sets for the characterization and mapping of plant communities and their habitats. Two types of data were collected.

I. Field data. These are obtained from punctual recording of vegetation and environment features along transects covering the study area.
II. Raster data layers. The first layer is a digitized color IR-aerial photograph. The second data layer is a precise DEM of the study area. It was made using a ground positioning system (GPS) based on satellite navigation technology. Additional significant information such as exposure, sloping and potential radiation were derived from the DEM. They cover the study area as a continuum in raster format and at high resolution.

The result showed that it is possible to produce a vegetation map by classifying a scanned IR-aerial photograph which aim to reproduce the spatial distribution of defined plant communities. A better conformity was achieved between classification of vegetation data and the raster data using additional information derived from the DEM. However, the statistical model fails to distinguish the present distribution of plant communities in the recently deglaciated moraine area, indicating that a separate model has to be made for this region.

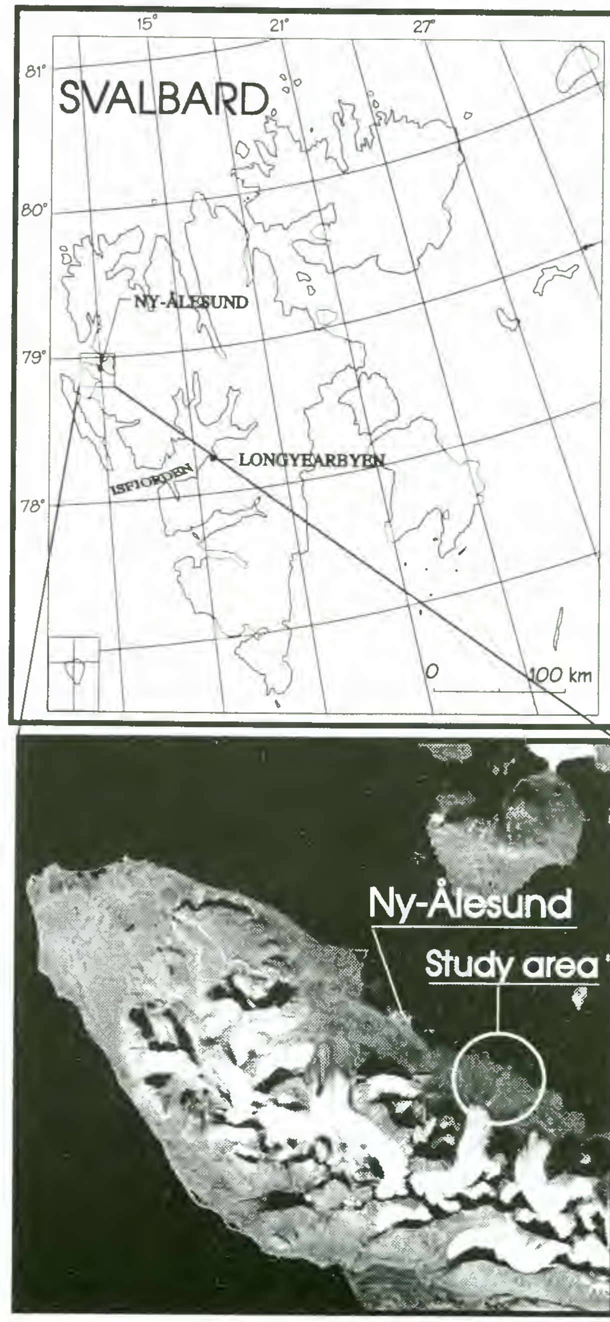

Figure 1. Svalbard and a panchromatic SPOT satellite image showing Brøggerhalvøya and the study area 6 km east of Ny-Ålesund.

STUDY AREA.

The study area is located in front of the Midtre Lovénbreen glacier about 6 km east of Ny-Ålesund (78°54'N) at Kongsfjorden, northwestern Spitsbergen, Svalbard (Fig. 1). The mean July temperature at Ny-Ålesund is 5.1° C and mean annual precipitation is 385 mm. Further eastwards along Kongsfjorden the climate is more favourable, and the mean July temperature in the study area is probably near 6° C.

The area is heterogeneous as to vegetation and abiotic environmental factors such as geo-morphology, texture, age, and origin of soils, micro-climatology and disturbance regime. Series of raised beaches and sandbars, a small calcareous ridge running in east-west direction, large recent and active outwash plains and a big terminal moraine created by the Midtre Lovénbreen glacier are dominating the landscape. The bedrock is mainly calcareous but siliceous erratic blocks have been scattered all over the area during the retreat of the glacier. Soil structure like hummocks, stone rings, small and large polygons, striped ground and solifluction lobes are common (Brossard et al. 1984). Vegetation cover is generally sparse as large areas are unstable and disturbed from fluvial, glacial and soil cryoturbation activity. Minor areas are densely covered by calciphilous ridges and moderate snowbed vegetation, corresponding to the phytosociological alliances *Caricion nardinae* on the exposed ridges, *Luzulion nivalis*, respectively. The nomenclature of the syntaxa follow Elvebakk (1989). Small areas also have well developed mire, moss tundras and late snowbed vegetation. Areas completely devoid of vegetation are confined to seasonally active outwash plains and deposits just in front of the glacier.

METHOD.

Vegetation data were sampled systematically along transects. The transects were positioned in such a way as to cover the major geomorphologic features and plant communities in the area. A sampling quadrat of 0.25 m^2 was placed at fixed intervals of 35 m. Inside the square all plants (vascular plants, bryophytes, lichens) and substrate were recorded giving a frequency estimate. The square is referred to as a relevé in the subsequent text. A total of 200 relevés were sampled. The relevé data can not be included here, but they are available on request from one of the authors (L.Nilsen).

The position of each relevé was determined using a GPS. This was done in order to ensure that the relevé could be traced in a very precise manner and compared to a digital counterpart in the scanned IR-aerial photo. The vegetation data was then classified using a computer program for multivariate data analysis in ecology and systematic; SYN-TAX version 5.1 (Podani 1994).

The IR-aerial photograph provided by Norsk Polarinstitutt was transformed into raster format with a scanning device. The basic red, green and blue components (RGB) were stored in different image files as usually done with the different channels of satellite images. The DEM of the area was constructed by mean of a GPS (Trimble 4000 SE) used in the differential and kinematic modes. Altogether 4300 points were positioned in the field using GPS. According to control measurements, the accuracy of the system keeps the error within 10 cm. The DEM layer is processed by interpolation between the 4300 points. From the DEM several sub-layers such as gradient, aspect and solar energy can be derived. In the subsequent text these sub-layers are named topographic data's. The resolution of the pixels are 2 x 2 m for all raster data and the Universe Transverse Mercator (UTM) projection makes it possible to superimpose the different layers.

The modeling method operates by crosslinking field data (i.e. the defined plant communities) and the raster data layers of the GIS. If all the considered data layers contained quantitative or pseudo-quantitative values, the criterion of distance can be used for analyzing the relationships between these data and field observations (Brossard et al. 1992). But, in the present case, the data layers are heterogeneous as they also include non-quantitative values such as the categories which define the slope aspect. To overcome this problem, the quantitative values were discretised and turned into Boolean items.

Hence, the statistic links between vegetation types and GIS data can be analyzed in terms of occurrence and frequency vector. This approach rests upon binomial law (Spiegel 1982) and proceeds to establish empirical probability models (Tom & Miller 1984). Spjelkavik (1995) proposed the term comparison matrix, and Brossard & Joly (1994) have explored, in a similar way, the statistical links between plant communities and classification of satellite data.

The next step is to use the empirical probability model as an operator for mapping plant communities by means of GIS layers including scanned IR-aerial photograph as well as information derived from the DEM. The presented matrix (Tab. 1) is the core of the model and indicates how it works. As the UTM position of each observation point is known, it is possible to extract from the GIS database the values of pixels corresponding to RGB components of the IR image. The quantitative values are then turned into Boolean characters. The occurrence of each positive Boolean item inside the different plant communities is counted up and converted into percentage as done in Table 1. The sum of each row is 100%. According to the Boolean value of a given pixel, the probability for it to be ranked in the different plant communities are known. As each pixel is characterized by six Boolean items (one per data layer), the corresponding probability values are to be summed up column by column. The considered pixel is allocated to the plant community for which the probability score is the highest. Thus it is possible to make probability maps showing the actual and potential distribution of plant communities (Fig. 4).

RESULTS.

I. Vegetation classification.

The relevé data were subjected to non-hierarchical clustering (fuzzy c-mean clustering) as described by Podani (1994). It differs from other non-hierarchical classification by calculating a membership weights expressing the affinity of the relevés to all the clusters rather than assigning them to a single cluster like deterministic partitioning techniques. The number of clusters have to be specified in advance and relevés are assigned to the cluster for which it has the highest membership weights. The fuzzy clustering was performed specifying 8 clusters. There are certain restrictions to the choice of number of clusters as there has to be a sufficient number of relevés inside each clusterto make a reliable statistical model for classification of the raster data.

In order to find a suitable number of clusters (plant communities) from a mathematical point of view Bezdek's partition coefficient (Bezdek 1981) were computed and plotted against cluster number (Fig. 2). But Bezdek's cluster coefficient is a rather crude measure of optimal cluster number. Coefficients that were not normalized seems to produce bias towards a small number of clusters, while a normalized

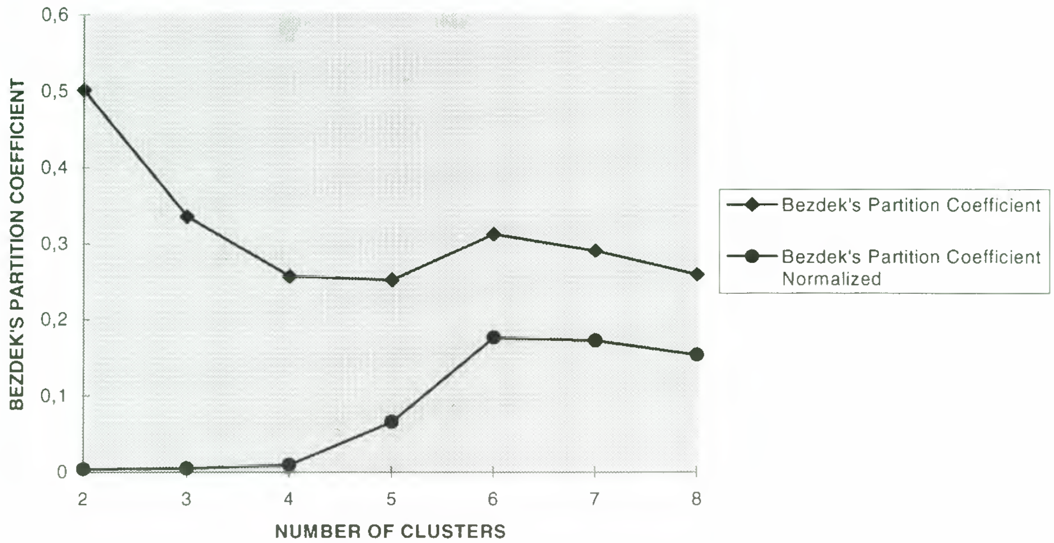

Figure 2. Bezdek's partition coefficient plotted against cluster number 2 to 8.

Table 1. The probability model used as an operator for mapping. The values are expressed as percent probability. Abbreviations; IRR=red, IRG=green, and IRB=blue components of the infrared aerial photograph. GR=gradient, AS=aspect, SO=solar radiation, KW=radiation in kilo watt pr. m². CL=cluster and refers to the plant community 1 to 8.

	CL-1	CL-2	CL-3	CL-4	CL-5	CL-6	CL-7	CL-8		CL-1	CL-2	CL-3	CL-4	CL-5	CL-6	CL-7	CL-8
IRR-1	0	0	0	0	0	100	0	0	IRB-1	0	0	52	0	0	48	0	0
IRR-2	0	0	0	0	0	100	0	0	IRB-2	69	0	8	0	0	23	0	0
IRR-3	0	0	71	0	0	0	29	0	IRB-3	23	11	0	0	0	0	17	49
IRR-4	38	0	0	0	19	0	38	4	IRB-4	0	57	0	0	0	0	43	0
IRR-5	14	32	0	0	25	0	0	30	IRB-5	0	0	0	0	93	0	7	0
IRR-6	0	14	0	77	0	0	0	9	IRB-6	0	0	0	81	19	0	0	0
IRG-1	0	0	0	0	0	100	0	0	GR=0	0	10	3	15	26	21	23	3
IRG-2	0	0	59	0	0	41	0	0	GR=1-2	9	15	15	17	13	15	13	2
IRG-3	46	3	3	0	0	0	5	43	GR=3-4	39	17	22	11	0	0	0	11
IRG-4	0	52	0	0	0	0	45	3	GR=5-7	28	11	17	0	0	6	0	39
IRG-5	0	0	0	0	100	0	0	0	GR>=8	0	0	0	0	0	0	0	100
IRG-6	0	0	0	100	0	0	0	0	SO<3.0KW	0	0	0	0	0	67	33	0
AS=NNE	44	0	22	4	11	0	15	4	SO<4.0KW	25	0	40	10	10	0	15	0
AS=E	42	0	25	8	0	8	0	17	SO<4.5KW	31	0	6	31	12	6	12	0
AS=SSE	0	0	6	12	0	35	0	47	SO<5.0KW	21	0	0	14	29	11	18	7
AS=SSW	0	81	0	0	0	6	0	12	SO<5.5KW	4	0	17	26	13	9	17	13
AS=W	0	0	100	0	0	0	0	0	SO<6.0KW	0	25	25	12	12	12	12	0
AS=NNW	0	0	0	44	25	0	19	12	SO<7.0KW	0	52	0	0	0	33	0	14
AS=FLAT	0	10	3	15	26	21	23	3	SO>=7.KW	0	33	0	0	0	0	0	67

coefficient leads to bias in the opposite direction (Equihua 1990). From Fig.2 it is suggested that within the range of clusters number 4 to 8 there is a slightly better separation (on average) at the 6 cluster level. But a visual inspection of the tabular vegetation data reveals that a reduction of number of clusters from 8 to 6 would result in loss of important floristic information as two plant communities are combined. A further separation beyond the eight clusters level resulted in clusters with too few relevés inside.

Restricted by the above mentioned assumption the vegetation data set seems to support a stratification into eight plant communities. Pairwise separation coefficients for the 8 clusters were then calculated indicating which of the different plant communities (clusters) that are clearly separated from each other and which are not (Tab. 2).

II. Vegetation mapping.

Two tests were made in order to estimate the efficiency of the model. The first one (Tab. 3) was made using only the RGB components of the IR-aerial photograph. The confusion matrix makes it possible to estimate the fit between classification of the vegetation data and the results obtained from the model leading to the cartography. Most of the values are high (ranging from 46 to 92%) indicating that the IR-aerial photograph makes an efficient discrimination of plant communities as defined by classification of the vegetation data.

The second test was made adding topographic data for processing. Fig.3 display raster maps of the topographic data covering the study area. Fig.3 A show a raster map of the constructed DEM, while Fig.3 B,C and D shows gradient, aspect and solar

Table 2: Pairwise separation coefficients for the 8 clusters. Clusters that have a coefficient less than 0.6 (weakly separated) are shown with white text.

Pairwise Separation Coefficients for cluster 1 to 8								
Cluster no.	1	2	3	4	5	6	7	8
1	0							
2	33,77	0						
3	46,62	47,83	0					
4	00,30	33,00	46,60	0				
5	05,49	33,40	50,63	03,65	0			
6	03,92	43,30	55,99	05,61	14,93	0		
7	12,95	50,33	58,49	11,87	20,18	18,35	0	
8	00,11	32,52	45,85	00,00	04,24	05,09	12,96	0

Table 3: Confusion matrix between vegetation classification (in rows) and results (in columns) of the mapping procedure. The model is applied to the RGB components only.

	PRBIR-1	PRBIR-2	PRBIR-3	PRBIR-4	PRBIR-5	PRBIR-6	PRBIR-7	PRBIR-8
ORIG-1	64	0	4	0	0	4	0	28
ORIG-2	1	92	0	0	1	0	0	6
ORIG-3	14	0	81	0	0	5	0	0
ORIG-4	0	0	0	89	0	6	0	5
ORIG-5	0	0	1	3	73	12	11	0
ORIG-6	13	1	7	0	0	75	2	2
ORIG-7	6	1	7	2	11	5	56	12
ORIG-8	7	3	3	0	7	20	14	46

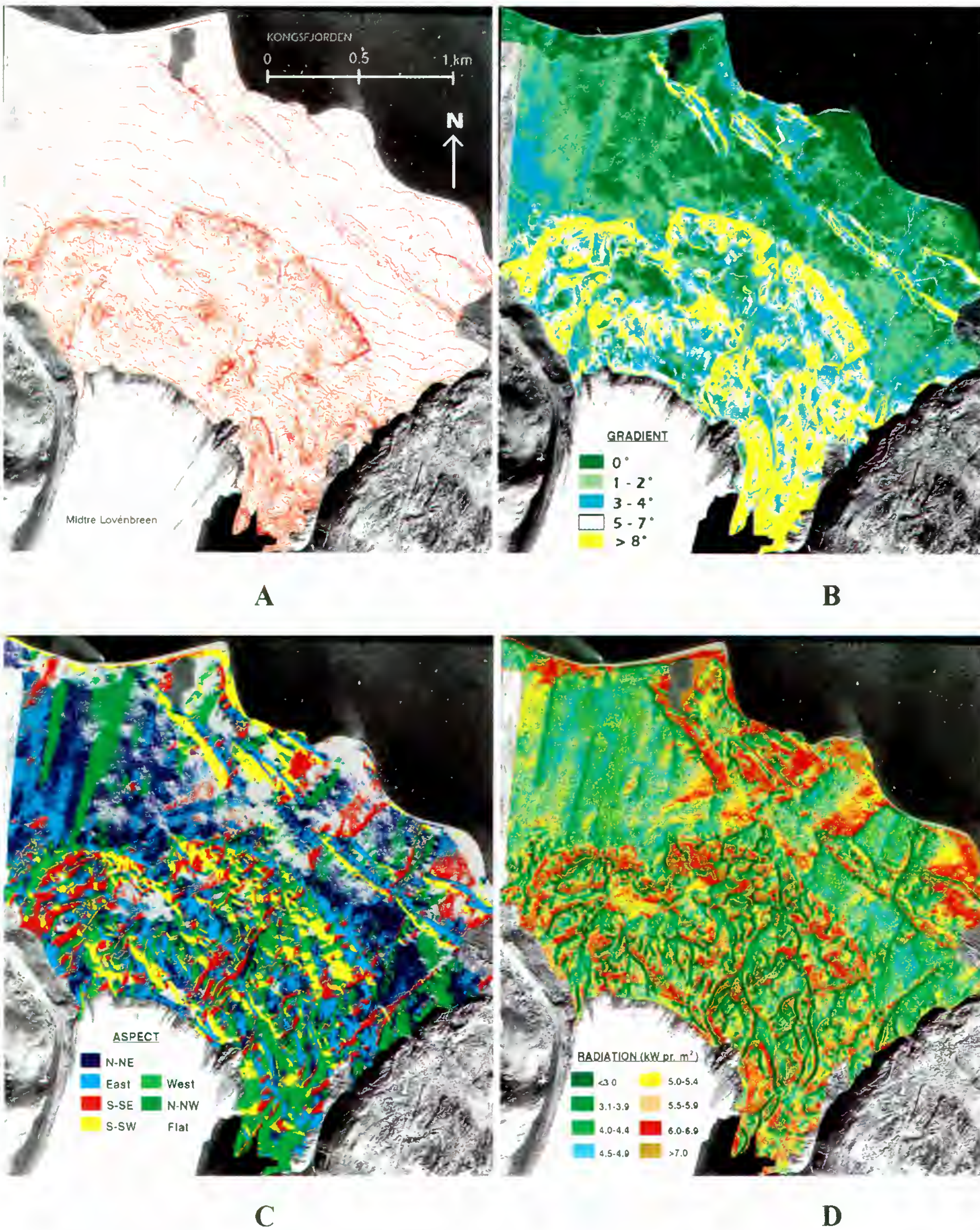

Figure 3. **A**: A digital elevation model(DEM) of the study area. The equidistance is 2 m. **B**: Gradient calculated from the DEM. **C**: Aspect calculated from DEM. **D**: Solar radiation calculated from DEM.

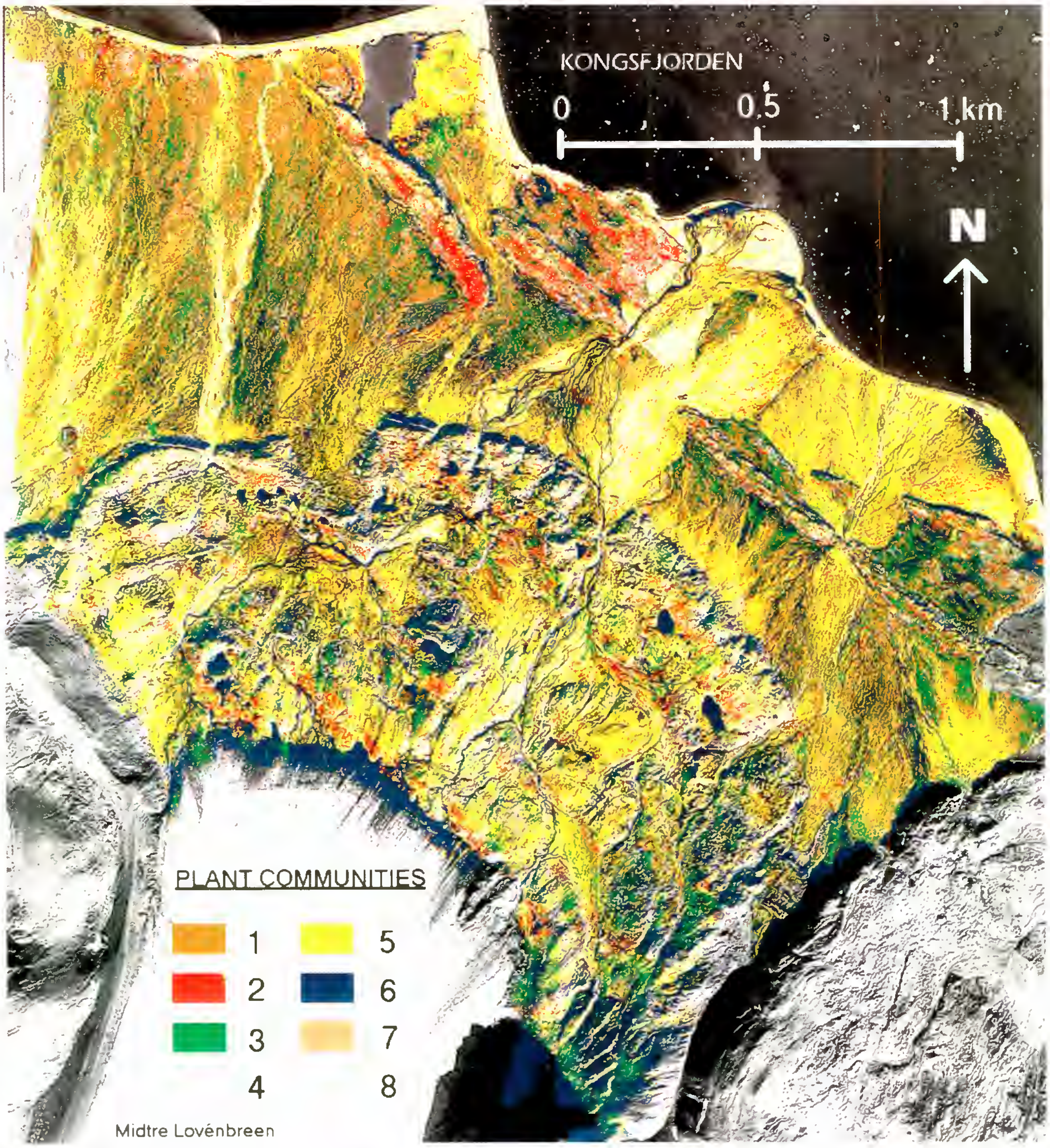

Figure 4. Vegetation map derived from the scanned IR-aerial photograph using additional information from the DEM.

Legend to Fig. 4 with vegetation description of plant community 1-8.

No	REPRESENTATIVE SPECIES	ECOLOGICAL CHARACTERISTIC	PHYTOSOSIOLOGICAL NAME
1	*Scorpidium cossonii - Alopecurus alpinus*	Mire, 50-70% cover, bryophyte dominated	Alliance: Eriophorion scheuchzeri
2	*Cassiope tetragona*	Mesic plains and slopes, 100 % cover	Alliance: Caricion nardinae
3	*Cetrariella delisei - Luzula arcuata* ssp. *confusa*	Mesic plains to moderate exposed ridges, 70-90 % cover	Alliance: Luzulion arcuatae
4	*Saxifraga oppositifolia- Salix polaris*	Mesic plains to moderate snowbed, 40-60 % cover	Alliance: Luzulion nivalis
5	*Stereocaulon rivulorum- Fulgensia bracteáta*	Dry to mesic river fans, moraines, moderate snowbeds, lichen dominated, <25 % cover	Alliance: Unknown, immature vegetation at different successional stages
6	*Deschampsia alpina- Catoscopium nigritum*	Tundra mire, wet to moist cryoturbation soil, <25 % cover	Alliance: Eriophorion scheuchzeri
7	*Saxifraga oppositifolia- Stereocaulon rivulorum*	Mesic plains, disturbed, >50 % cover	Alliance: Eriophorion scheuchzeri
8	*Dryas octopetala- Carex rupestris*	Exposed ridge, cover <50 %	Alliance: Caricion nardinae

Table 4: Confusion matrix improved by adding into the statistical model topographic data derived from the DEM (see Tab.1).

	PRBTO-1	PRBTO-2	PRBTO-3	PRBTO-4	PRBTO-5	PRBTO-6	PRBTO-7	PRBTO-8
ORIG-1	88	0	4	0	0	4	0	4
ORIG-2	0	97	0	0	0	0	0	3
ORIG-3	11	0	81	0	0	4	0	4
ORIG-4	5	0	2	91	0	2	0	0
ORIG-5	1	2	3	3	75	8	5	3
ORIG-6	10	1	8	0	0	77	1	3
ORIG-7	11	2	9	2	11	5	60	0
ORIG-8	3	3	3	0	3	19	10	59

radiation, respectively. The confusion matrix (Tab.4) emphasizes that residuals are less important than previously. A map generated from the model using only the RGB component of the IR-aerial photograph, refered to as Map 1 in the subsequent text, and a map (Fig.4) derived from the model applying additional information from the DEM were produced. Map 1 is not presented here.

DISCUSSION.

The classification of the vegetation data revealed 8 floristically and ecologically different plant communities. The requirement of a sufficient number of relevés inside each cluster can force some of the relevés together although they are very different thus making the average cluster somewhat special and heterogeneous regarding plant species composition. The decision of cluster number must therefore be carefully inspected looking for species that obviously should not occur together by means of their habitat requirement. If this happens it is an indication of an artificial grouping solely resulting from the specified number of clusters. This means a loss of ecological and floristic information.

How well the statistical model for classification of the scanned IR-photo performs, rely on the initial classification of vegetation data. A bad classification of vegetation data (heterogeneous units) are likely to give results that fail to reproduce the spatial distribution of the defined plant communities. Comparing Tab. 2 with Tab. 3 there is an overall agreement between the two tables. Those plant communities that seem to be poorly separated in the vegetation classification are those who have high probability of belonging to more than one probability class in Tab. 3. If the confusion is very large this can indicate that the obtained plant community is too heterogeneous and a subdividing should take place in order to make smaller and more homogeneous vegetation units. The results from Tab. 2 and 3 indicate that plant community 5, 6 and 7 are heterogeneous. And these communities are also those which contain the largest number of relevés.

When looking for differences between the map derived from the model using only the RGB-values of the IR-aerial photograph (Map 1) and the map in Fig. 4 the main point is that the distribution of plant communities is hardly manipulated on the marine terraces and outwash plains close to the fjord. This can normally be expected as the topographical conditions are less contrasted in these areas. The large scale of the DEM makes it possible to model precise differences which appear when the map is constructed using topographic information. The relationship between plant communities and topographical data is weaker than with RGB components of the image, as shown by the probability matrix in Tab.1. However, the topographical data are effective and contributes to improving the mapping procedure. For the 8 plant communities there is an average improvement of 8.3% in terms of probability using the additional topographic information from the DEM. And for plant community 1 and 8 the improvement was 27.3% and 22 %, respectively.

Concerning the moraine, the differences are more distinct. Plant communities only present on the lower marine terraces and outwash plains in Map 1 also appear in the newly exposed moraine on the map in Fig. 4. The reason for this is the great topographical contrasts in the moraine which supply information that makes it possible to discriminate new sites.

The classification of the digitized image sometimes fails to distinguish between sparsely vegetated areas an non-vegetated areas. Areas close to the glacier and in active river fans that obviously are devoid by vegetation are classified into one of the 8 plant communities. There are two explanations for this inconsistency:

1. In cases were the vegetation cover is scattered and sparse the soil component will be the primary determinant of color, texture and shade in the IR-image and hence the digital value of the scanned image. In these cases the map actually show the soil type distribution rather than reflecting the plant community distribution. This is the case for plant communities number 4 and 5 in Fig. 4.

2. Obviously, some of the plant communities which appear in Fig. 4 can not be found on the moraines as they correspond to advanced colonization stages. This fact reveals the limit of the test as it was done here, because the considered environmental factors have not affected the vegetation within the same time scale. It is necessary to make separate models for the moraine and the rest of the study area with an appropriate sampling protocol.

By using scanned IR-aerial photographs we gain a high spatial resolution, but loose the additional information supplied by satellite sensors operating with more than three channels and in a broader range of the electromagnetic spectrum. However, in the near future (1996-2002), the new planned satellites will provide images at a metric resolution (Crepeau & Pierre 1996). At the moment the Russian satellite RESURS-F2 is equipped with a sophisticated true multi-spectral camera system recording in six bands (460-900 nanometers) with a ground resolution of 6-8 meters, each scene covering an area of 150x150 km.

An interesting issue for probability models can be explored by experimenting with integration of different environmental factors like landforms and temperatures. In our planned future projects these features will be recorded at large scale (micro-scale) in the field and estimated according to very precise topographical conditions using models that integrate multi-source data (Joly & Fury 1995).

CONCLUSIONS.

1. The results showed that it is possible to produce a vegetation map by classifying a scanned IR-aerial photograph which aim to reproduce the spatial distribution of the defined plant communities. The IR aerial photography coupled with the GPS provides the technical resources for making a GIS data base when requiring a high resolution data set.

2. The results showed that using additional information derived from the DEM improved the conformity between classification of vegetation data and the raster RGB-data. The improvement in mapping accuracy that can be gained using this method relies heavily on which environmental factors that are selected to be recorded and included in the model.

3. The developed probability model is an appropriate method for mapping plant communities based on heterogeneous data layers originating from different sources. However, when adding the additional information from the DEM the model does not performe satisfactorily for areas containing unstable and scattered vegetation such as recently deglaciated moraines. This problem can be solved by incorporating the time factor in the model.

4. Using data from the present day vegetation in combination with auxilliary environmental data (from GIS and DEM), it is possible to generate maps showing the potential (future) vegetation distribution according to the considered environmental factors.

5. Using quantitative methods for processing the collected field data, it is possible to experiment with different floristic and environmental parameters in combinations and adjust and adapt them for cartography.

ACKNOWLEDGMENTS.

Thanks to Philippe Cour (UNISFERE Company, Besançon) for the geometrical correction of the IR-image, Gerard Desservy (BRETON-DESSERVY Company, Besançon) for his technical cooperation on the GPS, LEPONT EQUIPEMENT Company, Lyon, for the loan of a supplementary GPS set. Thanks also to Arve Elvebakk, University of Tromsø, Norway, who has been most helpful analysing plant species data and contributing with comments on the manuscript.

The Norwegian Polar Institute, the University of Tromsø, and the French-Norwegian Foundation kindly gave financially support which made it possible to perform our study on Svalbard.

REFERENCES.

Bezdek, J.C. 1981. *Pattern recognition with fuzzy objective function algorithms*. Plenum Press, New York.

Brattbakk, I. 1981. Vegetasjonskart Brøggerhalvøya, Svalbard. Trondheim. *K. Norske Vidensk. Selsk. Mus., Bot. Avd. Trondheim.* 1:10 Norsk Polarinstitutt.

Brossard, T., Deruelle, S. & Nimis, P.L. 1984. An interdisciplinary approach to vegetation mapping in high arctic environment, Ny-Aalesund, Svalbard. *Phytocoenol.* 12; 433-453.

Brossard, T., Elvebakk, A. & Joly, D. 1993. Bioclimatology at Kongsfjorden (Svalbard) studied by a phytogeography based method and by G.I.S. applied to the indicator species *Cassiope tetragona*. Fondation Franco-Norvégienne (Fransk-Norsk Stiftelse) *Proceedings of the Arctic Research Seminar, Paris, Oct. 15.-16.* 1992, 1-14.

Brossard, T. & Joly, D. 1994. Probability models, remote sensing and field observations: test for mapping some plant distributions in the Kongsfjord area (Svalbard). *Polar Res.* 13; 153-161.

Brown, D.G. 1994. Predicting vegetation types at treeline using topography and biophysical disturbance variables. In: Walsh SJ, Davis FW, Peet RK. (eds.). Special feature in vegetation science 6. *J. Veg. Sci.* 5; 641-656.

Craighead, J.J. et al. 1988. Mapping arctic vegetation in northwest Alaska using LANDSAT MSS imagery. *Nat. Geogr. Res.* 4; 496-527.

Crépeau, C. & Pierre, G. 1996. Télédétection satellitale : état de l'art. *S.I.G. et Télédétec.* 16; 7-12.

Elvebakk, A. 1994. A survey of plant associations and alliances from Svalbard. *J. Veg. Sci.* 5; 791-801.

Elven, R. et al. 1990. Gipsdalen, central Svalbard; flora, vegetation, and botanical values. In: Brekke, B. & Hansson, R. (eds.): Envirnonmental atlas Gipsdalen, Svalbard. II. *Norsk Polarinst. Rapp.* 61; 27-66.

Equihua, M. 1990. Fuzzy clustering of ecological data. *J. Ecol.* 78, 519-534.

Evans, B.M., Walker,D.A., Benson, C.S., Nordstrand, E.A. & Peterson, G.W. 1989. Spatial interrelationship between terrain, snow distribution and vegetation patterns at an arctic foothills site in Alaska. *Holarc. Ecol.*. 12: 270-278.

Frank, T.D. and Thorn, C.E. 1985. Stratifying alpine tundra for geomorphic studies using digitized aerial imagery. *Arc. Alp. Res.*. 17; 179-88.

Goodchild, M.F. 1994. Integrating GIS and remote sensing for vegetation analysis and modeling: methodological issues. In: Walsh SJ, Davis FW, Peet RK. (eds.). Special feature in vegetation science 6. *J. Veg. Sci.* 5; 615-626.

Joly, D. & Fury, R. 1995. Interpolation spatiale à maille fine des températures journaliéres. *La Météorol.* 8; 36-43.

Mosbech, A. & Hansen, B.U. 1994. Comparison of satellite imagery and infrared aerial photography as vegetation mapping methods in an arctic study area; Jameson Land, East Greenland. *Polar Res.* 13; 139-152.

Nilsen, L. 1992. *Phytososiological and remote sensing studies of changes in vegetation pattern on a glacier forefield at Uversøyra, north-west Spitsbergen.* Unpubl. cand. scient. thesis. Tromsø. University of Tromsø; pp 92.

Ostendorf, B. & Reynolds, J.F. 1993. Relationship between a terrain-based hydrologic model and patch-scale vegetation patterns in an arctic tundra landscape. *Landsc. Ecol.* 8; 229-237.

Podani, J. 1994. Multivariate data analysis in ecology and systematics -a methodological guide to the SYN-TAX 5.0 package. *Ecol. Comp. Ser.* 6; 1-316 SPB Academic Publishing.

Spiegle, M.R. 1982. *Theory and problems of statistics.* Mc Graw Hill, New-York.

Spjelkavik, S. 1995. A satellite based map compared to a traditional vegetation map of arctic vegetation in the Ny-Ålesund area, Svalbard. *Polar Record.* 31; 257-269.

Tom, C.H. & Miller, L.E. 1984. An automated land-use mapping comparison of the Bayesian maximum likelihood and linear discriminant analysis algorithms. *Photogram. Eng. Remote Sens.* 50; 193-207.

Øritsland, N. & Ødegaard, H.1980. Mapping polar vegetation at Spitsbergen by use of Landsat. Final Report.:*Report MAB/IBM* Oslo. pp 69.

SUMMER ENVIRONMENTAL MAPPING APPLICATIONS OF A LARGE-SCALE MOSAIC OF THE STATE OF ALASKA GENERATED FROM ERS-1 SAR IMAGES

Shusun Li, Rick Guritz, Tom Logan, Michael Shindle, Joanne Groves,
Frank Carsey, John MacMahon, and Coert Olmsted

Alaska SAR Facility, University of Alaska Fairbanks
Fairbanks, AK 99775, USA
phone: +1 907 474 7676, fax: +1 907 474 7290

Abstract

A large-scale mosaic of the state of Alaska has been created from more than 800 ERS-1 SAR images generated at the Alaska SAR Facility (ASF). We used SAR images acquired during the summer of 1992 and 1993 for mosaicking. The reason that the summer season SAR images were selected is that the microwave wavelength used by the ERS-1 SAR, i.e., C band at 5.65 centimeter, is sensitive to centimeter and larger scale surface roughness, surface moisture status, and foliage abundance. Thus, summer season SAR is ideal for investigation of variations of rock outcrop types, vegetation cover, surface and near surface moisture content, etc. Because of rain events, significant temporal changes of soil moisture during the summer season caused substantial changes in the signature of the adjacent SAR images acquired on different dates. This complicates the efforts in making a seamless mosaic of the huge area of the state of Alaska. An extensive search of suitable images from an extremely large database of the available 1992 and 1993 summer images leads to final successful generation of a nearly seamless large scale digital mosaic of Alaska at a pixel resolution of 100 meters. During the process of selection, images considerably darker or brighter than their surrounding images were discarded and replaced by middle signature images of the same areas. Consequently, the images included represent the average conditions of their areas. Therefore, the mosaic created is an ideal information source for statewide and regional mapping. The potential applications of this mosaic include statewide or regional soil moisture mapping, classification of forest and other vegetation types, classification and zoning of arctic and subarctic glaciers, geological mapping, and volcanic investigations. This mosaic can also assist topographic mapping by identifying areas with poor DEM quality.

1. Introduction

Spaceborne SAR systems are providing scientists with a great deal of information on the phenomena associated with surface processes. SAR data have proven useful in studies of sea ice, volcanology, geology, glaciology, vegetation cover, soil moisture, surface hydrology, and oceanography. The utility of SAR derives from its all-weather and day-night capability, its fine spatial resolution, and its sensitivities to changes in the Earth's surface characteristics. It is especially useful in remote regions of Alaska where darkness and cloud cover limit the application of optical sensors.

2. Background

While the spaceborne SAR instruments have unique capabilities, there are certain technical issues which have to be addressed. It is well known that SAR images have severe geometric and brightness distortions over rugged terrain due to the nature of their peculiar slant range mapping. According to SAR principles [Curlander and McDonough, 1991], when both the satellite orbit position and slant range act as functions of time, and the mathematical reference model for the earth surface (e.g., sea level surface) is known, SAR can depict a very accurate picture of features on the reference plane. In fact, as a routine product, a standard Alaska SAR Facility (ASF) SAR image maps the ground to a reference surface with a constant elevation. However, most land features, e.g., rivers, hills, and mountains, run through varying terrain, introducing some geometric distortion. The distortion is a function of both terrain elevation and the incidence angle of the radar beam to the geoid surface (global incidence angle). The larger the relative elevation, the larger the geometric distortion. Also, the smaller the incidence angle, the larger the distortion. The result is foreshortening and layover for rugged terrain. For the European satellite ERS-1, the global incidence angle ranges from 19.5 to 26.5 degrees, inducing a position offset about 2.0-2.8 times as large as the relative elevation. This magnitude of position error is critical to most land applications.

Once this problem is overcome, the all-weather capability and fine-ground resolution available from the satellite SAR instruments will provide scientists in land applications with a unique tool for accurate surface mapping and change detection.

Geometric correction of SAR image is a necessary yet computationally intensive task. A correction of a 64MB full-resolution SAR image (with ground resolution 12.5 meters) to a 30-meter resolution image will take more than 6 hours using a SPARC2 workstation at the ASF Interactive Image Analysis System (IIAS) Laboratory. Due to our effort in the previous two years, this technical problem has been solved well by porting the original code to the Massive Parallel Processor Cray T-3D at the Arctic Region Supercomputing Center (ARSC) [Logan, 1994, 1995]. During 1994, code porting, conversion and significant improvement were completed. A 90 meter resolution image can be terrain corrected in just under 7 minutes. A single SAR image of the Bering Glacier and a 24 scene Mosaic of the Arctic National Wildlife Refuge (ANWR) were generated

Proceedings of the Fourth Symposium on Remote Sensing of the Polar Environments, Lyngby, Denmark, 29 April – 1 May 1996
(ESA SP-391, July 1996)

to demonstrate scientific applications of terrain corrected SAR imagery. This work continued through 1995, fully automating all aspects of the process and minimizing the need for operator involvement. These efforts make possible terrain correcting over 800 SAR images at 100 meters resolution and constructing a nearly seamless mosaic of Alaska within 6 months.

3. Processing Methods and Implementation Procedures

The SAR image processing methods used to produce the State of Alaska mosaic include: tape ingest, radiometric calibration, low-pass filtering, creation of simulated SAR image based on digital elevation model (DEM), image to image correlation, terrain correction, and large scale mosaicking. These procedures have been streamlined and are used in generation of the mosaic. They have also been documented to comply with the ASF software development standards and made available to interested users through Internet.

The actual implementation involves: collecting 90-m DEM data for Alaska, ordering ASF ERS-1 lo-res (low resolution) SAR images for Alaska, checking qualities of DEM data and SAR images prior to terrain correction, searching through ASF SAR image database and reordering SAR data wherever the boundary between image swaths is too noticeable to create a seamless mosaic, terrain correcting individual SAR images, and mosaicking the terrain corrected SAR images.

All the available 90-m DEM data for Alaska have been obtained from the US Geological Survey. There still exist a few gaps in the DEM with each being about 100 km by 100 km in size. For these areas, no terrain correction of the SAR can be performed. However, the non-corrected SAR images of these areas are still included in the mosaic to avoid a distracting appearance of black windows. These areas are enclosed in white boxes to separate terrain corrected data from non-corrected data.

The ASF ERS-1 SAR images were collected during two stages. During the initial effort, selection criteria of SAR images included reasonable lateral overlapping, continuity along image swath, and summer season coverage. These criteria lead to our choice of the summer images acquired in 1992 and 1993 when the 35-day repeat cycles of the ERS-1 SAR provide complete coverage of Alaska. Since the amount of lateral overlapping during a single 35 day repeat cycle offers 60-75% redundancy, we only selected every other swath for our mosaic. During this initial stage, 800 images were ordered. The second stage of image collection was during and after the quality control step. More than 500 additional images were collected.

The reason that the summer season SAR images were selected is due to the fact that the microwave wavelength used by the ERS-1 SAR, i.e., C band at 5.65 cm, is sensitive to centimeter and larger scale surface roughness, surface moisture status, and foliage abundance [Ulaby, 1986], and thus is ideal for investigation of variations of rock outcrop types, vegetation cover, surface and near surface moisture content, etc.

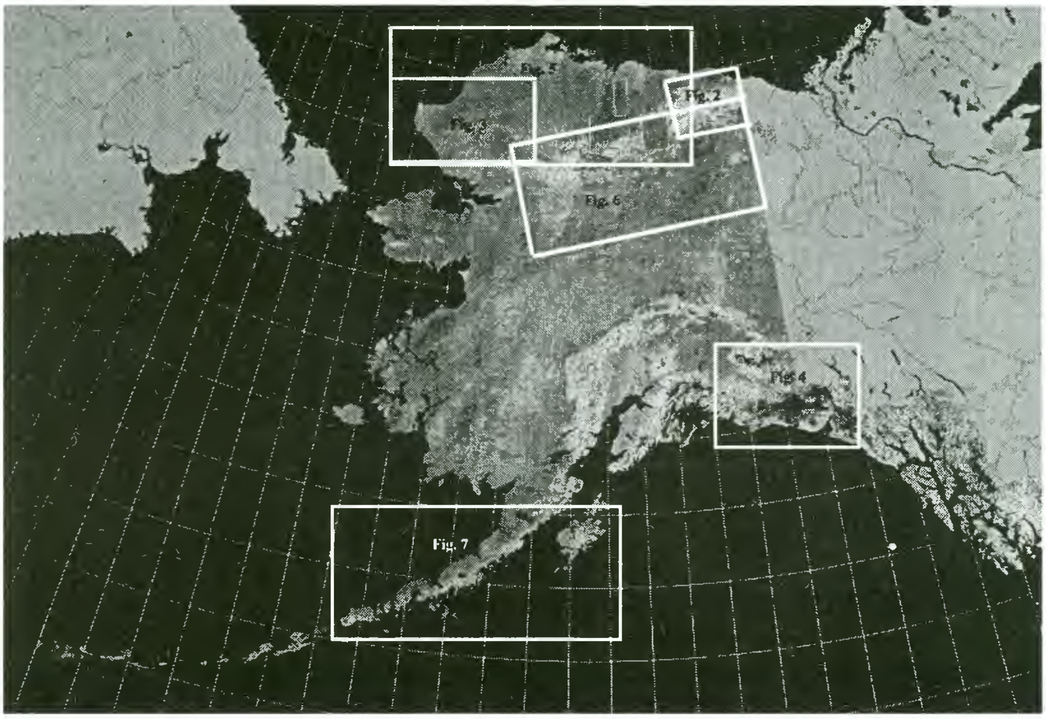

Fig. 1. Mosaic of the State of Alaska generated from ERS-1 SAR images acquired in 1992 and 1993 summer. The locations of the subimages discussed in the other sections are shown on this mosaic.

Quality controls of the DEM data and SAR images were performed by mosaicking. Mosaicking of DEM data met no evident problems. However, mosaicking SAR images, which were radiometrically calibrated but not terrain corrected, revealed that a few noticeable and sometimes even distinct seams existed between swaths. The seams were caused by rain events because adjacent swaths were acquired on different dates, depicting significant temporal changes of soil moisture due to rain. This fact complicated the efforts in making a seamless mosaic of the huge area encompassed by the State of Alaska. An extensive search of the suitable images from an extremely large database of the available 1992 and 1993 summer images leads to final success in generation of a nearly seamless large scale digital mosaic of Alaska at a pixel resolution of 100 meters without terrain correction. During the process of selection, images considerably darker or brighter than their surrounding images were discarded and replaced by middle signature images of the same areas. Consequently, the images included represent the average conditions of their areas.

Terrain correction of individual SAR images were implemented on a Cray T-3D processor at ARSC. Then, the terrain-corrected SAR images were mosaicked together. During these processes we had some difficulties with flat areas where correlation failed. With certain effort, this problem has been solved. During terrain correction and mosaicking, a modified Universal Transverse map projection was used, with the 150° W meridian as the central meridian, which is typical for mapping Alaska. This procedure yielded an image (Fig. 1) which was geocoded to this particular map projection with terrain effect minimized.

4. Application Examples

In the following sections, examples of sub-images extracted from the mosaic will be used to demonstrate applications of the mosaic in different fields.

4.1 Geology

The SAR mosaic has the unique ability to show large, sweeping patterns and at the same time provides details to those who need it. In the study of geology, two examples are provided to illustrate the usage of the SAR mosaic in identifying rock types and delineating geological structures, respectively.

The northern Brooks Range of northeastern Alaska is a Cenozoic-age Fold and Thrust belt primarily involving Proterozoic to Mesozoic carbonate and clastic rocks [Hanks, and Guritz, 1994]. On the Mosaic, carbonate rocks give a bright radar response due to its rough angular surface, while fine-grain clastic rocks give a dark signature because of their rounded and smooth surface. Coarse-grained clastic rocks have an intermediate radar backscatter because their surface roughness is intermediate. The variation of SAR signatures with different rock types emphasizes the expression of the convoluted geological structures of the area [Fig. 2].

Fig. 2. SAR Mosaic of the Northeastern Brooks Range

The northern foothills of the western Brooks Range is characterized by folding and faulting along eastward-trending axes generally parallel to the northern front of the Brooks Range [Fig. 3]. The intensity of the deformation decreases northward, from tight folds with many faults in the southern part of the foothills to broad open folds with few faults under the coastal plain. Between them, in the area between the Cape Lisburne and the Colville River, the folds are moderately open with their shapes well defined via the revelation of layers of bedrock on their limbs. Especially, dozens of elongated folds with rounded ends form the most noticeable concentric elliptic features in the area. A comparison with geological maps reveals that these elongated folds are coal basins, i.e., synclines formed by coal-bearing Cretaceous rocks. The sizes of these coal basins range from tens to hundreds of square kilometers. The mosaic will definitely be very useful in investigation of the coal resources in the region. This application can become economically important in future because it is estimated that Northwestern Alaska may contain the largest bituminous and subbituminous coal deposits in the U.S.A. [Barnes, 1967].

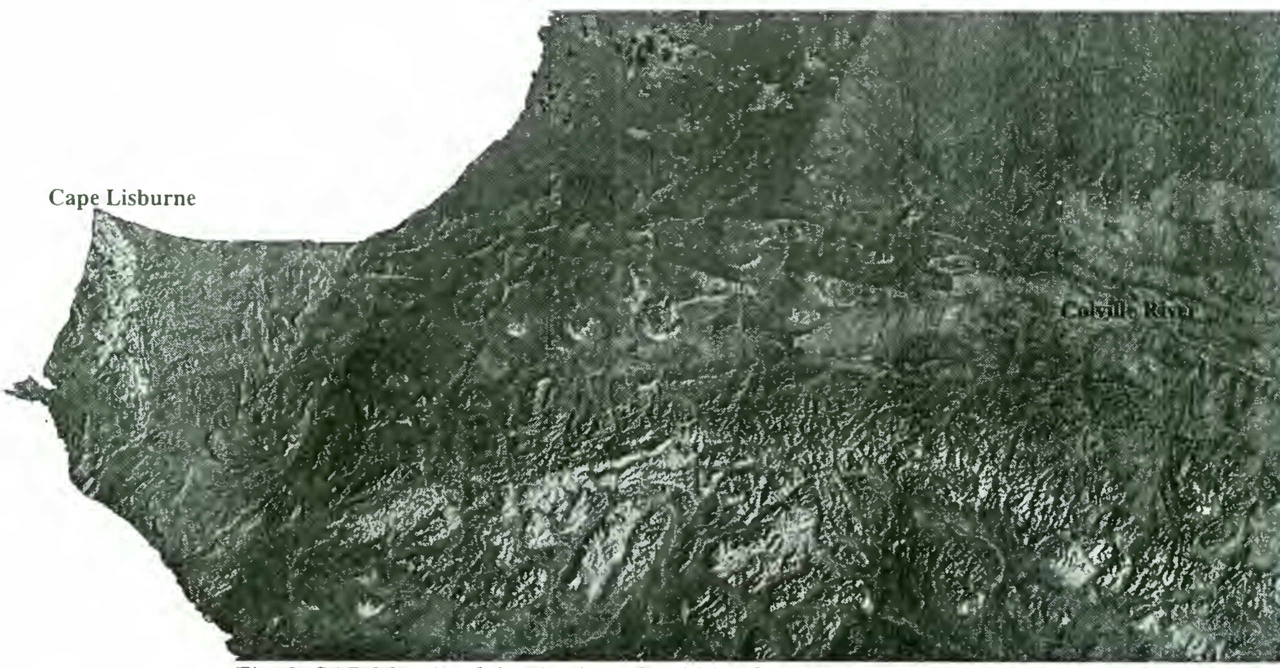

Fig. 3. SAR Mosaic of the Northern Foothills of the Western Brooks Range

4.2 Glaciology

The summer mosaic reveals very dark bands in the southeastern Alaska glaciers [Fig. 4]. Those bands are located above relatively brighter bands in lower portions of glaciers. The interpretation of the difference in radar backscatter in different portions of glaciers is that the upper part with dark appearance is in the zone with snow cover, while the lower part is bare ice [Lingle, et al., 1993]. The summer snowmelt moistens the snow cover, and consequently, the moisture-rich snow pack becomes a strong microwave absorber, hence the dark signature. For example, the Bering Glacier near the coast of the Gulf of Alaska, centered at 60°15' N and 143°30' W, has a moderate signature in its lower portion below 1500 feet elevation.

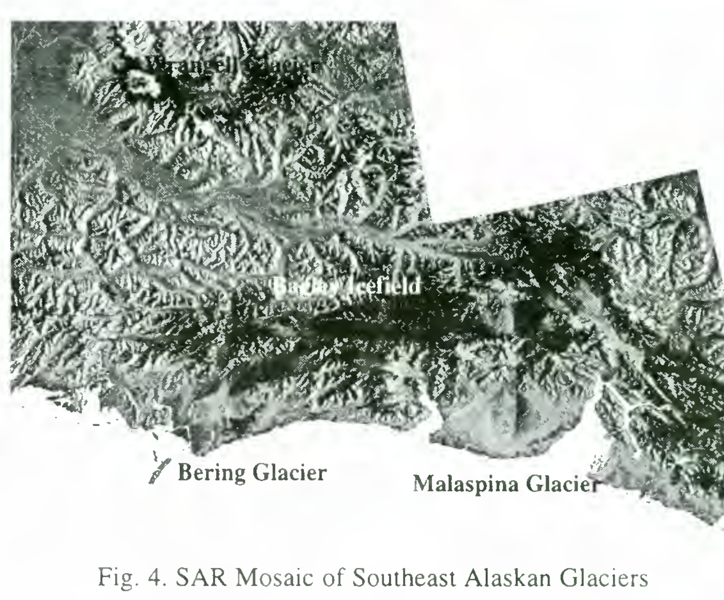

Fig. 4. SAR Mosaic of Southeast Alaskan Glaciers

Upper-valley portions to the east show a very dark response. This dark belt merges into an even larger east-west dark belt – Bagley Ice Field, located above 3600 feet. These areas are glaciers covered by wet snow packs. Similar patterns of dark bands located in upper-valleys of relatively moderate signature bare glaciers can be seen in most of the nearby glaciers. Such information can be used for glacial zoning and classification.

4.3 Soil Moisture

Because the radar return is strongly related to soil moisture content [Dobson and Ulaby, 1986; Beaudoin et al., 1990; Yisok et al., 1992], ERS-1 SAR can be used to map soil moisture conditions. The mosaic is particularly useful for this application. On the mosaic, three gigantic bands with each having backscatter values distinctively different from those in the other bands are seen between the Brooks Range and the arctic coast [Fig. 5].

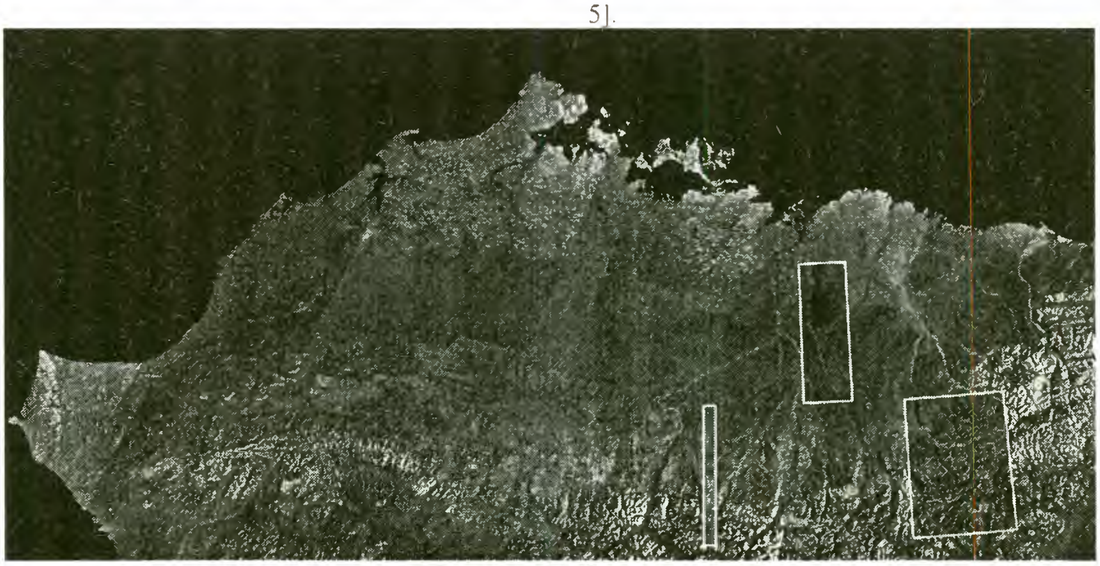

Fig. 5. SAR Mosaic of the North Slope of Alaska

The first band of high backscatter values along the arctic coast stretches about 500 km between the delta of the Cannining River in the east and the Ice Cape in the west. This band has a width ranging from 50 to more than 100 km and is characterized by numerous arctic lakes and flat terrain. Geographically, the band coincides with the Arctic coastal plain. The existence of numerous lakes exerts a strong influence on the high backscatter level of the band. On the mosaic, most lakes look very bright. This fact agrees with other investigators' observations [Morris et al., 1995] that arctic lakes usually have high backscatter during short summer. The high radar backscatter from lakes in summer is caused by roughening of lake surface due to strong winds. In fact, weather records have documented that surface wind speeds along the Arctic coast are persistent and strong compared to those in more interior regions. It is of particular interest to note that the areas between the lakes also significantly contribute to the high backscatter values of this band. For example, near the Oliktok Point, to the west of the Sagavanirktok River, the coastal plain appear quite bright in the mosaic. A close examination indicates that land between lakes has higher backscatter value than lakes in the area and the overall high backscatter level in the vicinity is mainly caused by backscatter from land. A previous geological survey of the area [Brown and Kreig, 1983] reports that the ground cover of this area is wet tundra where the peaty soil has a shallow, active layer and is saturated throughout the summer.

To the south of the first band lies the second band of distinct radar backscatter values. This band of relatively low backscatter values is about 50 km wide on average. This band is the Arctic foothills characterized by rolling uplands of moist tundra.

Further south is the third band of the Brooks Range with distinct mountainous radar backscatter characteristics, i.e., very bright foreslopes and dark backslopes.

The bright appearance of wet tundra and dark signature of moist tundra agree with the model and laboratory experimental results regarding the proportional relation between soil moisture and radar backscatter values for bare soils [Dobson and Ulaby, 1986]. The low biomass in tundra makes application of the bare soil moisture model relatively straightforward.

4.4 Forest Fire Scars

It is well known that the boreal forest in the Upper Yukon and Koyukuk regions is especially prone to destruction by fire. Many trees have branches to the ground and commonly are covered with lichens and mosses. Shrub undergrowth abounds. Relatively low precipitation, long hours of sunshine, and very high air temperatures accompanied by low relative humidity in summer, greatly increase the fire hazard in an already flammable community where mosses and lichens are

Fig. 6. SAR Mosaic of the Upper Yukon Region of Alaska

extremely dry. Once caused by either lightning or human accident, fire spreads readily in such an environment [Lutz, 1960]. Because the forest fires in the region are widespread over large inaccessible areas, it is essential to map the extent of forest fires, especially the extent of the most recent ones, using satellite imagery. The Alaska SAR mosaic fits in this application extremely well. On the mosaic, several conspicuous bright patches have been found in the Upper Yukon and Koyukuk regions [Fig. 6]. Those patches range from 10,000 to 500,000 acres in size. A comparison of the mosaic with the forest fire records collected at the U.S. Bureau of Land Management shows that all those bright patches are recent forest fire scars. Table 1 lists the five largest bright patches in the region. Of those five patches, four are scars of 1991 forest fires and the remaining one is a 1990 fire scar. Also, the sizes of the fire scars estimated from the SAR mosaic compare with the fire records quite well. Considering that the component SAR images were acquired in 1992, the ability of the mosaic for mapping the recent boreal forest fire scars is very encouraging.

According to Kasischke et al. [1994], recent boreal forest fire scars can be identified on ERS-1 SAR images based on the difference of their radar backscatter from the surrounding areas. The difference of image intensities between burned and unburned areas is mainly caused by exposure of soil in the burned areas. Many boreal forest scars have brighter SAR signature because severe forest fires burn the forest canopy completely and expose bare soil to radar illumination. Furthermore, severe fires consume the surface peat layer which insulates the ground and helps lower the average ground temperature. Elimination of this insulating layer causes a 5-7°C increase in average ground temperature for at least several years after the fire [Dyrness and Norum, 1983],

Table 1 Comparison of Forest Fire Scars Identified in Alaska SAR Mosaic and Recorded in Forest Fire Files.

Site Name	Coleen_1	Coleen_2	Black River	Hughes	Bettle
Location	Rabbit Mtn - Lake Creek - Spike Mtn	Graphite Lake - Coleen Mtn	NE of Little Black R., W of Black R.	Zane Hills - Koyukuk R.	Koyukuk R. - Alatna Hills
Center Lat/Lon	67°30'N / 142°W	67°08'N / 143°15' W	66°25'N / 143° W	66°15'N / 154°50' W	66°40'N / 152°15' W
SAR Signature	Bright	assorted dark and bright	Bright	assorted dark and bright	Bright
Fire Record No.	A143 (1990)	A144 (1988) B562 (1991)	B460 (1991)	B541 (1991)	B569 (1991)
Fire Duration	6/29-9/14	6/28-10/1 6/30-9/27	6/26-9/16	6/29-9/30	6/30-9/30
Estimated Size (km^2)	1,190	720	300	870	1,240
Fire Size in record (km^2)	1,880	580 500	330	750	1,010

which in turn causes a melting of the underlying permafrost and an increase in soil moisture. As mentioned in the previous soil moisture section, higher moisture content in bare soil leads to stronger radar backscatter in general. This explains why many recent forest scars appear brighter on SAR images. On the other hand, the burned areas may have low soil moisture due to better drainage, resulting in lower SAR backscatter values. Also, regrowth of vegetation on fire-disturbed areas can either increase or decrease the image intensities by masking the effect of soil moisture on radar backscatter.

It is interesting to note that variation of SAR backscatter within individual patches may even give a clue to local forest fire history or the variation in damage caused by the fire. For example, the patch Coleen_2 between Graphite Lake and the Coleen Mountain, centered at 67°08'N and 143°15'W, has an assorted dark and bright appearance in image intensities. Further examination of the fire records shows that the dark middle part of the patch also experienced an earlier fire between June 28 and October 1, 1988. To the north and south this part, the areas with only the damage of recent fire (1991) show a much brighter radar signature. Another example is the patch Coleen_1 between Rabbit Mountain and Spike Mountain, with its central location at 67°30'N and 142°W. This patch experienced fire between June 24 and September 14, 1990. Detailed fire records show that this fire scar is actually related to five smaller fires in the vicinity. In other words, this area was not uniformly burned. This explains the variation of SAR signatures within this large patch.

4.5 Volcanology

The distribution of Alaska volcanoes is very well presented on the mosaic. Particularly, the morphological details of individual volcanoes are clearly demonstrated in the magnified sub-images on the mosaic [Fig. 7]. A series of secondary craters of the giant west crater of the Shishaldin Volcano, and the sharp summit of the central peak are just examples of the high level of detail which can been seen on the mosaic. Also, the dark appearance of the top of the Veniaminof Volcano indicates that wet snow pack covers the entire crater and a large portion of the cone.

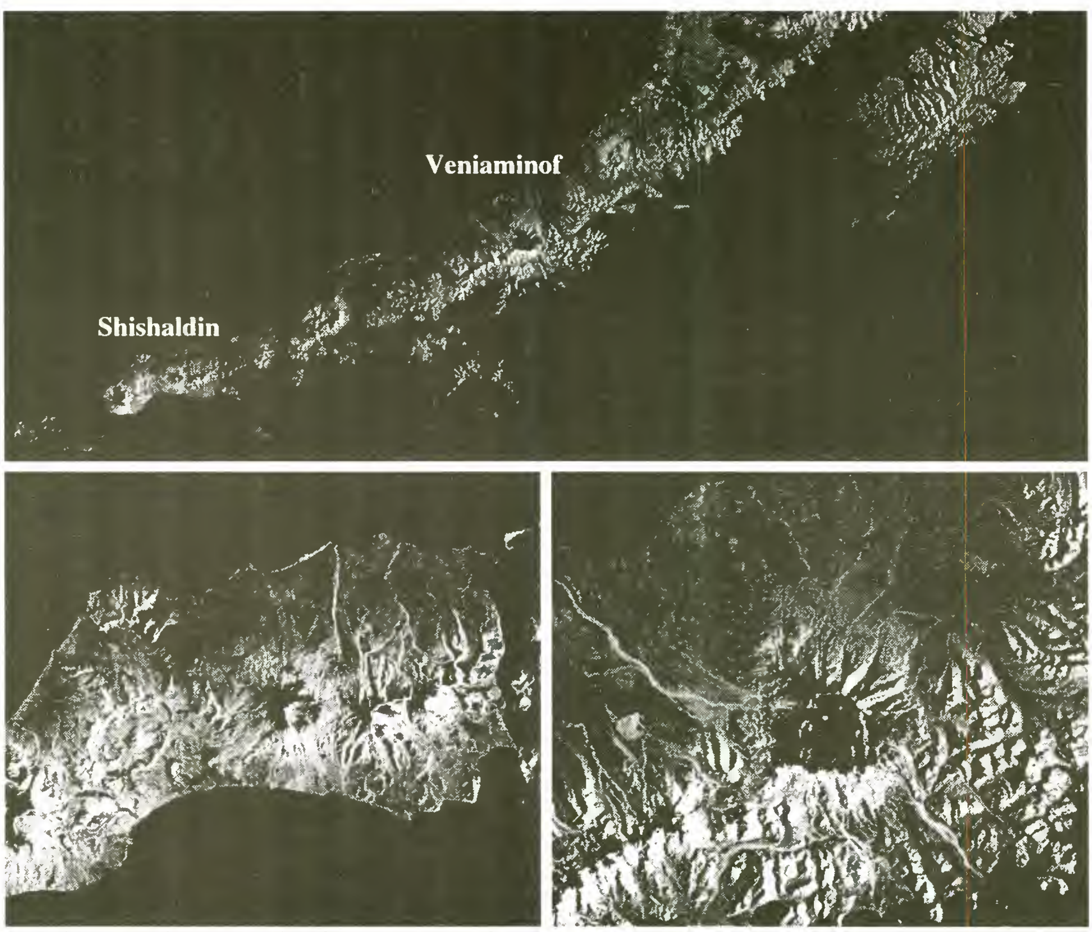

Fig. 7. (a) SAR Mosaic of the east part of the Aleutian Islands (b) Shishaldin (c) Veniaminof

4.6 Topographic Mapping

Although we did not find apparent quality problems except for some areas without DEM during the initial stage of DEM-only mosaicking, we did find, in the southern part of the Kuskokwim mountains, discrepancies between the features expressed on the final terrain corrected SAR mosaic and on the background DEM data. A simple way to identify the areas of discrepancies is to find remaining V-shape features on the terrain corrected SAR images. The reason for this simple diagnosis is based on the fact that the V-shape features, caused by foreshortening of the foreslope and elongating of the backslope on the non terrain corrected SAR images, should be removed during terrain correction. A close comparison of DEM data with 1:250,000 scale topographic maps confirms that the DEM data of the Goodnews Bay USGS quadrangle are actually inaccurate. Therefore, the mosaic can also be used to check the quality of the available DEM.

5. Remarks and Future Plan

The mosaic created is an ideal information source for regional mapping. The potential applications of this mosaic include statewide or regional soil moisture mapping, classification of forest and other vegetation types, classification and zoning of arctic glaciers, geological mapping, and volcanic investigations. The mosaic can also be used to check the quality of DEM data.

Further effort will be made to create an incidence angle normalized mosaic of the state of Alaska, which will further improve the mapping capabilities of the mosaic. Also, more graphical work will be done to upgrade the mosaic to publication standards.

6. Acknowledgments

This research was supported by the CRAY-Sponsored University Research & Development Grant Program and the National Aeronautics and Space Administration grant to the Alaska SAR Facility, Geophysical Institute, University of Alaska Fairbanks. The authors would like to thank Don Barry for making forest fire data available to this study.

7. References

Barnes, F.F., *Coal Resources of the Cape Lisburne-Colville River Region, Alaska*, Geological Survey Bulletin 1242-E, United States Government printing Office, Washington, 1967.

Beaudoin, A., T. L. Toan, and Q. H. J. Gwyn, SAR Observations and Modeling of the C-band Backscatter Variability due to Multiscale Geometry and Soil Moisture, *IEEE Trans. Geosci. Remote Sensing, Vol. 28*, pp. 886-894, 1990.

Brown, J. and R. A. Kreig, ed. *Guidebook to Permafrost and Related Features Along the Elliott and Dalton Highways, Fox to Prudhoe Bay, Alaska, Fourth International Conference on Permafrost, July 18-22, 1983, University of Alaska, Fairbanks, Alaska, U.S.A.*, Division of Geological & Geophysical Surveys, Department of Natural Resources, State of Alaska, Fairbanks, p.1-230, 1983.

Curlander, J.C., and R.N. McDonough, *Synthetic Aperture Radar, Systems and Signal Processing*, John Wiley & Sons, New York, 1991.

Dobson, M. C., and F. T. Ulaby, Active Microwave Soil Moisture Research, *IEEE Trans. Geosci. Remote Sensing, Vol. GE-24*, pp. 23-36, 1986.

Dyrness, C. T., and R. A. Norum, The Effects of Experimental Fires on Black Spruce Forest Floors in Interior Alaska, *Can. J. Forest Res., 13*, pp. 879-893, 1983.

Hanks C. L., and R. M. Guritz, Synthetic Aperture Radar (SAR) and Geologic Reconnaissance in Arctic Regions: A Pilot Study in the Northeastern Brooks Range of Alaska, *Geological Society of America, 1994 Annual Meeting, Seattle, Washington, Oct. 24-27, 1994,* Abstracts with Program, pp. A-266, 1994.

Kasischke, E. S., L. L. Bourgeau-Cahvez, and N. H. F. French, Observations of Variations in ERS-1 SAR image intensity associated with Forest Fires in Alaska, *IEEE Transactions of Geosciences and Remote Sensing, Vol. 32(1)*, pp. 206-210, 1994.

Lingle, C. S., A. Post, U. C. Herzfeld, B. F. Molnia, R. M. Krimmal, and J. J. Roush, Bering Glacier Surge and Ice-Berg-Calving Mechanism at Vitus Lake, Alaska, U.S.A., *Journal of Glaciology, Vol. 39(133),* pp. 722-727, 1993.

Logan, T., Terrain Correction of Synthetic Aperture Radar Imagery Using the Cray T3D Parallel Processor, M.S., Computer Sciences, University of Alaska Fairbanks, 1994.

Logan, T., Terrain Correction of Synthetic Aperture Radar Imagery Using the Cray T3D, *Proceedings of the Thirty-Fifth Semi-Annual Cray User Group Meeting, Denver, Colorado, March 13-17, 1995*, pp. 268-274, 1995.

Lutz, H. J., Fire as an Ecological Factor in the Boreal Forest of Alaska, *Journal of Forestry, 58,* pp. 454-460, 1960.

Morris, K., M. O. Jeffries, and W. F. Weeks, Ice Processes and Growth History on Arctic and Sub-Arctic Lakes Using ERS-1 SAR Data, *Polar Records, 31 (177),* pp. 115-128, 1995.

Ulaby, F. T., R. K., Moore, and A.K. Fung, *Microwave Remote Sensing: Active and Passive, Vol. 3*, Addison-Wesley, Reading, Mass, 1986.

Yisok, O., K. Sarabandi, and F. T. Ulaby, An Empirical Model and an Inversion Technique for Radar Scattering from Bare Soil Surfaces, *IEEE Trans. Geosci. Remote Sensing, Vol. 31*, pp. 370-381, 1992.

ERS-1 SAR MONITORING OF ICE GROWTH ON SHALLOW LAKES TO DETERMINE WATER DEPTH AND AVAILABILITY IN N.W. ALASKA

Martin Jeffries, Kim Morris

Geophysical Institute, University of Alaska,
903 Koyukuk Drive, P. O. Box 757320, AK 99775–7320, U.S.A.
phone: 1–907–474–5257, fax: 1–907–474–7290
martin.jeffries@gi.alaska.edu, kmorris@images.alaska.edu

Glen Liston

Department of Atmospheric Science, Colorado State University,
Fort Collins, CO 80523, U.S.A.
phone: 1–970–491–7473, fax:1–970–491–8449
liston@tachu.atmos.colostate.edu

ABSTRACT

ERS–1 SAR images are used to identify and differentiate between lakes that freeze completely to the bottom and those that do not on the North Slope in N.W. Alaska. At Barrow, on the coast of the Arctic Ocean, 60% of the lakes freeze completely to the bottom in mid–January alone and by the end of winter 77% of the lakes are completely frozen to the bottom. In contrast, 100km to the south in the 'B' Lakes region, only 23% of the lakes freeze completely to the bottom by the end of winter. The ice thickness at the time each lake froze completely to the bottom, and thus maximum water depth, is determined with a physically based, numerical ice growth model that gives a simulated maximum ice thickness of 2.2m. At Barrow, 60% of the lakes are up to 1.4m/1.5m deep and 25% are >2.2m deep. At the 'B' Lakes, 75% of the lakes are >2.2m deep. This method is simple to implement, and the SAR data are relatively inexpensive and have good spatial and temporal coverage. Thus, the method could be used to determine lake depth and water availability on the entire North Slope and in other polar and sub–polar areas where shallow lakes are common.

1. INTRODUCTION

Shallow thaw lakes are a major component of the tundra landscape of the Alaskan North Slope, where they comprise as much as 40% of the area of the Coastal Plain (Sellmann et al., 1975a). All or part of most lakes are <2m deep; consequently, a significant area of water freezes completely to the bottom each winter (Sellmann et al., 1975a; Mellor, 1982). There are only a few weeks each year when the lakes are ice–free. The lake depth and ice growth and decay determine the value of the lakes as habitats for wildlife and acquatic fauna, and their usefulness as sources of fresh water for settlements and industrial development (Sellmann et al., 1975a; Mellor, 1982; 1994). While it is known that few lakes exceed 2m depth, the bathymetry of most lakes is unknown and the geographic variability of lake depth in different watersheds is poorly mapped. More precise information of this kind would help to define natural resource values, assist in the development, management and enhancement of the water resources, and mitigate the impacts of potentially conflicting uses (Mellor, 1994).

This paper describes a method that combines the use of ERS–1 SAR images and numerical ice growth modelling to determine lake depth and water availability in two regions of the North Slope in N.W. Alaska. The first study area is located in the vicinity of Barrow on the Arctic Ocean coast. The second study area, the 'B' Lakes, is located 100km south of Barrow. In general, the 'B' Lakes are greater in number and smaller in size, and have a more dense areal coverage than those at Barrow (Fig. 1). The SAR images used in this study were Alaska SAR Facility Standard Low Resolution products comprising 1024 lines each containing 1024 pixels, with 100m pixel size and 240m resolution. A full SAR image has ground dimensions of 100km by 100km.

2. SAR REMOTE SENSING OF LAKE ICE GROWTH AND BOTTOM FREEZING

2.1 Background

In the SAR image (Fig. 1), the lakes are characterized by a variety of dark and light tones; some lakes are completely dark, while others have a combination of dark tones around the margin and light tones in the centre. The proportion of light and dark tones in individual lakes changes during the course of the winter (Fig. 2). The area of dark tone increases from the margins towards the centres of lakes, and while an area of bright tone might remain in the centre of some lakes all winter (Lakes I and II, Fig. 2), other lakes become completely dark (Lakes III and IV, Fig. 2).

The grey tones in the SAR images are a visual measure the strength of the radar backscatter from the ice, which is determined by the presence of tubular air inclusions in the ice and whether the ice has water at the base or it is frozen to the bottom of the lake (Sellmann et al., 1975b; ; Weeks et al., 1977, 1978, 1981; Jeffries et al., 1994; Wakabayashi et al., 1994). The light tones denote strong backscatter from ice that has water beneath it. The dark tones denote low backscatter from ice that is frozen to the bottom of the lake.

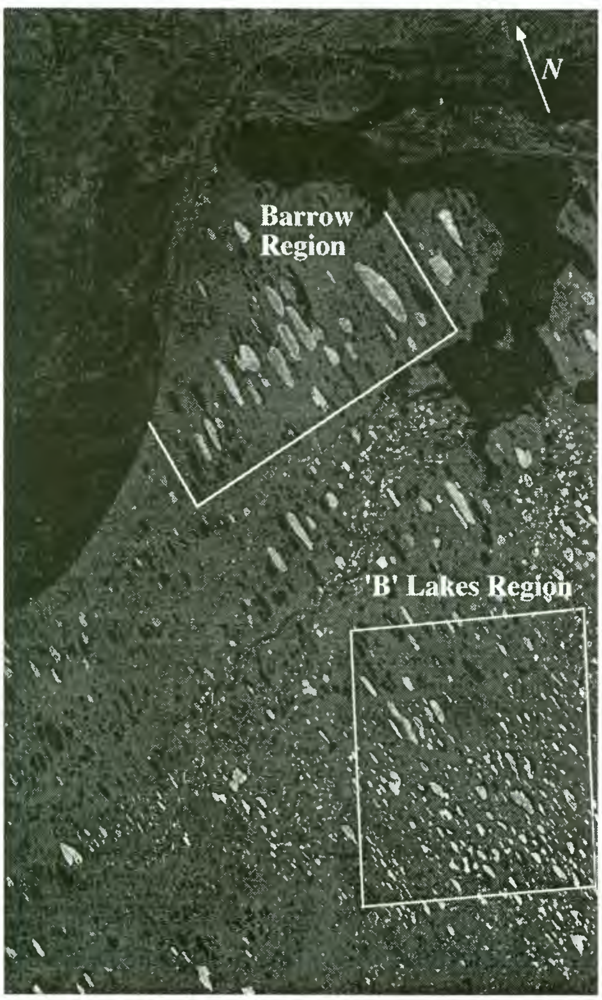

Figure 1. Mosaic of two SAR images showing the location of the Barrow (71°N, 157°W) and 'B' Lakes study areas. Note the spatial variation in the density of lakes and the variability of the grey tones of the lake ice. SAR images are © ESA.

In Figure 1, then, it is apparent that the entire lake ice cover on many lakes had frozen completely to the bottom by early March. At other lakes at that time, there remained a significant area of ice with water at the base. The gradual increase in area of dark tones from the margins of lakes towards their centres (Fig. 2) reflects their bathymetry; the margins are shallower than the centres and as the winter progresses and the ice thickens, it first freezes to the bottom around the perimeter and then progressively inwards towards the centre. If some part of a lake is deep enough, i.e., the water depth exceeds the maximum possible annual ice thickness, water will remain below the ice at the end of winter (Lakes I and II, Fig. 2), but if the deepest water is shallower than the maximum ice thickness, then the entire area of lake ice will freeze completely to the bottom (Lakes III and IV, Fig. 2). The timing of complete freezing will depend on the maximum water depth.

2.2 Timing and Number of Lakes Freezing to the Bottom

For this study, a time series of SAR images from the onset of ice growth in early September 1991 until the onset of melt in May 1992 was assembled for each region. A total of 32 and 18 images were used for the Barrow and 'B' Lakes regions respectively. The backscatter or tonal changes of the ice on 180 lakes in the Barrow and on 293 lakes in the 'B' region were monitored during the course of the winter. The difference in lake numbers reflects the greater number of lakes in the 'B' Lakes region (Fig. 1). With the aid of the time series of SAR images, the date when the tone of a lake went completely dark, i.e., the entire area of lake ice became frozen to the bottom, was noted. In this way, a record was compiled of the dates on which individual lakes froze completely and of the number of lakes that did and did not freeze completely to the bottom. Since SAR images are not available every day, the date on which a lake was observed to have frozen completely to the bottom represents the latest time that complete freezing occurred.

The results of the SAR image analysis are summarized in Figure 3. In both regions, lakes first freeze completely to the bottom in mid– to late November. By the end of winter in the 'B' Lakes and Barrow regions respectively, 68 lakes (23% of the total) and 139 lakes (77% of the total) had frozen completely to the bottom. Not only does the number of lakes that freeze completely differ in each region, but the pattern of timing of freezing is different. The freezing curve for the 'B' Lakes shows a steady increase in the number of completely frozen lakes, while at Barrow the number of completely frozen lakes remains constant until mid–January when 108 lakes (60% of the total) froze completely to the bottom.

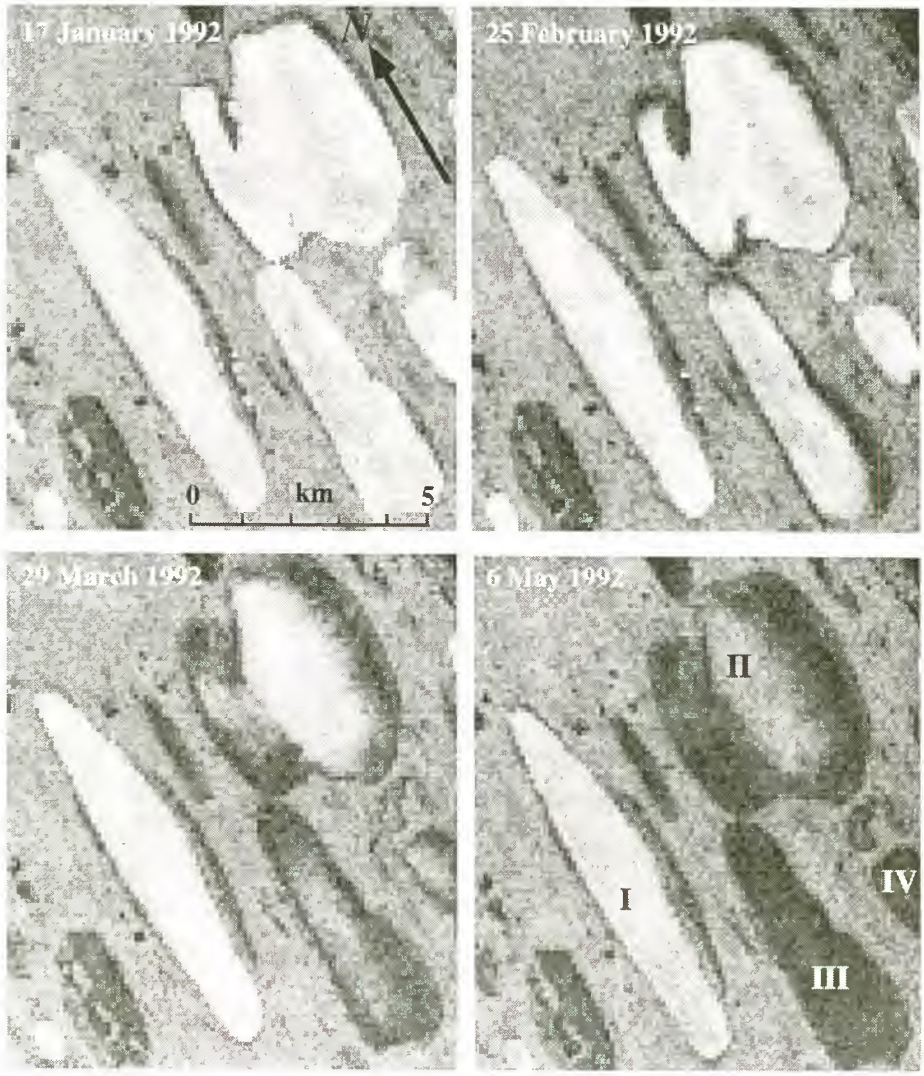

Figure 2. SAR sub–scenes of lakes from January to May 1992 in the Barrow region illustrate spatial changes in tone, i.e., backscatter intensity, due to the progressive freezing of ice to all or part of the bottom of the lakes. Bright tones are areas of ice where there is water between the ice and the lake bottom. Dark tones are areas of ice that are frozen to the lake bottom. Lakes I, II, II and IV are referred to in the text. SAR images are © ESA.

3. NUMERICAL ICE GROWTH MODELLING AND WATER DEPTH VARIATIONS

3.1 Model Description

When and how many lakes had frozen completely to the bottom has been determined from SAR images. The time scale in Figure 3 is converted into ice thickness using a physically-based, one-dimensional, non-steady, numerical model to simulate lake ice growth and thickness. For the lakes that froze completely to the bottom, the ice thickness represents the maximum water depth. Lakes that do not freeze completely to the bottom have some water deeper than the maximum possible ice thickness for winter 1991-92.

The equations governing the model are presented in Liston and Hall (1995a, 1995b). The model is composed of four coupled sub–models. First, a *lake–mixing, energy transport sub-model* describes the evolution of lake water temperature and stratification; ice growth is initiated when the upper lake water temperature falls below freezing.

Second, a *snow sub-model* describes snow depth and density as it accumulates, metamorphoses and melts on top of the lake ice. Third, a *lake ice growth sub-model* produces ice by two mechanisms: (1) congelation ice grows at the ice-water interface due to the transfer of energy from the base to the surface of the ice; and (2)

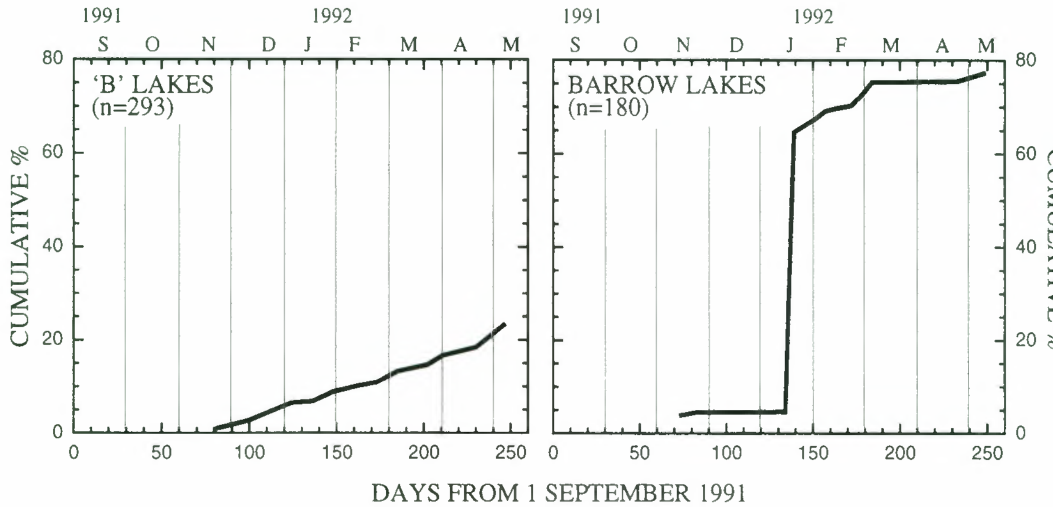

Figure 3. Graphs illustrating the number of lakes that froze completely to the bottom, and when that occurred in winter 1991–92 in the Barrow and 'B' Lakes regions. The number of lakes (y axis) is given as a cumulative percentage of the total number (n) of lakes that were monitored during the winter.

snow ice forms at the lake ice surface from the freezing of water-saturated snow or slush. Fourth, a *surface energy balance sub-model* is implemented to determine the surface temperature and energy available for freezing or melting.

The surface energy balance is driven, at a minimum, by observed inputs of minimum and maximum daily air temperatures, wind speed and precipitation. When the surface energy balance is coupled to the lake, lake ice and snow sub-models, it provides the surface temperature boundary condition which forces lake water temperatures, lake ice growth, and snow accumulation and metamorphism. In addition to complete energy balance components over the annual cycle, the key outputs are: 1) the time of initial ice formation; 2) time-dependent ice thickness; 3) maximum ice thickness; and, 4) time of complete removal of the ice cover.

A National Weather Service station at Barrow is the source of air temperature, precipitation and wind speed and direction data for inputs to the ice growth model which is used to simulate lake ice growth in both study areas. No weather data are available for the 'B' Lakes, and the use of Barrow weather data to represent the 'B' Lakes is considered reasonable since the ice growth and decay history at Barrow and at the 'B' Lakes is similar each year, i.e., the timing of freeze–up and initial ice formation in autumn, and the onset of melt in spring are coincident (Morris et al., 1995). Additional snow and ice thickness data that were obtained in April 1992 at a number of Barrow lakes (Jeffries et al., 1994) are used for running and validating the ice growth model.

The model results are shown in Figure 4. There are three ice growth and decay curves that represent different approaches to running the model and dealing with uncertainties in the precipitation input. We believe that the Ice Run provides an ice growth curve which is more representative of the mean ice conditions than the curves produced by the Deep and Shallow snow depth integrations. The Ice Run gives a maximum ice thickness of 2.2m.

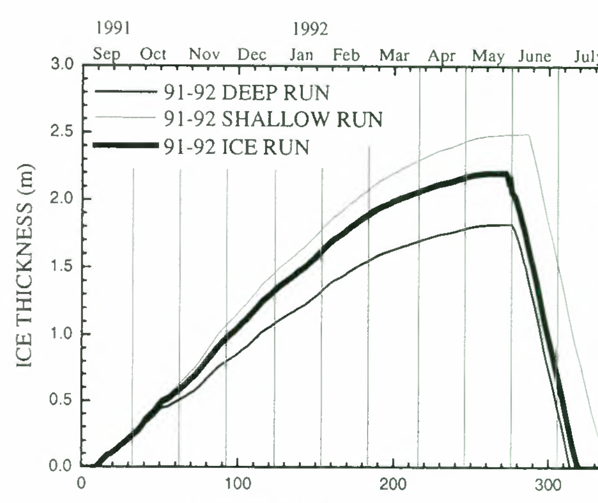

Figure 4. Simulated lake ice thickness curves illustrate ice growth and decay on the Barrow and 'B' Lakes under three different scenarios. The Deep and Shallow Runs are the results of varying the snow depth input to the numerical ice growth model. The Ice Run is the result of prescribing an ice thickness of 2.15m as measured in late April 1992 at a number of Barrow lakes where there was water below the ice.

3.2 Lake Depth Variability

The results of the ice growth model (Fig. 4) allow us to convert the time scale in Figure 3 into a maximum lake depth scale (Fig. 5). Lake depth curves for the Deep, Shallow and Ice Runs are shown, but we consider only the Ice Run curve. The results can be summarized as follows:

In the 'B' Lakes region:
75% of the lakes are >2.2m deep.

In the Barrow Lakes region:
25% of the lakes are >2.2m deep,
10% of the lakes are up to 1.5m to 2.2m deep,
60% of the lakes are up to 1.4m to 1.5m deep,
5% of the lakes are <1.4m deep.

4. DISCUSSION AND CONCLUSION

We have described a method to convert space– and time–dependent lake ice backscatter signatures into water depth data using numerical ice growth modelling to determine ice thickness and thus water depth. In this case, we have documented the maximum water depth of many individual lakes where no depth data were previously available. The results clearly show that there is significant spatial contrast in water depth

between coastal and inland regions on the North Slope in N.W. Alaska. Furthermore, since the inland 'B' Lakes region has a greater number and more dense coverage of deep lakes (>2.2m) than the coastal Barrow region, there is probably a greater amount of water available at any time of year in the inland region.

The variability of lake depth and water availability in this small area of the North Slope suggests that there might be similar variability throughout the entire region. This combined remote sensing and numerical ice growth modelling technique is simple to implement, and the SAR data sufficiently inexpensive and of adequate geographic coverage, that the method could be applied to the entire North Slope and elsewhere. Shallow thaw lakes are widespread in other regions of the Arctic, e.g., (1) the Yukon Kuskokwim Delta (Morris et al., 1995), (2) east Siberia (Mellor, 1994), and (3) northern Yukon Territory, including the Mackenzie River Delta, and the adjacent Northwest Territories.

The variability of lake depth and water availability in this small area of the North Slope suggests that there might be similar variability throughout the entire region. This combined remote sensing and numerical ice growth modelling technique is simple to implement, and the SAR data sufficiently inexpensive and of adequate geographic coverage, that the method could be applied to the entire North Slope and elsewhere. Shallow thaw lakes are widespread in other regions of the Arctic, e.g., (1) the Yukon Kuskokwim Delta (Morris et al., 1995), (2) east Siberia (Mellor, 1994), and (3) northern Yukon Territory, including the Mackenzie River Delta, and the adjacent Northwest Territories.

Ever since the first airborne radar images of lake ice on the Alaskan North Slope were acquired in the early 1970s it has been known that the radar signatures were related to lake water depth variability (Sellmann et al., 1975b; Elachi et al., 1976; Weeks et al., 1977, 1978). Mellor (1982) was the first to make a field survey of the bathymetry of a few lakes on the North Slope, and to make occasional ice thickness measurements during the winter. In so doing, he was able to show that the

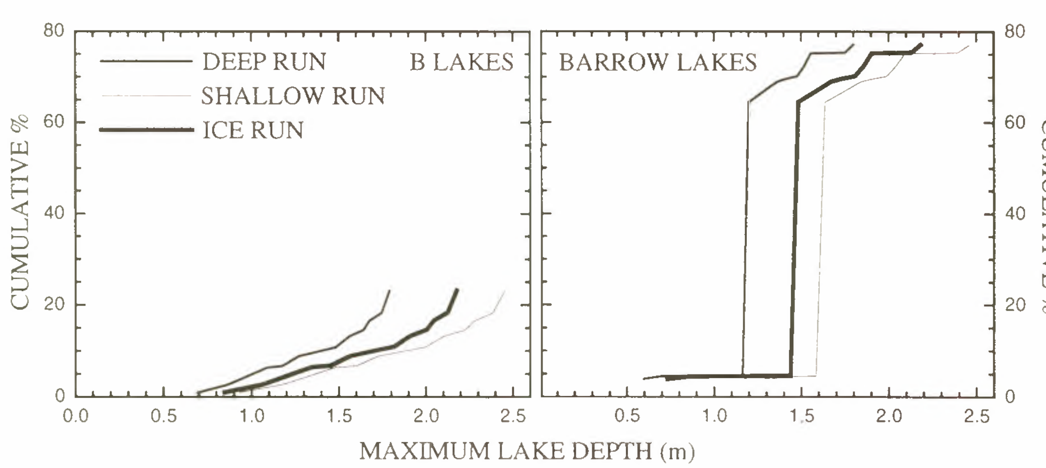

Figure 5. Graphs illustrating the maximum depth of lakes in the Barrow and 'B' Lakes regions according to the three different ice growth model runs. The number of lakes (*y* axis) with a particular depth are given as a number of lakes that were monitored during the winter.

temporal and spatial changes of SAR backscatter signatures from the lakes during the course of the winter were closely related to the bathymetry and its effects on ice growth and grounding on the bottom. The SAR and numerical ice growth modelling technique that we have described could be used to map lake bathymetry without the need to visit the lakes, except perhaps for validation purposes at a few selected lakes.

For those lakes where some part of the ice cover does not freeze completely to the bottom each winter, our method determines the depth of the remaining water as being greater than the maximum ice thickness. In winter 1991–92 this was 2.2m. Mellor (1982, 1994) has shown that there are subtle SAR image grey scale variations in ice on water that is up to 4m deep due to the reduction in the density of tubular bubbles in the ice and the resultant reduction in backscatter. Our method of lake depth determination could be improved by more detailed mapping of the backscatter signatures of ice that has water below it at the end of winter. This would yield information on how much lake water is between the depth of maximum ice thickness and 4m deep, and how much is >4m deep. Ice on very deep lakes has a uniformly dark tone because the ice is essentially inclusion–free since deep water provides a large reservoir that does not become supersaturated with the gases rejected during ice growth (Morris et al., 1994). Thus, the combined SAR and numerical modelling technique for lake depth determination is best applied to shallow lakes where a large portion of the water body is ≤4m deep.

ACKNOWLEDGEMENTS

This work was supported by NASA Polar Program Grant NAG 5–1731, Dr. R. H. Thomas, Program Manager.

REFERENCES

Jeffries, M. O., K. Morris, W. F. Weeks and H. Wakabayashi. 1994. Structural and stratigraphic features and ERS–1 synthetic aperture radar backscatter characteristics of ice growing on shallow lakes in N.W. Alaska, winter 1991–1992. *J. Geophys. Res.*, 99, 22,459–22,471.

Liston, G. E. and D. K. Hall. 1995a. An energy balance model of lake–ice evolution. *J. Glaciol.*, 41, 373–382.

Liston, G. E. and D. K. Hall. 1995b. Sensitivity of lake freeze–up and break–up to climate change: a physically based modeling study. *Ann. Glaciol.*, 21, 387–393.

Mellor, J. 1982. Bathymetry of Alaskan Arctic lakes: a key to resource inventory with remote sensing methods, *Ph.D. Thesis*, Institute of Marine Science, University of Alaska.

Mellor, J. 1994. ERS–1 SAR use to determine lake depths in Arctic and sub–Arctic regions. In, *Proceedings of the Second ERS–1 Symposium – Space at the Service of our Environment*, 11–14 October 1993, Hamburg, Germany. European Space Agency Special Publication SP –361, 1141–1146.

Morris, K., M. O. Jeffries and W. F. Weeks. 1995. Ice processes and growth history on Arctic and sub–Arctic lakes using ERS–1 SAR data. *Polar Rec.*, 31, 115–128.

Sellmann, P. V., J. Brown, R. I. Lewelen, H. McKim and C. Merry. 1975a. The classification and geomorphic implications of thaw lakes on the Arctic Coastal Plain, Alaska. U.S. Army CRREL (Cold Regions Research and Engineering Laboratory) *Res. Rep.* 344.

Sellmann, P. V., W. F. Weeks and W. J. Campbell. 1975b. Use of sidelooking airborne radar to determine lake depth on the Alaskan North Slope. U.S. Army CRREL (Cold Regions Research and Engineering Laboratory) *Spec. Rep.* 230.

Wakabayashi, H., M. O. Jeffries and W. F. Weeks. 1994. C band backscatter variation and modelling for lake ice in northern Alaska. *J. Japan. Rem. Sens. Soc.*, 14, 18–27.

Weeks, W. F., Sellmann, P. V. and W. J. Campbell. 1977. Interesting features of radar imagery of ice–covered North Slope lakes. *J. Glaciol.*, 18, 129–136.

Weeks, W. F., A. G. Fountain, M. L. Bryan and C. Elachi. 1978. Differences in radar returns from ice–covered North Slope lakes. *J. Geophys. Res.*, 83, 4069–4073.

FOREST BIOMASS ESTIMATION IN NORTHERN EUROPE USING NOAA AVHRR DATA

Tuomas Häme

CEC Joint Research Centre, Visiting Scientist from VTT Automation
Space Applications Institute, Environmental Mapping and Modeling, T.P. 442, I-21020 Ispra, Italy
tel. + 39 - 332 - 78 9897, fax + 39 - 332 - 78 9469, e-mail Tuomas.Haeme@jrc.it

Arto Salli, Kaj Andersson, Anssi Lohi

VTT AUTOMATION, Space Technology, Remote Sensing,
P. O. Box 13031, FIN-02044 VTT, Finland
tel. + 358 0 4561, fax + 358 0 456 4496, e-mail Firstname.Lastname@vtt.fi

ABSTRACT

A new methodology to estimate biomass (organic matter) of conifer dominated Boreal forests was developed. The method aims to estimate biomass of extensive areas where ground data are limited. The principal models are first computed using ground measurements and high resolution satellite data. The spectral models are then directly applied to a calibrated AVHRR image mosaic covering the entire area of interest. The method was quantitatively tested in Finland where detailed forest measurement data were available. It was demonstrated on an area reaching from the West coast of Norway to the Ural mountains. The performance of the methodology was better than expected.

1. INTRODUCTION

Boreal coniferous forests or Taiga forests form a continuous circumpolar vegetation zone. They are the largest terrestrial biome on Earth (Syrjänen *et al.* 1994). Mineral soil lands and peatlands of the Boreal forests form a significant pool in the global carbon cycle. It has been estimated that in Boreal forests there are 31×10^{12} kg of carbon stored in the trees alone (Kuusela 1990). Some studies indicate that the forests of the Boreal forest zone are considerably more important as sinks of carbon than has been thought previously (Kauppi *et al.* 1992). Information on forest resources and the structure of forests is accurate over Fennoscandia. In other parts of the Boreal forests there is much more uncertainty in the estimates of the forest biomass and other forest characteristics. The foreseen warming of the climate would cause moving of the tree line upper North. Amount of biomass close to the tree line would be a good indicator of the effects of the climatic changes and changes in the global carbon cycle.

The Boreal forests are dominated by conifers: spruce, larch, fir and pine. The proportion of the coniferous trees of the growing stock is usually 75 to 80 percent but it can be as low as 30 percent in some areas in Russia (Kuusela 1990). From the point of view of remote sensing, the conifers and broadleaved trees differ significantly because the near infrared reflectance of the broadleaved trees is usually 1.5 to two times the reflectance of conifers (Kalensky and Wilson 1975, Häme 1984). This causes problems in image interpretation, particularly in mixed forests.

The objective of this study was to develop a new methodology to estimate biomass (organic matter) of conifer-dominated Boreal forests on mineral soil lands. Methods were also developed to estimate the proportion of broadleaved trees of the total biomass. The methods were based on optical remote sensing data. The study has been reported earlier in (Häme *et al.* 1992 and 1995). The study aims to estimate forest characteristics over extensive areas where no ground data are available or are very limited.

2. MATERIALS

Three study areas were used: 1) area 'Orivesi', in Southern Finland, centered at 61^{o} 51' N, 24^{o} 17' E; 2) area 'Lammi', centered at 61^{o} 10' N, 25^{o} 08' E; and 3) Northern Europe. 'Orivesi' was the primary area for model development to estimate forest characteristics using ground data and a Landsat TM image. At 'Lammi' similar models to those of 'Orivesi' were computed to test how much the parameters change when another image and ground data are utilized. The third area comprised Northern Europe from the west coast of Norway up to Ural Mountains. On this area, the models developed using ground data and Landsat TM image were applied to the NOAA AVHRR weather satellite mosaic.

Ground data for the 'Orivesi' area were taken from sample plots of the National Forest Inventory (NFI). The ground data for the 'Lammi' area were stands from the forest management plan maps of private forest estates.

Proceedings of the Fourth Symposium on Remote Sensing of the Polar Environments, Lyngby, Denmark, 29 April – 1 May 1996
(ESA SP-391, July 1996)

To estimate the biomass, models were first computed for tree stem volume because the stem volume has a close connection with the biomass (the organic matter of the trees) (Nihlgård 1972, Mälkönen 1974 and 1977) and because the stem volume is measured on the ground in practical forestry. In the ground data the stem volume was given as a total value, including all tree species. The abundance of tree species was given as a proportion of the total stem volume. A model was developed to transform the tree stem volume into dry organic matter of the trees including bark, branches and roots. Furthermore, the organic matter in the undergrowth vegetation and soil was estimated.

The Landsat TM image for the 'Orivesi' area was acquired on June 21, 1985. The Landsat image for the 'Lammi' area was recorded on July 27, 1989. The Landsat images were rectified to a map coordinate system in the Gauss-Krüger projection. In area 'Orivesi', the spectral intensities were given for the field plots by selecting the closest pixel to the plot. In the 'Lammi' area the mean intensity value of spectral channels was computed within each stand. This mean value was used in the statistical analyses.

It was decided to make the NOAA AVHRR mosaic using Summer time images from as few years as possible. Images from several years had to be selected due to cloud cover. It was assumed that during the Summer the phenological phase of the forest ecosystems is relatively stable. A total of fifteen AVHRR Local Area Coverage images were used to make the mosaic over the study area. The images had been acquired during Summers 1990 to 1993. The majority of the images were from Summers 1991 and 1992.

The AVHRR images were first rectified using the orbital parameters of the satellite. The spectral effect caused by different angles between the sun and the surface was corrected using the cosine transformation. No atmospheric corrections were made at this stage.

The rectification was further adjusted using a second rectification based on the measurement of control points. Two images, one reaching far west and another, reaching far east, were first rectified to the map coordinate system using ground control points. Then, the other images were co-registered to the coordinate system of the two reference images.

3. FOREST BIOMASS ESTIMATION

A semi physical approach was chosen for biomass estimation (Fig. 1). In this approach the principal models are first computed using ground measurements and Landsat TM data. An image mosaic is made from the AVHRR data. The relationship between the Landsat data and the AVHRR data is determined using intensities of the original spectral channels. One benefit of this methodology is, that any forest characteristic model, suitable for use with Landsat data, can be directly applied to the AVHRR mosaic. The selected method should be seen as a first step towards a fully physical approach where only very limited ground data are used.

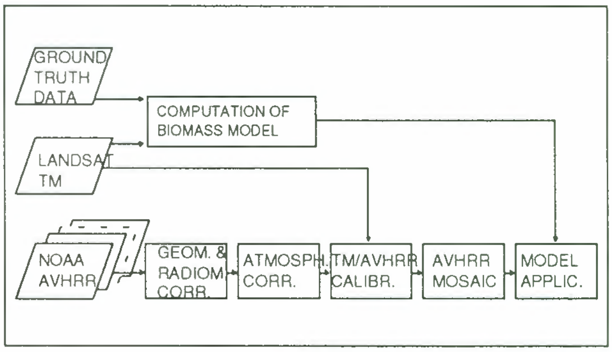

Fig. 1. Components of the procedure to estimate biomass.

Linear multiple regression analysis was used to estimate the tree stem volume. Channel 3 (red light) and channel 4 (near infrared radiation) intensities of Landsat Thematic Mapper were used as predictor variables, since their wavelength ranges corresponded to the wavelengths of the two first NOAA AVHRR channels. The form of the tree stem volume models (formula 2) was as follows:

$$V = a + b_1 x_1 + b_2 x_2 + \ldots + b_n x_n + \varepsilon ; \qquad (1)$$

where

V	is	tree stem volume (m^3/ha)
a		constant
b_k		regression coefficient for a spectral feature k
x_k		value of a spectral feature k on a pixel
n		number of spectral features used in the model
ε		residual error of the model

The spectral feature could be, in addition to an original spectral channel, a ratio of the channels or the NDVI (Normalized Differential Vegetation Index).

The models to estimate the amount of broadleaved trees were computed in two ways: 1) by estimating the proportion of the broadleaved trees of the total stem volume; and 2) by estimating the volume of the broadleaved trees directly.

4. MAKING THE AVHRR MOSAIC

Since the atmospheric path of reflected radiation is longer at the image edges than at the nadir, the intensities in the visible and the near infrared channels of AVHRR images tend to increase towards East and West from the image nadir (Myneni and Astrar 1994). A relative atmospheric correction method was implemented separately for each image to correct this atmospheric effect. The method used the intensities of water in line direction of an AVHRR image.

A relative calibration method was used to match the intensities of AVHRR channels 1 and 2 and Landsat TM channels 3 and 4 (Häme 1991, Olsson 1994). The matching was done to make it possible to directly apply forest characteristic models, computed for the Landsat data. Two approaches for the radiometric matching were tested:

1. Linear regression analysis;
2. Matching of means and standard deviations.

An AVHRR image from July 26, 1992 (in which the atmospheric effects had been corrected and in which the intensity matching to the Landsat TM image had been made) was used as a master image to make the AVHRR image mosaic. Intensities of other AVHRR images in which atmospheric correction had been made were matched to this master image using mean and standard deviation matching. First, AVHRR images that overlapped with the scaled master image (AVHRR July 26, 1992) were matched. Then the scaling moved from this base image to East and West using overlapping areas.

After the relative calibration, the actual mosaic was computed as weighted averages of pixel intensities of overlapping images. Pixels with lower intensities had higher weights. The first of overlapping pixels had a weight of 1, the second one had a weight of 1/2, the third one 1/3, and so on.

Two mosaics were produced: the 'regression mosaic' and the 'mean and standard deviation matching mosaic' according to the TM/AVHRR matching method. Before generation of the mosaic, water and clouds were extracted from each AVHRR image.

After the corrections, a systematic increase of intensities towards East was detected in AVHRR1 channel. Intensities were corrected using a linear scaling procedure in an East-West direction. The AVHRR1 intensities of similar forests in Urals and Finland were scaled the same. In the correction, the AVHRR1 intensities East of Finland decreased. At the study area 'Orivesi' they remained the same whereas they somewhat increased West of Finland. In the near infrared channel AVHRR2 no systematic errors in the intensities could be detected.

5. APPLICATION OF FOREST CHARACTERISTICS MODELS

5.1 Relationships between stem volume and reflected optical radiation

Figures 2 and 3 indicate the general relationship between coniferous forest biomass and reflected optical radiation. The correlation is negative throughout the optical wavelength area including the near infrared radiation which is an opposite result to the situation found over agricultural lands and grasslands (Tucker *et al.* 1975). Because of the very similar relationship between biomass and reflected red and near infrared radiation, the vegetation index, *i.e.* the ratio between near infrared and red, is a very poor indicator of the forest biomass.

Table 1 shows computed biomass models. The models for the 'Orivesi' and 'Lammi' areas are similar. For instance, the models to estimate total and coniferous stem volume (V and $V_{conifer}$) using the red channel (models I, II, V and VI in Table 1) coincide surprisingly well. Note that the ground data were different and no scaling was done to match the two Landsat TM images. The similarity between the study areas is somewhat less for models having both red and near infrared channels as predictors (models III, IV, VII and VIII).

The results indicate that a biomass model using the red channel TM3 as a single predictor is rather robust to the presence or absence of broadleaved trees. Models for coniferous stem volume using vegetation indeces as predictor variables are very poor (models IX, X). Corresponding models for the broadleaved stem volume are slightly better but still inappropriate (models XIII and XIV).

The highest values for coefficient of determination (R^2) can be seen in models to estimate the proportion of the broadleaved trees from the total stem volume (models XV and XVI). Note that these models can give high values even if the total biomass is low because the values are relative. The predictor variable in these models was actually the widely used 'Vegetation index', *i.e.* ratio of near infrared and red.

Models were also computed for the coniferous plots using all combinations of Landsat TM channels as predictors. The best combinations are shown in Fig. 4. The best single spectral feature was TM3. The best two feature combination was TM3 and TM4. The value of

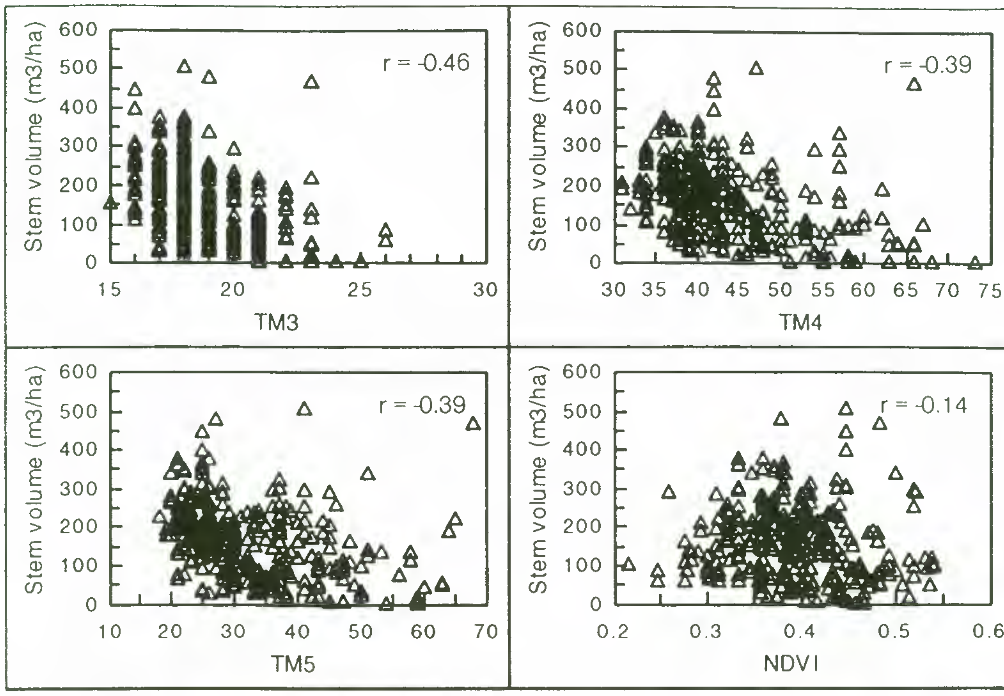

Fig. 2. Tree stem volume vs. spectral features. Study area 'Orivesi', no. of observations 324. r is the correlation coefficient.

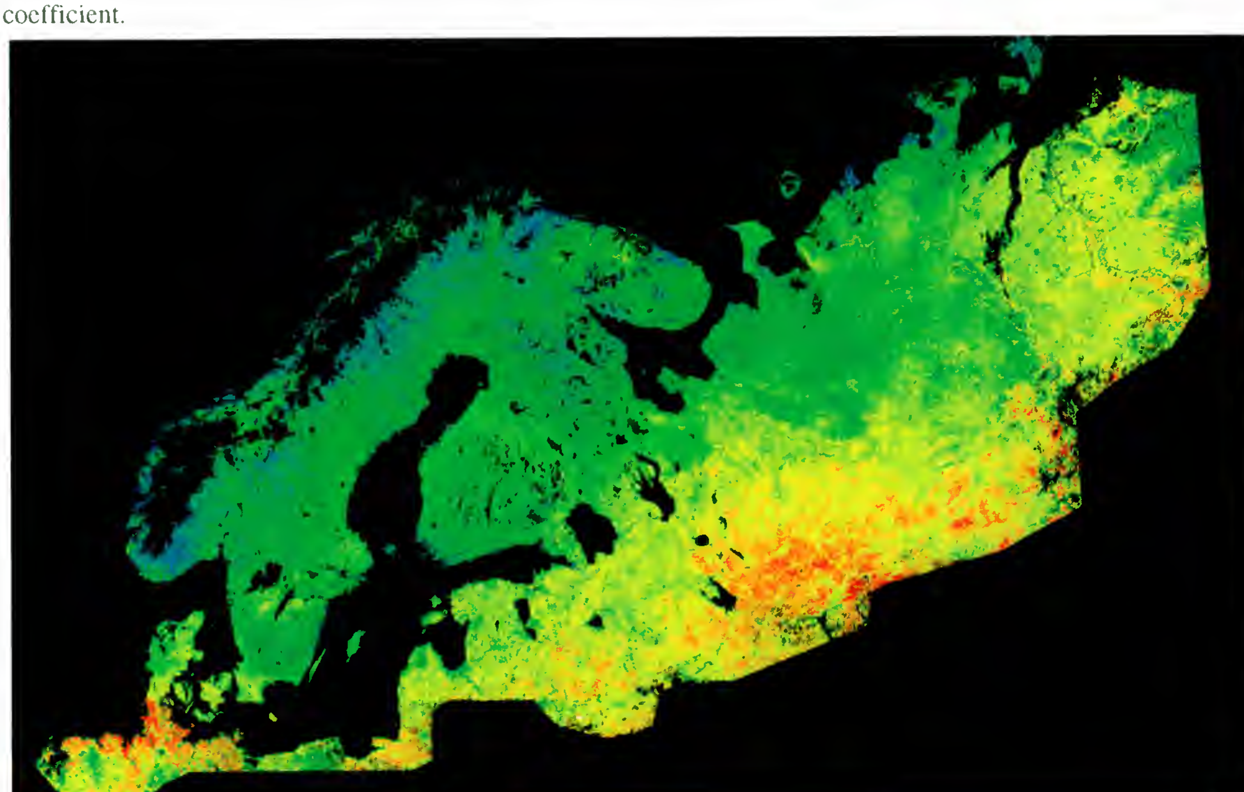

Fig. 3. NDVI computed from the mosaic. NDVI scale from low to high values: blue-green-yellow-red.

Table 1. Summary of the models for biomass estimation.

Model identifier	Predicted variable	Constant	Coeff. for TM3	Coeff. for TM4	Std. error for constant	Std. error for TM3	Std. error for TM4	R^2	Number of obs.	Area
I	V	562	-21.5	none	44.4	2.36	none	0.20	345	Orivesi
II	V	522	-22.1	none	21.4	1.32	none	0.15	1595	Lammi
III	V	567	-15.1	-2.80	42.8	2.58	0.539	0.25	345	Orivesi
IV	V	474	-9.58	-3.20	20.7	1.58	0.245	0.23	1595	Lammi
V	$V_{conifer}$	572	-22.0	none	48.1	2.55	none	0.23	250	Orivesi
VI	$V_{conifer}$	566	-23.1	none	33.8	2.12	none	0.15	685	Lammi
VII	$V_{conifer}$	590	-16.4	-2.87	47.0	2.90	0.761	0.27	250	Orivesi
VIII	$V_{conifer}$	520	-11.2	-3.25	33.0	2.57	0.431	0.21	685	Lammi
IX	$V_{conifer}$	265	-46.1 M4/TM3		39.3	17.1 (TM4/TM3)		0.029	250	Orivesi
X	$V_{conifer}$	242	-213 NDVI		37.3	96.0 (NDVI)		0.019	250	Orivesi
XI	$V_{broadleaf}$	31.5	-2.69	0.591	9.03	0.545	0.114	0.093	345	Orivesi
XII	$V_{broadleaf}$	31.7	-4.33	1.17	6.64	0.506	0.0786	0.12	1595	Lammi
XIII	$V_{broadleaf}$	-20.8	11.8 TM4/TM3		5.28	2.18 (TM4/TM3)		0.079	345	Orivesi
XIV	$V_{broadleaf}$	-40.7	19.8 TM4/TM3		3.90	1.29 (TM4/TM3)		0.13	1595	Lammi
XV	BroProp	-0.505	0.240 TM4/TM3		0.0415	0.0172 (TM4/TM3)		0.36	345	Orivesi
XVI	BroProp	-0.533	0.233 TM4/TM3		0.0273	0.00905 (TM4/TM3)		0.29	1595	Lammi

V Stem volume (m^3/ha) including all tree species
$V_{conifer}$ Stem volume (m^3/ha) using grond data stronly dominated by conifers (BroProp < 0.05)
$V_{broadleaf}$ Stem volume (m^3/ha) of broadleaved deciduous trees
BroProp Proportion of deciduous trees of the total stem volume of a plot or a stand

the coefficient of determination (R^2) hardly increased after two predictor variables. According to this test, the AVHRR optical channels are the optimal two channels for coniferous biomass estimation.

5.2 Applying the biomass models to the AVHRR mosaic

After the relative calibration of the AVHRR data with the TM data and after the linear correction to channel AVHRR1, models developed using Landsat TM image and ground data from the 'Orivesi' area were applied to the AVHRR image mosaic. The results were tested against the National Forest Inventory (NFI) data of Finland. The test data were obtained from the Yearbook of Forest Statistics that includes results of the inventory by twenty forestry board districts (Aarne (ed.) 1992, Aarne (ed.) 1994).

Table 2 summarizes the results of application of the biomass models. The test data are the total stem volume by the Forestry Board Districts. Generally the correlations between the true stem volume and the estimated volume are high but the models have given overestimates. The exception to this are the models for broadleaved trees which have resulted in poor results with huge underestimates. The main reason for such poor results is the lack of training data for the broadleaved trees.

The highest correlation with the total stem volume was obtained using a model were the only predictor was the red light channel (model Ir in Table 2). However, this model gave relatively high biomass values on pasture lands in Central Russia (and also in Northern Germany that is outside the Boreal forest zone). In other words, it was a poor model to separate forests from non forest.

The model in which both red and near infrared channels were predictors and in which the TM/AVHRR matching was done using means and standard deviations (model IIIm in Table 2, Fig. 5, Fig. 6), was able to separate forest and non forest better than the red channel model Ir. However, this model underestimated biomass in such forestry board districts which had a significant proportion of broadleaved trees. Overestimates occurred on areas with small lakes in mountain valleys.

The mean stem volume value is 73.9 m^3/ha for pixels with biomass estimate value above 0 which corresponds to organic matter of 42'552 kg/ha or of 47'352 kg/ha including the undergrowth vegetation. The maximum stem volume estimate is 472 m^3/ha. The area of the forested pixels (non zero biomass) in Fig. 6 is 256 million ha which gives the total tree stem volume of 18'900 million m^3 and organic matter of 10'900'000 million kg or 12'100'000 million kg including the undergrowth. The dry weight values were computed from the stem volume values using formulae developed in this study. They are only indicative.

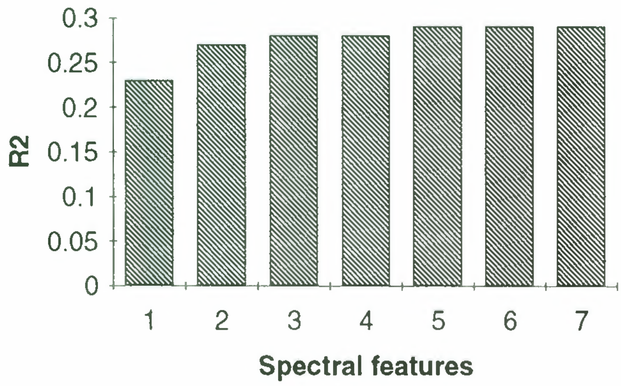

1 TM3
2 TM3, TM4
3 TM3, TM4, TM6
4 TM3, TM4, TM5, TM7
5 TM3, TM4, TM5, TM6, TM7
6 TM1, TM3, TM4, TM5, TM6, TM7
7 TM1, TM2, TM3, TM4, TM5, TM6, TM7

Fig. 4. Performance (R^2) of best Landsat TM models to estimate tree stem volume in area 'Orivesi', coniferous forests. No. of observations 250.

6. CONCLUSIONS

Despite certain inaccuracies, the performance of the biomass estimation method developed in this study exceeded the expectations. It was shown that the models, computed using ground data and Landsat TM images, can be successfully utilized with the AVHRR data. The selected modeling approach in which the parameters of a physical model are computed using regression analysis seemed to be appropriate because the models worked reasonably well over the whole of Finland and because models, computed for two independent areas using two independent images, were found to be similar. The models were biased usually producing overestimates of biomass. Some bias was expected because no calibration of the estimates was made in this estimation procedure.

A big benefit of the approach is that different models can be very easily applied to the AVHRR image mosaic. In this study, a total of five models were applied to two different mosaics. The drawback of the two phase method is that the predicted variable (biomass) should be a linear combination of the predictor variables. Nonlinear combinations of the predictor variables (ratios) would be effective in estimation of the broadleaved trees.

The red light channel was the best single channel for biomass estimation. Models having a red channel as the only predictor gave good results and were robust when changing images and when using different combinations of conifers and broadleaved trees. However, these models were not effective to separate forests and non forests. They gave forest biomass estimates for some grassland areas as well. Models with both red and near infrared as predictors could separate forested areas much better. The main problems with these models are mixed pixels in areas with small lakes, where the biomass tends to be overestimated and broadleaved tree forests tend to be underestimated.

The vegetation index appeared to be inappropriate to estimate the biomass of the coniferous forests. The index seems to be effective in biomass estimation only when the amount of biomass is related to the proportion of bare soil covered by the vegetation. This is the case in arid areas and on agricultural lands. This is not the case in Boreal forests where the whole ground is usually covered by green vegetation.

Table 2. Summary of the test results. Roman number in the column 'Model identifier' refers to Table 1. The letter after the model number indicates the TM/AVHRR matching method.

Model identifier	Predicted variable	Predictors	TM/AVHRR matching	Correlation with District V (n=20)	Bias for whole Finland, %
Im	Stem V, all species	Red	mean & std. dev.	0.66	-16
Ir	Stem V, all species	Red	regression	0.98	14
IIIm	Stem V, all species	Red, NIR	mean & std. dev.	0.94	8
IIIr	Stem V, all species	Red, NIR	regression	0.92	32
Vm	Stem V, conifers	Red	mean & std. dev.	0.62	-1
Vr	Stem V, conifers	Red	regression	0.97	36
VIIm	Stem V, conifers	Red, NIR	mean & std. dev.	0.85	11
VIIr	Stem V, conifers	Red, NIR	regression	0.93	39
XIm	Stem V, broadleaved	Red, NIR	mean & std. dev.	0.39	-91
XIr	Stem V, broadleaved	Red, NIR	regression	0.48	-86

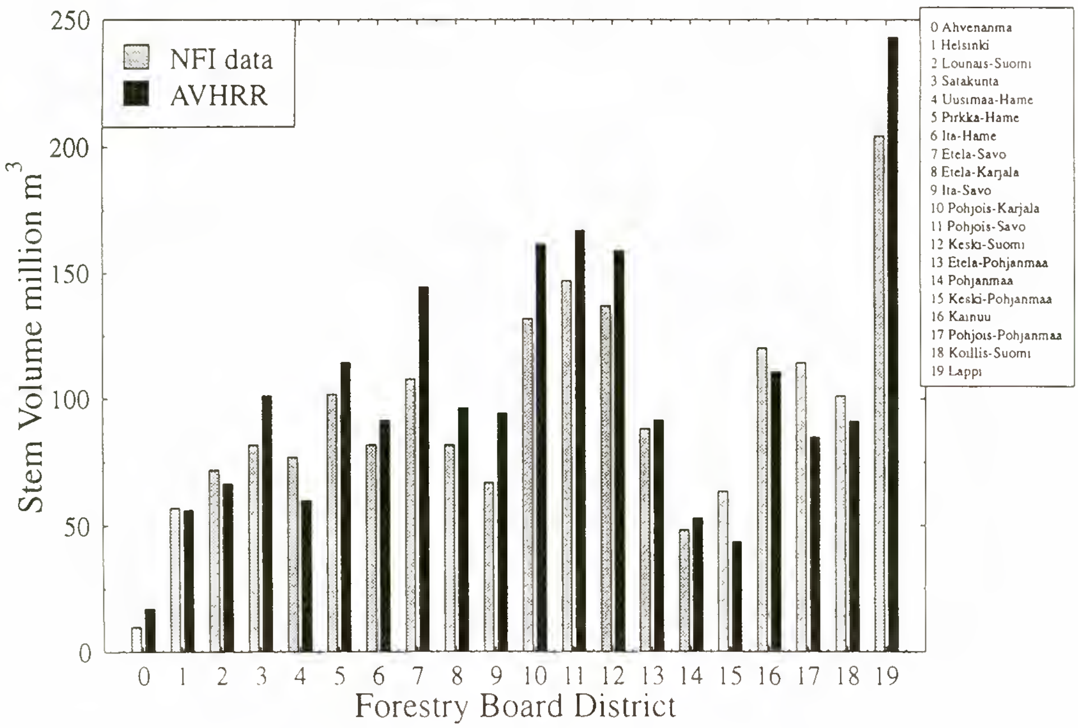

Fig. 5. Estimated (black bar) and measured (grey bar) total stem volume by Forestry Board Districts in Finland. Model IIIm in Table 2.

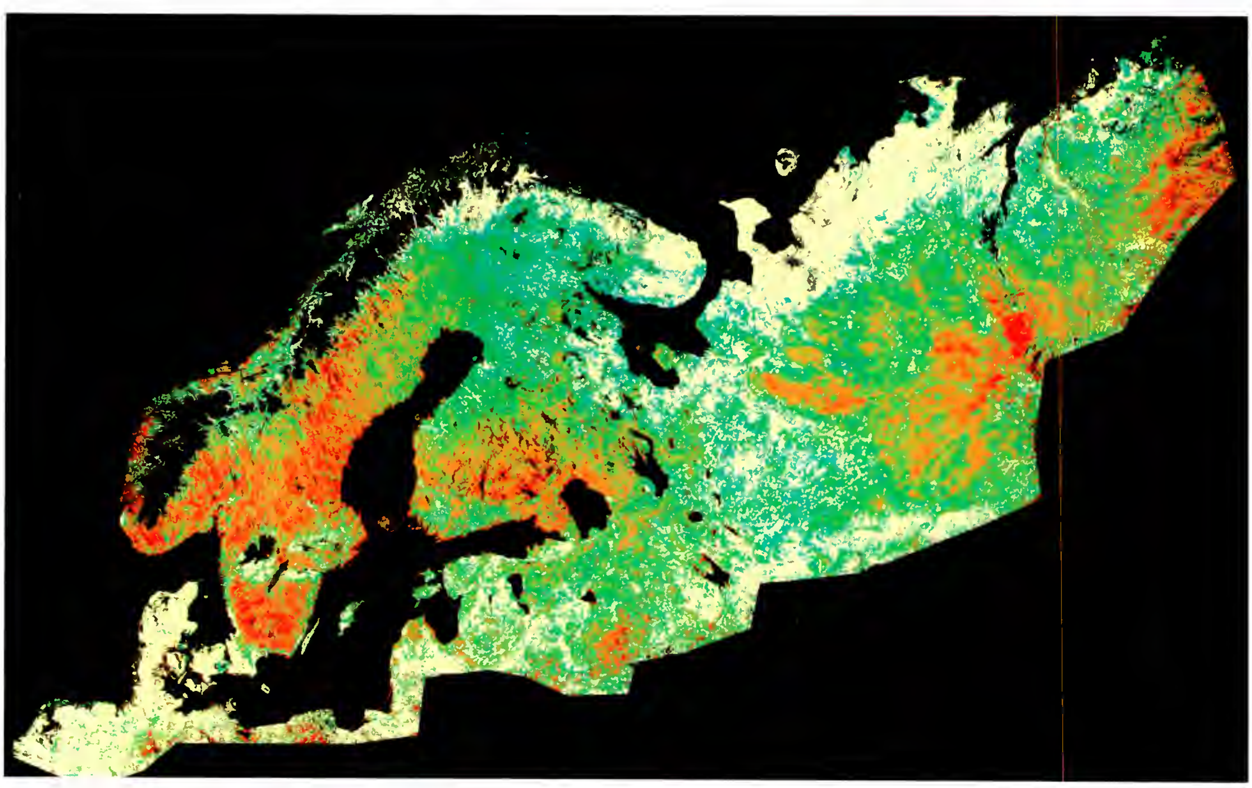

Fig. 6. Application of the model IIIm (Table 2) to the AVHRR mosaic. Colors: light yellow - zero biomass; turquoise 1 - 50 m^3/ha; green 26 - 50 m^3/ha; brownish green 51 - 100 m^3/ha; brownish red 101 - 150 m^3/ha; bright red above 150 m^3/ha; black - water, mountains and clouds.

Neither the mean and standard deviation scaling between TM and AVHRR images nor regression scaling gave optimal results. The mean and standard deviation scaling produced intensity dynamics in the AVHRR images which were too high whereas the dynamics in regression scaling mosaic may have been too low.

In the future, procedures to improve the radiometric calibration and atmospheric correction of the images will be developed. A method to calibrate the biomass estimates for bias reduction will be incorporated.

Acknowledgements

The majority of the funding for this study came from The Finnish Research Program on Climate Change (SILMU) of The Academy of Finland. The Forestry Board District of 'Itä-Häme' (Mr. Kai Lindh, M.For.) provided the stand data for the 'Lammi' area. Mr. Kimmo Syrjänen (M.Sc.) also provided unpublished ground data from Russia. Dr. Vasily I. Sukhikh from the International Forestry Institute, Moscow, gave forest maps (1 : 2'500'000) of Russia. Dr. Thomas Häusler from GAF, Germany, lent Landsat MSS images from Russia for testing. Dr. Pamela Kennedy from the Joint Research Centre, Space Applications Institute, gave very useful suggestions to improve the paper.

7. REFERENCES

Aarne, M. (ed.) 1992. Yearbook of forest statistics 1990 - 91. *Folia Forestalia* 790. 281 p.

Aarne, M. (ed.) 1994. Yearbook of forest statistics 1993 - 94. SVT Agriculture and Forestry 1994:7. 348 p. ISBN 951-40-1380-8

Häme, T. 1984. Landsat-Aided forest site type mapping. Photogrammetric Engineering and Remote Sensing 50(8), p. 1175 -1183.

Häme, T. 1991. Spectral interpretation of changes in forest using satellite scanner images. Acta Forestalia Fennica 222. 111 p.

Häme, T., Salli, A., Andersson, K. Lohi, A. & Rauste, Y. 1995. Estimation of biomass and other characteristics of Boreal forests over extensive areas using NOAA AVHRR data. In: Multispectral and Microwave Sensing of Forestry, Hydrology, and Natural Resources, eds. Mougin, E., Ranson, J. & Smith, J. A. Proc. SPIE 2314. p. 200 - 210.

Häme, T., Salli, A. & Lahti, K. 1992. Estimation of carbon storage and organic matter in Boreal forests using optical remote sensing data. Proc. of the Central Symposium of the 'International Space Year' Conference, Munich, March 30 - April 4, 1992. ESTEC, Noordwijk, ESA SP-341. p. 75 - 78. ISSN 0379-6566.

Kalensky, R. & Wilson, D. A. 1975. Spectral signatures of forest trees. In Proc. of the Third Canadian Symposium on Remote Sensing. Edmonton, Alberta. Sept. 22 - 24. 18 p. Reprint.

Kauppi, P. E., Mielikäinen, K. & Kuusela, K. 1992. Biomass and carbon budget of European forests, 1971 to 1990. Science 256: 70 - 74.

Kuusela, K. 1990. The dynamics of Boreal coniferous forests. Helsinki. SITRA. 172 p. ISBN 951-563-274-9.

Myneni, R. B. & Astrar, G. 1994. Atmospheric effects and spectral vegetation indices. Remote Sensing of Environment 47(3): 390 - 402.

Mälkönen, E. 1974. Annual primary production and nutrient cycle in some Scots pine stands. *Communicationes Instituti Forestalis Fenniae* 84(5).

Mälkönen, E. 1977. Annual primary production and nutrient cycle in a birch stand. *Communicationes Instituti Forestalis Fenniae* 91(5).

Nihlgård, B. 1972. Comparative studies on beech and planted spruce forest ecosystems in Southern Sweden. Lund. University of Lund, Ph.D. Thesis. 139 p. [Stencil]

Olsson, H. 1994. Changes in satellite-measured reflectances caused by thinning cuttings in Boreal forest. Remote Sensing of Environment 50: 221-230.

Syrjänen, K., Kalliola, R., Puolasmaa, A. & Mattsson, J. 1994. Landscape structure and forest dynamics in subcontinental European Taiga. Ann. Zoll. Fennici 31:19-34.

Tucker, C. J., Miller, L. D. & Pearson, R. L. 1975. Shortgrass prairie spectral measurements. Photogrammetric Engineering and Remote Sensing, Vol. 41, No. 9. p. 1175 -1183.

IMPROVING THE CLASSIFICATION OF SATELLITE IMAGES FROM HIGH ARCTIC ENVIRONMENT BY MEANS OF MODELLING THE TOPOGRAPHIC INFLUENCE ON THE ILLUMINATION

Jostein Amlien[1] and Odd Willy Brude[2]

Norwegian Polar Institute, Postboks 5072, Majorstua, N-0301 Oslo, Norway,
Ph.: [1]+47 22 95 95 05, [2]+47 22 95 96 22, e-mail: jostein@npolar.no / oddbr@npolar.no

Satellite remote sensing of terrestrial environments are affected by the fact that the illumination of the ground may vary within a scene, due to variation in topographic parameters as slope and aspect. This effect gives differences in the reflected signal between locations with different illumination, but with the same reflection properties. The classification of the ground cover in a satellite scene is therefore influenced by the topography. Because of the low solar elevation angles this effect is more prominent in polar environments. There is therefore a special need to reduce the effect of the topography in high arctic environments in order to obtain better classification results.

Several methods for reducing the topographic effect are found in the litterature. The various correction methods are carried out by first estimating the illumination for each pixel and then calculating what the pixel value would have been with an invariant illumination. Some of the present methods have been tested and evaluated for a part of a Landsat TM scene covering an area near Longyearbyen, Svalbard. There exists a digital elevation model (DEM) for the area, from which the terrain slope and aspect were calculated. The TM scene was also resampled to the same map coordinate system as the DEM before the testing.

The direct solar illumination is given by the cosine of the illumination angle (cos(i)), which can be calculated directly from the terrain slope and aspect, and the solar elevation and azimuth. One simple method is to correct the image by dividing the pixel value with the term cos(i) and then multiplying by a scaling factor. Due to atmospheric effects, this method did not give satisfactory results. This method could therefore not be used directly. A method called c-correction (1) tries to overcome this problem by introducing a spectrally dependent parameter c, determined by a linear regression between each band and the term cos i. Each band are now corrected by dividing the pixel value with the term (cos(i) + c). The parameter c were expected to catch up both the diffuse irradiation as well as the path radiance for that spectral band, and it were showing higher values for shorter wavelengths. This method showed a clear improvement of the result of a non-supervised classification.

The illumination can also be estimated without a DEM. By means of a method called hyperspherical transformation (2) the illumination is calculated as the distance in the multispectral space to origin, which is defined as the point in multispectral space where only path radiance is present. This method were showing somewhat better results than the c-correction did.

One important difference between the two last methods is the level of preprocessing before carrying out the illumination correction. In addition to take the path radiance into account when calculating the illumination in the hyperspherical correction, it was also removed from each band before dividing with the illumination term. We have therefore tried a modified c-correction where path radiance is removed before the rest of the correction is carried out. The parameter c is now expected to catch up only the indirect illumination, which is veryfied by lower values than before. The testing of modified method is not yet finished, but the preliminary results show improvements.

(1) Meyer et al 1993: Radiometric corrections of topographically induced effects on Landsat TM data in alpine environments. *ISPRS J.- of PH. and Rem.S., 48(4), pp. 403-410.*

(2) Pouch and Campagna 1990: Hyperspherical direction cosine transformation for separation of spectral and illumination information in digital scanner data. *Photogr. Eng. and Rem.S, 56(4), pp.475-479.*

MODELLING EVAPOTRANSPIRATION BY MEANS OF SATELLITE AND SYNOP DATA - AN EXAMPLE FROM THE JAMESON LAND, EAST GREENLAND.

Anne Eiby

COWI - Consulting Engineers & Planners
Parallelvej 15, DK-2800 Lyngby, Denmark
Ph.:+ 45 45 97 22 11, fax: + 45 45 97 22 12, e-mail: ane@cowi.dk

In a high-arctic terrestrial ecosystem precipitation and temperature are limiting factors for vegetation growth. Perhaps the best factor to describe the potential for plant growth is the actual evapotranspiration, that reflects the availability of water and energy and forms an important part of the water budget. In this study it was investigated if the actual evapotranspiration can be modelled and analyzed by means of Landsat TM data, synop climatological data from a stationary ground measuring station and soil surveys.

Nearly all precipitation on Jameson Land (app. 220 mm) is falling in winter as snow or is bounded in permanent frozen layers. The mean summer temperature does not exceed 10°C. Thus, the vegetation is expected to be sparse and the evapotranspiration rate low. The calculated evapotranspiration from a climatological station shows medium-high values betweeen 1 and 3 mm/day and the satellite-derived vegetation map shows a high concentration of luxuriant vegetation on the slopes facing south and in small pockets in the landscape. How can this occur in a polar almost desert-like area?
The analysis shows that satellite-measured surface temperature is highly correlated with the evapotranspiration calculated from synop data on a vegetated surface, whereas there is a week reverse correlation over an extended area. In warmer climates, the surface temperature normally decreases when evapotranspiration increases, other things being equal, due to cooling of the surface when energy is used for evapotranspiration. However, if the surface temperature is raised, this normally indicates water deficit or stomatal resistance. The result of this study indicates, that evapotranspiration in the arctic climate has a strong dependence on the temperature-dependent content of air humidity just outside the stomata of plants and the resulting gradient to the dry arctic air masses.

The big amount of vegetation on the south-facing slopes can partly be explained by the relative higher temperature due to the role of surface geometry in radiation exchange, partly by available water. Earlier studies in the area showed, that the snowfall during winter is redistributed due to wind direction and relief, resulting in snowpatches on south-facing slopes leeward and bare surfaces on the north-facing wind-exposed slopes. During growth season the vegetation is supplied with meltwater from those snowpatches. Capillary melt water from the permafrost zone in the lowlands, where soils are organic and have a higher content of nutrients, contributes to development of plant communities in the pockets of the landscape.

Based on this, it is assessed, that there is a considerable amount of water available for plants on Jameson Land in spots connected with snowpatches on south-facing slopes, where energy is sufficient, and in pockets where melting soil ice is ascending due to capillary forces. The combined favourable conditions leaves a characteristic landscape mosaic with vegetation in stripes and spots among wind-eroded plains. This means, that modelling of evapotranspiration from satellite data has a chance to succeed with input of vegetation parametres.

MOVEMENTS AND SWIMMING SPEED OF NARWHALS (MONODON MONOCEROS) INSTRUMENTED WITH SATELLITE TRANSMITTERS IN MELVILLE BAY, NORTHWEST GREENLAND

Rune Dietz[1] and Mads Peter Heide-Jørgensen[2]

[1] Department of Arctic Environment, National Environmental Research Institute
Tagensvej 135, DK-2200 Copenhagen N, Denmark
Ph: +45 35 82 14 15, Fax: 35 82 14 20, e-mail: gfomgeri@inet.uni-c.dk

[2] Greenland Institute of Natural Resources
Tagensvej 135, DK-2200 Copenhagen N, Denmark.
Ph: +45 35 82 14 15, Fax: 35 82 14 20, e-mail: grfimphj@inet.uni-c.dk

The remoteness and inaccessiblility of areas inhabited by narwhals make these animals difficult to study in the field using traditional methods. Recent advances in satellite tracking have made it possible to monitor the movements of narwhals. Positions were obtained for up to 100 days from nine narwhals (Monodon monoceros) representing both sexes and all age categories instrumented with satellite-linked UHF radio transmitters in Melville Bay (76°03'06"N, 61°14'90"W), Northwest Greenland, in August-September 1993 and 1994.

In both years whales stayed within Melville Bay during the open-water portion of the tracking period. Most of the coastal positions obtained were inside the Melville Bay Wildlife Sanctuary. The narwhals also moved up to 100 km offshore to areas where water depths exceed 1000 m. By early to mid October, the narwhals left Melville Bay and started migrating southward along the continental slope where water depths range from 500 to 1000 m. This southward movement ceased some 700 km further south in late November, still in water with depths of 500-1000 m. The mean swimming speed of the whales during September varied between 2.9 and 8.2 km/h. No size- or sex-related pattern could be detected in the swimming speed data, nor could any diurnal differences be found.

The use of longer intervals between consecutive positions resulted in significantly lower calculated swimming speeds, suggesting that svimming speed will be underestimated if calculated over longer time span. The mean swimming speed of two males tracked for more than three month during the autumn showed a significant decrease. This decrease in swimming speed indicated a less horizontally directed movements during the winter period, where ice is restricting the movements of the whales in the surface. Information from the dive data revealed that the whales dove more frequent to greater depths in that period.

SOME CHARACTERISTICS OF NARWHAL (MONODON MONOCEROS) DIVING BEHAVIOUR IN BAFFIN BAY

Mads Peter Heide-Jørgensen[1] and Rune Dietz[2]

[1] Greenland Institute of Natural Resources
Tagensvej 135, DK-2200 Copenhagen N, Denmark.
Ph: +45 35 82 14 15, Fax: 35 82 14 20, e-mail: grfimphj@inet.uni-c.dk

[2] Department of Arctic Environment, National Environmental Research Institute
Tagensvej 135, DK-2200 Copenhagen N, Denmark.
Ph: +45 35 82 14 15, Fax: 35 82 14 20, e-mail: gfomgeri@inet.uni-c.dk

Dive data were collected from nine narwhals, Monodon monoceros, instrumented with satellite-linked dive recorders in Northwest Greenland in August-September 1993 and 1994. Data were collected for periods ranging from a few weeks to nine months.

The narwhals made daily dives to depths of more than 500 m and frequently dove to 1000 m or more. However, most of the time spent below the surface was in the water column at depths of between 8 and 52 m. For two males that were tracked from September through November the maximum dive depth increased steadily through time. There were no consistent differences in the duration of dives or the number of dives to depths larger than 8 m during four 6-hour periods that were monitored. There were significant differences in dive rates (number of dives per hour) between the large males, the small male and the females. More than half of the dives lasted less than 5 minutes and few lasted more than 20 minutes. These relatively short dive times suggest that narwhals do not exceed their aerobic dive limit. The average period spent in the upper 5 m of the water column was 39.3% (SD=13.5, n=632) for seven of the whales, combined. Speed of vertical movements increased significantly from 1 ms^{-1} for 100 m dives to more than 2 ms^{-1} for dives deeper than 900 m. A female accompanied by a calf had dive parameters and surfacing times that were identical to those of the other females.

REMOTE SENSING DATA USED DURING AERIAL SURVEYS OF SPRING CONCENTRATIONS OF SEABIRDS IN THE SEA ICE IN EASTERN BAFFIN BAY

Anders Mosbech[1], David Boertmann[1], Niels Bagger[2] and Preben Gudmandsen[3]

[1] National Environmental Research Institute, Department of Arctic Environment
Tagensvej 135, DK-2200 Copenhagen N
Ph.: +45 35 82 14 15, Fax: +45 32 82 14 20

[2] Institute of Electromagnetic Systems, Technical University of Denmark
DK-2800 Lyngby, Denmark

[3] RS-Consult ApS, Holmebjerg 12, DK-2950 Vedbæk, Denmark
Ph.: +45 45 25 37 88, fax: +45 45 93 16 34, e-mail: pg@emi.dtu.dk

During aerial surveys of seabirds in May 1995 remote sensing data were used to obtain a description of the ice conditions in the area of the survey in support of the planning of survey. Later the data were used to analyse the relationship between bird distributions and ice conditions. Ice maps compiled by the Danish Meteorological Institute and data from NOAA AVHRR instrument, and the ERS SAR were used in this context.

During spring when an ice edge zone develops between the shore-fast ice and the mooing drift ice en eastern Baffin Bay a large number of seabirds, particularly Auks and eiders, migrate north from the open water area off the south-west coast of Greenland to breeding areas in North Greenland and Arctic Canada. Seabirds in the shear zone and at the progressing ice edge zone were surveyed from a small twin-engine aircraft flying at 90 knots 250 feet above sea level. GPS-positions were sampled automatically every 5 seconds by a portable PC and observations were recorded on tape via the headset microphone with an automatic time signal. Estimates of ice cover and ice type were made every two minutes, triggered by an automatic time signal.

NOAA AVHRR data were available from the local receiving station whereas ERS SAR data were relayed from Copenhagen using FTP on Internet by way of a portable PC with modem. The SAR data were the UILR data broadcasted from Kiruna and received on the BDDN station in Copenhagen where they were compressed before transmission to Greenland.

SAR data proved to be a useful complement to the NOAA data especially during long periods of cloud cover but also because they provide a finer spatial resolution so that even narrow leads could be observed. On the other hand, their applicability is limited because of the relative narrow swath and the low repetition frequency of observation of the area of interest. Also, it was found that the SARA data shall be interpreted with caution when no ground information is available.

PARTICIPANTS

Jostein Amlien
Norsk Polar Institutt
Postboks 5072
Majorstua
N-0301 Oslo
Norge

Trygve Aspenes
UNIS
Boks 156
N-9170 Longyearbyen
Norway

Axel Bochert
Alfred-Wegener-Institut
Polar - & Meeresforschung
Columbusstraße
D-27568 Bremerhaven
Germany

Laine Boresjö Bronge
Dept. of Physical Geography
Stockholm University
S-106 91 Stockholm
Sweden

Thierry Brossard
CNRS Laboratoire de Geographie Physique
30, rue Megavand
F-25 030 Besancon
France

Carl Egede Bøggild
Søborg Hovedgade 215, 4.th.
DK-2860 Søborg

Ronny Bøhn
University of Oslo
Fagerheimgt. 9C
N-0567 Oslo
Norway

Ruggero Casacchia
CNR- Area Ficerca Frascati
Via E. Fermi, 70-C.P. 70
I-0+0044 Frascati, Roma
Italy

Vladimir Chernook
Knipovich Polar Research Institute
PINRO
6, Knipovich St
Murmansk, 183763
Russia

Charlotte Christensen
Danish Defence Command
P.O. Box 202
DK-2950 Vedbæk

Pu Bu Ci Ren
Geophysical Institute
University of Bergen
Allegaten 70
N-5007 Bergen
Norway

Ken Dean
Geophysical Institute
P.O. Box 757320
Fairbanks, AK 99775-7320
USA

Rune Dietz
Danmarks Miljøundersøgelser
Afdelingen for Arktisk Miljø
Tagensvej 135, 4. sal
DK-2200 København N
Denmark

Rune Engeset
Department of Physical Geography
P.O. Box 1042
Blindern
N-0316 Oslo
Norge

Helmut Epp
NWT Centre for Remote Sensing
Dept. of Renewable Resources 600
5102 50 Avenue
Yellowknife, NWT X1A 3S8
Canada

Tom George
Geophysical Institute
P.O. Box 757320
Fairbanks, AK 99775-7320
USA

Rasphal Gill
Danmarks Meteorologiske Institut
Lyngbyvej 100
2800 Lyngby

Professor
Preben Gudmandsen
Danmarks Tekniske Universitet
Elektromagnetisk Institut
Bygning 348
DK-2800 Lyngby

Vicedivisionschef
Jens Guldberg
ČRI A/S
P.O. Box 173
Bregnerødvej 144
3460 Birkerød

Christian Haas
Alfred Wegener Institut
Columbusstrasse
D-27568 Bremerhaven
Germany

Eivind Haneberg
UNIS
Boks 156
N-9170 Longyearbyen
Norway

Birger Ulf Hansen
Geografisk Institut
Øster Voldgade 10
DK-1350 København K.

Keld Q Hansen
Danmarks Meteorologiske Institut
Lyngbyvej 100
DK-2100 København

Mads Peter Heide-Jørgensen
Grønlands Fiskeriundersøgelser
Tagensvej 135, 1.
DK-2200 København N
Denmark

Ute Christina Herzfeld
Geomathematik
Fachbereich, Gewissenschaften
Universität Trier
D-54286 Trier
Germany

Ole P Hobberstad
University of Oslo
Sogn Stud By 5130
Oslo
Norway

Tuomas Häme
CEC Joint Research Centre
Institute for Remote Sensing Applications
Environmental Mapping and Modelling, T.P. 4-
I-21020 Ispra
Italy

Anne Jacobsen
National Environmental Research Institute
Dept. of Landscape Ecology
Grenåvej 12, Kalø
8410 Rønde

Johnny Johannessen
ESA-ESTEC OEE/VRO
Postbox 299
NL-2200 AG Noordwijk
The Netherlands

Daniel Joly
CNRS Laboratoire de Geographie Physique
30, rue Megavand
F-25030 Besancon
France

Stein Rune Karlsen
NORUT Information Technology
Tromsø Science Park
N-9005 Tromsø
Norway

Nicolai Kliem
Danmarks Meteorologiske Institut
Lyngbyvej 100
DK-2100 Copenhagen

Jukka Käyhkö
Laboratory of Physical Geography
University of Helsinki
P.O. Box 9
Fin-00014 Helsinki
Finland

Hans Christian Langager
Råstofforvaltningen for Grønland
Kompagnistræde 15
DK-1208 København K.

Shusun Li
Geophysical Institute
P.O. Box 757320
Fairbanks, AK 99775-7320
USA

Michael Manore
Canada Center for Remote Sensing
588 Booth str.
Ottawa, On, K1A 047
Canada

Thomas Martin
Alfred-Wegener Institut für Polar und Meeresforschung
P.O. Box 120161
Am Handeshaven 12
D-27515 Bremerhaven
Germany

Helmut Mayer
Dept. of Geomathematics
University of Trier
D-54286 Trier
Germany

Martin Miles
Nansen Environment and Remote Sensing Ce
Edvard Griegsvej 3a
N-5037 Solheimsvik
Norge

Kim Morris
Geophysical Institute
P.O. Box 757320
Fairbanks AK, 99775
USA

Kayhan Nadji
41 Gold City Court
Yellowknife, NWT, X12A 3P7
Canada

Poul Nielsen
Danmarks Meteorologiske Institut
Lyngbyvej 100
2800 Lyngby

Lennart Nilsen
University of Tromsø
Institute of biology
Department of Plant Ecology
N-9037 Tromsø
Norway

Fumihiko Nishio
Hokkaido University of Education
1-15-55 Shiroyama
Kushiro 085
Japan

E Parlow
MCR Lab
Department of Geography
University of Basel
Spalenring 145
CH-4055 Basel
Switzerland

Morten Hundahl Pedersen
Grønlands Forundersøgelser
P.O. Box 1003
3900 Nuuk

Mats Pettersson
Department of Radio and Space Science
Chalmers University of Technology
S-412 96 Göteborg
Sweden

Cecilie Rolstad
Norsk Polarinstitutt
Postbox 5072
Majorstua
N-0301 Oslo
Norway

Jung Rothenhäusler
Alfred Wegener Institut für Polar und Meeresforschung
Columbusstrasse
D-27515 Bremerhaven
Germany

Rosamaria Salvatori
Progetto Antartide
Via Tiburtina 770
I-000159 Roma
Italy

Axel Schweiger
Applied Physics Laboratory
Polar Science Center
University of Washington
Seattle, WA
USA

Alberto Blanco Sequeiros
Department of Geophysics
University of Helsinki
P.O. Box 4
00014 University of Helsinki
Helsinki
Finland

Michael Shindle
Alaska SAR Facility, Geophysical Institute
University of Alaska
P.O. Box 75 73 20
903 Koyukuk Dr
Fairbanks, AK 99775-7320
USA

Robert W Sidjak
Geography UNBC
3333 University Way
Prince George, BC
Canada V2N 4Z9

Sigmund Spjelkavik
UNIS
Postboks 156
N-9170 Longyearbyen
Norway

Andy Standley
Centre for Remote Sensing
University of Bristol
University Road
UK-Bristol BS8 1SS
England

Monika Stauber
Dept. of Geomathematics
University of Trier
D-54286 Trier
Germany

Mikkel Tamstorf
University of Copenhagen
Geographical Institute
Øster Voldgade 10
DK-1350 Copenhagen

Bjørn B Thomsen
Electromagnetics Institute
Technical University of Denmark
Lundtoftevej
DK-2800 Lyngby

Henrik Højmark Thomsen
Danmarks og Grønlands Geologiske Undersøg
Øster Voldgade 10
DK-1350 København K

Leif Toudal
Danmarks Tekniske Universitet
Elektromagnetisk Institut
Bygning 348
DK-2800 Lyngby
Denmark

Hans H. Valeur
Danmarks Meteorologiske Institut
Observationsafdelingen
Oceanografisk Sektion
Lyngbyvej 100
DK-2100 København Ø

Dagrun Vikhamar
University of Oslo
Ruths vei 22
N-0980 Oslo
Norway

Laurie Weir
Canadian Ice Services
Environment Canada
313 Sussex D r. Lasalle, Academy Block 3E
Ottawa K1A oH3
Canada

Roger Wheate
Geography, UNBC
3333 University Way
Prince George, BC
Canada V2N 4Z9

Jan-Gunnar Winther
Norsk Polarinstitutt
P.O.Boks 5072 Majorstua
Middelthunsgate 29
N-0301 Oslo
Norway

Therese With Berge
Skagesundveien 19
N-9010 Tromsø
Norway

Vladimir Zabavnikov
Remote Sensing Laboratory PINRO
6, Knipovich Street
183763 Murmansk
Russia

Oliver Zahner
Dept of Geomathematics
University of Trier
D-54286 Trier
Germany